



**HAL**  
open science

# Development of biosensors based on randomly oriented silicon nanowire networks for electrochemical or field-effect detection

Mónica Vallejo Pérez

► **To cite this version:**

Mónica Vallejo Pérez. Development of biosensors based on randomly oriented silicon nanowire networks for electrochemical or field-effect detection. Materials Science [cond-mat.mtrl-sci]. Université Grenoble Alpes [2020-..], 2021. English. NNT : 2021GRALI066 . tel-03607476

**HAL Id: tel-03607476**

**<https://theses.hal.science/tel-03607476>**

Submitted on 14 Mar 2022

**HAL** is a multi-disciplinary open access archive for the deposit and dissemination of scientific research documents, whether they are published or not. The documents may come from teaching and research institutions in France or abroad, or from public or private research centers.

L'archive ouverte pluridisciplinaire **HAL**, est destinée au dépôt et à la diffusion de documents scientifiques de niveau recherche, publiés ou non, émanant des établissements d'enseignement et de recherche français ou étrangers, des laboratoires publics ou privés.

## THÈSE

Pour obtenir le grade de

### DOCTEUR DE L'UNIVERSITÉ GRENOBLE ALPES

Spécialité : **Matériaux, Mécanique, Génie civil, Electrochimie**

Arrêté ministériel : 25 mai 2016

Présentée par

**Mónica VALLEJO PÉREZ**

Thèse dirigée par **Valérie STAMBOULI**  
et co-encadrée par **Nicolas SPINELLI** et **Céline TERNON**

Préparée au sein du **Laboratoire des Matériaux et du Génie Physique (LMGP)** et le **Département de Chimie Moléculaire (DCM)**  
dans l'**École Doctorale I-MEP2 - Ingénierie - Matériaux, Mécanique, Environnement, Énergétique, Procédés, Production**

**Développement de biocapteurs à base de réseaux de nanofils de silicium aléatoirement orientés pour une détection électrochimique ou à effet de champ**

**Development of biosensors based on randomly oriented silicon nanowire networks for electrochemical or field-effect detection**

Thèse soutenue publiquement le **12 juillet 2021**  
devant le jury composé de :

**Mr Michael HOLZINGER**

Directeur de Recherche, CNRS, Président du jury et Examinateur

**Mr Benoit PIRO**

Professeur, Université Paris Diderot, Rapporteur

**Mme, Hafsa KORRI YOUSOUFI**

Directrice de recherche, CNRS, Rapporteuse

**Mr Thierry NOGUER**

Professeur, Université de Perpignan, Examinateur

**Mme Valérie STAMBOULI**

Chargée de recherche, CNRS, Directrice de thèse

**Mr Nicolas SPINELLI**

Maitre de conférences, Université Grenoble Alpes, Invité

**Mme Céline TERNON**

Maitresse de conférences, Grenoble INP, Invitée

**Mme Chantal GONDRAN**

Maitresse de conférences, Université Grenoble Alpes, Invitée



*To my parents, Doris and Rubén Darío  
my grandparents, Hilda and Fernando  
and my brother, Juan David*

# Acknowledgments

Writing the acknowledgements of my thesis is how I conclude this stage, which will undoubtedly remain in my memory as one of the most important chapters of my life.

Doing a PhD is far from being simply a professional choice, it is an adventure full of contrasts and nuances, which you could not have even imagined before embarking on such a journey. It is a back-and-forth between moments of absolute happiness when things finally go well and you get the long awaited results, but whose attainment implies the existence of difficult moments, many endless working days and a quite considerable dose of stress and frustration. And although the latter does not sound like the ideal task, at the end of the story you look back and realize that everything, absolutely everything was worth it.

This achievement would not have been possible without the help and support of many wonderful people who accompanied me throughout this adventure. These people will always hold an important place in my heart, and I would like to express my deepest feelings of gratitude to them.

First of all, I would like to thank my thesis directors, Valérie Stambouli and Nicolas Spinelli. I still remember as if it was yesterday the interview in which I applied for the PhD. From that moment on, I was certain that this was the path I should choose. Thank you for giving me the opportunity to develop this project, for guiding and accompanying me through it, and for helping me to stay motivated and confident in the moments when things did not go as expected.

To Franz Bruckert and Carmen Jimenez, thank you for opening the doors of the LMGP for me. As we once discussed, the LMGP has the right environment to make each of its students feel welcome and supported, and this is thanks to their daily effort and work. I feel very fortunate to have been part of the lab for a little more than three years. To Didier Boturyn and Serge Cosnier,

thank you for allowing me to develop an important part of my project at the DCM, where I was finally able to obtain the most gratifying results of my thesis.

One of the most important thanks goes to Chantal Gondran, with whom I feel deeply honored to have been able to work. A thousand thanks for having taken on the role of supervisor of my thesis, even when you did not have that role officially, and for leading me through the exciting world of electrochemistry, of which I had no idea before starting this project. It was a great fortune to have been guided in this field by such an excellent professional. Thank you for each of the explanations, ideas, pieces of advice and for the confidence that you gave me when I decided to venture into a new domain that was not envisaged in the initial plans of the thesis. Finally, thank you for all the time you reserved for me even when I know you did not really have it, for all the afternoons you extended your working day so that I could stay in the lab finishing my long experiments, and for helping me to stay motivated and confident in difficult moments.

Céline, I really appreciated working with you. Thank you for so many enriching conversations in which you were always able to clarify each of my doubts in the right way. It was very inspiring to work with such a great scientist and advocate of equality between men and women in science and work.

Christoforos, thank you for your valuable help in the electrical characterization section of my thesis. Thank you for always being available for discussion and for the good humor that characterizes you.

To all the other people who in one way or another were part of the development of this project, thank you very much. I would like to extend a special thanks to Karine Gorgy, Xavier Mescot, Marianne Weidenhaupt, Laetitia Rapenne, Etienne Pernot and Isabelle Gélard, who gave me their time and expertise in each of their respective specialties. I would also like to thank each of the administrative staff of both laboratories, Michèle, Josiane, Annie and Arielle, all of whom were

always friendly and helpful, allowing everything to run properly in the workplace while we were busy doing science.

To the members of the jury, Hafsa Korri-Youssoufi, Benoît Piro, Michael Holzinger and Thierry Noguier, I am deeply indebted to you for evaluating this thesis work and for each of your constructive comments.

And the section of acknowledgements to friends has to start without any doubt with you, Guillaume. We started our PhD on the same day, a little later than the other students of that year, and we became doctors practically at the same time. From the first day I knew that our relationship would go far beyond being just colleagues, and I was not wrong, in you I found one of the most valuable friendships of my life. Thank you for the countless good times we have had together, for the support, advice and encouragement in times of difficulty and for being the best office mate ever. Sharing the burden of the hard writing period with you made it a lighter time, thanks to the daily mood drawings, the morning (and often afternoon) coffees and the countless laughs throughout the working days.

To Damir and Maxime, thank you for your invaluable friendship. I never imagined that I would meet such good friends far away from home. I will always keep in my memory all the good times we shared together inside and outside the lab (where Guillaume was also always present), the endless coffee breaks and the karaoke soirées. I am convinced that this friendship will go beyond the PhD.

José, Chiara and Carlos, thank you for all the good times we spent at La Choza. For the series afternoons and the always fun soirées. You are present in a great part of the good memories of my stay in Grenoble, which I will always carry with me.

Guislain, thank you for all the cakes you baked for me, whether for my birthday or to cheer me up when there were problems, which I must say worked perfectly.

And each of the PhD students, postdocs and interns with whom I had the opportunity to share happy moments in and out of the lab, thank you very much. Especially to Dorina, who was always concerned about the welfare of all of us around her, Raquel, Clément, Adrià, Tabassom, Danial, Morgane, Fanny, Camilo, Mathilde, Lorenzo, Pierre, Thuy, Etienne, Octavio, Rosa, Alexandre, Laëtitia, Shruti, Abdou, Ragnar, Fidel, Alexander, Thanasis, Masoud, Huy, Chieu, Bastien, Anastasiia and Isaac, whom I thank deeply for his valuable help during my last days of experiments.

To my roommates during my last year of thesis, Ari and Katee, thank you very much. I am so happy and grateful to have shared an important part of my stay in Grenoble and so many good moments with you girls, you are without any doubt the best colocs ever.

Y ahora, la sección de agradecimientos en español, para mi familia y amigos Colombianos.

Cuando estas lejos de tu país buscas sumergirte en esa nueva cultura, vivirla y disfrutarla. Pero al mismo tiempo, y de manera instintiva, también quieres encontrar personas que se parezcan un poco a ti, que comprendan tus costumbres, tus gustos, tus chistes. Así puedes sentirte un poco como en casa cuando estás con ellos (bueno, al menos ese fue mi caso). Eso lo encontré con Nohora, Marcela, Andrés, Ame, Daniel A. y Elena. Gracias por hacer parte de mi historia en Grenoble.

Por supuesto, tengo muchísimo que agradecer a mi familia y amigos que desde Colombia me han apoyado, animado y alentado a luchar por cada uno de mis sueños, y quienes a pesar del tiempo y la distancia siempre me han acompañado con amor en cada uno de mis pasos. Miles de gracias a Alba, Hugo, Camilo, Natalia, Cristina, Erika, Xiomara, y cada uno de los integrantes de mi familia y amigos que siempre han estado presentes para mí.

Y finalmente, los agradecimientos más importantes de esta tesis doctoral van dirigidos a mis padres, Doris y Rubén Darío, a mis abuelos, Hilda y Fernando y a mi hermano, Juan David. Sin ellos

simplemente nada hubiera sido posible. No me alcanzaría la vida para agradecerles cada gesto de amor puro, que poco a poco guio mi camino para construir la mujer que soy hoy en día. A mis padres, gracias infinitas por cada uno de sus sacrificios y esfuerzos sobrehumanos, gracias por ser el mejor ejemplo a seguir. A mis abuelos, mil gracias por el amor y el apoyo incondicional que siempre nos han brindado. Ese apoyo nos permitió alcanzar nuestros sueños. Y a mi hermano, gracias por apoyarme incondicionalmente en los momentos complejos, gracias por cada uno de los sabios consejos que siempre sabes brindarme en los tiempos difíciles.

*Merci, Thanks, gracias.*

# Contents

<b>Acknowledgments</b> .....	<b>I</b>
<b>Contents</b> .....	<b>VI</b>
<b>List of abbreviations</b> .....	<b>X</b>
<b>Introduction</b> .....	<b>1</b>
<b>Chapter I: State of the art</b> .....	<b>4</b>
I.1.    The biological recognition element or bioreceptor.....	7
I.1.1.    Nucleic acid bioreceptors.....	7
I.1.2.    Aptamers.....	9
I.2.    Nanomaterial-based transducers.....	10
I.2.1.    Silicon nanowires: properties and applications in biosensing technologies.....	11
I.2.2.    Si nanonets: a new and promising alternative .....	13
I.2.2.1.    Si nanonets as building blocks for electrical devices .....	15
I.2.2.2.    Si nanonets as building blocks for electrochemical devices.....	19
I.3.    Bioreceptor immobilization methods.....	20
I.3.1.    Adsorption.....	21
I.3.2.    Encapsulation.....	21
I.3.3.    Covalent bonding.....	21
I.3.4.    Immobilization by affinity interactions.....	22
I.4.    Transduction techniques used for biosensing .....	23
I.4.1.    Field-Effect Transistor (FET)-based biosensors.....	24
I.4.1.1.    Theoretical background.....	24
I.4.2.    Electrochemical biosensors.....	29
I.4.2.1.    Theoretical background.....	31
I.4.2.2.    Voltammetric biosensors.....	38
I.4.2.3.    Impedimetric biosensors.....	41
I.5.    Objective of the PhD thesis.....	47
References .....	49

**Chapter II: Development of Si nanonet-based FET biosensors ..... 61**

- II.1. Si nanonet-based FETs ..... 63
  - II.1.1. Si nanonet fabrication ..... 63
  - II.1.2. Si nanonet-based FET fabrication ..... 66
- II.2. Biofunctionalization processes..... 69
  - II.2.1. APTES-based biofunctionalization process ..... 70
    - II.2.1.1. Effect of the chip position during the imine bond reduction step..... 74
    - II.2.1.2. Effect of the NaBH<sub>4</sub> concentration and duration of the imine bond reduction step .. 75
  - II.2.2. GOPS-based biofunctionalization process ..... 77
    - II.2.2.1. Optimization of the GOPS-based biofunctionalization process using UV radiation.... 79
      - II.2.2.1.1. Wettability analyses ..... 81
      - II.2.2.2. Si nanonet-based FETs biofunctionalization by UV-assisted GOPS-based process..... 82
        - II.2.2.2.1. Biofunctionalization monitoring by STEM-EDS..... 82
        - II.2.2.2.2. Biofunctionalization monitoring by AFM..... 84
- II.3. Conclusions..... 89
- References..... 91

**Chapter III: Electrical detection of DNA hybridization in dry environment using Si nanonet-based FET biosensors ..... 94**

- III.1. Electrical characterizations of Si nanonet-based FETs..... 96
- III.2. Electrical detection of DNA hybridization ..... 99
  - III.2.1. Study of the biosensor formation.....101
    - III.2.1.1. Stability of the transfer characteristics of biofunctionalized Si nanonet-based FETs..... 101
    - III.2.1.2. Hybridization capacity in time ..... 103
    - III.2.1.3. Impact of the surface environment on the Si nanonet-based FET properties ..... 105
- III.3. Conclusions..... 108
- References.....111

## **Chapter IV: Development of Si nanonet-based electrochemical biosensors ..... 113**

IV.1. Au/Si nanonet-based electrodes.....	116
IV.1.1. Effect of the APTES-based functionalization process on bare Au electrodes.....	118
IV.1.1.1. Electrochemical analyses of the APTES functionalization process using different redox probes.....	119
IV.1.1.2. X-ray photoelectron spectroscopy analysis of APTES functionalized Au surfaces.....	126
IV.1.2. Effect of the GOPS-based functionalization process on bare Au electrodes.....	126
IV.1.2.1. Electrochemical analyses of the GOPS functionalization process using different redox probes.....	127
IV.1.3. Fabrication process of the Si/Au nanonet-based electrodes.....	131
IV.1.4. Electrochemical stability over time of Au/Si nanonet-based electrodes.....	132
IV.2. C/Si nanonet-based electrodes.....	134
IV.2.1. Fabrication process of the C/Si nanonet-based electrodes.....	134
IV.2.2. Choice of the redox probe.....	135
IV.2.3. Biofunctionalization of C/Si nanonet-based electrodes using poly(pyrrole-NTA) films....	138
IV.2.3.1. Poly(pyrrole-NTA) film fabrication processes.....	140
IV.2.3.1.1. Polypyrrole-NTA film fabrication by monomer adsorption in liquid conditions followed by chemical polymerization.....	141
IV.2.3.1.2. Polypyrrole-NTA film fabrication by monomer adsorption in dry conditions followed by electropolymerization.....	148
IV.2.3.2. Immobilization of the biotin labelled bioreceptor (TBA-15 aptamer).....	152
IV.2.3.2.1. Nitrilotriacetic acid (NTA)-Cu <sup>2+</sup> interaction.....	152
IV.2.3.2.2. Cu <sup>2+</sup> -biotin interaction.....	157
IV.3. Conclusions.....	160
References.....	161

**Chapter V: Electrochemical detection of thrombin using Si nanonet-based biosensors.. 166**

V.1. Detection protocol..... 168

V.2. Detection ability without Si nanonet..... 169

V.3. Optimization of the Si nanonet-based electrochemical biosensors..... 169

    V.3.1. Effect of the TBA-15 bioreceptor concentration on thrombin detection..... 170

    V.3.2. Effect of the Si nanonet density on thrombin detection..... 174

        V.3.2.1. Effect of the Si nanonet density on the electrochemical properties of the Si nanonet-based biosensors..... 176

        V.3.2.2. Choice of the Si nanonet density ..... 180

V.4. Sensitivity of the Si nanonet-based electrochemical biosensor ..... 181

    V.4.1. Biosensor sensitivity evaluated by cyclic voltammetry ..... 181

    V.4.2. Biosensor sensitivity evaluated by electrochemical impedance spectroscopy..... 183

V.5. Specificity of the Si nanonet-based electrochemical biosensor ..... 188

V.6. Conclusions..... 190

References..... 191

**General conclusion.....194**

**Résumé de la thèse en Français.....197**

**Abstract/Résumé.....203**

# List of abbreviations

**AFM** Atomic Force Microscopy

**APTES** (3-Aminopropyl)triethoxysilane

**BB** Blown–Bubble method

**BSA** Bovine Serum Albumin

**$C_{dl}$**  Double layer capacitance

**CPE** Constant Phase Element

**CV** Cyclic Voltammetry

**CVD** Chemical Vapor Deposition

**Cy3** Cyanine-3

**$D$**  Diffusion coefficient

**DNA** Deoxyribonucleic Acid

**EIS** Electrochemical Impedance Spectroscopy

**$f$**  Characteristic frequency

**FET** Field-Effect Transistor

**GOPS** (3- Glycidyloxypropyl) trimethoxysilane

**IgG** Human Immunoglobulin G

**$I_{off}$**  Off-state drain current

**$I_{on}$**  On-state drain current

**$I_{pa}$**  Anodic current

**$I_{pc}$**  Cathodic current

**$k^0$**  Heterogeneous rate constant

**LB** Langmuir– Blodgett method

**MOSFET** Metal-Oxide-Semiconductor Field-Effect Transistor

**NW** Nanowire

**Poly(Pyrrole-NTA)** Poly(pyrrole-nitrilotriacetic acid)

**$R_{ct}$**  Charge transfer resistance

**$R_s$**  Resistance of the solution

**SCE** Saturated Calomel Electrode  
**SEM** Scanning Electron Microscopy  
**SLS** Solution-Liquid-Solid mechanism  
**SS** Subthreshold Slope  
**STEM-EDS** Scanning Transmission Electron Microscopy  
**TBA-15** Thrombin Binding Aptamer  
 **$V_d$**  Drain voltage  
 **$V_g$**  Gate voltage  
**VLS** Vapor-Liquid-Solid mechanism  
 **$V_{th}$**  Threshold voltage  
**Z** Impedance modulus  
 **$Z_w$**  Warburg impedance

# Introduction

The growing need to develop portable devices allowing the detection and quantification of biological species in a reliable, fast and economical way is one of challenges facing science today. The rise of nanotechnology in the last decades has allowed the development of a new generation of biosensors based on nanostructures, which present very interesting characteristics, such as a high specific surface area, and a size comparable to most biological molecules. These properties have opened the door to the development of ultrasensitive sensors, capable of providing real-time information.

Among these nanostructures, semiconducting silicon nanowires have been extensively studied. In addition to the aforementioned properties, these nanostructures benefit from a wide expertise regarding their fabrication processes and integration into electronic devices. However, the devices fabricated from this type of nanostructures require the use of complex, long and expensive technological processes, often presenting problems of reproducibility.

In this context, and for the first time, this project investigates the possibility of using a 2D assembly of randomly oriented Si nanowires, so called *Si nanonet*, as a building block for the fabrication and development of two different types of biosensors: Si nanonet-based Field-Effect Transistor (FET) biosensors and Si nanonet-based electrochemical biosensors. Indeed, such a 2D network benefits from the intrinsic properties of each 1D nanowire constituting it, and particularly from their very large specific surface. Moreover, compared to devices composed of single Si nanowires, the use of a 2D network structure offers other very interesting properties such as high fault tolerance, better electrical reproducibility and mechanical flexibility.

These two kinds nanonet based biosensors aim to detect, on the one hand, the DNA hybridization in dry conditions in the case of the FET biosensor, and on the other hand, the thrombin in the case of the electrochemical biosensor.

Both of these fabricated devices were biomodified using the same bioreceptor: the TBA-15 aptamer. However the way of biomodification was different depending on the considered device.

Thus, this work is divided into five chapters:

Chapter I presents an overview about the components of a biosensor, the different methods used for its biofunctionalization, and the transduction techniques employed. Special emphasis was made on the state of the art of biosensors based on silicon nanostructures (1D Si NWs and 2D Si nanonets).

Chapter II discusses the fabrication process of Si nanonet-based FET devices, as well as the different routes studied for their biofunctionalization. The objective of this part was to develop a process allowing the proper immobilization of the bioreceptor on the Si nanonet-based FET devices.

Chapter III concerns the electrical detection of DNA hybridization, using Si nanonet-based FET devices in a dry environment. For this purpose, the different parameters involved in the detection process were studied and optimized.

Chapter IV presents the development of the Si nanonet-based electrochemical biosensor, for thrombin detection. For this purpose, different studies were carried out, such as the choice of the working electrode material to be used as substrate for the Si nanonet, the development of a protocol enabling the fabrication and biofunctionalization of the Si nanonet-based electrodes and the choice of the appropriate redox probe for the electrochemical system.

Finally, chapter V explores the detection of thrombin using Si nanonet-based electrochemical biosensors. Thus, the different parameters involved in the performance of the biosensor, such as the density of the Si nanonet and the concentration of the bioreceptor, were optimized.

As can be noted, this multidisciplinary work involved the convergence of different fields, notably materials science, microelectronics, electrochemistry, surface functionalization and biology. The project was carried out mainly in two laboratories in the frame of an “Initiative de Recherche Stratégique” from the IDEX Univ. Grenoble Alpes:

- Laboratoire des Matériaux et Génie Physique (LMGP), where it was performed the fabrication process of the Si nanonets, as well as the biofunctionalization of the Si nanonet-based FET devices.
- Département de Chimie Moléculaire (DCM), where the fabrication and analyses of Si nanonet-based electrochemical biosensors were carried out.

In addition, for full completion, this work has received funding from the EU H2020 RIA project Nanonets2Sense, and from the EU H2020 ERA-NET project Convergence. This project also benefited from several collaborations, notably with the Laboratoire des Technologies de la Microélectronique (LTM), where the Si NWs were fabricated, the Plateforme Technologique Amont (PTA), cooperated by CNRS Renatech and CEA Grenoble, which allowed the fabrication of the Si nanonet-based FET devices, and L'Institut de Microélectronique Electromagnétisme et Photonique (IMEP-LaHC), where the electrical characterizations of the FET devices were performed. Finally, this work benefited from the facilities and expertise of the OPE)N(RA characterization platform of FMNT, supported by CNRS, Grenoble INP and UGA.

**Chapter I: State of the art**

## Chapter I: State of the art

---

<b>Chapter I: State of the art .....</b>	<b>4</b>
I.1.  The biological recognition element or bioreceptor.....	7
I.1.1.  Nucleic acid bioreceptors.....	7
I.1.2.  Aptamers.....	9
I.2.  Nanomaterial-based transducers.....	10
I.2.1.  Silicon nanowires: properties and applications in biosensing technologies.....	11
I.2.2.  Si nanonets: a new and promising alternative .....	13
I.2.2.1.  Si nanonets as building blocks for electrical devices .....	15
I.2.2.2.  Si nanonets as building blocks for electrochemical devices.....	19
I.3.  Bioreceptor immobilization methods.....	20
I.3.1.  Adsorption.....	21
I.3.2.  Encapsulation.....	21
I.3.3.  Covalent bonding.....	21
I.3.4.  Immobilization by affinity interactions.....	22
I.4.  Transduction techniques used for biosensing .....	23
I.4.1.  Field-Effect Transistor (FET)-based biosensors.....	24
I.4.1.1.  Theoretical background.....	24
I.4.2.  Electrochemical biosensors.....	29
I.4.2.1.  Theoretical background.....	31
I.4.2.2.  Voltammetric biosensors.....	38
I.4.2.3.  Impedimetric biosensors.....	41
I.5.  Objective of the PhD thesis.....	47
<b>References .....</b>	<b>49</b>

A biosensor has the function of detecting and in some cases also quantifying a specific target, through the interaction between a *biological element or bioreceptor* capable of generating a recognition event at the moment of interacting with its *target*, and a physical element that acts as a *transducer*, converting the recognition event into a detectable *signal* (Figure I-1)[1].

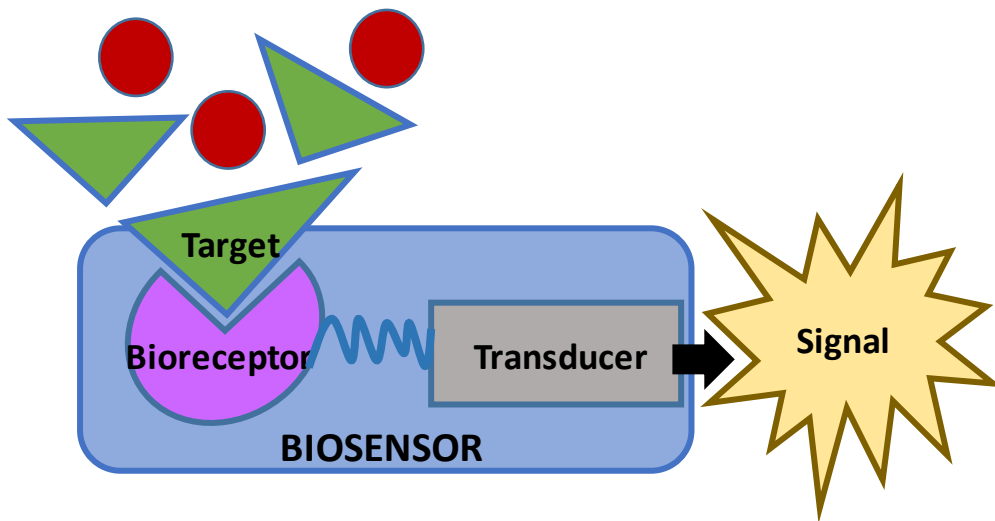


Figure I-1: Schematic representation of the working principle of a biosensor

These devices are currently used in a wide variety of fields, such as the clinical diagnostics, food traceability, quality and safety, detection of drugs or dangerous substances, water quality management and pollution monitoring [1]. Research in this field is currently directed towards the miniaturization due to several reasons, such as the need of developing portable devices for rapid analysis (results obtained in minutes), where skilled personnel and infrastructure with complex analysis equipment are unavailable, and for patients who do not have easy access to centralized healthcare facilities [2], or because of the growing demand for the development of disposable biosensors, especially for medical applications. Another important reason is the permanent search for cost reduction, as generally the most expensive part of a biosensor is the biomolecule used as bioreceptor, and normally the smaller is the biosensor, the less biomolecule is required.

Each of the constituent parts of a biosensor will be discussed in detail below.

### **I.1. The biological recognition element or bioreceptor**

The bioreceptors are the key to specificity for the biosensor methods and the significant distinguishing feature of the device. A bioreceptor is a molecular species that uses a biochemical mechanism for the recognition of the target analyte, and is responsible for binding the analyte of interest to the sensor surface for the measurement [3]. Essentially, it is crucial for a bioreceptor to be selective and sensitive towards the specific target, preventing the interference with other substances present in the sample matrix [4]. The most common forms of bioreceptors used in biosensing are based on enzymes, antibodies, nucleic acids and cells. Here, we will focus on nucleic acids and aptamers, as they are the type of bioreceptor used in the project.

#### **I.1.1. Nucleic acid bioreceptors**

Deoxyribonucleic acid (DNA) is the carrier of genetic information and the foundation material of biological heredity. Nucleic-acid sequences, which are unique in any living organism, virus or pathogen, provide practical ways to recognize and diagnose numerous diseases [5]. The term nucleic acid is the overall name for Deoxyribonucleic acids (DNA) and Ribonucleic acids (RNA). DNA is a double-stranded molecule, composed of four nitrogen bases or nucleotides: adenine, thymine, cytosine, and guanine, and RNA is a single-stranded molecule, composed of the same bases as DNA, but instead of thymine, it has uracil.

Identification and sequencing of DNA molecules have received much attention since 1953, when Watson and Crick proposed the double helix structure of DNA, and research in this field continues to grow extensively [5,6]. The base-pairing interactions between complementary sequences are highly specific and robust, and they are the principle on which DNA biosensors are based.

Watson and Crick demonstrated that DNA is a double-helical structure, made of two strands that wrap around each other on the same axis (Figure I-2(a)). As mentioned before, it is composed of base units called nucleotides, each consisting of a deoxyribose (a sugar), a phosphate group and a nitrogenous base (Figure I-2(b)). There are four major nitrogenous bases: adenine (A), thymine (T), cytosine (C) and guanine (G).

The formation of a double-stranded structure is possible because of the complementarity of the nucleotides. Indeed, each base can only bond with one other, A with T, and C with G (Figure I-2(a)). The two strands are held together by hydrogen bonds between the bases (showed in Figure I-2(b)). Furthermore, in terms of its morphology, the diameter of the double helix is 2 *nm*, and its length depends on the number of nucleotides as the distance between two nucleotides is 0.34 *nm*. Finally, it is important to note that DNA molecules are negatively charged, due to the negative charge of the phosphate component in each base (highlighted in green circles in Figure I-2(b)). The change in global charge generated by the hybridization of complementary strands is the basis of the principle of detection of the Si nanonet-based FET biosensors developed in this project.

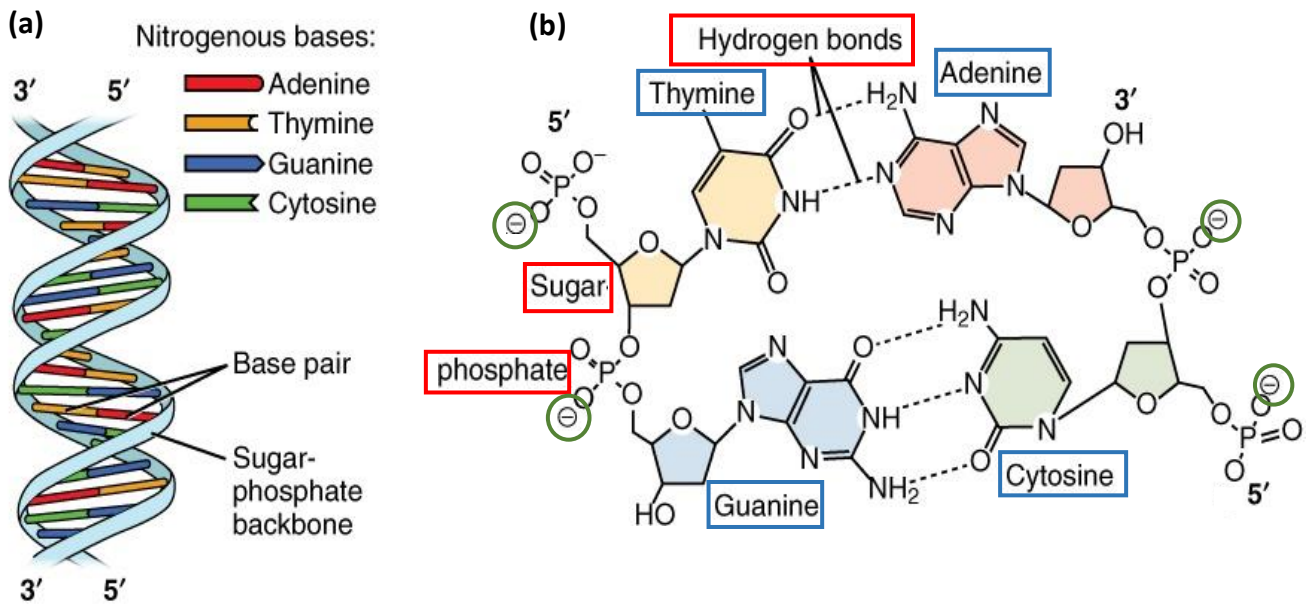


Figure I-2: (a) Schematic representation of the double helix structure of DNA composed of two complementary strands (b) Nucleotide bonding in the DNA molecule (Image Source: Albert.io).

Some of the applications of the DNA hybridization sensors are diagnostic test for mutations, monitoring gene expression, screening for targets known to play a role in disease, assessment of medical treatment, environmental investigations and biological warfare agent detection [1].

### I.1.2. Aptamers

Aptamers are short RNA, DNA, or synthetic XNA (Xeno Nucleic Acids: synthetic nucleic acid analogues, that have a different sugar backbone than the natural nucleic acids) molecules, which can fold into stable and unique three-dimensional structures through intermolecular interactions such as electrostatic and van der Waals interactions, the stacking of aromatic rings or hydrogen bonds, and can interact with their targets with high specificity and affinity [7–9]. Thus, aptamers interact with and bind to their targets through structural recognition (Figure I-3), a process similar to the antigen-antibody interaction [10].

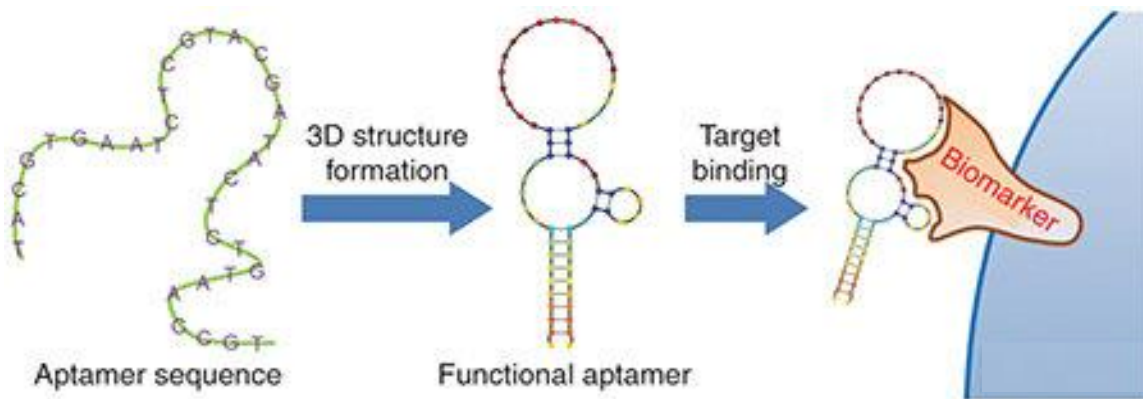


Figure I-3: Schematic diagram of an aptamer binding its target [10].

Therefore, aptamers are nucleotide analogous to antibodies, but they present many advantages. Both aptamers and antibodies have high affinity with their target molecule in concentrations up to the picomolar range and both are highly specific. However, the production of antibodies involves expensive biological processes and often need the use of laboratory or farm animals, which can lead to batch-to-batch variation and ethical problems, while the aptamers are produced from chemical processes, giving them an excellent reproducibility and significantly lower production costs. In addition, aptamers are more stable and can be chemically modified more easily [11,12]. Moreover, thanks to their nucleic acid nature, aptamers are easier to handle and to keep than antibodies. For example, if both can be denaturated when submitted to chaotropic conditions (temperature, organic solvent, etc), denaturation of antibodies (i.e loss of

structuration and consequently recognition properties) is irreversible, whereas aptamers can refold in a structure allowing the recognition of the analyte of interest.

Each aptamer is selected specifically to bind to its target. The technique used to identify aptamers with high affinity and specificity for different targets is called systematic evolution of ligands by exponential enrichment (SELEX). This method employs a random library of oligonucleotides from which the sequences with desired characteristics of affinity and specificity are selected [11,13,14]. Range and size of aptamer targets spread from mere ions, nucleotides, small molecules, RNA structures, proteins, viruses, bacteria, or even whole living cells [15].

In this project, we used the Thrombin Binding Aptamer (TBA-15)[16] as bioreceptor for the electrochemical detection of thrombin. Indeed, not only this protein plays an important physiological role in regulating hemostasis and maintaining blood coagulation cascade [17], but also this aptamer has been extensively studied and thus provides a good model.

### **1.2. Nanomaterial-based transducers**

The use of materials at the nanodimension scale (between 1 and 100 nm in size) offers numerous improvements in terms of analytical features including sensitivity, rapidity of response, selectivity, and robustness, demonstrating the multiple advantages of using nanomaterials over micromaterials in the development of smart and high-performant analytical tools [18]. One of the reasons why nanoscale materials are particularly interesting for the construction of biosensors is the fact that the interaction between the nanomaterial-based transducer and the analyte is highly efficient due to the very large surface to volume ratios in nano-size devices [19]. This property in turn allows to increase the quantity of bioreceptor units that can be grafted on the biosensor surface, thus optimizing its sensitivity.

Among such nanomaterials, silicon nanowires, carbon nanotubes, graphene, gold nanoparticles, semi-conductor quantum dots, polymer nanoparticles and nanodiamonds have been among the most studied nanostructures for biosensing applications [20–22]. As Si nanowires are the base material in this project, their properties and use in the field of biosensors will be detailed below.

### **I.2.1. Silicon nanowires: properties and applications in biosensing technologies**

Silicon is the second most abundant element in the Earth's crust (about 28% by mass), after oxygen. This element is specially known for its very good semiconducting properties and in particular for its excellent carrier mobility. Indeed, electrons and holes have a respective mobility of about 1000 and 500 cm<sup>2</sup> V<sup>-1</sup> s<sup>-1</sup> at room temperature. Silicon has been the dominant material in the microelectronics industry for over 40 years, and its fundamental and technological properties are well known [23–25].

Moreover, silicon nanowires (Si NWs) present important characteristics that make them very attractive for applications in the field of biosensors. First, at present it is possible to finely fabricate and control their chemical configuration, morphology, and arrangement either separately or in combination with other materials, leading to the development of a nanomaterial with specific and efficient electronic properties [20]. Second, today it exists the technology and expertise necessary to integrate Si NWs into transistor structures, notably in the area of MOSFETs (Metal-Oxide-Semiconductor Field-Effect Transistor), which will be detailed later. Third, as nanostructures are dominated by surface effects, Si NWs are extremely sensitive to their external electrical environment, making them excellent candidates for electrical biosensing. Finally, their size is comparable to that of many biological entities, such as DNA, proteins and important subcellular structures, which make them an ideal alternative for transducer biosensing [23,26].

In 2001, Lieber's group reported for the first time the promising of single Si NWs as transducers in biosensors. They produced a Boron-doped single Si NW-based biosensor. First, they used amine-functionalized Si NWs to produce a pH sensor with a pH-dependent conductance that was linear over the pH 2 to 9 range. Second, biotin-modified Si NWs were used to detect streptavidin down to at least a picomolar concentration range. Third, they studied the reversible binding of monoclonal anti-biotin (m-anti-biotin) with biotin, which showed reversible antibody binding and concentration-dependent detection in the nanomolar range. Finally, they modified the Si NW surface with calmodulin for the detection of Ca<sup>2+</sup> ions, which are in charge of important biological

process in the body, such as cell development and death, muscle contraction and protein secretion [27]. Twenty years after, numerous groups have succeeded in using Si NWs as transducer for the detection of different molecules, through different techniques such as Surface-Enhanced Raman Scattering, biosensing by Field-Effect transistors, and fluorescence and electrochemical methods [20].

Single Si NWs have been widely used in the construction of Field -Effect Transistor biosensors, as can be observed in Table I-1, which shows some of the reports found for the biosensing of different molecules and their limit of detection.

*Table I-1: Some examples of single Si NW-based FET biosensors for electrical biosensing.*

<b>Target molecule</b>	<b>Detection limit</b>	<b>Reference</b>
DNA hybridization	0,1 fM [28], 100 pM [29], 1 nM [30]	[28–30]
Interleukin-1 $\beta$ genes	2,5 fM	[31]
Adenosine triphosphate	100 pM	[32]
Streptavidin	10 fM	[33]
IgG, IgA	100 fM	[33]

There are two possibilities for the fabrication of Si NW-based FET biosensors: either by top-down approach or by bottom up approach. The first case (top-down approach) implies to turn a bulk wafer into nanowire structure, by means of techniques such as Electron Beam Lithography (EBL) [34], Nanoimprint Lithography (NIL) [35], and Sidewall Transfer Lithography (STL) [36]. Subsequently the microfabrication processes are carried out. However, this option remains complex because of the need for precise instrumentation, and because these techniques are time consuming and costly.

The second option is to fabricate the biosensor from Si NWs grown by the bottom-up approach. In that case, the silicon atoms are assembled atom-by-atom to form the Si NW, through techniques as vapor-liquid-solid (VLS) growth or solution-liquid-solid (SLS) mechanism. Then, the single Si NW is transferred on a substrate and it is subsequently integrated into the FET biosensor

structure [37]. Nevertheless, this type of fabrication also presents some disadvantages, such as limitations in the channel length/width size, which are subject to the original Si NW dimensions, reproducibility problems due to differences between the Si NWs and requirement of precise alignments of the Si NWs [38]. These alignments should be carried out through complex methods such as Langmuir–Blodgett (LB), blown–bubble (BB), microfluidic flow, electric field and contact printing alignment [37].

To overcome these drawbacks, an alternative approach consists of using 2D networks of randomly oriented Si NWs (Si nanonets), which can be transferred on a wide range of substrates and are fully compatible with MOSFETs fabrication processes.

### **I.2.2. Si nanonets: a new and promising alternative**

In 2006, G. Gruner introduced the term “nanonet”, which is an acronym for NANOstructured NETwork, referring to an assembly of nanowires randomly oriented on a substrate [39]. Depending on the thickness of the film, it could be a three-dimensional nanonet, presenting a thickness comparable to the length of the nanostructure (Figure I-4a)), or a two-dimensional nanonet, presenting film thickness comparable to the diameter of the nanostructures (Figure I-4(b)) [40,41].

These structures, whether three-dimensional or two-dimensional, are governed by the percolation theory, which describes the way in which a system with randomly distributed objects of a given geometry can form or not form connections between them [42]. A nanonet is then defined as percolating when a network of infinite size can communicate over the entire network via percolation paths (highlighted in Figure I-4b)), which are constituted by the nanostructures and connections between them [23]. In this project, we will work with two-dimensional nanonets in which the current flows through percolation paths.

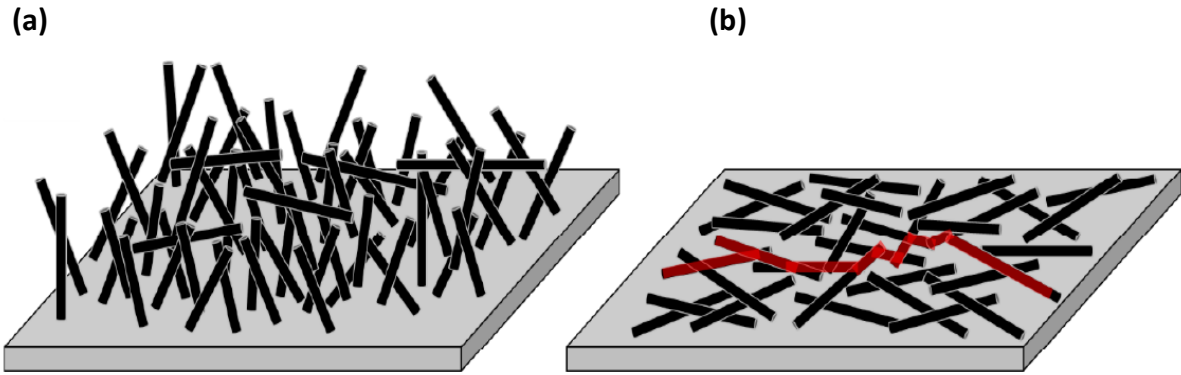


Figure I-4: Schematic representation of a (a) three-dimensional and (b) two-dimensional nanonet. A percolation path is highlighted in red in the figure (b) [23]

This type of nanostructure benefits from the aforementioned properties of their base components (NWs), but at the same time presents new advantages that appear when the nanomaterials are assembled to form a network [23,39]:

- **Electrical conductance:** When the base material of which the nanonet is composed is a conductor or a semiconductor, the charge carriers can circulate through the network. However, the overall conductivity of the nanostructure depends on the junctions between its individual components (NWs).
- **Porosity and optical transparency:** Due to the very high aspect ratio of nanostructures, nanonets are transparent even when NWs are not. This property is related to the NW density, and make them particularly attractive for the fabrication of transparent electrodes.
- **Mechanical resistance and flexibility:** In general, a network of wires has a significantly higher mechanical flexibility than that of a film, making the architecture particularly interesting to flexibility-requiring applications. In addition, it has been demonstrated that this type of structures has the ability to adapt to the morphology of the underlying substrate [43].

- **Fault tolerance:** Even if a conducting path is broken, many others will remain open, ensuring current flow in the nanonet. Moreover, the macroscopic properties of the nanonet result from an important number of nanowires, which makes it possible to average out the differences between individual nanostructures.

Several nanonet-based materials have been studied during the last decades. They have been used for different applications, some of which are shown below. Carbon nanotube (CNT) networks have been used as transducers in biosensors and have also been successfully integrated in the fabrication flexible circuits [44,45]. Silver nanonets have been studied for the development of transparent electrodes and flexible transparent thin film heaters [46,47]. Tin oxide (SnO<sub>2</sub>) nanonets have been used in the fabrication of High-Performance Field-Effect Transistors and ultraviolet photoelectrodes [48,49]. Zinc oxide (ZnO) nanonets have been integrated in the fabrication of Field-Effect transistors and gas sensors [50,51]. Germanium-based nanonets have been used as active layers for photodetection [52,53]. Finally, Indium oxide (In<sub>2</sub>O<sub>3</sub>) nanonets have been integrated in the fabrication of biosensors [54].

As far as nanonets based on Si NWs are concerned, there are few reports regarding their use and applications. A review about the information found in the literature concerning their use in the fabrication of electrical and electrochemical devices will be detailed below.

### **1.2.2.1. Si nanonets as building blocks for electrical devices**

As mentioned above, there is not much information regarding the use of networks of Si NWs for the fabrication of electrical devices. This is probably due to the formation the native oxide (SiO<sub>2</sub>) around the nanowires when they are exposed to air. This oxide is an electrical insulator and thus affects the conduction through the junctions between the Si NWs, then limiting the use of Si nanonets to transistors in which the length of the channel remains close to the length of the Si NWs, and consequently the current can flow directly from one contact to another [23,55,56]. Another strategy that was studied by Heo *et al*, was to put intermediate metal contact on long Si NW network channels, allowing the current to flow despite insulating junctions between the Si

NWs [57]. Moreover, none of these geometries allowed to produce devices taking advantage of the percolation.

The electrical properties of Si nanonets and their improvement as a function of various treatments for their integration in electrical devices have been extensively studied at LMGP for about a decade. On the one hand, during her PhD thesis, Pauline Serre carried out a study on electrical devices based on highly doped Si nanonets [40]. A schematic representation and a SEM image of one of the devices developed during her work are shown in Figure I-5(a) and (b). She demonstrated that once the native oxide is removed by exposure to HF 49% vapor flow during 30 s, if the nanonet is kept under an N<sub>2</sub> atmosphere, its conductance is highly stable over many months compared to the results obtained when the nanonet is kept in air, where the conductance decreases exponentially with a characteristic decay time of 2.2 days (Figure I-5(c))[58].

Additionally, she proved that the Si nanonet-based devices showed excellent electrical reproducibility by comparing the current variation obtained for resistors fabricated from single Si NWs (6 devices), with the current variation obtained for Si nanonet-based resistors (100 devices). She obtained a fluctuation range of 18% for the Si nanonet-based devices, versus 64% for the Si NW-based devices, which proves the averaging effect of the electrical properties resulting from the nanonet [40]. It is important to mention that both types of resistors were fabricated from the same Si nanonet synthesis.

Finally, she demonstrated that a thermal treatment (annealing at 400°C under N<sub>2</sub> atmosphere after native oxide removal by HF) improves the electrical properties of the Si nanonet resistors by two orders of magnitude (Figure I-5(e) and I-5(f)), and makes them insensitive to oxidation in the air, solving the problem of the need to keep the devices in an N<sub>2</sub> atmosphere, which was an important issue for the use of the devices in environmental conditions. Such improvement in electrical properties is explained by a sintering which implies the formation of necks at the junctions between the Si NWs, as schematized in Figure I-5(d). Thus, the electrons can flow freely through nanowires without crossing any oxidized interface. In addition, she proved that the

devices were stable over months, even under oxidizing conditions [59]. These results positioned Si nanonets as a promising material that could be integrated into standard microelectronic processes.

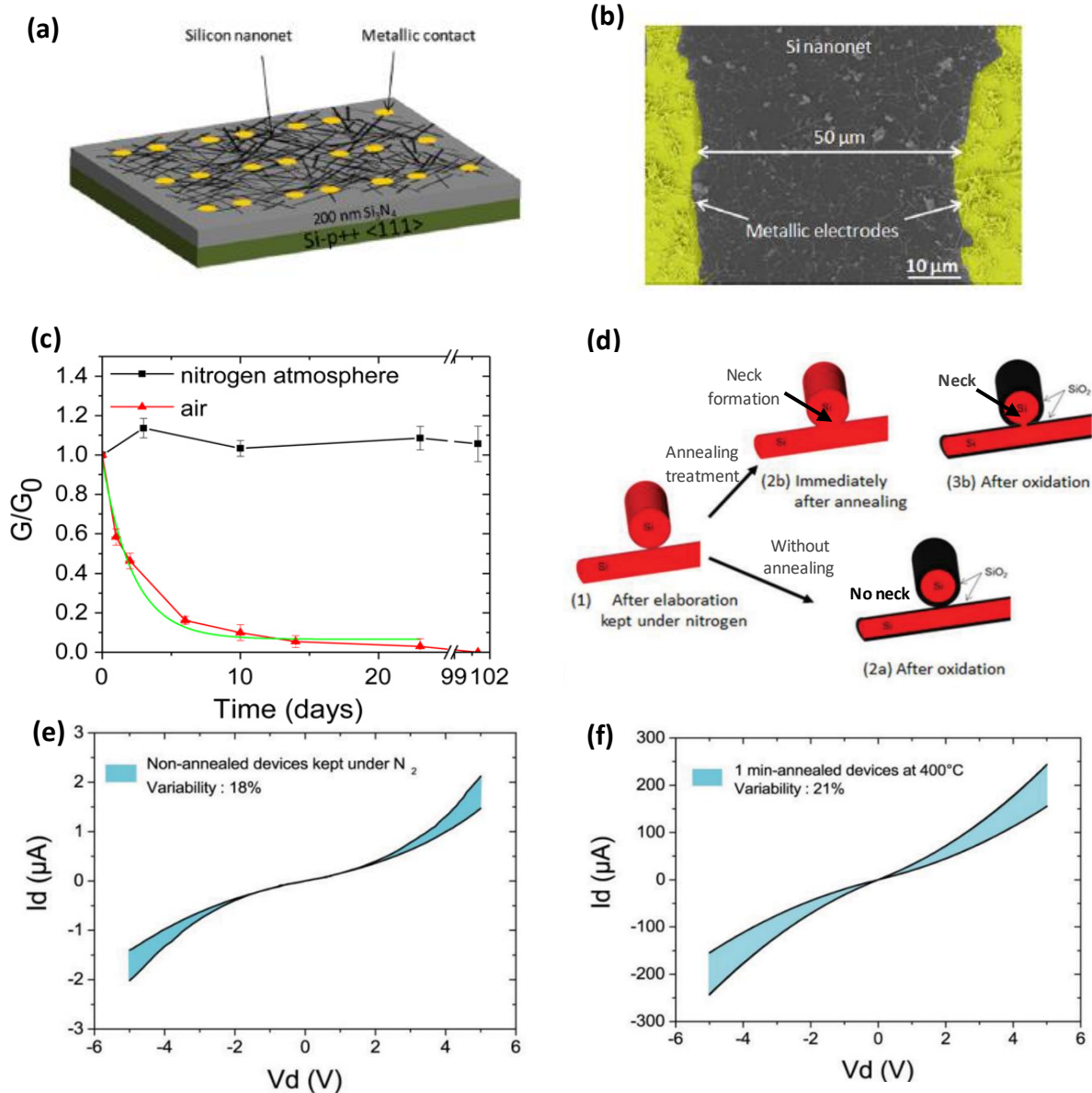


Figure I-5: (a) Schematic representation of Si nanonet-based devices [58]. (b) SEM top view of one device [58]. (c) Conductance evolution over the course of 102 days for Si nanonet devices stored in different atmospheres: in nitrogen atmosphere (black curve) or in ambient atmosphere (red curve) [58]. (d) Schematic illustration the two oxidation ways depending on whether the devices are annealed ((1), (2b), (3b)) or not ((1), (2a)) [59]. (e) Electrical properties of Si nanonets without annealing treatment. The colorized area corresponds to the fluctuation range (100 devices tested) (f) Electrical properties of Si nanonets annealed at 400 °C under N<sub>2</sub> (20 devices tested) [59].

On the other hand, during the following PhD, Maxime Legallais worked on the development of a process for the integration of Si nanonets into Field-Effect Transistors [23]. This was performed through standard microelectronics techniques, limiting the maximum temperature of the processes to 400°C. This makes fabrication stages fully compatible with a large-integration on top of CMOS backend, unlike single Si NW transistors, which usually require complex, time consuming and expensive technological steps [23,60].

Furthermore, he has shown that encapsulation of the Si nanonets with 8 nm thick alumina layer significantly improves the electrical properties of the Si nanonet-based FETs. This is due to a decrease in the trap density at the NWs-oxide interface. Indeed, the non-intentionally growth of native SiO<sub>2</sub> in air induces the formation of a high density of dangling bonds, acting as interface traps. On the contrary, a thin alumina layer grown by well-controlled process allows the formation of an interface of better quality and enhances the electrical characteristics of the devices. He found that for alumina encapsulated Si-nanonet FETs,  $I_{on}$  increased by more than 3 orders of magnitude in comparison with non-encapsulated ones (Figure I-6(a)), obtaining devices with very good performance ( $I_{on}/I_{off}$  ratio exceeding 10<sup>5</sup>) and good device-to-device reproducibility (Figure I-6(b))[38,61].

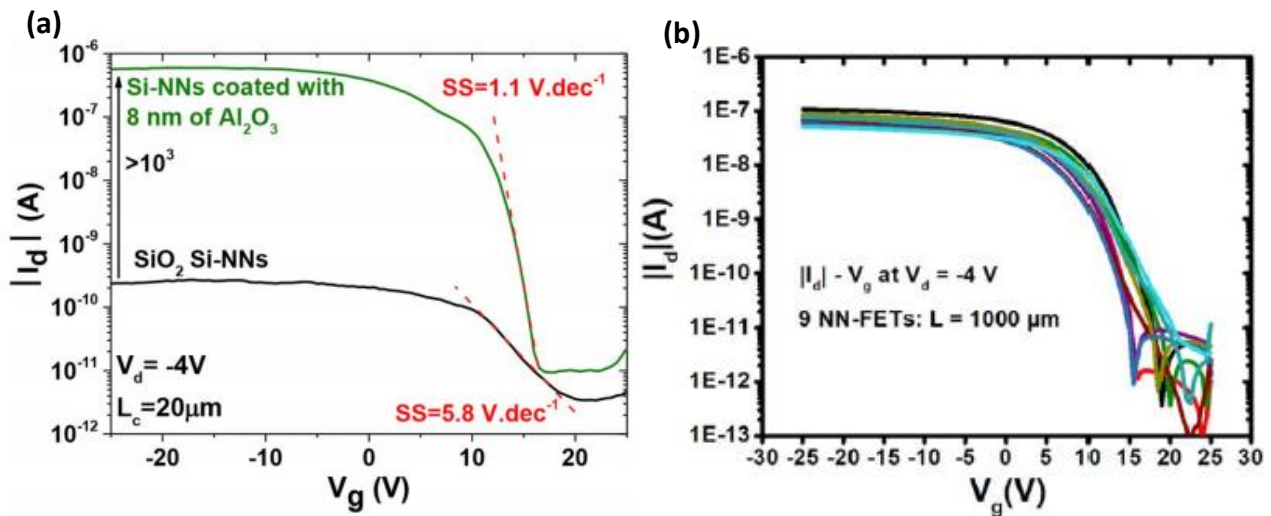


Figure I-6: Transfer characteristic comparison between devices constituted by either native SiO<sub>2</sub>-Si nanonet or 8 nm alumina coated Si nanonet. For both, the channel length was 20 µm and the drain voltage ( $V_d$ ) was set at -4 V [38]. (b) Transfer characteri of nine Si nanonet-based FETs (channel dimensions: 1000 µm length, 120 µm width.  $V_d = -4$  V), demonstrating the very good performance and reproducibility of the devices[61].

Finally, M. Legallais and T.T.T Nguyen carried out the first studies concerning the use of Si nanonet-based FETs in view of the electrical detection of DNA hybridization [23,62,63]. However, they encountered several problems related to the biofunctionalization of the devices and the reproducibility of the results obtained, which will be detailed later.

Motivated by the excellent results previously obtained regarding the performance of Si nanonet-FETs, it was decided to continue with the investigation about the feasibility of using these devices for biosensing applications. FET biosensors built from nanonets of different materials have been reported in the literature. In most cases, these are carbon-based nanonets [64–67], and more rarely other materials such as ZnO [51] and In<sub>2</sub>O<sub>3</sub> [54]. However, to our knowledge, apart from the results reported by our group, there have not been any other works related to the study of FET biosensors based on Si nanonets. Then, among the objectives of this thesis project, the optimization of the Si nanonet-based FETs biofunctionalization, and the study of their use for the electrical detection of DNA hybridization were proposed. The results obtained will be discussed in detail in Chapters II and III.

### **I.2.2.2. Si nanonets as building blocks for electrochemical devices**

The few reports found in the literature corresponding to electrochemical sensors based on Si NWs are shown in Table II-2. As can be seen, most of them correspond to electrochemical biosensors built from 3D structures, which are fabricated from vertically aligned Si NW arrays. This type of arrays are fabricated by chemical etching, thermal evaporation or Chemical Vapor Deposition (CVD) processes. In most cases, the Si array is decorated with metallic nanoparticles, with the aim of creating non-enzymatic sensors detecting electroactive targets (e.g. glucose, H<sub>2</sub>O<sub>2</sub>, ascorbic acid, ethanol) [68–70], or the nanostructure is completely coated with a metallic layer (in these cases a gold layer), to improve the sensor performance [71,72].

As specified previously, this thesis work will focus on 2D nanonets, which are even less common in electrochemical sensors. As shown in Table II-2, to our knowledge, only two electrochemical biosensors based on 2D Si nanonets have been reported so far. These devices were used for

glucose and DNA hybridization detection, obtaining detection limit values of 0,01 mM and 0,01 nM respectively [73,74]

Therefore, the second objective of this thesis work is to study for the first time the detection of thrombin through 2D Si nanonet-based electrochemical biosensors, which will be functionalized by a poly(pyrrole)-NTA layer. The development of electrochemical devices and the results obtained will be detailed in chapters IV and V.

*Table II-2: Overview of Si nanonet-based electrochemical sensors reported in the literature.*

Target molecule	Detection Limit	Type de Structure	Reference
H <sub>2</sub> O <sub>2</sub>	3,2 μM [75], 0,2 μM [76], 1,6 μM [69]	3D	[69,75,76]
H <sub>2</sub> O <sub>2</sub> , glucose, ascorbic acid, dopamine	20 μM, 1 μM, 500 nM, 40 nM	3D	[68]
BSA	1 μM	3D	[78]
Mebendazole	1 nM	3D	[79]
Avidin	10 pM	3D	[71]
Acetylthiocholine chloride	40 pM	3D	[80]
Ethanol	6 μM	3D	[70]
Glutathione	0,33 μM	3D	[81]
Antibody against GFAP protein	2,9 ng mL <sup>-1</sup>	3D	[82]
E.coli microbial cells	10 <sup>3</sup> cells	3D	[83]
Cell-secreted cytokines	150 T-cells/mL	3D	[72]
Glucose	2,88 μM [77], 0,01 mM [73]	3D[77], 2D[73]	[73,77]
DNA hybridization	0,01 nM	2D	[74]

### I.3. Bioreceptor immobilization methods

The immobilization of the bioreceptor on the surface of the transducer plays a key role in the development of a biosensor and it directly impacts its performance. The detection of the target molecule depends on the proper grafting of the bioreceptor on the surface of the transducer, and has a direct effect on the different parameters obtained, such as the sensitivity, selectivity and response time of the biosensor.

Various immobilization methods have been employed in the biosensing field. Some of the most commonly used biofunctionalization techniques will be described below.

### **I.3.1. Adsorption**

Adsorption is the simplest technique for immobilization of bioreceptors such as enzymes, antibodies, and DNA probes. The bioreceptor is adsorbed directly onto the transducer by non-covalent interactions like ionic interactions, hydrogen bonds and van der Waal forces (Figure I-7(a)). This type of immobilization has several advantages such as the fact that no reactant is needed, it is cheap, direct and easy. At the same time, however, it presents important disadvantages such as lower efficiency and lack of selectivity due to the fact that the immobilization is not oriented, and also it presents poor stability over time due to the phenomenon of desorption [84].

### **I.3.2. Encapsulation**

In this case, the immobilization is performed by enclosing the bioreceptors in a membrane capsule, so the bioreceptor is not linked to the membrane by chemical bonds, but is mechanically trapped inside it (Figure I-7(b)). Different materials are used to create the membranes, some of the most commonly used are polymers, composite materials, inorganic or organic gels. The pore size limitation is the main disadvantage of this technique [84,85].

### **I.3.3. Covalent bonding**

This technique is widely used for the immobilization of bioreceptors. The latter are modified with different functional groups such as amines ( $\text{NH}_2$ ) or thiols ( $\text{S-H}$ ), which may subsequently react with the surface of the transducer modified with functional groups including amino, hydroxyl, carboxyl, thiol, methylthiol, guanidyl, imidazole, epoxy or phenol rings, which are able to create covalent bonds with the functional group of the bioreceptor [84] (Figure I-7(c)). This technique generates a good stability and highly binding strength of the bioreceptor from the transducer surface.

Regarding the immobilization of bioreceptors on the surface of Si NWs, organosilanes have been commonly employed to introduce functional groups on them. Over the course of this project, we worked on the optimization of the Si nanonet-based FET biofunctionalization by covalent bonding, using two different organosilanes: (3-Aminopropyl)triethoxysilane (APTES) and (3-Glycidyloxypropyl) trimethoxysilane (GOPS). The processes and results obtained for each of the biofunctionalization methods used will be deeply detailed in Chapter II.

### 1.3.4. Immobilization by affinity interactions

This method is based on the use of different affinities existing between molecules to ensure the immobilization of the bioreceptor. Some examples of these affinities are metal complexation and antibody-antigen recognition [85] (Figure I-7(d)). A common example of this biofunctionalization method involves the immobilization of biotinylated biomolecules on biotinylated surfaces via avidin bridges. However, the weak point of this immobilization method is the size of compact avidin bridge layers (each avidin chain is composed of 128 amino acids [86]), which has an unfavorable effect on the biosensor sensitivity. As an alternative, it can be used systems that mimic the biological avidin-biotin interaction, replacing the protein bridge by smaller metal ions [87]. This immobilization technique was first described by Cooper's group in 1999, and it involved the immobilization of  $\text{Ni}^{2+}$ ,  $\text{Zn}^{2+}$  or  $\text{Cu}^{2+}$  coordinated within electrogenerated polypyrrole films containing carboxylate or imidazole groups [87,88]. This immobilization method was employed for the biofunctionalization of nanonet-based electrochemical biosensors. This procedure and the obtained results will be deeply detailed in chapter IV.

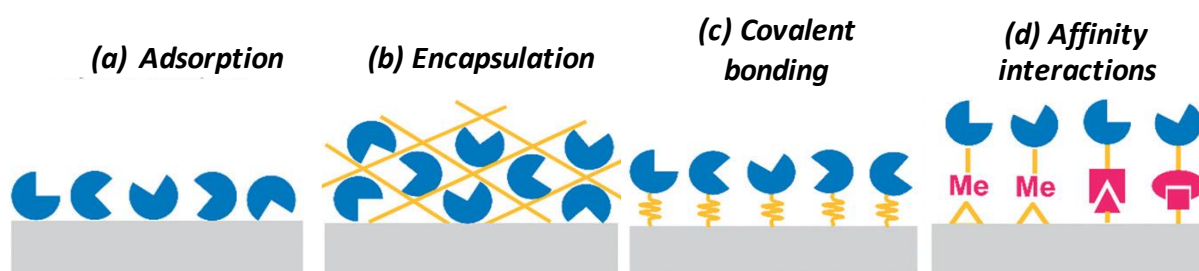


Figure I-7: Schematic representation of some of the most commonly used immobilization methods [89].

### I.4. Transduction techniques used for biosensing

The biosensor transduction system is in charge of converting the recognition event of the target molecule into an electrical signal that can be processed, saved and transmitted by using electronic systems [90]. Biosensors can be classified according to the transduction mechanism they employ. Some of the most commonly used transduction techniques in use today are optical, piezoelectric, calorimetric and electrical methods [4].

- **Optical biosensors:** This kind of sensors make use of optical principles for the transduction of a biochemical interaction into a suitable output signal: the biomolecular interaction on the surface of the sensor modulates the light characteristics of the transducer (i.e., intensity, phase, polarization, etc.). Then, the biosensing event is detected by the change in diverse optical properties such as absorption, fluorescence, luminescence or refractive index, among others [91].
- **Piezoelectric biosensors:** This kind of sensors are based on the property of piezoelectric crystals of vibrating under the influence of an electric field. The bonding of the target molecule on the biosensor surface modifies its frequency of oscillation, which is proportional to the amount of bonded analyte [92,93].
- **Calorimetric biosensors:** Generally, physical, chemical and biological reactions involve exchange of heat [94]. Calorimetric biosensors measure the changes in temperature during the reaction between biorecognition element and a suitable analyte. This change in temperature can be correlated to the amount of reactants consumed or products formed in the calorimetric device [3].
- **Electrical biosensors:** In very general terms, an electrical biosensor reports the recognition of the biological target by the bioreceptor-modified device through a generated current or voltage signal (or perturbation thereof) [95]. In turn, the Field-Effect Transistors (FET) and electrochemical biosensors are part of this category. Their characteristics and

principle of operation are detailed in the sections I.4.1 and I.4.2, since they are the core of this doctoral project.

### **I.4.1. Field-Effect Transistor (FET)-based biosensors**

In Field-Effect Transistor biosensors (FETs), the recognition event is based on the detection of the electrical charges of the target molecules. In 1972 Bergveld P. introduced the concept of Ion-Sensitive Field-Effect Transistor (ISFET) [96]. It was a MOS (Metal-Oxide-Semiconductor) transistor capable of measuring ion activities in biological environments. In the past few decades, important progress has been attained in designing FET devices. Their exceptional electronic properties, compactness, and scalability are very desirable for designing rapid, label-free, and detection of biomolecules, especially for biomedical diagnosis and cell-based assays. However, there are still some important challenges that need to be addressed before they find their way from the laboratory to the market, such as the ability to be massively produced with high accuracy of fundamental representative properties, including rate, reliability, and shelf-life [97].

#### **I.4.1.1. Theoretical background**

There are different categories of transistor-based sensors. However, the most used structures for biological applications are Metal-Oxide-Semiconductor (MOS) Field-Effect Transistors (MOSFETs) and Ion-Sensitive Field-Effect Transistors (ISFETs) [97].

A MOSFET consists of a drain and a source electrodes separated by a semiconductor channel. A dielectric and a metal gate electrode are deposited at the top of the device (Figure I-8(a)). When the source and drain are subjected to a potential difference ( $V_d$ ), the gate voltage can influence the density of the charge carriers in the semiconducting channel.

This type of transistors are classified as P-type and N-type. In P-channel MOSFETs, the majority of the current flowing are holes moving through the channel, while in N-channel MOSFETs the current carrier are mostly electrons. Figure I-8(b) explains how an N-channel MOSFET works. The source and drain are negatively doped, and are separated by a p-type semiconductor. When a

positive voltage is applied to the gate ( $V_g$ ), the semiconductor charge carriers which are also positive, are repelled to the bottom of the semiconductor, generating a region called *depletion region*. As the voltage at the gate increases, the depletion region expands and the minority carriers in the semiconductor, which in this case are electrons, begin to be exposed. If the increase in the gate voltage continues, it reaches a point where electrons are attracted to the top of the semiconductor, creating an *N-channel* that will allow the current to flow between the source and the drain. The voltage value from which the channel is generated is called the *threshold voltage* ( $V_{th}$ ). This voltage thus determinates the transition from a blocking state to a state in which current can flow. These two states constitute the two logical states of the MOSFET transistors called 'Off' and 'On' states respectively. Once the channel is created, the current is produced by applying a potential difference between the drain and the source ( $V_d$ ). To summarize, the MOSFET transistor can thus be compared to an electrostatic switch controlled by the gate voltage [23,96,98]. In the opposite situation, where the semiconductor is N-type, the gate voltage must be lower than the threshold voltage to allow the depletion and attract holes close to the dielectric.

In Ion-Sensitive Field-Effect Transistor (ISFETs), the working principle is the same, but in this case the gate is replaced by the solution to be analyzed, the charges within it and a reference electrode (Figure I-8(c)).

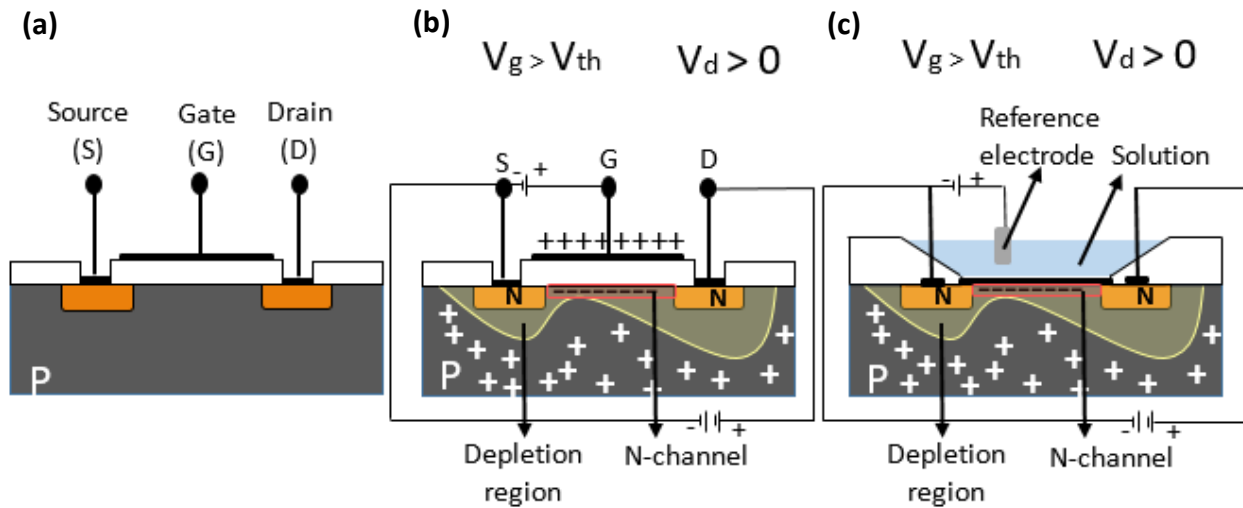


Figure I-8: Schematic representation of a MOSFET. (b) N-channel MOSFET working principle. (c) ISFET working principle.

Both, the gate voltage ( $V_g$ ) and the drain voltage ( $V_d$ ) will affect the measured drain current ( $I_d$ ). Indeed, the gate voltage controls the carrier density, and thus allows the modulation of the channel resistance by field effect. In addition to this, the longitudinal polarization between the drain and the source influences the depletion region. Then, a study of the drain current as a function of these two voltages allows to understand the electrical behavior of FET devices [23].

### - $I_d - V_d$ output characteristics [23,99]

The curve showed in Figure I-9 represents the evolution of the drain current as a function of the drain voltage, for different gate voltages, for a N-channel MOSFET. In general, a MOSFET exhibits three operating regions: the ohmic or linear region, the non-linear and the saturation region.

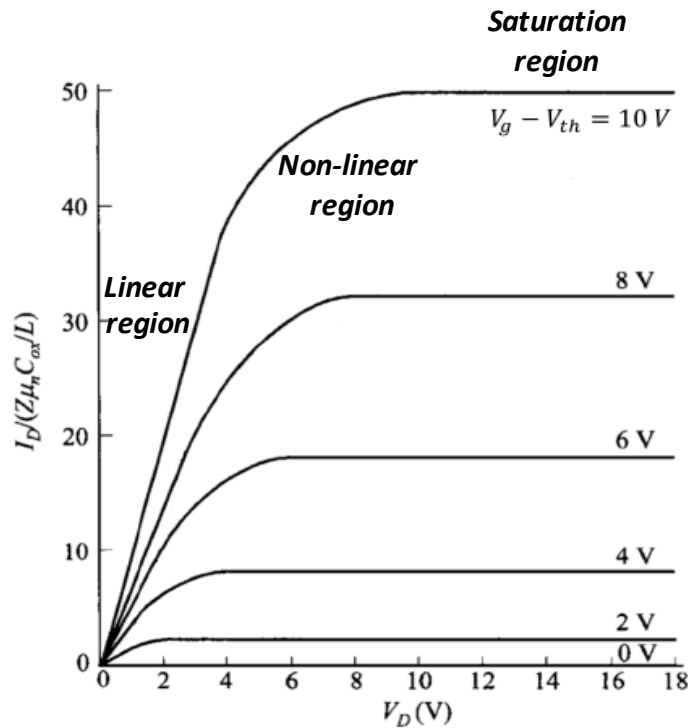


Figure I-9: Output characteristics ( $I_d - V_d$ ) of a N-channel MOSFET and three operating regions: ohmic or linear, non-linear and saturation regions [99].

For low drain voltages, the transistor works as a resistor, controlled by the gate voltage. The  $I_d - V_d$  relationship is then linear (Figure I-9). The drain current can be calculated by Equation I-1, in the case where  $V_g - V_{th} \gg V_d$ :

$$I_d = \frac{w_c}{L_c} \mu C_{ox} (V_g - V_{th}) V_d \quad \text{Equation I-1}$$

Where  $w_c$  and  $L_c$  are the width and length of the channel respectively,  $\mu$  is the carrier mobility (in this example carriers are electrons) and  $C_{ox}$  represents the capacitance per unit area of the gate oxide.

As the drain voltage increases, the voltage drop along the channel must be taken into account. The  $I_d$ - $V_d$  relationship then becomes non-linear (Figure I-9) and is expressed through Equation I-2:

$$I_d = \frac{w_c}{L_c} \mu C_{ox} \left( V_g - V_{th} - \frac{V_d}{2} \right) V_d \quad \text{Equation I-2}$$

Finally, in the saturation region  $V_d$  reaches the “*pinch off voltage*”. From this point the MOSFET shows an  $I_d$  constant (Figure I-9), whatever further  $V_d$  increases beyond the *pinch-off voltage* ( $V_g - V_{th} < V_d$ ), the drain current can be calculated by Equation I-3.

$$I_d = \frac{w_c}{2L_c} \mu C_{ox} (V_g - V_{th})^2 \quad \text{Equation I-3}$$

### - $I_d - V_g$ Transfer characteristics [23,99]

The drain current ( $I_d$ ) can be studied as a function of the gate voltage ( $V_g$ ) (for  $V_d \neq 0$ , and with a constant value). The  $I_d - V_g$  curve, so-called transfer characteristics, is shown below, in a linear and logarithmic scale.

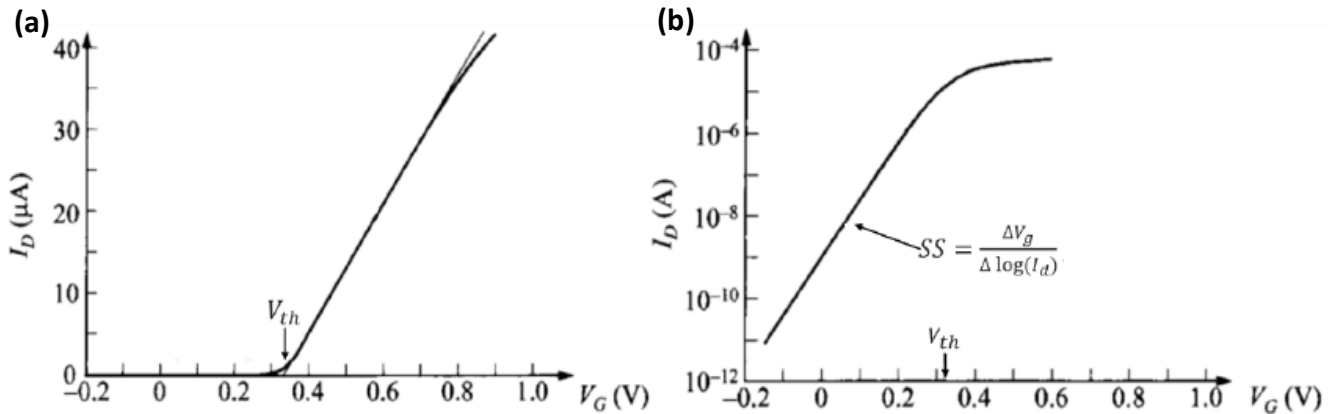


Figure I-10 Transfer characteristics of a N-channel MOSFET (a) linear scale  
b) logarithmic scale [99].

As mentioned before, FETs present two different states, a blocking state (Off) and a state in which current can flow (On). In Figure I-10(a), it can be observed that these two states are separated by the threshold voltage “ $V_{th}$ ”. The latter can be extracted by extrapolating the linear part of the  $I_d - V_g$  transfer characteristics along the x-axis. This threshold voltage is therefore one of the fundamental parameters of MOSFETs characterization.

Furthermore, the transfer characteristic in logarithmic scale, shown in Figure I-10(b), also gives important information about the MOSFET. In this representation, a linear zone appears for a gate voltage lower than the threshold voltage. This zone, called the subthreshold region, allows to extract another important parameter, which is the subthreshold slope “ $SS$ ”. Indeed, the latter translates the gate voltage required to increase the drain current by one decade. In other words, it provides information about the efficiency of the electrostatic control of the channel by the gate. The reduction of the subthreshold slope is important to optimize the electrical properties of MOSFETs, as this would allow to minimize the operating voltages of the transistor and thus the power consumption.

Finally, from transfer characteristic curves can also be extracted the  $I_{On}/I_{Off}$  ratio. The latter represents the ratio between the current in the On-state (maximum current) and the current in the Off-state (minimum current). A high  $I_{On}/I_{Off}$  ratio means a good performance of the MOSFET.

The Si nanonet-based devices cannot be considered as classical MOSFETs, because in our case the source and drain are built from metallic materials. Nevertheless, the previous equations remain valid as the Si nanonet-based FET current is electrostatically controlled.

Concerning the use of Si nanonet-based FETs as biosensors, the attachment of charged biomolecules to the surface of the Si nanonet (either from the bioreceptor or from the target molecule) results in variations in the transfer characteristics. As a consequence, a change in the threshold voltage or drain current is the signature of the biological modification of the Si nanonet-based FET, or to the biorecognition of the analyte of interest, depending on the moment of the electrical characterization.

### I.4.2. Electrochemical biosensors

Electrochemistry is defined as “the science that analyses and describes the transformations of matter on the atomic scale by shifts of electronic charge which can be controlled by means of electric devices” [100]. More than fifty years ago, in 1962, Clark and Lyons developed the first generation of electrochemical biosensors, devices capable of monitoring dissolved oxygen with an enzyme (glucose oxidase) [101]. This method of bio-quantitative-assaying was quick, simple and cheap, and is the precursor of the devices used for diabetes monitoring.

According to the working principle and the signal being measured, electroanalytical techniques can be divided into four different types: (i) potentiometric, (ii) voltammetric and amperometric, (iii) impedimetric and (iv) conductometric techniques [102].

- **Potentiometric sensors:** They constitute an important class of electrochemical sensors, which are able to detect the relationship between the activity of the analyte species and the observed potential response, using a two-electrode system: an indicator electrode and a reference electrode [103]. The most widely used potentiometric sensors are ion-selective electrodes (ISEs), built from polymeric membranes containing selective carriers (ionophores), which have been used for determining several inorganic and organic ions in medical, environmental and industrial analyses [104,105].

- **Voltammetric and amperometric sensors:** These devices measure the current flow between the electrodes when a redox reaction takes place. In the case of amperometric sensors, the analyte concentration is measured through a current response at a fixed potential. In voltammetric sensors a variable potential is applied (either step by step or in continues mode), to obtain a current response as a function of the cells potential,  $I = f(E)$ . The resulting graph of this function is called a voltammogram [106]. The principle of operation and the characteristics of this type of sensors will be discussed in depth later, as this was one of the types of sensors studied in the project
- **Impedimetric sensors:** This type of sensors quantifies the changes in charge conductance and capacitance at the electrode surface when a recognition event occurs. Here, Electrochemical impedance spectroscopy (EIS) is used to study both, the resistive and capacitive properties of the device, based on the perturbation of a system at equilibrium (or around at stationary operating point) by a small amplitude sinusoidal excitation signal [107–109]. One of the characteristics that makes this technique very attractive is that that the impedance of the system can be scanned over a wide range of alternating signal (current or potential) frequencies. The data can be interpreted by equivalent circuit models, which are extensively used for the characterization of coatings, conducting polymers, batteries, fuel cells, corrosion phenomena, electrode kinetics, among many other applications [107]. These types of sensors were also investigated during the thesis, so they will also be treated in detail later.
- **Conductometric sensors:** This kind of sensors provides sensory information as a result of changes in the electrical conductivity of the material in contact with the analyte. Conductometric sensors do not require a reference electrode for working, reducing the cost of production and making them simpler to use. They are extensively employed for the detection of gases [110].

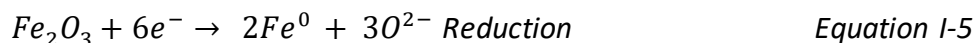
### I.4.2.1. Theoretical background

Electrochemistry allows to study reactions involving electron transfers, relating the flow of electrons to chemical changes. The resulting chemical change is often generated by a redox reaction [111].

#### - Redox reactions

A redox reaction (reduction-oxidation reaction) is a reaction in which a transfer of at least one electron from one molecule to another occurs. Oxidants or oxidizers are substances capable of removing electrons from another substance. When an oxidant accepts electrons from other substances, the oxidant is reduced. Reductants or reducers are substances capable of transferring electrons to other substances. When a reductant donates electrons to other substances, the reductant is oxidized. In other words, oxidation is when there is an increase in charge, and reduction occurs when there is a decrease in charge [106].

The following equations are examples of a chemical redox reaction:



In the previous example, the driving force for the reaction is the difference in energy levels of the reactants:  $Fe_2O_3$  and  $CO$ .

In an electrochemical redox reaction, the driving force is obtained by the polarization of a conductor electrode, typically platinum, gold, glassy carbon or mercury. A voltage is applied to the electrode to modulate the energy of the electrons in the metal, through use of an external power source (such as a potentiostat), allowing the redox reaction to take place [111]. The electrochemical reaction (either oxidation or reduction) takes place at the electrode/electrolyte

interface. In order to close the electrical circuit, a second electrode is necessary. The inverse reaction (either oxidation or reduction) takes place on the second electrode. Thus, these two electrodes allow to carry out the oxidation and reduction reactions separately. The current passes through an electrochemical cell, and the electrons have to be transported within the metal wires connecting a current (or voltage) source with the two electrodes, reaching the electrode/electrolyte interface. During the process of charge transfer, the electrons can be transferred to the species in the solution (reduction), or on the contrary, join the metal electrode (oxidation) [112].

### - **The electrochemical cell [111]**

Redox reactions are commonly studied in an electrochemical cell composed of three-electrodes, as showed in Figure I-11:

- **Working electrode (WE):** The working electrode carries out the studied electrochemical event. A potentiostat is used to control the applied potential on this electrode with respect to the reference electrode potential.
- **Reference Electrode (RE):** The reference electrode should have a well-defined and stable equilibrium potential. It is used as a reference point, against which the potential of other electrodes are measured in an electrochemical cell. The applied potential is consequently reported as “vs” a specific reference. The most common reference electrodes used in aqueous media include the saturated calomel electrode (SCE), and the AgCl/Ag electrode in KCl 3M solution.
- **Counter Electrode (CE):** When a potential is applied to the working electrode, the reduction or oxidation of the analyte can occur, resulting in a current flow. The counter electrode is used to complete the electrical circuit. Current is recorded as electrons flow between the working electrode and the counter electrode. Typically, a platinum wire or disk are used as counter electrodes.

The electrochemical reaction takes place in an electrolyte solution, which is composed of a mixture of the solvent and a supporting electrolyte, in high concentrations to increase solution conductivity and to limit analyte migration.

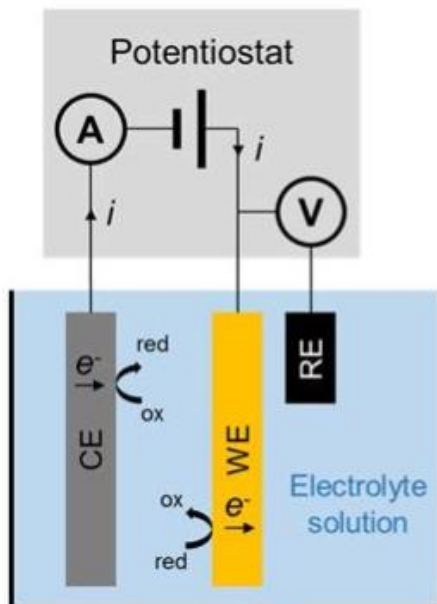


Figure I-11: General three-electrode electrochemical cells. A: Working (WE), counter (CE) and reference electrode (RE) in solution, connected to a potentiostat [113].

### - The electrolyte/electrode interface

The Nernst equation provides a powerful way to predict how an electrochemical system will respond to a change in the electrode potential or a change in concentration of species in solution [111]. Equation I-7 describes the potential of an electrochemical cell ( $E$ ). This is valid only at equilibrium and at the surface of the electrode [114]:

$$E = E^0 + \frac{RT}{nF} \ln \left( \frac{a_{Ox}}{a_{Red}} \right) \quad \text{Equation I-7}$$

where  $E$  is the potential of the cell,  $E^0$  is the standard potential of the species,  $n$  the number of transferred electrons per molecule,  $a_{Ox}$  and  $a_{Red}$  are the relative activities of the oxidized and reduced analyte in the system.  $F$  is the Faraday's constant ( $9.6485 \times 10^4 \text{ C mol}^{-1}$ ) and  $R$  is the universal gas constant ( $8.314 \text{ J mol}^{-1} \text{ K}^{-1}$ ). For dilute solutions, the relative activities can be

approximated simply as the concentrations of the oxidized and reduced species ( $[Ox]$  and  $[Red]$ ) leading to the Equation I-8 [106]:

$$E = E^0 + \frac{RT}{nF} \ln \left( \frac{[Ox]}{[Red]} \right) \quad \text{Equation I-8}$$

### - The electrochemical double layer (EDL):

The concept of electrochemical double layer (EDL) is of utmost importance in electrochemistry. In contact with a solution, a solid surface assumes a surface charge. The charged solid surface generates an interfacial charge distribution, which is different from the charge distribution in the liquid phase, behaving like a capacitor. This surface charge results in a surface potential, which decays with increasing distance from the solid surface [115].

Figure I-12(a) shows a simplified scheme for the case of a metal electrode in contact with an electrolyte solution. First, at the very interface, there is a layer of adsorbed and oriented dipole solvent molecules. Moreover, some ions can specifically adsorb at the interface (the dark green ball in Figure I-12(a)). The so-called *inner Helmholtz plane (IHP)* corresponds to the plane passing through the center of these ions, and the region contained in that distance is commonly called the *compact layer* [112,116]. Then, solvated ions from the solution phase approach the electrode, but only as far as their solvation sheath allow. The so-called *outer Helmholtz plane (OHP)* corresponds to the line drawn through the center of such solvated ions at a distance of closest approach [117]. Finally, the *diffuse layer* beyond the *OHP*, is composed of free ions. There, the excess charge compensating the charge on the metal side is decaying toward the solution bulk, because the numbers of cations and anions are changing in such a way that their charges compensate [112].

As can be seen in Figure I-12(b), the potential varies in the EDL linearly within the compact layer and up to the outer Helmholtz plane. Then, it decays exponentially in the diffuse layer. Outside the EDL, there is no electric field resulting from the charged electrode. The thickness of the EDL depends primarily on the number of ions per volume of solution, the charge of ions, and on the

charge density on the metal side. Capacitive currents flow at electrodes because charge can be accumulate on the two sides of the EDL [112].

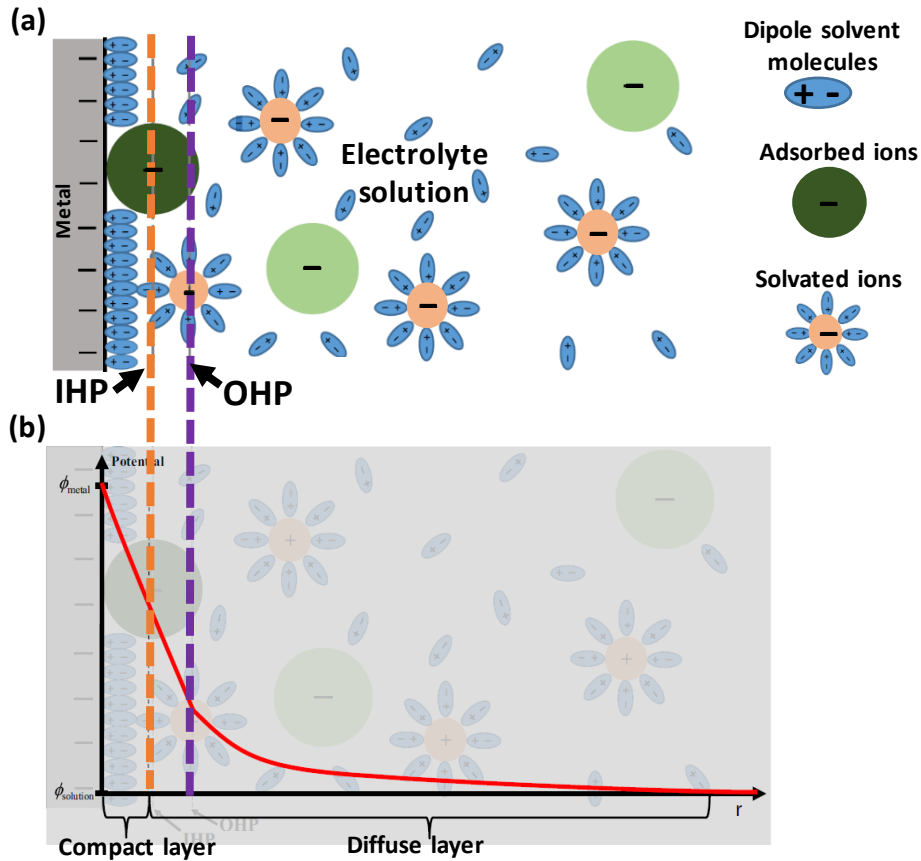


Figure I-12: (a) Scheme of an electrochemical double layer. IHP and OHP corresponds to the inner Helmholtz plane and the outer Helmholtz plane respectively. (b) Potential distribution the electrochemical double layer.  $\Phi_{metal}$  and  $\Phi_{solution}$  are the inner potentials potentials in the metal and solution, respectively, and  $r$  is the distance from the interface [112].

- **The current through the electrochemical cell**

The current allowing the redox reaction is called faradaic current because it follows Faradays law: “Assuming that there are no parallel processes, the number of moles of a substance produced or consumed during an electrode process, is proportional to the electric charge passed through the electrode” [118].

This relationship is described by Equation I-9:

$$q = nFm \quad \text{Equation I-9}$$

Where  $q$  is the electric charge passed through the electrode,  $n$  is the number of transferred electrons per molecule,  $F$  is the Faraday constant ( $9.6485 \times 10^4$  C/mol) and  $m$  is the number of moles of the substance.

However, in an electrochemical reaction, the current density ( $i$ ) comprises the faradaic current ( $i_{far}$ ), which is a direct measure of the rate of the electrochemical reaction, and a capacitive current ( $i_{cap}$ ), which appears when an electrochemical double layer is formed. This relationship is expressed by Equation I-10:

$$i = i_{far} + i_{cap} \quad \text{Equation I-10}$$

The reaction rate depends on the way in which the species can move within the solution, so called mass transport, and is the result of the contribution of different phenomena, which will be explained below.

- **Mass transport on electrode processes**

Mass transport to an electrode can be described by the Nernst–Planck equation [119]. For one-dimensional mass transport along the x-axis, it can be written as Equation I-11:

Here,  $J$  is the flux ( $\text{mol cm}^{-2} \text{s}^{-1}$ ) of redox species  $i$ , which is constituted by different contributions.

$$J_i(x) = \underbrace{-D_i \left[ \frac{\partial C_i(x,t)}{\partial x} \right]}_{\text{Diffusion}} - \underbrace{\left( \frac{z_i F}{RT} \right) D_i C_i \frac{\partial \Phi(x,t)}{\partial x}}_{\text{Migration}} + \underbrace{C_i v(x,t)}_{\text{Convection}} \quad \text{Equation I-11}$$

Firstly, the diffusion transport term, where  $\frac{\partial C(x,t)}{\partial x}$  is the concentration gradient at a distance from the electrode surface, and at a time  $t$ . Second, we have the contribution of migration transport due to the electric field, where  $z$  and  $C$  are the charge and concentration of the species

respectively and  $\frac{\partial \Phi(x,t)}{\partial x}$  is the potential gradient. Finally, we have the convective contribution, where  $v(x)$  is the velocity of a volume element of the solution. The constants that appears correspond to: Faraday's constant  $F$  ( $9.6485 \times 10^4 \text{ C mol}^{-1}$ ),  $D$  is the diffusion coefficient of the species in the solution,  $R$  is universal gas constant ( $8.314 \text{ J mol}^{-1} \text{ K}^{-1}$ ) and  $T$  is the temperature.

It is possible to control certain experimental parameters in order to limit or make very small the transport by migration and convection. For example, by adding a high concentration of a supporting electrolyte (a salt), which does not undergo electrolysis itself but helps to shield the reactants from migratory effects. Concerning the convection, it is possible to control by performing the experiments in an unstirred solution, or with constant and controlled stirring [120]. Under these conditions the mass transport described by Equation I-11 will be determined only by the diffusion (Equation I-12):

$$J_i(x) = -D_i \frac{\partial C_i(x,t)}{\partial x} \quad \text{Equation I-12}$$

Moreover, the current density  $i$  (different from redox species  $i$ ) is proportional to the flux of species  $J$  reaching the electrode surface for the electrochemical reaction, and its relationship can be described by the equation I-13:

$$i = -nFAJ(x,t) \quad \text{Equation I-13}$$

Where  $A$  is the electrode area ( $\text{cm}^2$ ) and  $n$  is the number of transferred electrons per molecule. And finally, substituting Equation I-12 in Equation I-13, we find that the obtained current will be determined by the diffusion of the electroactive species, and will be proportional to their concentration gradient, as can be seen in Equation I-14:

$$i = nFAD \frac{\partial C(x,t)}{\partial x} \quad \text{Equation I-14}$$

### I.4.2.2. Voltammetric biosensors

As previously mentioned, in voltammetric sensors a variable potential is applied to system in order to obtain a current response as a function of the cells potential,  $I = f(E)$ .

There are different techniques related to voltammetry, and uniqueness of each rests on subtle differences in the manner and timing in which the potential is applied and the current is measured [121]. Some of the most widely used voltammetric techniques currently in use are linear sweep voltammetry (LSV), cyclic voltammetry (CV), differential pulse voltammetric (DPV), and square-wave voltammetry (SWV) [122]. In this work, the cyclic voltammetry technique was used to characterize the different stages of the biofunctionalization process on the working electrode and to perform the detection of the target molecule.

#### - Cyclic voltammetry (CV)

The current response of a redox active solution is measured in response to a linearly cycled potential sweep between two or more set values. During the scan, the redox species (redox probe) either loses an electron (oxidation) or gains an electron (reduction), depending on the direction of the ramping potential. The resulting graph correspond to a cyclic voltammogram. An example of the latter is displayed in Figure I-13 [123].

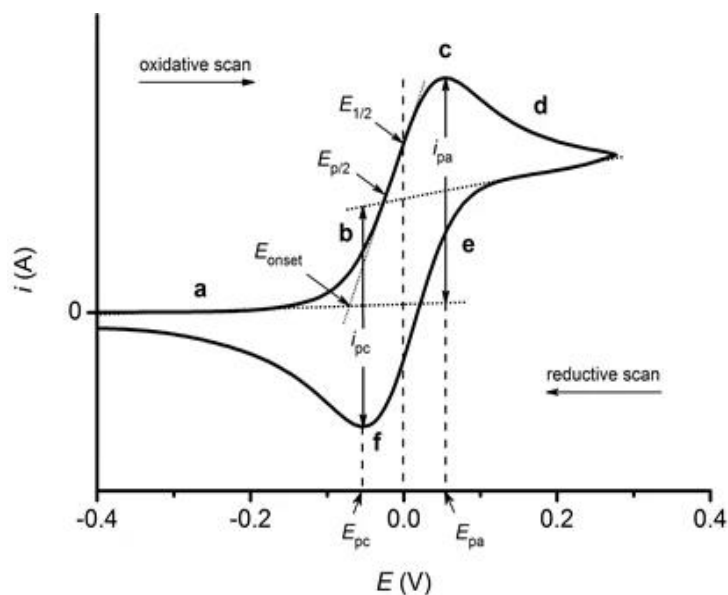


Figure I-13: Cyclic voltammogram for a one-electron redox process [123].

In Figure I-13, the scan starts at negative potentials and sweeps forward to more positive, oxidative potentials. At the beginning, the potential is not sufficient to oxidize the redox probe (from  $E, I = 0$  up to point a). As the onset ( $E_{\text{onset}}$ ) of oxidation is reached, the current exponentially increases (up to point b) as the redox probe is being oxidized on the surface of the working electrode. From that point, the process is under electrochemical control with the current linearly increasing as the potential increases, and with a constant concentration gradient of the redox species near the electrode surface within the electrochemical double layer [123].

Then, the current response decreases from linearity as the oxidized species are depleted and the electrochemical double layer grows in size. The current reaches peak maximum for oxidation at point c, called *anodic peak current* ( $i_{pa}$ ), at a potential value called *anodic peak potential* ( $E_{pa}$ ). From that point, upon scanning to more positive potentials, the rate of diffusion of the redox species from the bulk solution to the working electrode becomes slower, resulting in a decrease in the current as the scan continues. The current is limited by the mass transport of the redox probe from the bulk to the interface, which is slow on the electrochemical timescale and consequently does not satisfy the Nernst equation. The current decreases until a steady-state is reached, in which further increases in potential no longer has any effect [111,123].

Scan reversal to negative potentials (reductive scan) continues to oxidize the redox probe until the applied potential reaches the value where the reduction process can start (point e). The reduction process is similar to the oxidation process, but with an opposite scan direction and a *cathodic peak current* ( $i_{pc}$ ) at the *cathodic peak potential* ( $E_{pc}$ ) (point f) [123].

### - **Electrochemical reversibility**

Reversibility needs that the electron transfer kinetics are fast enough to maintain the surface concentrations of oxidized and reduced species at the values required by the Nernst equation (Equation I-7). If the process is electrochemically *reversible* (Figure I-14(a)), the difference between the anodic and cathodic peak potentials, called peak-to-peak separation ( $\Delta E_p$ ) should be  $56,5/n$  mV at 25 °C, where  $n$  is number of electrons transferred per molecule. For this kind of

processes,  $\Delta E_p = E_p - E_{p/2}$  (56,5/n mV at 25°C), where  $E_{p/2}$  corresponds to the potential at 1/2 of the peak current. Under these conditions, the process is diffusion controlled [124,125].

An electrochemically *irreversible* process presents a slow electron transfer (Figure I-14(b)). This type of process is defined by the following Equation I-15:

$$E_p - E_{p/2} = \frac{47.7}{\alpha n} \text{ (mV at 25°C)} \quad \text{Equation I-15}$$

Where  $E_{p/2}$  is the potential at 1/2 of the peak current,  $\alpha$  is the charge transfer coefficient and  $n$  is the number of transferred electrons per molecule. In this case, the electrochemical reaction is controlled by charge transfer [124].

Finally, the intermediate processes between reversible and irreversible are called *quasi-reversible* (Figure I-14(c)). Under these conditions, the rate of the electrochemical reaction is controlled by both, charge transfer and diffusion and  $\Delta E_p > 59/n$  mV [124].

It can then be concluded that  $\Delta E_p$  provides valuable information regarding system reversibility, and it is directly related to the rate of charge transfer. This parameter, combined with the current intensity will provide important information about the oxidation/reduction mechanism on the surface of the electrode, which in our case will act as a biosensor, allowing us to characterize the different steps of the biofunctionalization process and the detection of the target molecule

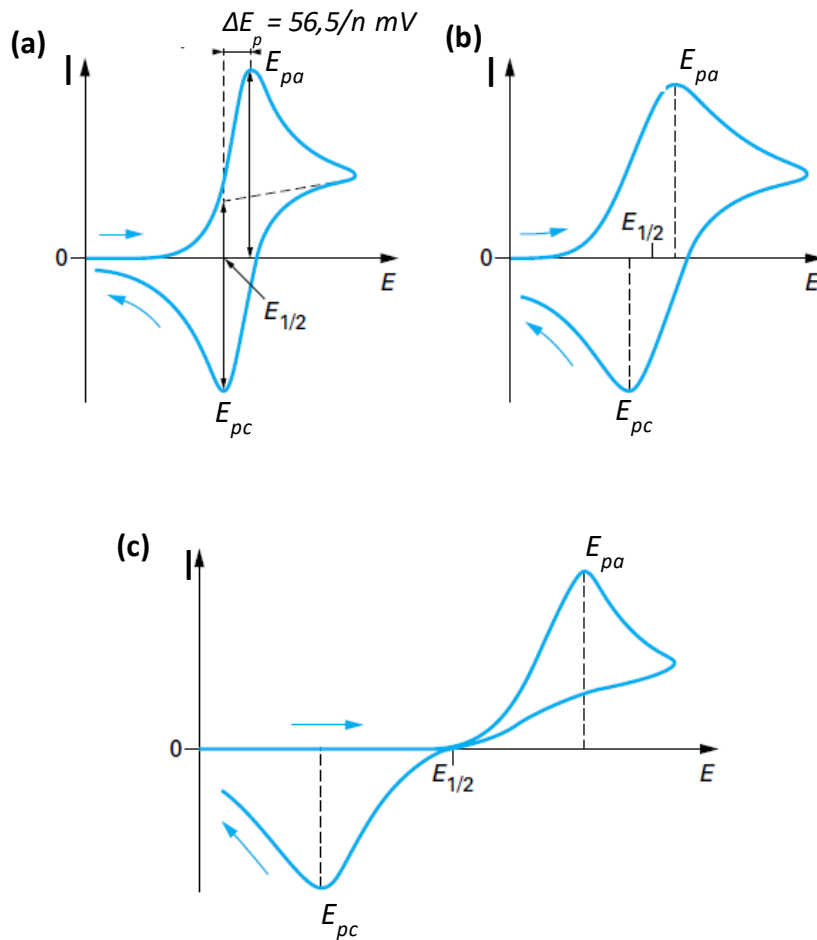


Figure I-14: Comparison of cyclic voltammetric wave-shapes for (a) a reversible process, (b) a quasi-reversible process and (c) an irreversible process [124].

### 1.4.2.3. Impedimetric biosensors

As mentioned before, this type of sensors are based in the quantification of the changes in charge conductance and capacitance at the electrode surface when a recognition event occurs by using Electrochemical Impedance Spectroscopy (EIS).

#### - Electrochemical Impedance Spectroscopy (EIS): Theoretical background

Impedance spectroscopy is a powerful technique that allows to study an electrochemical process in which resistive, capacitive and/or inductive phenomena are concerned. EIS measurements involve the application of an alternating potential “ $\Delta E$ ”, which corresponds to a small amplitude

sinusoidal potential to the system under investigation, followed by measurement of the response in the form of a sinusoidal current “ $\Delta I$ ” as a function of frequency (Figure I-15(a)). Therefore, the potential varies sinusoidally around a constant value  $E_c$ , and the obtained current is then also sinusoidal, varying around a constant current value  $I_c$ . The procedure described above corresponds to the potentiostatic mode, and is the one we will use in this project. However, there is also the galvanostatic mode, in which an alternating current is applied, and the response is obtained as an alternating potential [102,126,127].

The system to be studied must present a linear behavior. However, the latter is not the type of behavior exhibited by the electrochemical systems. Nevertheless, as mentioned before, the sinusoidal potential applied to the electrochemical cell has a small-amplitude (1 to 10 mV). Analyzing the current – voltage relationship of electrochemical system (Figure I-15(b)), if we take a small portion of the  $I = f(E)$  curve (area delimited by the square), it appears to be linear. Then, under a small-amplitude sinusoidal excitation around the  $E_c$  potential, the system can be considered as linear. Consequently the current response  $\Delta I$  will be linear around the  $I_c$  value [126–128].

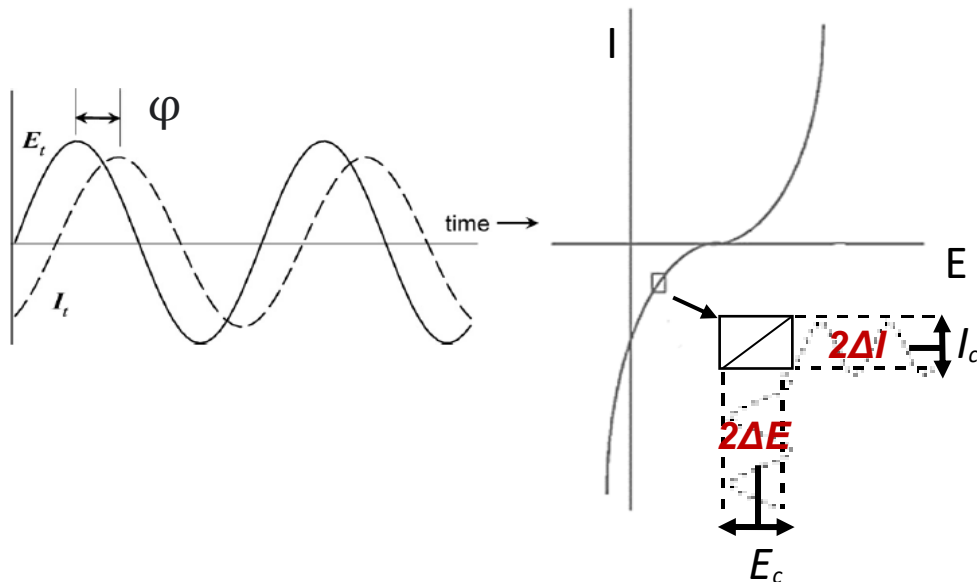


Figure I-15: (a) AC sinusoidal potential applied and sinusoidal current response in an electrochemical system. (b) Linear behavior in a small portion of a current – voltage curve of electrochemical system.

## Chapter I: State of the art

---

In general terms, impedance is the measure of the opposition that a system presents to an alternating current (AC). It is a concept similar to the resistance ( $R$ ) of a circuit when a direct current is applied, which is defined as the ratio of the applied potential ( $E$ ) to the current ( $I$ ) through it (Ohm's law):

$$R = \frac{E}{I} \quad \text{Equation I-16}$$

However, the impedance takes into account conduction properties of the system, at the same time with its dielectric properties. The first ones are schematized by equivalent resistances, and the second ones by capacitors [129].

The applied potential  $E$  and the resulting current  $I$  are time ( $t$ ) dependent, and can be described as follow (Equation I-17 and I-18)

$$E(t) = E_c + \Delta E(t) = E \sin(\omega t) \quad \text{Equation I-17}$$

$$I(t) = I_c + \Delta I(t) = I \sin(\omega t + \varphi) \quad \text{Equation I-18}$$

Where  $\omega$  is the angular frequency (given by  $\omega=2\pi f$ , where  $f$  is the frequency) and  $\varphi$  is the phase shift, showed in Figure I-15(a).

By using Fourier Transform it is possible to convert the above equation from the time-domain to the frequency-domain[127]. Then, as in the case of a resistance, the impedance of the system  $Z(\omega)$  can also be calculated using Ohm's law as:

$$Z(\omega) = \frac{E(\omega)}{I(\omega)} \quad \text{Equation I-19}$$

The impedance of the system  $Z(\omega)$  is a complex quantity with a magnitude and a phase shift which depends on the frequency of the signal, and it can be represented in Cartesian as well as in polar coordinates.

In polar coordinates the impedance of the data is represented by the Equation 20:

$$Z(\omega) = |Z|e^{j\varphi} \quad \text{Equation I-20}$$

Where  $|Z|$  is the magnitude of the impedance (also called impedance modulus),  $j = \sqrt{-1}$  and  $\varphi$  is the phase shift, which is represented in Figure I-15.

In Cartesian form, impedance is defined as Equation I-21:

$$Z(\omega) = Re[Z(\omega)] + j Im[Z(\omega)] \quad \text{Equation I-21}$$

Where  $Re[Z(\omega)]$  the real is part of the impedance and  $Im[Z(\omega)]$  is the imaginary part. The real part comes from any resistive component in the system, while the imaginary part is related to the formation of insulating layers (namely the electrochemical double layer, or any added barrier). EIS allows to model the phenomena occurring in the studied electrochemical system by using combination of resistors and capacitors. Then, a RC circuit giving the same current response as that produced by the electrochemical system can be built, by using the principle of equivalent circuits (Figure I-16(a)). Steps happening simultaneously will be represented as processes in parallel, and sequential steps will be represented by an association of processes in series. Then, the experimental spectrum can be fitted with the theoretical curve corresponding to the selected circuit model, thus obtaining the values of the electrical parameters [127,130].

One of the most common graphical representations of impedimetric data is the Nyquist plot, where the imaginary part of the impedance  $-Im[Z(\omega)]$  is plotted versus the real part  $Re[Z(\omega)]$ . In this representation, each measured point corresponds to a different frequency. Measurements are performed starting from the highest frequencies, which are represented on the left part of the diagram, whilst low frequencies are represented on the right one (Figure I-16(b)).

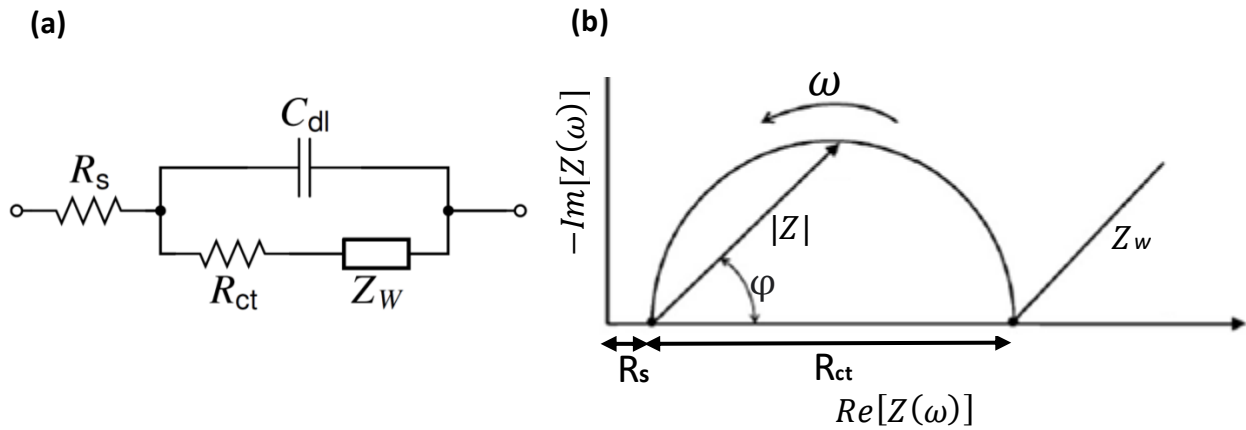


Figure I-16 (a): Randles' equivalent circuit for an electrode in contact with a solution. (b) Schematic representation of the Randles' equivalent circuit in the Nyquist plot [131].

The interpretation of impedimetric spectra obtained for the electrochemical system under study is based on the correlation with the selected equivalent circuit. In the case of a fast charge transfer reaction at a planar electrode, the Randles' equivalent circuit, which was introduced nearly seven decades ago, is the most frequently used (Figure I-16(a) and (b)) [130,131].

$R_s$  corresponds to the resistance of the solution (electrolyte). This value depends on the type of electrolyte, the ionic concentration, the temperature and the electrode's geometric surface area. At high frequencies its value is given by Equation I-22:

$$Z_{R_s}(\omega) = R_s \quad \text{Equation I-22}$$

$C_{dl}$  corresponds to the double layer capacitance. It represents the overall charge stored at the electrode/solution interface and is generated by the charges in the electrode material which induce an accumulation of ions on the electrode surface acting as a capacitor. Its impedance is given by Equation I-23.

$$Z_{c_{dl}} = 1/j\omega C_{dl} \quad \text{Equation I-23}$$

where  $C_{dl}$  is the capacitance of the double layer.

The charge transfer resistance  $R_{CT}$ , is the opposition experienced to the electron movement at the electrode interface when the electrochemical reactions takes place, and is given by Equation I-24:

$$Z_{R_{ct}}(\omega) = R_{ct} \quad \text{Equation I-24}$$

Finally, the Warburg impedance  $Z_w$  reflects the impedance of the current due to the diffusion phenomena of the electroactive species towards the conducting surface. There are three types of Warburg impedance, but we will be focused only in the case when the diffusion occurs in a semi-infinite layer (natural diffusion). On a Nyquist plot, the Warburg term appears typically as a diagonal line with a 45° slope [127,130].

EIS technique separates faradaic currents from capacitive currents. Thus, in the Randles' equivalent circuit, the charge transfer and Warburg resistances ( $R_{ct} + W_Z$ ) in series are associated in parallel with the double layer capacitance  $C_{DL}$ , since the total current flowing through the active surface is the sum of the contributions from the faradaic ( $I_f$ ) and capacitive ( $I_c$ ) processes. Finally,  $R_s$  is associated in series with the previous circuit because all the currents must pass through the electrolytic solution resistor [127,132].

### - **Non-Faradaic and Faradaic impedance spectroscopy**

On the one hand, non-faradaic is based on the study of the capacitance of the double layer formed between the solution and the electrode surface. In this case no additional reagent is required. In fact, the biomodification of the sensor surface generates a variation in the capacitance value, due to the displacement of water and ions from the surface upon biomolecule binding [130, 133]. In a characteristic non-faradaic Nyquist plot, the absence of redox species eliminates the parameters associated with electron transfer such as charge transfer resistance ( $R_{ct}$ ) and Warburg impedance by becoming infinite. This is represented by the large incomplete semicircle due to the extremely slow electron transfer step, which is not followed by the typical diffusion tail. Therefore, in a non-faradaic electrochemical system, the imaginary part of impedance is inversely proportional to the electrical double layer capacitance [134–136].

On the other hand, in Faradaic impedance spectroscopy, the redox species added to the bulk solution are alternatively oxidized and reduced at the working electrode surface. This process is thus exploited to observe the change of the charge transfer resistance between the solution and the electrode surface, which is associated to the modification of the latter due to the different steps involving the biosensing event [130].

In our case, Faradaic impedance spectroscopy will be used to characterize the different stages of biofunctionalization process, and to elucidate the detection of the target molecule, by means of the changes observed in the electrical properties of the working electrode.

### **I.5. Objective of the PhD thesis**

This thesis aims to explore the possibility of using Si nanonets as building blocks for nanomaterial-based biosensors. For this purpose two different axes were studied:

- (i) The development of a Si nanonet-based FET biosensor for the electrical detection of DNA hybridization in dry environment
- (ii) The development of a Si nanonet-based electrochemical biosensor for thrombin detection.

This in turns requires to divide the development of each type of sensor into three different parts:

- The fabrication of a Si nanonet-based biosensor
- The immobilization of the TBA-15 bioreceptor on the device
- The detection of the target molecule: DNA or thrombin.

In the case of the Si nanonet-based FET biosensors (first axis), the fabrication process of the devices was previously developed at LMGP during the thesis project of P. Serre and M. Legallais, who obtained devices presenting very good electrical properties, and carried out the first tests in view of the electrical detection of DNA hybridization. However, they encountered several

problems related to the bioreceptor immobilization on the devices and the reproducibility of the results obtained. Thus, the first objective of this axis was to optimize the bioreceptor immobilization protocol. For this purpose, two different processes based on organosilanes were studied: (3-Aminopropyl)triethoxysilane (APTES) and (3-Glycidyloxypropyl) trimethoxysilane (GOPS). The second objective comprised the study of the electrical detection of DNA hybridization using Si nanonet-based biosensors in dry environment. The results obtained for this axis will be detailed in chapters II and III.

Regarding the second axis, as mentioned before, to our knowledge only two electrochemical biosensors based on 2D Si nanonets have been reported so far. Therefore, the first objective of this axis consisted in the fabrication of the Si nanonet-based electrochemical biosensor. This involves the study of different parameters such as the choice of the working electrode material to be used as conducting substrate for the Si nanonet, the development of a protocol to transfer the Si nanonet onto the working electrode, and the selection of the appropriate redox probe for the system. Second, a bioreceptor immobilization method compatible with the Si nanonet-based working electrode had to be established. For this purpose, it was developed an immobilization process based on the chemical deposition of a poly(pyrrole)-NTA film, which enables the subsequent grafting of the bioreceptor on the surface of the device by affinity interactions, thanks to the generation of metal-chelate complexes. The final objective of this axis was the electrochemical detection of thrombin by cyclic voltammetry and electrochemical impedance spectroscopy techniques. The results obtained will be detailed in chapters IV and V.

# References

- [1] N. Bhalla, P. Jolly, N. Formisano, P. Estrela, Introduction to biosensors, *Essays Biochem.* 60 (2016) 1–8. <https://doi.org/10.1042/EBC20150001>.
- [2] L. Soleymani, F. Li, Mechanistic Challenges and Advantages of Biosensor Miniaturization into the Nanoscale, *ACS Sensors.* 2 (2017) 458–467. <https://doi.org/10.1021/acssensors.7b00069>.
- [3] C. Karunakaran, R. Rajkumar, K. Bhargava, Introduction to Biosensors, in: *Biosens. Bioelectron.*, Elsevier Inc., 2015: pp. 1–68. <https://doi.org/10.1016/B978-0-12-803100-1.00001-3>.
- [4] V. Perumal, U. Hashim, Advances in biosensors: Principle, architecture and applications, *J. Appl. Biomed.* 12 (2014) 1–15. <https://doi.org/10.1016/j.jab.2013.02.001>.
- [5] A. Liu, K. Wang, S. Weng, Y. Lei, L. Lin, W. Chen, X. Lin, Y. Chen, Development of electrochemical DNA biosensors, *TrAC - Trends Anal. Chem.* 37 (2012) 101–111. <https://doi.org/10.1016/j.trac.2012.03.008>.
- [6] J.D. WATSON, F.H.. CRICK, Molecular Structure of Deoxyntose Nucleic Acids, *Nature.* 171 (1953) 738–740.
- [7] Y. Zhang, B.S. Lai, M. Juhas, Recent advances in aptamer discovery and applications, *Molecules.* (2019). <https://doi.org/10.3390/molecules24050941>.
- [8] S. Gao, B. Hu, X. Zheng, D. Liu, M. Sun, J. Qin, H. Zhou, B. Jiao, L. Wang, Study of the binding mechanism between aptamer GO18-T-d and gonyautoxin 1/4 by molecular simulation, *Phys. Chem. Chem. Phys.* 18 (2016) 23458–23461. <https://doi.org/10.1039/c6cp00777e>.
- [9] M. Vallejo-Perez, C. TERNON, N. Spinelli, F. Morisot, C. Theodorou, G. Jayakumar, P.E. Hellström, M. Mouis, L. Rapenne, X. Mescot, B. Salem, V. Stambouli, Optimization of GOPS-based functionalization process and impact of aptamer grafting on the si nanonet FET electrical properties as first steps towards thrombin electrical detection, *Nanomaterials.* 10 (2020) 1–20. <https://doi.org/10.3390/nano10091842>.
- [10] H. Sun, X. Zhu, P.Y. Lu, R.R. Rosato, W. Tan, Y. Zu, Oligonucleotide aptamers: New tools for targeted cancer therapy, *Mol. Ther. - Nucleic Acids.* 3 (2014). <https://doi.org/10.1038/mtna.2014.32>.
- [11] L.N. Cella, P. Sanchez, W. Zhong, N. V. Myung, W. Chen, A. Mulchandani, Nano aptasensor for Protective Antigen Toxin of Anthrax, *Anal. Chem.* 82 (2010) 2042–2047. <https://doi.org/10.1021/ac902791q>.
- [12] A. V. Lakhin, V.Z. Tarantul, L. V. Gening, Aptamers: Problems, solutions and prospects, *Acta Naturae.*

- 5 (2013) 34–43.
- [13] C. Tuerk, L. Gold, Systematic evolution of ligands by exponential enrichment: RNA ligands to bacteriophage T4 DNA polymerase, *Science* (80-. ). 249 (1991) 550–510. [papers2://publication/uuid/EF348D9B-CCD3-4ED1-B6E7-0B7E96F68C4C](https://doi.org/10.1126/science.1226935).
- [14] A.D. Ellington, J.W. Szostak, In vitro selection of RNA molecules that bind specific ligands, *Nature*. 346 (1990) 818–822. <https://doi.org/10.1038/346818a0>.
- [15] M. Menger, A. Yarman, J. Erdossy, H.B. Yildiz, R.E. Gyurcányi, F.W. Scheller, MIPs and aptamers for recognition of proteins in biomimetic sensing, *Biosensors*. 6 (2016). <https://doi.org/10.3390/bios6030035>.
- [16] L.C. Bock, L.C. Griffin, J.A. Latham, E.H. Vermaas, J.J. Toole, Selection of single-stranded DNA molecules that bind and inhibit human thrombin, *Lett. to Nat.* 355 (1992) 564–566. <https://doi.org/10.1038/255242a0>.
- [17] E. Di Cera, Thrombin, *Mol. Aspects Med.* 29 (2008) 203–254. <https://doi.org/10.1016/j.mam.2008.01.001>.
- [18] F. Arduini, S. Cinti, V. Scognamiglio, D. Moscone, Nanomaterial-based sensors, in: *Handb. Nanomater. Anal. Chem.*, 2020: pp. 1–9. <http://mpoc.org.my/malaysian-palm-oil-industry/>.
- [19] A. Mokhtarzadeh, R. Eivazzadeh-Keihan, P. Pashazadeh, M. Hejazi, N. Gharaatifar, M. Hasanzadeh, B. Baradaran, M. de la Guardia, Nanomaterial-based biosensors for detection of pathogenic virus, *TrAC - Trends Anal. Chem.* 97 (2017) 445–457. <https://doi.org/10.1016/j.trac.2017.10.005>.
- [20] P. Namdari, H. Daraee, A. Eatemadi, Recent Advances in Silicon Nanowire Biosensors: Synthesis Methods, Properties, and Applications, *Nanoscale Res. Lett.* 11 (2016). <https://doi.org/10.1186/s11671-016-1618-z>.
- [21] M. Holzinger, A. Le Goff, S. Cosnier, Nanomaterials for biosensing applications: A review, *Front. Chem.* 2 (2014) 1–10. <https://doi.org/10.3389/fchem.2014.00063>.
- [22] H. Su, S. Li, Y. Jin, Z. Xian, D. Yang, W. Zhou, F. Mangaran, F. Leung, G. Sithamparanathan, K. Keman, Nanomaterial-based biosensors for biological detections, *Adv. Heal. Care Technol. Volume 3* (2017) 19–29. <https://doi.org/10.2147/ahct.s94025>.
- [23] M. Legallais, Conception, étude et modélisation d’une nouvelle génération de transistors à nanofils de silicium pour applications biocapteurs, Université Grenoble Alpes, 2017. <http://www.theses.fr/s119813>.
- [24] C. Jacoboni, C. Canali, G. Ottaviani, A. Alberigi Quaranta, A review of some charge transport properties of silicon, *Solid State Electron.* 20 (1977) 77–89. <https://doi.org/10.1016/0038->

- 1101(77)90054-5.
- [25] S.M. Sze, J.C. Irvin, Resistivity, mobility and impurity levels in GaAs, Ge, and Si at 300°K, *Solid State Electron.* 11 (1968) 599–602. [https://doi.org/10.1016/0038-1101\(68\)90012-9](https://doi.org/10.1016/0038-1101(68)90012-9).
- [26] L.A. Bauer, N.S. Birenbaum, G.J. Meyer, Biological applications of high aspect ratio nanoparticles, *J. Mater. Chem.* (2004) 517–526. <https://doi.org/10.1039/b312655b>.
- [27] Y. Cui, Q. Wei, H. Park, C.M. Lieber, Nanowire nanosensors for highly sensitive and selective detection of biological and chemical species, *Science* (80-. ). 293 (2001) 1289–1292. <https://doi.org/10.1126/science.1062711>.
- [28] A. Gao, N. Lu, Y. Wang, P. Dai, T. Li, X. Gao, Y. Wang, C. Fan, Enhanced sensing of nucleic acids with silicon nanowire field effect transistor biosensors, *Nano Lett.* 12 (2012) 5262–5268. <https://doi.org/10.1021/nl302476h>.
- [29] T. Adam, U. Hashim, Highly sensitive silicon nanowire biosensor with novel liquid gate control for detection of specific single-stranded DNA molecules, *Biosens. Bioelectron.* 67 (2015) 656–661. <https://doi.org/10.1016/j.bios.2014.10.005>.
- [30] P. Dai, A. Gao, N. Lu, T. Li, Y. Wang, A back-gate controlled silicon nanowire sensor with sensitivity improvement for DNA and pH detection, *Jpn. J. Appl. Phys.* 52 (2013). <https://doi.org/10.7567/JJAP.52.121301>.
- [31] J.Y. Wu, C.L. Tseng, Y.K. Wang, Y. Yu, K.L. Ou, C.C. Wu, Detecting Interleukin-1 $\beta$  Genes Using a N2O Plasma Modified Silicon Nanowire Biosensor, *J. Exp. Clin. Med.* 5 (2013) 12–16. <https://doi.org/10.1016/j.jecm.2013.01.002>.
- [32] W.U. Wang, C. Chen, K. Lin, Y. Fang, C.M. Lieber, Label-free detection of small-molecule-protein interactions by using nanowire nanosensors, *Proc. Natl. Acad. United States Am.* 102 (2005) 3208–3212. <https://doi.org/10.1073/pnas.0406368102>.
- [33] E. Stern, J.F. Klemic, D.A. Routenberg, P.N. Wyrembak, D.B. Turner-Evans, A.D. Hamilton, D.A. LaVan, T.M. Fahmy, M.A. Reed, Label-free immunodetection with CMOS-compatible semiconducting nanowires, *Nature.* 445 (2007) 519–522. <https://doi.org/10.1038/nature05498>.
- [34] M. Nuzaihan, U. Hashim, M.K.M. Arshad, A. Rahim Ruslinda, S.F.. Rahman, M.F.. Fathil, M.H. Ismail, Top-down nanofabrication and characterization of 20 nm silicon nanowires for biosensing applications, *PLoS One.* 11 (2016) 20–23. <https://doi.org/10.1371/journal.pone.0152318>.
- [35] A. Müller, X.T. Vu, V. Pachauri, L.A. Francis, D. Flandre, S. Ingebrandt, Wafer-Scale Nanoimprint Lithography Process Towards Complementary Silicon Nanowire Field-Effect Transistors for Biosensor Applications, *Phys. Status Solidi Appl. Mater. Sci.* 215 (2018) 1–10.

- <https://doi.org/10.1002/pssa.201800234>.
- [36] G. Jayakumar, M. Legallais, P.E. Hellström, M. Mouis, I. Pignot-Paintrand, V. Stambouli, C. TERNON, M. Ostling, Wafer-scale HfO<sub>2</sub> encapsulated silicon nanowire field effect transistor for efficient label-free DNA hybridization detection in dry environment, *Nanotechnology*. 30 (2019). <https://doi.org/10.1088/1361-6528/aaffa5>.
- [37] M.O. Noor, U.J. Krull, Silicon nanowires as field-effect transducers for biosensor development: A review, *Anal. Chim. Acta*. 825 (2014) 1–25. <https://doi.org/10.1016/j.aca.2014.03.016>.
- [38] M. Legallais, T.T.T. Nguyen, T. Cazimajou, M. Mouis, B. Salem, C. TERNON, Material engineering of percolating silicon nanowire networks for reliable and efficient electronic devices, *Mater. Chem. Phys.* 238 (2019). <https://doi.org/10.1016/j.matchemphys.2019.121871>.
- [39] G. Gruner, Carbon nanotube films for transparent and plastic electronics, *J. Mater. Chem.* 16 (2006) 3533–3539. <https://doi.org/10.1039/b603821m>.
- [40] P. Serre, Etude des propriétés structurales et électriques de réseaux aléatoires de nanofils de silicium. Application à la détection d'ADN., Université Grenoble Alpes, 2014. <https://www.theses.fr/2014GRENT110>.
- [41] M. Legallais, T.T.T. Nguyen, M. Mouis, B. Salem, E. Robin, P. Chenevier, C. TERNON, An innovative large scale integration of silicon nanowire-based field effect transistors, *Solid. State. Electron.* 143 (2018) 97–102. <https://doi.org/10.1016/j.sse.2017.11.008>.
- [42] J.M. Hammersley, Percolation processes, *Math. Proc. Cambridge Philos. Soc.* 53 (1957) 642–645. <https://doi.org/10.1017/s0305004100032692>.
- [43] C. TERNON, P. Serre, G. Rey, C. Holtzinger, P. Periwal, M. Martin, T. Baron, V. Stambouli, M. Langlet, High aspect ratio semiconducting nanostructure random networks: Highly versatile materials for multiple applications, *Phys. Status Solidi - Rapid Res. Lett.* 7 (2013) 919–923. <https://doi.org/10.1002/pssr.201308047>.
- [44] Q. Cao, H.S. Kim, N. Pimparkar, J.P. Kulkarni, C. Wang, M. Shim, K. Roy, M.A. Alam, J.A. Rogers, Medium-scale carbon nanotube thin-film integrated circuits on flexible plastic substrates, *Nature*. 454 (2008) 495–500. <https://doi.org/10.1038/nature07110>.
- [45] M. Delalande, S. Clavaguera, M. Toure, A. Carella, S. Lenfant, D. Deresmes, D. Vuillaume, J.P. Simonato, Chemical functionalization of electrodes for detection of gaseous nerve agents with carbon nanotube field-effect transistors, *Chem. Commun.* 47 (2011) 6048–6050. <https://doi.org/10.1039/c1cc11517k>.
- [46] H. Lu, D. Zhang, J. Cheng, J. Liu, J. Mao, W.C.H. Choy, Locally Welded Silver Nano-Network

- Transparent Electrodes with High Operational Stability by a Simple Alcohol-Based Chemical Approach, *Adv. Funct. Mater.* 25 (2015) 4211–4218. <https://doi.org/10.1002/adfm.201501004>.
- [47] C. Celle, C. Mayousse, E. Moreau, H. Basti, A. Carella, J.P. Simonato, Highly flexible transparent film heaters based on random networks of silver nanowires, *Nano Res.* 5 (2012) 427–433. <https://doi.org/10.1007/s12274-012-0225-2>.
- [48] C. Sun, N. Mathews, M. Zheng, C.H. Sow, L.H. Wong, S.G. Mhaisalkar, Aligned tin oxide nanonets for high-performance transistors, *J. Phys. Chem. C.* 114 (2010) 1331–1336. <https://doi.org/10.1021/jp909673j>.
- [49] H. Chen, L. Hu, X. Fang, L. Wu, General fabrication of monolayer SnO<sub>2</sub> nanonets for high-performance ultraviolet photodetectors, *Adv. Funct. Mater.* 22 (2012) 1229–1235. <https://doi.org/10.1002/adfm.201102506>.
- [50] H.E. Unalan, Y. Zhang, P. Hiralal, S. Dalal, D. Kuo, W.I. Milne, G.A.J. Amaratunga, Zinc Oxide Nanowire Networks for Macroelectronic Devices, *Appl. Phys. Lett.* (2009) 561–564.
- [51] F. Morisot, C. Zuliani, J. Luque, Z. Ali, M. Mouis, V.H. Nguyen, D. Munoz-Rojas, O. Lourhzal, M. Texier, T.W. Cornelius, C. Ternon, ZnO based nanowire network for gas sensing applications, *Mater. Res. Express.* 6 (2019) 0–9. <https://doi.org/10.1088/2053-1591/ab1f60>.
- [52] B. Aksoy, S. Coskun, S. Kucukyildiz, H.E. Unalan, Transparent, highly flexible, all nanowire network germanium photodetectors, *Nanotechnology.* 23 (2012). <https://doi.org/10.1088/0957-4484/23/32/325202>.
- [53] M.G. Rabbani, S.R. Patil, A. Verma, J.E. Villarreal, B.A. Korgel, R. Nekovei, M.M. Khader, R.B. Darling, M.P. Anantram, Zero-bias photocurrents in highly-disordered networks of Ge and Si nanowires, *ArXiv.* (2017).
- [54] D. Zhang, Z. Liu, C. Li, T. Tang, X. Liu, S. Han, B. Lei, C. Zhou, Detection of NO<sub>2</sub> down to ppb levels using individual and multiple In<sub>2</sub>O<sub>3</sub> nanowire devices, *Nano Lett.* 4 (2004) 1919–1924. <https://doi.org/10.1021/nl0489283>.
- [55] D. Whang, S. Jin, Y. Wu, C.M. Lieber, Large-scale hierarchical organization of nanowire arrays for integrated nanosystems, *Nano Lett.* 3 (2003) 1255–1259. <https://doi.org/10.1021/nl0345062>.
- [56] E. Mulazimoglu, S. Coskun, M. Gunoven, B. Butun, E. Ozbay, R. Turan, H.E. Unalan, Silicon nanowire network metal-semiconductor-metal photodetectors, *Appl. Phys. Lett.* 103 (2013). <https://doi.org/10.1063/1.4819387>.
- [57] K. Heo, E. Cho, J.E. Yang, M.H. Kim, M. Lee, B.Y. Lee, S.G. Kwon, M.S. Lee, M.H. Jo, H.J. Choi, T. Hyeon, S. Hong, Large-scale assembly of silicon nanowire network-based devices using

- conventional microfabrication facilities, *Nano Lett.* 8 (2008) 4523–4527. <https://doi.org/10.1021/nl802570m>.
- [58] P. Serre, M. Mongillo, P. Periwai, T. Baron, C. Ternon, Percolating silicon nanowire networks with highly reproducible electrical properties, *Nanotechnology.* 26 (2015). <https://doi.org/10.1088/0957-4484/26/1/015201>.
- [59] C. Ternon, P. Serre, J.M. Lebrun, V. Brouzet, M. Legallais, S. David, T. Luciani, C. Pascal, T. Baron, J.M. Missiaen, Low Temperature Processing to Form Oxidation Insensitive Electrical Contact at Silicon Nanowire/Nanowire Junctions, *Adv. Electron. Mater.* 1 (2015) 1–8. <https://doi.org/10.1002/aelm.201500172>.
- [60] M. Legallais, T.T.T. Nguyen, M. Mouis, B. Salem, E. Robin, P. Chenevier, C. Ternon, An innovative large scale integration of silicon nanowire-based field effect transistors, *Solid. State. Electron.* (2017). <https://doi.org/10.1016/J.SSE.2017.11.008>.
- [61] T.T.T. Nguyen, T. Cazimajou, M. Legallais, T. Arjmand, V.H. Nguyen, M. Mouis, B. Salem, E. Robin, C. Ternon, Monolithic fabrication of nano-to-millimeter scale integrated transistors based on transparent and flexible silicon nanonets, *Nano Futur.* 3 (2019). <https://doi.org/10.1088/2399-1984/ab1ebc>.
- [62] T.T.T. Nguyen, M. Legallais, F. Morisot, T. Cazimajou, M. Mouis, B. Salem, V. Stambouli, C. Ternon, On the Development of Label-Free DNA Sensor Using Silicon Nanonet Field-Effect Transistors, *Proceedings.* 1 (2017) 312. <https://doi.org/10.3390/proceedings1040312>.
- [63] T.T.T. Nguyen, M. Legallais, F. Morisot, T. Cazimajou, V. Stambouli, M. Mouis, B. Salem, C. Ternon, First evidence of superiority of Si nanonet field effect transistors over multi-parallel Si nanowire ones in view of electrical DNA hybridization detection, *Mater. Res. Express.* 6 (2019). <https://doi.org/10.1088/2053-1591/aae0d5>.
- [64] M. Thanihaichelvan, L.A. Browning, M.P. Dierkes, R.M. Reyes, A. V. Kralicek, C. Carraher, C.A. Marlow, N.O.V. Plank, Metallic-semiconducting junctions create sensing hot-spots in carbon nanotube FET aptasensors near percolation, *Biosens. Bioelectron.* 130 (2019) 408–413. <https://doi.org/10.1016/j.bios.2018.09.021>.
- [65] X. Dong, Q. Long, J. Wang, M.B. Chan-Park, Y. Huang, W. Huang, P. Chen, A graphene nanoribbon network and its biosensing application, *Nanoscale.* 3 (2011) 5156–5160. <https://doi.org/10.1039/c1nr11006c>.
- [66] J.P. Kim, B.Y. Lee, S. Hong, S.J. Sim, Ultrasensitive carbon nanotube-based biosensors using antibody-binding fragments, *Anal. Biochem.* 381 (2008) 193–198.

- <https://doi.org/10.1016/j.ab.2008.06.040>.
- [67] C. Li, M. Curreli, H. Lin, B. Lei, F.N. Ishikawa, R. Datar, R.J. Cote, M.E. Thompson, C. Zhou, Complementary detection of prostate-specific antigen using In 2O<sub>3</sub> nanowires and carbon nanotubes, *J. Am. Chem. Soc.* 127 (2005) 12484–12485. <https://doi.org/10.1021/ja053761g>.
- [68] S. Su, X. Wei, Y. Guo, Y. Zhong, Y. Su, Q. Huang, C. Fan, Y. He, A silicon nanowire-based electrochemical sensor with high sensitivity and electrocatalytic activity, *Part. Part. Syst. Charact.* 30 (2013) 326–331. <https://doi.org/10.1002/ppsc.201200076>.
- [69] J. Huang, Y. Zhu, H. Zhong, X. Yang, C. Li, Dispersed CuO nanoparticles on a silicon nanowire for improved performance of nonenzymatic H<sub>2</sub>O<sub>2</sub> detection, *ACS Appl. Mater. Interfaces.* 6 (2014) 7055–7062. <https://doi.org/10.1021/am501799w>.
- [70] B. Tao, J. Zhang, S. Hui, L. Wan, An amperometric ethanol sensor based on a Pd-Ni/SiNWs electrode, *Sensors Actuators, B Chem.* 142 (2009) 298–303. <https://doi.org/10.1016/j.snb.2009.08.004>.
- [71] L. Maiolo, D. Polese, A. Pecora, G. Fortunato, Y. Shacham-Diamand, A. Convertino, Highly Disordered Array of Silicon Nanowires: An Effective and Scalable Approach for Performing and Flexible Electrochemical Biosensors, *Adv. Healthc. Mater.* 5 (2016) 575–583. <https://doi.org/10.1002/adhm.201500538>.
- [72] Y. Liu, A. Rahimian, S. Krylyuk, T. Vu, B. Crulhas, G. Stybayeva, M. Imanbekova, D.S. Shin, A. Davydov, A. Revzin, Nanowire Aptasensors for Electrochemical Detection of Cell-Secreted Cytokines, *ACS Sensors.* 2 (2017) 1644–1652. <https://doi.org/10.1021/acssensors.7b00486>.
- [73] W. Chen, H. Yao, C.H. Tzang, J. Zhu, M. Yang, S.T. Lee, Silicon nanowires for high-sensitivity glucose detection, *Appl. Phys. Lett.* 88 (2006). <https://doi.org/10.1063/1.2206102>.
- [74] J.I. Abdul Rashid, N.A. Yusof, J. Abdullah, U. Hashim, R. Hajian, Surface modifications to boost sensitivities of electrochemical biosensors using gold nanoparticles/silicon nanowires and response surface methodology approach, *J. Mater. Sci.* 51 (2016) 1083–1097. <https://doi.org/10.1007/s10853-015-9438-6>.
- [75] Q. Yan, Z. Wang, J. Zhang, H. Peng, X. Chen, H. Hou, C. Liu, Nickel hydroxide modified silicon nanowires electrode for hydrogen peroxide sensor applications, *Electrochim. Acta.* 61 (2012) 148–153. <https://doi.org/10.1016/j.electacta.2011.11.098>.
- [76] J. Yin, X. Qi, L. Yang, G. Hao, J. Li, J. Zhong, A hydrogen peroxide electrochemical sensor based on silver nanoparticles decorated silicon nanowire arrays, *Electrochim. Acta.* 56 (2011) 3884–3889. <https://doi.org/10.1016/j.electacta.2011.02.033>.
- [77] S. Hui, J. Zhang, X. Chen, H. Xu, D. Ma, Y. Liu, B. Tao, Study of an amperometric glucose sensor based

- on Pd-Ni/SiNW electrode, *Sensors Actuators, B Chem.* 155 (2011) 592–597. <https://doi.org/10.1016/j.snb.2011.01.015>.
- [78] D.H. Kwon, H.H. An, H.S. Kim, J.H. Lee, S.H. Suh, Y.H. Kim, C.S. Yoon, Electrochemical albumin sensing based on silicon nanowires modified by gold nanoparticles, *Appl. Surf. Sci.* 257 (2011) 4650–4654. <https://doi.org/10.1016/j.apsusc.2010.12.109>.
- [79] H. Shashaani, M. Faramarzpour, M. Hassanpour, N. Namdar, A. Alikhani, M. Abdolahad, Silicon nanowire based biosensing platform for electrochemical sensing of Mebendazole drug activity on breast cancer cells, *Biosens. Bioelectron.* 85 (2016) 363–370. <https://doi.org/10.1016/j.bios.2016.04.081>.
- [80] S. Su, Y. He, M. Zhang, K. Yang, S. Song, X. Zhang, C. Fan, S.T. Lee, High-sensitivity pesticide detection via silicon nanowires-supported acetylcholinesterase-based electrochemical sensors, *Appl. Phys. Lett.* 93 (2008). <https://doi.org/10.1063/1.2959827>.
- [81] K. Yang, H. Wang, K. Zou, X. Zhang, Gold nanoparticle modified silicon nanowires as biosensors, *Nanotechnology.* 17 (2006). <https://doi.org/10.1088/0957-4484/17/11/S08>.
- [82] B. Nasr, G. Chana, T.T. Lee, T. Nguyen, C. Abeyrathne, G.M. D'Abaco, M. Dottori, E. Skafidas, Vertical Nanowire Electrode Arrays as Novel Electrochemical Label-Free Immunosensors, *Small.* 11 (2015) 2862–2868. <https://doi.org/10.1002/smll.201403540>.
- [83] N. Mintz-Hemed, T. Yoetz-Kopelman, A. Convertino, A. Freeman, Y. Shacham-Diamand, Whole-Cell Electrochemical Biosensor Integrating Microbes with Si Nanowire-Forest, *J. Electrochem. Soc.* 164 (2017) B253–B257. <https://doi.org/10.1149/2.1471706jes>.
- [84] B.D. Malhotra, M.A. Ali, *Nanomaterials in Biosensors. Fundamentals and Applications*, 2018. <http://mpoc.org.my/malaysian-palm-oil-industry/>.
- [85] Q. Palomar, *Intégration de matériaux nanostructurés dans la conception et la réalisation de biocapteurs sans marquage pour la détection de cibles d'intérêt*, Université Grenoble Alpes, 2018.
- [86] C. Rosano, P. Arosio, M. Bolognesi, The X-ray three-dimensional structure of avidin, *Biomol. Eng.* 16 (1999) 5–12. [https://doi.org/10.1016/S1050-3862\(99\)00047-9](https://doi.org/10.1016/S1050-3862(99)00047-9).
- [87] S. Cosnier, M. Holzinger, Electrosynthesized polymers for biosensing, *Chem. Soc. Rev.* 40 (2011) 2146–2156. <https://doi.org/10.1039/c0cs00090f>.
- [88] J. Davis, A. Glidle, A.E.G. Cass, J. Zhang, J.M. Cooper, Spectroscopic evaluation of protein affinity binding at polymeric biosensor films, *J. Am. Chem. Soc.* 121 (1999) 4302–4303. <https://doi.org/10.1021/ja984467+>.
- [89] Y. Zhu, Q. Chen, L. Shao, Y. Jia, X. Zhang, Microfluidic immobilized enzyme reactors for continuous

- biocatalysis, *React. Chem. Eng.* 5 (2020) 9–32. <https://doi.org/10.1039/c9re00217k>.
- [90] J.B. Cano, K. Buonasera, G. Pezzotti, Transduction methods used on biosensors: amperometry and fluorescence, *Rev. Fac. Ing. Univ. Antioquia.* (2014) 104–115.
- [91] L.M. Lechuga, Optical biosensors, in: *Compr. Anal. Chem.*, 2005: pp. 209–250. [https://doi.org/10.1016/S0166-526X\(05\)44005-2](https://doi.org/10.1016/S0166-526X(05)44005-2).
- [92] S. Tombelli, Piezoelectric biosensors for medical applications, in: *Biosens. Med. Appl.*, Elsevier Masson SAS., 2012: pp. 41–64. <https://doi.org/10.1533/9780857097187.1.41>.
- [93] R. Rebelo, A.I. Barbosa, S.C. Kundu, R.L. Reis, V.M. Correlo, Biodetection and sensing for cancer diagnostics, in: *Biomater. 3D Tumor Model.*, INC, 2020: pp. 643–660. <https://doi.org/10.1016/b978-0-12-818128-7.00026-5>.
- [94] B. Xie, K. Ramanathan, B. Danielsson, Principles of enzyme thermistor systems: applications to biomedical and other measurements., *Adv. Biochem. Eng. Biotechnol.* 64 (1999) 1–33. [https://doi.org/10.1007/3-540-49811-7\\_1](https://doi.org/10.1007/3-540-49811-7_1).
- [95] X. Luo, J.J. Davis, Electrical biosensors and the label free detection of protein disease biomarkers, *Chem. Soc. Rev.* 42 (2013) 5944. <https://doi.org/10.1039/c3cs60077g>.
- [96] P. Bergveld, Development, operation, and application of the ion-sensitive field-effect transistor as a tool for electrophysiology., *IEEE Trans. Biomed. Eng.* 19 (1972) 342–351. <https://doi.org/10.1109/TBME.1972.324137>.
- [97] D. Sadighbayan, M. Hasanzadeh, E. Ghafar-Zadeh, Biosensing based on field-effect transistors (FET): Recent progress and challenges, *TrAC Trends Anal. Chem.* 133 (2020) 116067. <https://doi.org/10.1016/j.trac.2020.116067>.
- [98] T.R. Kuphaldt, *Lessons In Electric Circuits, Volume III – Semiconductors*, 2009.
- [99] S.. Sze, K.. Ng, *Physics of Semiconductor Devices*, Third edit, 2006.
- [100] C. Lefrou, P. Fabry, J.-C. Poignet, *Electrochemistry: The basics, with examples*, Springer, 2012.
- [101] C. Lyons, L.C. Clark, Electrode systems for continuous monitoring in cardiovascular surgery, *Ann. N. Y. Acad. Sci.* 102 (1962) 29–45.
- [102] M. El-Azazy, Electrochemical Impedance Spectroscopy (EIS) in Food, Water, and Drug Analyses. Recent Advances and Applications, in: *Electrochem. Impedance Spectrosc.*, 2020: pp. 1–10.
- [103] T. Yin, W. Qin, Applications of nanomaterials in potentiometric sensors, *TrAC - Trends Anal. Chem.* 51 (2013) 79–86. <https://doi.org/10.1016/j.trac.2013.06.009>.
- [104] J. Bobacka, A. Ivaska, A. Lewenstam, Potentiometric ion sensors, *Chem. Rev.* 108 (2008) 329–351. <https://doi.org/10.1021/cr068100w>.

- [105] E. Bakker, E. Pretsch, Potentiometry at trace levels, *TrAC - Trends Anal. Chem.* 20 (2001) 11–19. [https://doi.org/10.1016/S0165-9936\(00\)00056-X](https://doi.org/10.1016/S0165-9936(00)00056-X).
- [106] J.X.J. Zhang, K. Hoshino, *Electrical transducers: Electrochemical sensors and semiconductor molecular sensors*, 2019. <https://doi.org/10.1016/b978-0-12-814862-4.00004-1>.
- [107] J.-G. Guan, Y.-Q. Miao, Q.-J. Zhang, Impedimetric biosensors, *J. Biosci. Bioeng.* 97 (2004) 219–226. [https://doi.org/10.1016/s1389-1723\(04\)70195-4](https://doi.org/10.1016/s1389-1723(04)70195-4).
- [108] A.W. Bott, *Electrochemical Techniques for the Characterization of Redox Polymers*, *Curr. Sep.* 19 (2001) 71–75.
- [109] E. Katz, I. Willner, Probing biomolecular interactions at conductive and semiconductive surfaces by impedance spectroscopy: Routes to impedimetric immunosensors, DNA-sensors, and enzyme biosensors, *Electroanalysis*. 15 (2003) 913–947. <https://doi.org/10.1002/elan.200390114>.
- [110] T. Nasir, *Electrochemical sensors of environmental pollutants based on carbon electrodes modified by ordered mesoporous silica*, Université de Lorraine, 2018.
- [111] N. Elgrishi, K.J. Rountree, B.D. McCarthy, E.S. Rountree, T.T. Eisenhart, J.L. Dempsey, A Practical Beginner's Guide to Cyclic Voltammetry, *J. Chem. Educ.* 95 (2018) 197–206. <https://doi.org/10.1021/acs.jchemed.7b00361>.
- [112] F. Scholz, *Voltammetric techniques of analysis: the essentials*, *ChemTexts*. 1 (2015) 1–24. <https://doi.org/10.1007/s40828-015-0016-y>.
- [113] F.T.G. van den Brink, *Microreactor for electrochemical conversion in drug screening and proteomics*, University of Twente, 2016. <https://doi.org/10.3990/1.9789036541459>.
- [114] M. Ciobanu, J.P. Wilburn, M.L. Krim, D.E. Cliffel, Fundamentals, in: *Handb. Electrochem.*, 2007: pp. 3–29. <https://doi.org/10.1016/B978-044451958-0.50002-1>.
- [115] T. Luxbacher, *Electrokinetic properties of natural fibres*, Elsevier Ltd, 2020. <https://doi.org/10.1016/B978-0-12-818782-1.00009-2>.
- [116] B. Bhattacharyya, *Electrochemical Machining*, in: *Electrochem. Micromach. Nanofabrication, MEMS Nanotechnol.*, 2015: pp. 25–52. <https://doi.org/10.1016/b978-0-323-32737-4.00002-5>.
- [117] Z. Ahmad, *Corrosion Kinetics*, in: *Princ. Corros. Eng. Corros. Control*, 2006: pp. 57–119. <https://doi.org/10.31399/asm.tb.ssde.t52310019>.
- [118] A.J. Bard, I. György, F. Scholz, *Electrochemical Dictionary*, Springer, 2012. <https://doi.org/10.1007/978-3-642-29551-5>.
- [119] F. Scholz, *Electroanalytical methods: Guide to experiments and applications*, 2010. <https://doi.org/10.1007/978-3-642-02915-8>.

- [120] B. Torbiero, Développement de microcapteurs électrochimiques pour l'analyse en phase liquide, Institut National des Sciences Appliquées de Toulouse, 2007.
- [121] S.P. Kounaves, Voltammetric Techniques, in: Handb. Instrum. Tech. Anal. Chem., 1997: pp. 709–725. <https://doi.org/10.1002/9781118684030.ch2>.
- [122] V.K. Gupta, R. Jain, K. Radhapyari, N. Jadon, S. Agarwal, Voltammetric techniques for the assay of pharmaceuticals-A review, Anal. Biochem. 408 (2011) 179–196. <https://doi.org/10.1016/j.ab.2010.09.027>.
- [123] H. Robson, M. Reinhardt, C. Bracher, Cyclic Voltammetry: Basic Principles & Set Up, (n.d.). <https://www.ossila.com/pages/cyclic-voltammetry>.
- [124] F. Bedioui, Voltampérométrie . Théorie et mise en œuvre expérimentale, 1999.
- [125] A. Reguig, Etude électrochimique des Complexes de Quelques Métaux de Transitions Dérivés des Ligands Hydrazides et Hydrazones, Université Abou Bekr Belkaid - Tlemcen, 2013.
- [126] J. Baur, Autoassemblage de macromolécules biologiques via des poly(pyrroles) et/ou des nanotubes de carbone fonctionnalisés, Université de Grenoble, 2010.
- [127] F. Giroud, Biomatériaux d'électrode appliqués à la réalisation et à la caractérisation d'un biocapteur immunologique et de biopiles enzymatiques, Université de Grenoble, 2011.
- [128] Gamry Instruments, Basics of Electrochemical Impedance Spectroscopy, (n.d.). <https://www.gamry.com/application-notes/EIS/basics-of-electrochemical-impedance-spectroscopy/>.
- [129] P. Fabry, C. Gondran, Capteurs impedancemétriques, in: Capteurs Électrochimiques, Ellipses, 2008: pp. 45–90.
- [130] A. Bonanni, M. Del Valle, Use of nanomaterials for impedimetric DNA sensors: A review, Anal. Chim. Acta. 678 (2010) 7–17. <https://doi.org/10.1016/j.aca.2010.08.022>.
- [131] J.E. Randles, Kinetics of rapid electrode reactions, Discuss. Faraday Soc. (1947) 11–19.
- [132] E. Barsoukov, J.R. Macdonald, Impedance Spectroscopy Theory, Experiment, and Applications, John Wiley & Sons, 2005.
- [133] F. Seland, R. Tunold, D.A. Harrington, Impedance study of methanol oxidation on platinum electrodes, Electrochim. Acta. 51 (2006) 3827–3840. <https://doi.org/10.1016/j.electacta.2005.10.050>.
- [134] A.S. Tanak, B. Jagannath, Y. Tamrakar, S. Muthukumar, S. Prasad, Non-faradaic electrochemical impedimetric profiling of procalcitonin and C-reactive protein as a dual marker biosensor for early sepsis detection, Anal. Chim. Acta X. 3 (2019) 100029. <https://doi.org/10.1016/j.acax.2019.100029>.

- [135] A. Bogomolova, E. Komarova, K. Reber, T. Gerasimov, O. Yavuz, S. Bhatt, M. Aldissi, Challenges of electrochemical impedance spectroscopy in protein biosensing, *Anal. Chem.* 81 (2009) 3944–3949. <https://doi.org/10.1021/ac9002358>.
- [136] J.S. Daniels, N. Pourmand, Label-free impedance biosensors: Opportunities and challenges, *Electroanalysis*. 19 (2007) 1239–1257. <https://doi.org/10.1002/elan.200603855>.

**Chapter II: Development of Si  
nanonet-based FET biosensors**

## Chapter II: Development of Si nanonet-based FET biosensors

---

<b>Chapter II: Development of Si nanonet-based FET biosensors .....</b>	<b>61</b>
II.1.    Si nanonet-based FETs.....	63
II.1.1.    Si nanonet fabrication .....	63
II.1.2.    Si nanonet-based FET fabrication.....	66
II.2.    Biofunctionalization processes.....	69
II.2.1.    APTES-based biofunctionalization process.....	70
II.2.1.1.    Effect of the chip position during the imine bond reduction step.....	74
II.2.1.2.    Effect of the NaBH <sub>4</sub> concentration and duration of the imine bond reduction step..	75
II.2.2.    GOPS-based biofunctionalization process.....	77
II.2.2.1.    Optimization of the GOPS-based biofunctionalization process using UV radiation ...	79
II.2.2.1.1.    Wettability analyses .....	81
II.2.2.2.    Si nanonet-based FETs biofunctionalization by UV-assisted GOPS-based process.....	82
II.2.2.2.1.    Biofunctionalization monitoring by STEM-EDS.....	82
II.2.2.2.2.    Biofunctionalization monitoring by AFM.....	84
II.3.    Conclusions.....	89
<b>References .....</b>	<b>91</b>

## Chapter II: Development of Si nanonet-based FET biosensors

---

This chapter discusses the fabrication process of Si nanonet-based FET devices, as well as the different routes studied for their biofunctionalization, which were based on two different organosilanes.

The objective of the biofunctionalization process is the proper immobilization of the bioreceptor on the surface of the Si nanonet-based FETs. Herein, Thrombin Binding Aptamer (TBA-15) was used as bioreceptor. The latter is a specific G-quadruplex oligonucleotide probe for detection of thrombin ( $K_d \sim 35 - 100 \text{ nM}$  [1]). However, as this aptamer is a DNA molecule, it can also recognize its complementary DNA sequence. This property was exploited here to evaluate the efficiency of the studied biofunctionalization processes, by characterizations carried out by epifluorescence microscopy, thanks to the hybridization of the TBA-15 bioreceptor with its complementary DNA sequence labeled with a fluorophore. Additionally, other characterization techniques, such as Atomic Force Microscopy (AFM) and Energy Dispersive X-ray Spectroscopy in Scanning Transmission Electron Microscopy (STEM EDS) were used to verify the correct immobilization of the TBA-15 bioreceptor on the surface of the Si nanonet-FET devices. Some of the results presented in this chapter were recently published [2].

### II.1. Si nanonet-based FETs

As described before, the fabrication process of Si nanonet-based FET devices was developed and optimized in the course of several previous thesis and a post-doctoral projects, which were carried out in LMGP [3–6]. This process can be divided into two parts: the fabrication of the Si nanonet, and the fabrication of the Field-Effect Transistor made from Si nanonets (Si nanonet-based FET). Both processes will be detailed below.

#### II.1.1. Si nanonet fabrication

The Si nanonet is fabricated from a suspension of Si nanowires produced by vapor-liquid-solid (VLS) mechanism. This is a technique used for the growth of 1-dimensional nanostructures, frequently employed for the fabrication of nanotubes and nanowires [7], allowing a careful control of important parameters, such as diameter of the NWs and their crystallinity [8]. The Si

NWs used in this project were fabricated at LTM (Laboratoire des Technologies de la Microélectronique). They present an average diameter of  $39 \text{ nm} \pm 7 \text{ nm}$ , and an average length of  $18 - 19 \text{ }\mu\text{m}$  after the growth process (Figure II-1(a) and (b)), and they are non-intentionally p-doped, with an estimated doping level about  $10^{16} \text{ at}\cdot\text{cm}^{-3}$ .

The fabrication of Si nanonets involves four different steps: (1) dispersion of the Si NWs in solution, (2) purification of the suspension by centrifugation, (3) Si NWs density control by absorption spectroscopy and (4) Si nanonet assembly by vacuum filtration. These steps are illustrated in Figure II-1 (c)-(f).

- 1. Dispersion of the Si NWs in solution (Figure II-2(c)):** The objective of this step is to detach the NWs from the silicon substrate on which they were synthesized. For this, the substrate containing the Si NWs is immersed in deionized water, and then it is subjected to ultrasound at 280 W, at a frequency of 37 KHz, for 5 min, resulting in a colloidal suspension. This process generates an important reduction in the size of the NWs, which present an average length of  $6.9 \text{ }\mu\text{m} \pm 2.8 \text{ }\mu\text{m}$  after the sonication process, according to a statistical study previously carried out in SEM images over 360 NWs [2].
- 2. Purification of the suspension by centrifugation (Figure II-2(d)):** The formation of aggregates during the growth process of Si NWs is unavoidable. Since these structures can generate problems in the future transistor, it is necessary to extract them from the suspension by a centrifugation process. This technique is commonly employed to separate different groups of particles within a solution. It involves the use of a centrifugal force to separate them, according to the size, shape or density of the particles. Herein, the process is carried out using relative centrifugal force (RFC) of 720 g, equivalent to 1892 rpm, for 20 min [2]. At the end of the process, it is possible to extract a part of the suspension containing mostly Si NWs (approximately 75% of the initial solution), and discard the solution containing the aggregates (about 25%).

- 3. Si NWs concentration control by absorption spectroscopy (Figure II-2(e)):** Previous investigations have shown that the absorbance of a colloidal suspension of Si NWs, at given wavelength, varies linearly with the concentration of the suspension for a given Si NW geometry [3]. This means that the quantity of Si NWs in the suspension is always the same for a specific absorbance value at a given wavelength. Then, the obtained Si NW suspension is diluted to an arbitrary fixed absorbance at 400nm of 0.06. This guarantees that the amount of Si NWs will be reproducible from one suspension to another.
- 4. Si nanonet assembly by vacuum filtration (Figure II-1(f)):** After the concentration control, the Si NW suspension is filtered in a Büchner funnel vacuum filtration system, through a nitrocellulose membrane (Millipore, diameter = 47 mm, pore size = 0.1  $\mu\text{m}$ ). During this step, the Si NWs are randomly trapped on the membrane surface, giving rise to the Si nanonet.

The nanonet density ( $D_{NN}$ ) ( $\text{NWs}\cdot\text{cm}^{-2}$ ) can be directly related to the filtered volume ( $V_{filtered}$ ) of suspension, and can be calculated by the equation II-1, when absorbance at 400 nm is equal to 0.06 for a given Si NW geometry [14]:

$$D_{NN} = 2.34 \times V_{filtered} \times 10^6 \quad \text{Equation II-1}$$

For this part of the project (Si nanonet-based FET devices), a volume of 18 mL was filtered, resulting in Si nanonets presenting a density of  $42 \times 10^6 \text{ NWs}\cdot\text{cm}^{-2}$ .

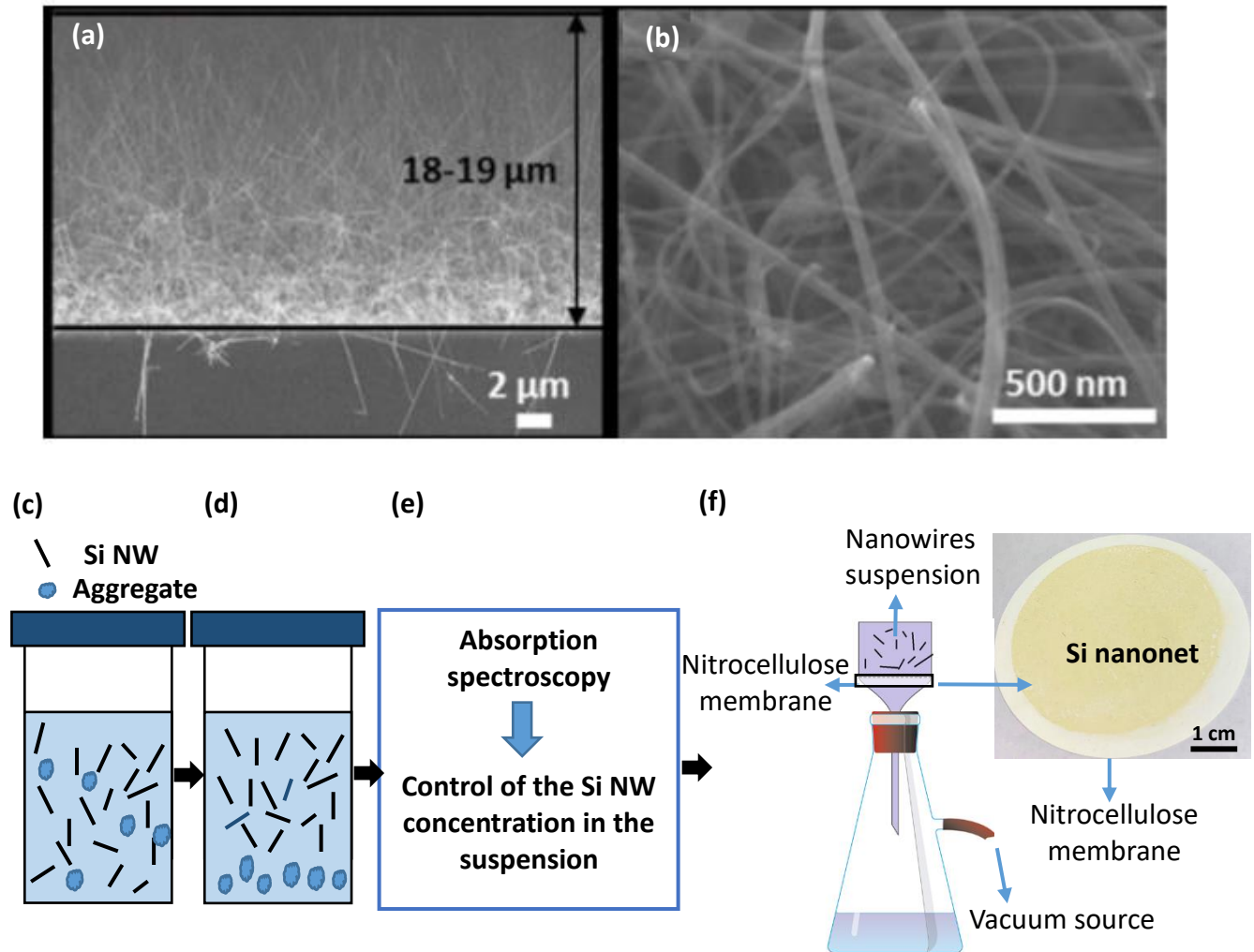


Figure II-1: SEM images of the Si NWs fabricated by VLS growth (a) cross-sectional view, and (b) top view [4]. (c) to (f) Schematic representation of the Si nanonet fabrication process: (c) dispersion of the Si NWs, (d) purification by centrifugation, (e) Si NW concentration control, and (f) Si nanonet assembly by vacuum filtration.

### II.1.2. Si nanonet-based FET fabrication

The fabrication of the Si nanonet-based FET devices relies on a process flow composed of 6 main technological steps, which are summarized in Figure II-2.

- 1. Si nanonet transfer to the substrate (Figure II-2(a)):** In this step, the Si nanonet is transferred to a heavily doped Si substrate covered with a 200 nm thick  $\text{Si}_3\text{N}_4$  layer (Si/  $\text{Si}_3\text{N}_4$  substrate), which will act as the oxide gate of the future Si nanonet-based FET device. For this purpose,

the substrate is subjected to ultrasonic cleaning during 5 min, in successive baths of acetone, ethanol and then deionized water. The filter nitrocellulose membrane containing the Si nanonet is cut a little smaller than the substrate size, and it is then immersed in a dichlorobenzene solution for 30 s, in order to remove the air within the pores, and achieve good adherence between the substrate and the Si nanonet. Then, the Si nanonet is immediately brought into contact with the Si/Si<sub>3</sub>N<sub>4</sub> substrate and the assembly is placed in an acetone bath for 35 min, in order to dissolve the nitrocellulose membrane. Finally, the whole is cleaned in acetone, and then isopropanol, and dried under nitrogen gas flow.

- 2. Si nanonet sintering (Figure II-2(b)):** The objective of this stage is to create conductive paths between the Si nanowires. For this purpose, the native oxide (SiO<sub>2</sub>) covering the Si nanonet is removed by using a HF/NH<sub>4</sub>F (6:1) solution (buffer oxide etching, BOE), and immediately the whole is subjected to a sintering process at 400°C for 1 min, under nitrogen atmosphere. This process results in the creation of necks between the Si NWs, improving the electrical properties of the Si nanonet-based FETs by two orders of magnitude and making them insensitive to oxidation in the air [9].
- 3. Si nanonet passivation (Figure II-2(c)):** During this step, the Si nanonet is covered with an 8 nm thick Al<sub>2</sub>O<sub>3</sub> layer deposited by Atomic Layer Deposition (ALD). This passivation layer significantly improves the electrical properties of the Si nanonet-based FETs. As mentioned before, this is generated by a decrease in the trap density at the NW-oxide interface. Indeed, the non-intentionally growth of native SiO<sub>2</sub> in air induces the formation of a high density of dangling bonds, acting as interface traps. On the contrary, alumina grown by well-controlled process allows the formation of an interface of better quality and enhances the electrical characteristics of the Si nanonet-based FET devices [10].
- 4. Si nanonet patterning (Figure II-2(d)):** The patterning process of the Al<sub>2</sub>O<sub>3</sub> passivated Si nanonet is carried out by the combination of wet (BOE) and dry (SF<sub>6</sub>) etching. This process allows to create different Si nanonet channel geometries, which will be detailed later.

5. **Formation of source and drain metal contacts (Figure II-2(e)):** This step is performed by combining photolithography and lift off processes. Before carrying out the metal deposition process, a wet etching (BOE) is performed in order to remove the  $\text{Al}_2\text{O}_3$  encapsulation layer from the zones of the Si nanonet that will be in contact with the source and drain metal contacts. Then, a metal bilayer (150 nm Ni/50 nm Au) is deposited by Electron Beam Evaporation.
  
6. **Metal contact silicidation (Figure II-2(f)):** Silicidation step consists of an annealing at 400 °C under  $\text{N}_2$  for 1 min. The objective of this stage is to create a low resistive phase (NiSi) between the Si from the nanonet and the Ni from the metal contacts, thus improving the electrical performance of the Si nanonet-based FET devices and the lift off process is carried out.

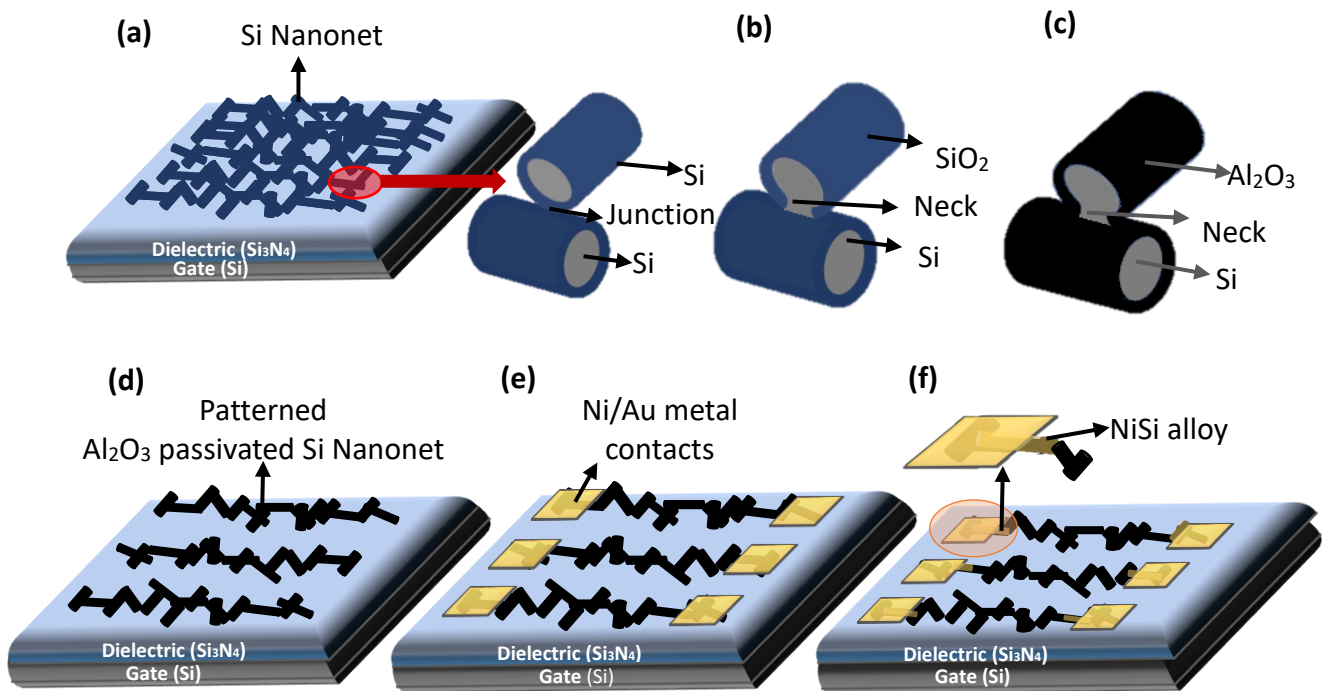


Figure II-2: Schematic representation of the Si nanonet-based process flow:(a) Si nanonet transferred on the Si/ $\text{Si}_3\text{N}_4$  substrate and zoom of two Si NW, highlighting the junction between them, (b) neck formation between two Si NWs thanks to the Si nanonet sintering, (c)  $\text{Al}_2\text{O}_3$  passivation of the Si nanonet (represented here by two Si NWs), (d) Si nanonet channels creation by patterning process, (e) formation of the metal contacts, and (f) NiSi alloy creation by silicidation process.

## Chapter II: Development of Si nanonet-based FET biosensors

A typical obtained chip is shown in Figure II-3. This device has a dimension of 7 mm x 7 mm. It contains about 180 Si nanonet-based FETs, with channel geometries ranging from 5  $\mu\text{m}$  to 200  $\mu\text{m}$  for the length (L), and from 10  $\mu\text{m}$  to 100  $\mu\text{m}$  for the width (W). The chip is composed of 4 similar quarters (Q), each containing 45 FETs with different geometries (W-L combinations).

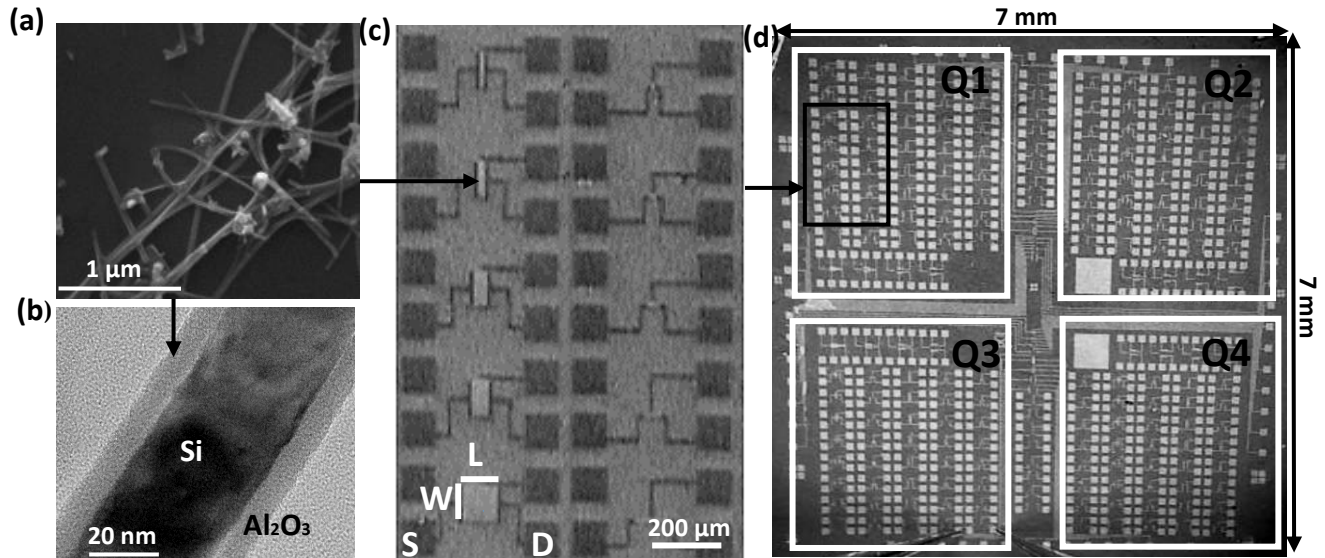


Figure II-3: (a) SEM image of the Si nanonet after transfer on Si/Si<sub>3</sub>N<sub>4</sub> substrate. (b) High-resolution TEM (HRTEM) image displaying an Al<sub>2</sub>O<sub>3</sub> passivated Si nanowire. (c) Optical image of Al<sub>2</sub>O<sub>3</sub> passivated Si nanonet FET, presenting different channel geometries. On the image, W, L, S and D refer to channel width, channel length, source and drain, respectively. (d) Optical image of the resulting chip. Q1, Q2, Q3 and Q4 denote the different quarters of the chip.

To produce a biosensor, these Si nanonet-based FET devices must be biofunctionalized. For this purpose, two biofunctionalization approaches were studied, both based on organosilanes: (3-Aminopropyl)triethoxysilane (APTES) and (3-Glycidyloxypropyl)trimethoxysilane (GOPS). The results obtained for each of the biofunctionalization methods studied are presented below.

### II.2. Biofunctionalization processes

The biofunctionalization process allows the immobilization of the bioreceptor (TBA-15) on the surface of the Si nanonet-based FET devices. As mentioned before, this stage plays a key role in the development of the FET biosensor, since it directly impacts its performance. Indeed, the detection of the target molecule depends on the proper grafting of the bioreceptor on the

biosensor surface, and the amount of target molecule that can be detected in turn depends on the amount of accessible bioreceptors. This has a direct effect on the different results obtained, such as the sensitivity, selectivity and response time of the device.

The two organosilane-based biofunctionalization approaches studied in this project are presented below.

### II.2.1. APTES-based biofunctionalization process

This protocol has been successfully used in the LMGP for the biofunctionalization of SiC NWs [11] and Si nanonets [4,12]. This is divided into 5 stages, which are summarized in Figure II-4.

- 1. Surface hydroxylation (Figure II-4(a)):** Prior to this step, the samples are cleaned in successive baths of acetone, ethanol and deionized water and then they are dried under a N<sub>2</sub> flow. Subsequently, they are exposed to an O<sub>2</sub>/air plasma during 4 min (Evactron plasma cleaning, XEI Scientific). This plasma process plays two essential roles. On the one hand, the oxygen radicals allow the removal of the carbonaceous residues still present on the samples by forming species such as carbon dioxide or carbon monoxide, which are then evacuated by the pumping system. On the other hand, this treatment modifies the surface of the Al<sub>2</sub>O<sub>3</sub> passivated Si nanonets, giving rise to the activation of the surface by the creation of hydroxyl groups (-OH), which are essential for the subsequent silanization process (*Figure II-4(a)*).
- 2. APTES silanization (Figure II-4(b)):** This process can be carried out either in the liquid or vapor phase. In this work, we chose the vapor phase silanization based on different reasons. First, previous studies have shown that the vapor deposition generates a more reactive self-assembled monolayer, compared to the liquid deposition [11,13]. Additionally, the liquid medium process is significantly longer than the vapor phase process (18 h vs. 2h).

The organosilane reaction with the hydroxyl groups involves sol-gel type mechanisms. Initially, it implies the hydrolysis of the silane, followed by its condensation on the surface of the sample. This vapor phase process is carried out under anhydrous conditions (N<sub>2</sub>

atmosphere, with a humidity percentage carefully controlled (less than 2%). The reaction takes place in a Teflon container in which the samples are placed together with a small glass vessel containing 150  $\mu\text{L}$  of APTES. The whole is placed in an oven at 80  $^{\circ}\text{C}$  for 1 h. This allows the evaporation of APTES and its reaction with the Si nanonet-based FET surface. Subsequently, the samples are cleaned with ethanol under stirring (5 min, at 50 rpm), and they are dried under argon flow. Finally, the samples are again placed in an oven at 110  $^{\circ}\text{C}$  for 1 h, in order to complete the reticulation process between the silane molecules and to remove any residual water.

- 3. Glutaraldehyde (GA) cross-linking (Figure II-4(c)):** In this case, the amine-modified bioreceptors ( $\text{NH}_2\text{-TBA-15}$ ) cannot react directly with the silanized surface, which is ending with amine groups. Then, the bioreceptor immobilization process requires the use of a cross-linker. For this purpose, we used a dialdehyde (glutaraldehyde). One of the aldehyde groups reacts with  $\text{NH}_2$  on the surface of the sample, giving rise to the generation of an imine group ( $\text{R-N=R'}$ ). The chains formed are terminated by the second aldehyde group, which will later allow the immobilization of the amine-modified bioreceptor ( $\text{NH}_2\text{-TBA-15}$ ). This step is carried out using a 2.5 % aqueous glutaraldehyde solution, for 1 h 30 min, followed by deionized water rinsing and argon flow drying.
- 4.  $\text{NH}_2\text{-TBA-15}$  immobilization (Figure II-4(d)):** Similarly to the previous step, the  $\text{NH}_2$  groups present in the amine-modified TBA-15 bioreceptor (sequence presented in Table II-1), react with the aldehyde group at the end of the chains formed in the previous step, giving rise to the generation of imine groups, which allow the bioreceptor grafting. For this purpose, the Si nanonet-based FET device is exposed to 28  $\mu\text{L}$  of phosphate buffer solution (PB) containing the amine-modified TBA-15 (10  $\mu\text{M}$ ). The sample is left to react overnight at room temperature and ambient conditions.
- 5. Reduction of the imine bonds (Figure II-4(e)):** The final step consists in the imine double bond reduction to an amine single bond. The objective of this stage is to obtain a structure that is

## Chapter II: Development of Si nanonet-based FET biosensors

more chemically stable. For this purpose, the Si nanonet-FET device is exposed to a 0.09 M NaBH<sub>4</sub> aqueous solution for 1 h. Subsequently, the samples are rinsed with deionized water, a 0.2% sodium dodecyl sulfate aqueous solution, and deionized water again, under stirring (30 rpm) during 5 min, for each solution.

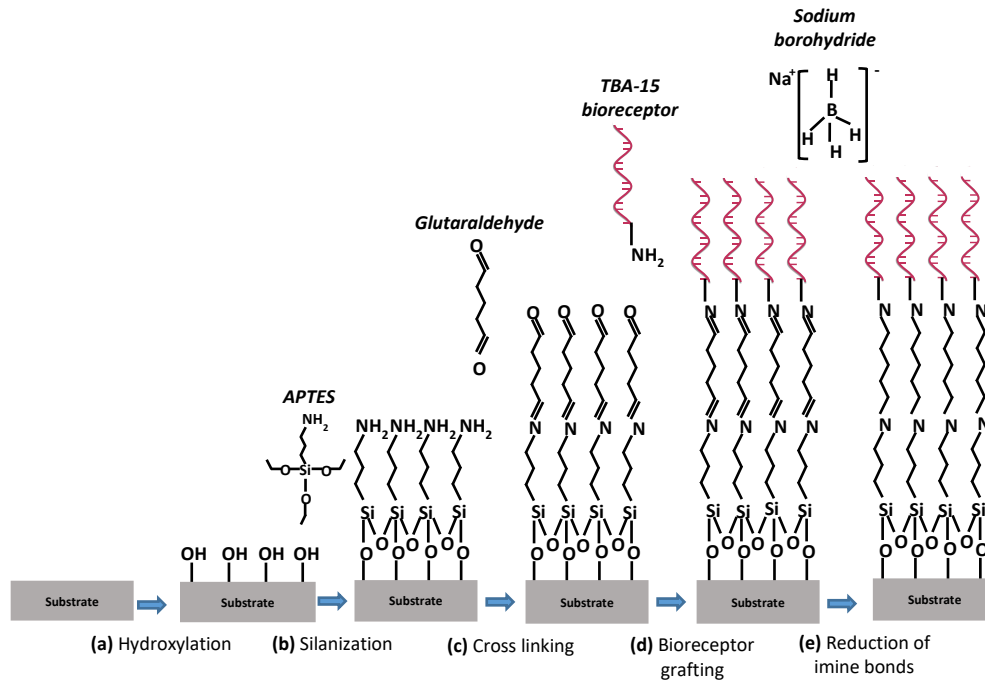


Figure II-4: Schematic representation of the different steps of the APTES-based biofunctionalization process.

Although the biofunctionalization process is considered to be completed at the stage of reduction of the imine bonds, an additional step is performed when it is necessary to evaluate whether the immobilization of the bioreceptor was carried out correctly. This additional step consists in the hybridization of the TBA-15 bioreceptor with its complementary DNA sequence (c-TBA). The later was labeled with a cyanine fluorophore (Cy3), in order to perform fluorescence intensity analyses. Indeed, the values obtained from the fluorescence intensity can be correlated with the amount of hybridized DNA, which in turn is directly proportional to the amount of grafted TBA-15 bioreceptor. The sequences corresponding to the TBA-15 bioreceptor and the c-TBA are described in the Table II-1.

## Chapter II: Development of Si nanonet-based FET biosensors

Table II-1: Sequences corresponding to the TBA-15 bioreceptor and its complementary DNA strand (c-TBA). The six thymines at the 3' end of the TBA-15 bioreceptor correspond to a spacer.

Name	Sequence
TBA-15	5'GGTTGGTGTGGTTGGTTTTT <sup>3'</sup> -NH <sub>2</sub>
c-TBA	Cy3-5'CCAACCACACCAACC <sup>3'</sup>

The hybridization step is carried out as follows:

**6. Hybridization step (Figure II-5):** To perform the hybridization of the TBA-15 with its Cy3 labeled DNA complementary sequence (c-TBA), a drop of 28  $\mu\text{L}$  of the c-TBA sequence (2  $\mu\text{m}$  in PBS) is deposited on the Si nanonet-based FET device, and subsequently it is spread over its entire surface using a thin plastic slide (Hybrislip<sup>®</sup>). The samples are then placed in a humidity chamber, and maintained at 42 °C for 45 min. Subsequently, they are successively rinsed for 2 min under stirring (50 rpm) in a 2X saline- sodium citrate aqueous solution (SSC), then 0.2X SSC, and finally in deionized water. This rinsing allows to remove the c-TBA strands that were not hybridized. Finally, the samples are dried under argon flow.

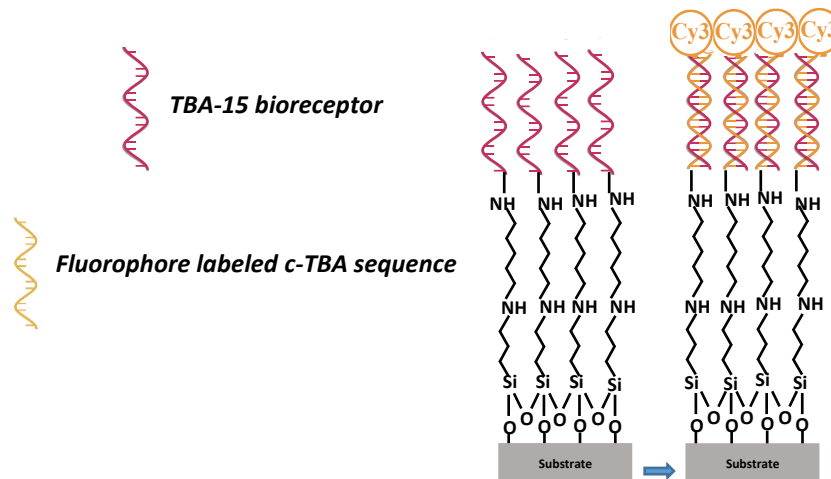
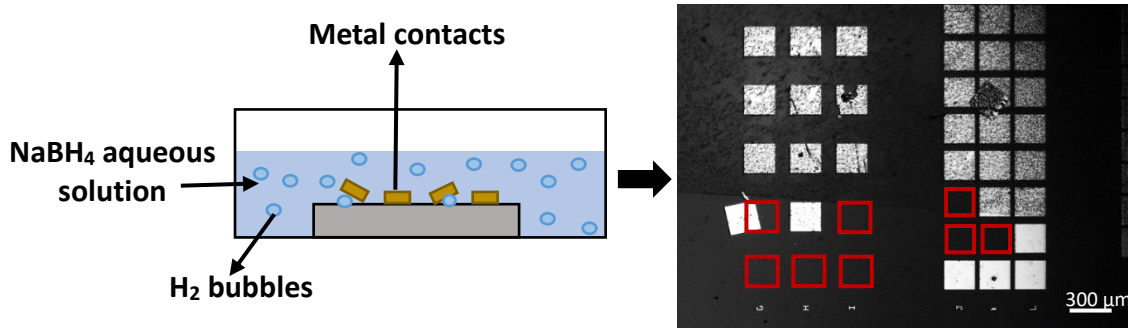


Figure II-5: Schematic representation of the TBA-15 hybridization with its complementary DNA sequence (c-TBA), which was labeled with a Cy3 fluorophore.

As previously mentioned, this APTES-based functionalization protocol had been successfully applied in our group for the functionalization of Si nanonets [12]. However, when this process was performed on Si nanonet-based FET devices, we observed that various issues occurred in the very last step of the functionalization. Indeed, as can be seen from Figure II-6, during the

reduction of imine bonds into amine ones by  $\text{NaBH}_4$ , a metal contact delamination took place, which was caused by the  $\text{H}_2$  bubbles generated as a by-product of imine reduction reaction in aqueous media.



*Figure II-6: (a) Schematic representation of the metal contact delamination due to the  $\text{H}_2$  bubbles generated during the  $\text{NaBH}_4$  reduction step. (b) Optical image of a chip containing Si nanonet-based FETs, evidencing the contact delamination issue. Red squares represent the contacts detached from the substrate after imine bonds reduction step.*

Two tracks were followed to solve this issue. The first one was related to the position of the samples during imine bond reduction step using  $\text{NaBH}_4$ . The second one was related to the  $\text{NaBH}_4$  concentration. Both studies will be detailed below

### II.2.1.1. Effect of the chip position during the imine bond reduction step

The position of the chip during the reduction step was changed, in order to analyze the effect of the type of exerted force (normal or tangential) by the bubbles on the metal contacts. As illustrated in *Figure II-7*, several positions were tested. However, none of them prevented the delamination of the metal contacts

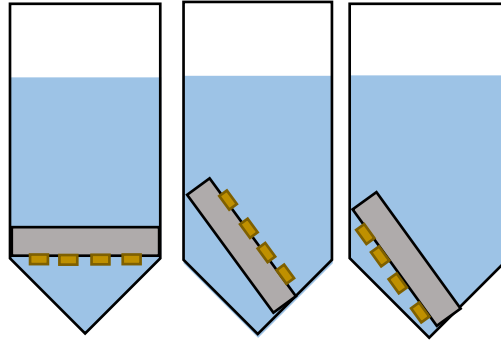


Figure II-7: Schematic representation of the different substrate positions studied for the  $\text{NaBH}_4$  imine bond reduction step.

### II.2.1.2. Effect of the $\text{NaBH}_4$ concentration and duration of the imine bond reduction step

Herein, in order to preserve the metal contact adhesion, it was decided to analyze the effect of the reduction of the  $\text{NaBH}_4$  concentration, seeking to reduce the amount of  $\text{H}_2$  produced during reaction, as well as the decrease in the duration time of the step. First of all, it was necessary to analyze if this changes did not affect the performance of TBA-15 bioreceptor grafting. For this purpose, the study was initially conducted on full wafer, corresponding to planar Si substrates covered with a 100 nm thick  $\text{SiO}_2$  layer (Si/ $\text{SiO}_2$  substrates). Indeed, this thickness of the  $\text{SiO}_2$  layer (100 nm) allows to observe a higher signal of the emitted fluorescence [3], after the hybridization of the TBA-15 bioreceptor with its Cy3-labeled complementary DNA sequence (c-TBA).

For this study, the concentration of  $\text{NaBH}_4$  was reduced from 0.09 M to 0.01 M, and different durations of the step were analyzed: 45 min, 30 min and 15 min (compared to 1 h for the reference process). The results were evaluated by epifluorescence microscopy, using an Olympus BX41M fluorescence microscope coupled with a 100W mercury lamp, for an exposure time of 3 s. The fluorescence analysis of the eight-bit jpg images was performed using the analysis software ImageJ. This software allows quantifying the fluorescence intensity of each image through a gray scale, having previously subtracted the background signal for each fluorescent spot. The fluorescence intensity values presented in this work were based on a scale from 0 to 25, where 0 represents black and 25 represents white. Three fluorescent spots were analyzed on

## Chapter II: Development of Si nanonet-based FET biosensors

each substrate, giving rise to the average fluorescence intensity ( $I_f$ ) values and standard deviations ( $\sigma$ ) reported. The results obtained for this study are shown in Figure II-8.

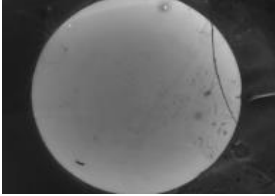
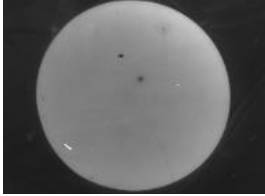
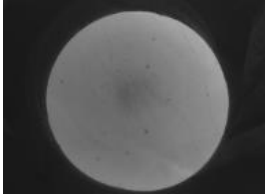
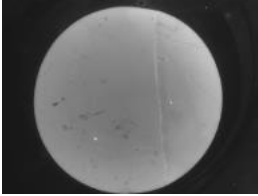
Reference	[NaBH <sub>4</sub> ] = 0.092 M t = 1 h	[NaBH <sub>4</sub> ] = 0.01 M t = 45 min	[NaBH <sub>4</sub> ] = 0.01 M t = 30 min	[NaBH <sub>4</sub> ] = 0.01 M t = 15 min
				
$I_f = 9.15$ $\sigma = 0.37$	$I_f = 10.21$ $\sigma = 0.81$	$I_f = 13.27$ $\sigma = 2.26$	$I_f = 12.25$ $\sigma = 0.06$	

Figure II-8: Analysis of the fluorescence intensity obtained after the hybridization of the TBA-15 bioreceptor with its complementary DNA sequence (c-TBA) on Si/SiO<sub>2</sub> substrates biofunctionalized by the APTES-based protocol. Study performed for different NaBH<sub>4</sub> concentrations and durations of the imine reduction step (t). The images were obtained by epifluorescence microscopy, using an exposure time of 3 s.

The results presented in Figure II-8 allowed us to conclude that reducing the NaBH<sub>4</sub> concentration from 0.09 M to 0.01 M, and the reaction time from 1 h to 15 min during the imine reduction step, does not affect the grafting of the TBA-15 bioreceptor. Indeed, as can be seen from the images corresponding to the fluorescent spots, and their respective fluorescence intensity values, the latter does not decrease when changing the parameters mentioned above. This results indicates that the amount of hybridized DNA, and consequently, the amount of immobilized TBA-15 bioreceptor, was not affected by decreasing both, the NaBH<sub>4</sub> concentration and the duration of the imine reduction step.

The next stage was to verify if this experimental change in the imine reduction step could prevent the delamination of the metal contacts in the Si nanonet-based FET devices. For this purpose, the Si nanonet-based FETs devices were biofunctionalized by the APTES-based protocol described before, but the last step was modified according to the results previously obtained. So, during the imine bond reduction step, the devices were exposed to a 0.01 M NaBH<sub>4</sub> aqueous solution for 15

min. Unfortunately, this experimental modification did not avoid the delamination of the metal contacts.

As a consequence, it was deduced that the APTES-based protocol should be used only on metal contact encapsulated devices. These technological developments are currently under investigation in a post-doctoral work at LMGP. Within this thesis project, taking into account that metal contacts are not encapsulated, and aiming to develop a shorter protocol safe for the metallic pads, we focused on the optimization of the Si nanonet-based FETs biofunctionalization using the GOPS-based process, which will be detailed bellow.

### II.2.2. GOPS-based biofunctionalization process

This protocol based on the vapor phase deposition of the GOPS aminosilane was developed at LMGP during the thesis work of T. Demes [14]. It presents several advantages over the APTES-based protocol, such as it is shorter in time and allows a direct covalent attachment of the  $\text{NH}_2$ -terminated bioreceptor on the surface, without the need to carry out the cross-linker step. This biofunctionalization process is performed in three stages, summarized in Figure II-9.

- 1. Surface hydroxylation (Figure II-9(a)):** As previously described, the objective of this step is to clean sample surface and activate it by the creation of pending hydroxyl groups (-OH) using an  $\text{O}_2$ /air plasma treatment. This step is carried out as previously described ( II.2.1 APTES-based biofunctionalization).
- 2. GOPS vapor phase silanization (Figure II-9(b)):** The reaction mechanisms involved in GOPS silanization are similar to those previously described for the APTES organosilane. As in the previous case, the vapor phase silanization is carried out under anhydrous conditions ( $\text{N}_2$  atmosphere, with a humidity percentage carefully controlled (less than 2%). The samples and the glass vessel containing 150  $\mu\text{L}$  of GOPS are placed in a hermetically sealed Teflon container. The whole is placed in an oven at 100 °C for 1 h. Subsequently, the samples are

cleaned with ethanol under stirring (5 min, at 50 rpm), and they are dried under argon flow. Finally, they are again placed in an oven at 135 °C for 1 h.

- NH<sub>2</sub>-TBA-15 immobilization (Figure II-9(c)):** In this case, the epoxy-terminated surface allows a direct covalent attachment of NH<sub>2</sub>-terminated TBA-15 bioreceptor on the surface, via ring-opening reaction of the epoxy group. The sample is left to react for 1 h at room temperature and ambient conditions, subsequently it is placed in a humidity chamber at 60 °C for 30 min, and then kept overnight at room temperature and ambient conditions. Finally, the samples are rinsed with deionized water, a 0.2% sodium dodecyl sulfate aqueous solution, and deionized water again, under stirring (30 rpm) during 5 min, for each solution.

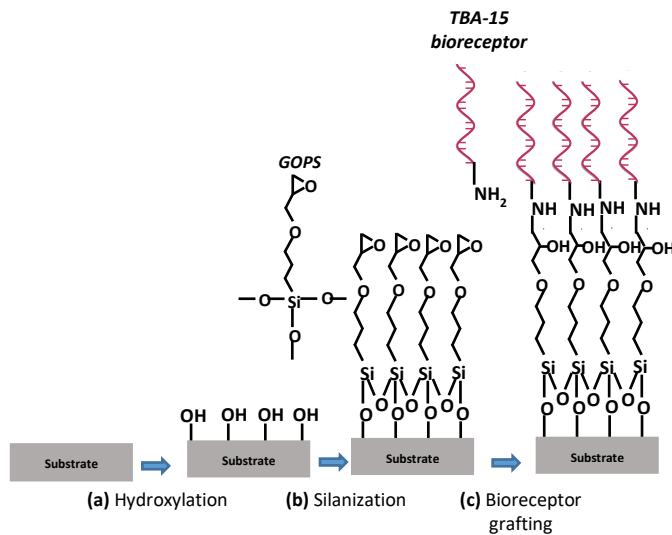
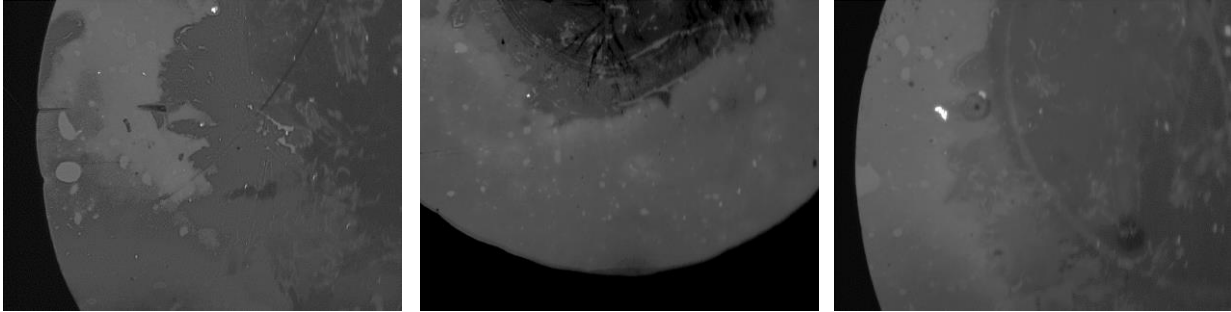


Figure II-9: Schematic representation of the different steps of the GOPS-based biofunctionalization process.

Despite the advantages of the GOPS biofunctionalization process previously mentioned, we found that this protocol presented some issues. In fact, the GOPS-based biofunctionalization was evaluated on planar Si/SiO<sub>2</sub> substrates and the verification of the grafting step was performed by hybridization with its Cy3 labeled complementary DNA sequence (c-TBA). As a result, we found that the fluorescence of the spots did not present a uniform distribution over the analyzed area (Figure II-10). This could mean that the distribution of the TBA-15 bioreceptor grafted over the surface of the sample was not being homogeneous.



*Figure II-10: Images obtained by epifluorescence microscopy corresponding to the fluorescent spots generated after the hybridization between the TBA-15 and the Cy3 labeled c-TBA. Study performed on Si/SiO<sub>2</sub> substrates, biofunctionalized using the GOPS-based protocol. The hybridization step was carried out following the previously described procedure (II.2.1 APTES-based biofunctionalization, 6. Hybridization step). Exposure time = 3 s.*

As a consequence, to avoid future issues in the reproducibility of the Si nanonet-based FET biosensors, we worked on developing a strategy to optimize the GOPS-based protocol, which, as detailed below, was based on the use of UV radiation.

### **II.2.2.1. Optimization of the GOPS-based biofunctionalization process using UV radiation**

Herein, we investigated the effect of using UV irradiation on the TBA-15 bioreceptor immobilization. Indeed, some previous studies showed the potential of the UV activation to enhance the immobilization of oligonucleotides [15–17]. In such UV-assisted biofunctionalization processes, the DNA is directly exposed to radiation during the grafting step. However, previous investigations have shown that UV exposition can cause mutations that are directly related to DNA damage when UVC radiation (UVC,  $\lambda=254$  nm) is used [18]. For this reason, we decided to work with a UVA radiation (UVA,  $\lambda=365$  nm), which carries less energy than UVC.

Here, we studied the influence of the use of UV radiation on GOPS silanized surfaces, just before and just after TBA-15 drop casting for different exposure times. The study was initially carried out on Si/SiO<sub>2</sub> substrates, and once the process was optimized, it was evaluated on Si nanonet-based FET devices.

## Chapter II: Development of Si nanonet-based FET biosensors

---

For this purpose, the Si/SiO<sub>2</sub> samples were silanized following the GOPS-based protocol previously described. Subsequently, the samples were exposed to 365 nm UVA radiation (39 mW·cm<sup>-2</sup>) using a UV-LED masking system (UV-KUB 2, Kloé). For this optimization study, different experimental conditions were chosen: three increasing exposure times were studied (10, 20 and 40 min). The effect of these exposure times was studied in two different cases: when the UV exposure took place just before the TBA-15 bioreceptor drop casting, and when the UV exposure took place just after the TBA-15 bioreceptor drop casting. Then, in order to analyze the effect of this UV exposure on TBA-15 grafting, the hybridization with its complementary DNA sequence (c-TBA) was carried out. The results were evaluated by epifluorescence microscopy, seeking to determine the parameters allowing to obtain an optimal grafting of the TBA-15 bioreceptor. For all conditions, three fluorescent spots were analyzed, giving rise to the average fluorescence intensity value showed in Figure II-11.

On the resulting histogram (Figure II-11), it can be observed that for each UV exposure time, the intensity of fluorescence is higher when the latter is performed before the TBA-15 bioreceptor drop casting. Additionally, it can be seen that when the UV exposure is applied after the TBA-15 bioreceptor drop casting, the fluorescence intensity decreases as the exposure time increases. Both observations suggest that the effect of UVA radiation on DNA bioreceptors is not negligible, and that the only way to ensure their integrity is to carry out the UV exposure before the DNA bioreceptor drop casting.

Furthermore, it can be noted that the highest fluorescence intensity is obtained when the sample is not exposed to UV radiation (Figure II-11). However, as shown on the corresponding image, in that case the fluorescence is not homogeneously distributed over the spot, which is also confirmed by the important error bar for the respective sample. These results led us to conclude that the use of UV irradiation reduces the mean fluorescence intensity obtained, but increases drastically its homogeneity, particularly for the case of the 20 min UV exposure. Then, the best result, combining high fluorescence intensity and good homogeneity, was obtained for 20 min UV exposure before the TBA-15 bioreceptor drop casting.

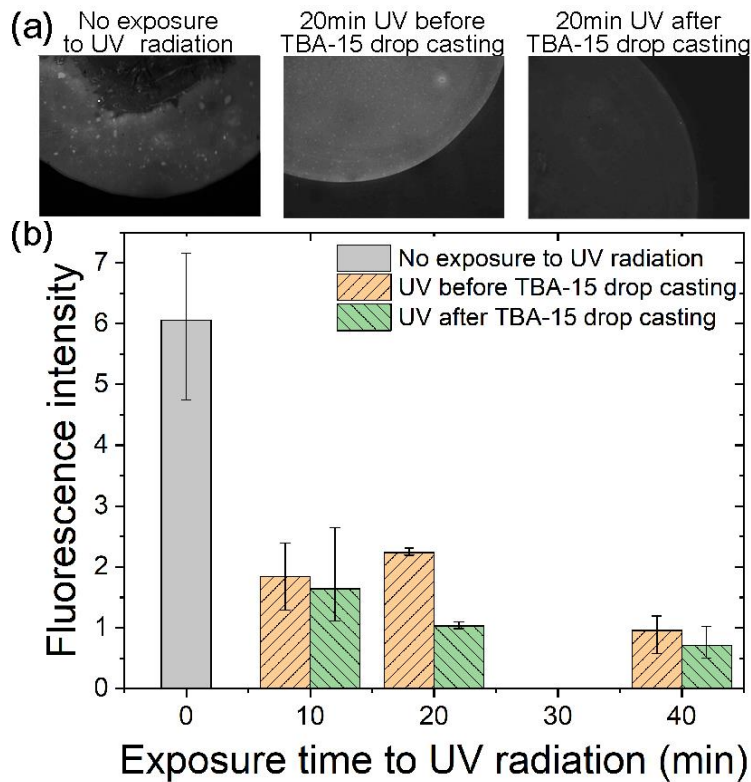


Figure II-11: Analyses of the fluorescence intensity obtained after the hybridization between the TBA-15 bioreceptor and its Cy3 labeled complementary DNA sequence (c-TBA). Study performed on Si/SiO<sub>2</sub> substrates biofunctionalized by GOPS-based protocol, with and without exposure to UV radiation. (a) Epifluorescence microscopy images of the samples after the hybridization step, in different cases regarding the UV treatment received (no UV exposure, 20 min UV exposure before, and 20 min exposure after the TBA-15 drop casting). Exposure time = 3 s.

(b) Fluorescence intensity measured on the fluorescence micrographs, as a function of the exposure time to UV radiation. For all conditions, three fluorescent spots were analyzed, giving an average fluorescence intensity value and the error bars corresponding to the minimum and maximum fluorescence intensity found for each experimental condition.

#### II.2.2.1.1. Wettability analyses

To enlighten this improvement in the fluorescence homogeneity, which in turn can be interpreted as a more uniform distribution of TBA-15 bioreceptor on the sample surface, water contact angle measurements were carried out on GOPS-silanized Si/SiO<sub>2</sub> surfaces with and without UV exposure. The analyses were performed by sessile droplets using a drop shape analysis system DSA10 Mk2 (Kruss GmgH). Three measurements were made for each sample, and the result reported corresponds to the average value.

Two cases were studied: GOPS silanized Si/SiO<sub>2</sub> surface (reference), and a GOPS silanized Si/SiO<sub>2</sub> surface exposed for 20 min UV radiation. The results gave a value of 78.4° ( $\sigma = 3.0^\circ$ ) for the surface that was not exposed to UV radiation, and 68.8° ( $\sigma = 1.4^\circ$ ) for the irradiated surface. This results indicates that UV radiation makes the surface more hydrophilic. Such an increase in hydrophilicity is probably responsible for the observed improvement in the fluorescence homogeneity. Indeed, as TBA-15 bioreceptor is dissolved in a saline solution at the moment of the grafting step, it can reach more easily the surface if the latter is more hydrophilic.

Finally, this UV-optimized GOPS-based functionalization protocol was evaluated on 8 nm thick Al<sub>2</sub>O<sub>3</sub> coated Si substrates (the latter is the same coating as the one used as passivation layer in Si nanonet-based FETs), obtaining a good and homogenous DNA hybridization, which was verified by epifluorescence microscopy. Consequently, the next step consisted in the evaluation of its efficiency for the biofunctionalization of the Si nanonet-based FET devices.

### **II.2.2.2. Si nanonet-based FETs biofunctionalization by UV-assisted GOPS-based process**

The optimized UV-assisted GOPS-based biofunctionalization protocol was evaluated on the Si nanonet-based FETs. In summary, the devices were subjected to the previously described surface hydroxylation and GOPS vapor phase silanization steps, and then they were exposed to UVA radiation (365 nm at 39 mW·cm<sup>-2</sup>) for 20 min. Upon completion of the UV exposure, the TBA-15 bioreceptor drop casting was immediately carried out.

To evaluate if this process works properly for the biofunctionalization of our FET devices, two characterization techniques were used: Energy Dispersive X-ray Spectroscopy in Scanning Transmission Electron Microscopy (STEM-EDS), and Atomic Force Microscopy (AFM).

#### **II.2.2.2.1. Biofunctionalization monitoring by STEM-EDS**

STEM-EDS characterizations were performed by scratching the surface of the chip using a diamond tip and spreading the obtained material on a holey carbon-coated TEM support copper

## Chapter II: Development of Si nanonet-based FET biosensors

---

grid. High-resolution TEM (HRTEM) analyses were performed on a JEOL 2010 LaB6 200KeV TEM. STEM-EDS spectra and maps of the Si nanonets were collected with a JEOL SDD Centurio detector having a large solid angle of up to 0.98 steradians, incorporated in the JEOL 2100F field-emission-gun scanning electron microscope operating at 200 kV and having a 0.2 nm resolution in the scanning mode.

The STEM-EDS analyses allowed to visualize the chemical distribution of elements within and at the surface of the Si NWs (Figure II-12). Herein, it was obtained an elemental mapping and quantitative analysis on Al<sub>2</sub>O<sub>3</sub> passivated Si nanonet-based FETs after biofunctionalization and TBA-15 hybridization by UV-assisted GOPS-based protocol. For the elemental mapping, several single Si NWs were studied, whereas the quantitative analysis was conducted on Si NWs assemblies, in order to increase the signal of the elements in low concentrations, such as phosphorous. The latter element is of particular importance in this analysis, because as mentioned above, each of the bases conforming the DNA structure contains a phosphate group. Therefore, confirming its presence on the surface of the Si nanonet-based devices would indicate that the biofunctionalization process was carried out properly. The typical bright field image (Figure II-12 (a)) shows a view of one of the single Si NW studied. The elemental mapping is coherent with the core-shell structure of the Al<sub>2</sub>O<sub>3</sub> passivated Si NWs: the presence of Si within the NW is clearly seen (Figure II-12(b)), while the presence of Al and O is particularly seen at the NW surface (Figure II-12(c) and (d)). Here, the phosphorous amount is too low on one single Si NW to have significant information on the mapping. However, the quantitative analysis (Figure II-12(e)) confirmed the presence of phosphorus, proving that DNA sequences were present at the surface of the Si NWs. This last result indicates that the Si nanonet were efficiently biofunctionalized.

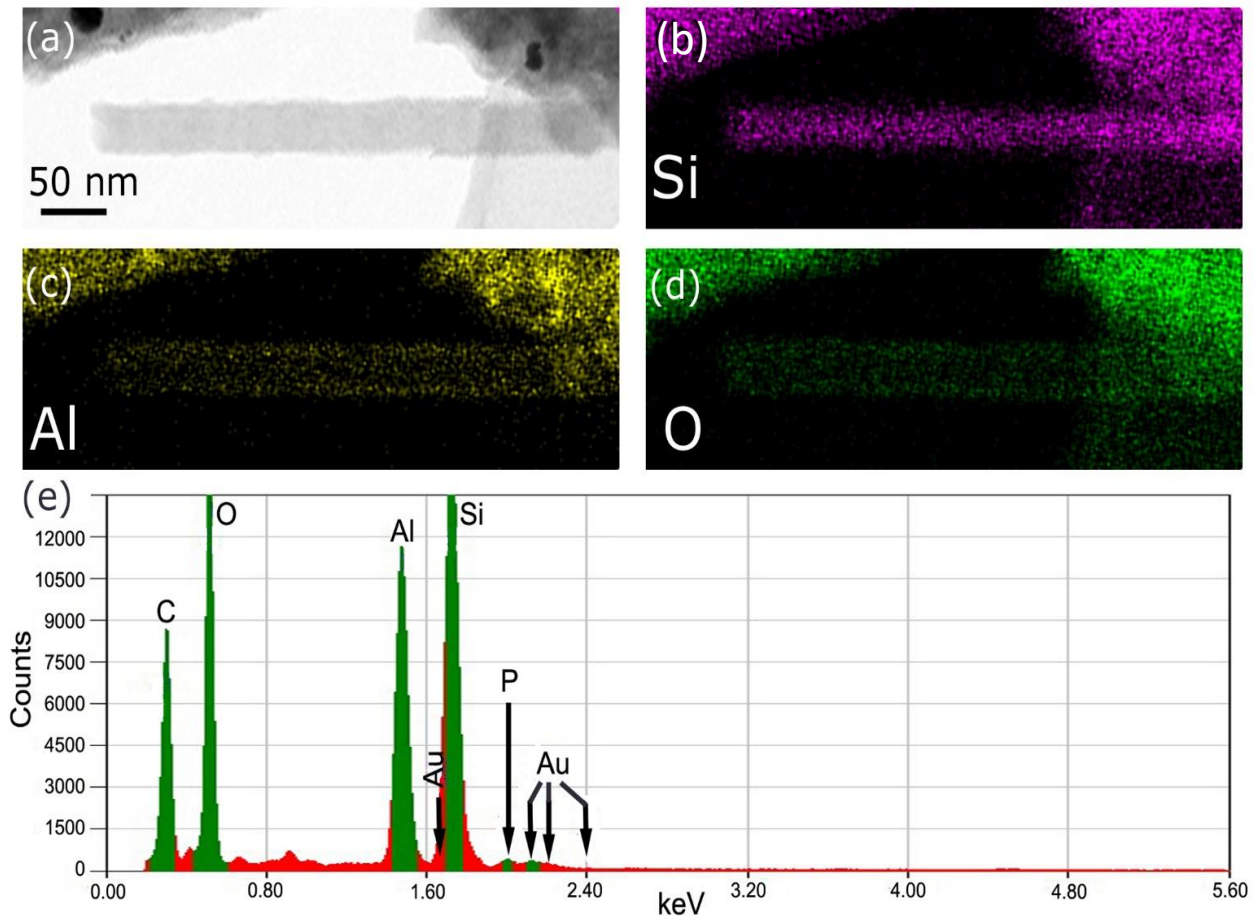


Figure II-12: STEM-EDS Chemical mapping and quantitative analysis of the elements presents on the surface of an  $\text{Al}_2\text{O}_3$  passivated Si nanonet-based FET after biofunctionalization and TBA-15 hybridization by UV-assisted GOPS-based process. (a) Bright field TEM micrograph of an  $\text{Al}_2\text{O}_3$  passivated Si NW. (b) Silicon map. (c) Aluminum map. (d) Oxygen map. (e) Quantitative analysis of the elements (Au in the results comes from residues of the metal contacts).

#### II.2.2.2.2. Biofunctionalization monitoring by AFM

$\text{Al}_2\text{O}_3$  passivated Si nanonet-based FETs were biofunctionalized using the UV-assisted GOPS-based process described above. The evolution of surface morphology was studied using AFM measurements after each main step of the biofunctionalization process, in order to better understand the modification in the surface morphology of the devices.

Analyses were performed using a Dimension Icon AFM (BRUKER). Images were acquired in air using non-contact/tapping mode, with a BRUKER AFM probe, model RTESP-300. All AFM experiments were performed with a scan size of 820 nm, a scan rate of 0.543 Hz and were taken

## Chapter II: Development of Si nanonet-based FET biosensors

with 256 samples/line × 256 lines. The surface topography, roughness and size of the observed structures on various locations of the Al<sub>2</sub>O<sub>3</sub> passivated Si nanonet-based FETs were explored by image processing using the software Gwyddion. All data were extracted from the height AFM images, and, when necessary, images were processed by flattening. For root mean square (RMS) roughness, three different zones on the Al<sub>2</sub>O<sub>3</sub> passivated substrate presenting the same area (100 nm × 100 nm) were analyzed, and the result presented corresponds to the average value for each sample. The dimension of the biomolecules (height) was extracted by line profiles of the molecules, and the value presented reflects the average of 10 measurements.

For this study, apart from the TBA-15 bioreceptor, and its complementary DNA sequence (c-TBA), we used an additional DNA bioreceptor (Seq 2), in order to study the impact of the DNA base composition on the changes generated on the surface of the Si nanonet-based FETs. The information related to these DNA sequences is shown in Table II-2. Except for TBA-15, which was synthesized at DCM using phosphoramidite protocol, the other sequences were purchased from Biomers.

*Table II-2: Summary of the DNA sequences used in this work.*

Name	Sequence	Elongated Length (nm)
TBA-15	5'GGTTGGTGTGGTTGGTTTTTT <sup>3'</sup> -NH <sub>2</sub>	7.1
Seq 2	5'NH <sub>2</sub> -TTTTTGATAAACCCACTCTA <sup>3'</sup>	6.8
c-TBA	Cy3-5'CCAACCACCAACC <sup>3'</sup>	5.1

The changes in the surface morphology were studied after each main step of the biofunctionalization process as follows:

- (i) At the end of the Si nanonet-based FET fabrication process (Figure II-14 (a))
- (ii) After UV-assisted GOPS silanization (Figure II-14(b))
- (iii) After Seq 2 bioreceptor grafting (Figure II-14(c)),
- (iv) After TBA-15 bioreceptor grafting (Figure II-14(e))
- (v) After TBA-15 hybridization with its complementary DNA sequence (c-TBA) (Figure II-14(f)).

(vi) Finally, we also studied the impact of the presence of a phosphate buffer on the GOPS-silanized surface (Figure II-14(d)). The analyzed buffer was the one used to dilute the DNA bioreceptors at the grafting step.

As can be observed from the AFM results, in the absence of DNA on the sample surface (Figure II-14(a),(b) and (d)), the latter is flat and the Si NWs exhibit a smooth shape, as shown on the line profiles, which is almost cylindrical apart from the bottom, where it can be seen the effect generated by the convolution with the AFM tip. Due to such convolution, only the height of the objects was considered in this analysis. For the Si nanonet-based FET device (Figure II-14(a)), the substrate exhibits a RMS roughness value of 0.6 nm ( $\sigma = 0.2$  nm). After GOPS deposition (Figure II-14(b)), the shape of the Si NW was not significantly modified, while the substrate roughness showed a slight decrease to 0.4 nm ( $\sigma = 0.1$  nm). This slight decrease seems to indicate that the GOPS molecules flatten the natural irregularities of the  $\text{Al}_2\text{O}_3$ -covered surface. This also suggests that the GOPS process does not significantly affect the Si nanonet and substrate morphology. Moreover, dipping the sample in the phosphate buffer did not modify the surface morphology (Figure II-14(d)), showing that no crystallized salts remained on the surface after the rinsing steps.

As expected, the bioreceptor grafting on the Si nanonet-based FET devices has a strong impact on their surface morphology (Figure II-14(c) and (e)). First, it can be noticed that new structures appeared, both on the substrate and on the Si nanonet, whether the TBA-15 bioreceptor (Figure II-14(e)) or Seq 2 bioreceptor (Figure II-14(c)) were grafted, but their geometries were quite different from one another. In the case of the TBA-15 bioreceptor (Figure II-14(e)), the surface roughness increased significantly to 4.0 nm ( $\sigma = 1.5$  nm) and the mean height of the observed structures was 23.7 nm ( $\sigma = 10.4$  nm). Besides, in the case of Seq 2 sequence (Figure II-14(c)), the mean height of the structures was reduced by a factor two, i.e., 12.6 nm ( $\sigma = 5.2$  nm), with a substrate surface RMS roughness of 2.3 nm ( $\sigma = 0.3$  nm). Such a difference is quite surprising, as both DNA sequences have more or less the same length (see Table II-2). However, it is known that guanine-rich nucleic acid sequences, such as TBA-15, can adopt intermolecular or intramolecular structures, named G-quadruplexes. The intramolecular G-quadruplex is the structure that adopt

TBA-15 for binding thrombin. This configuration contains a planar, tetrameric arrangement of guanines (Figure II-1(a)), which in turn can be stacked on top of each other, thanks to  $\pi$ - $\pi$  interactions, being stabilized by monovalent cations, such as  $K^+$  and  $Na^+$  [19–22]. These structures may build different types of multimers, such as wires, stacks of intramolecular structures, and interlocked dimers and trimers [23,24]. Therefore, the significant height observed in the case of the TBA-15 bioreceptor could correspond to stacks of G-quadruplexes TBA-15 structures. On the contrary, the Seq 2 probe cannot form G-quadruplex structures, which could indicate that the irregularities observed in the AFM images correspond to individual DNA bioreceptor molecules grafted on the surface. The dimensions found for this sequence are larger than expected, as the theoretical length of a 20-base DNA is about 6.8 nm [25]. However, different factors may have affected the results obtained. Indeed, in the case of oligonucleotide AFM analyses, the different level of hydration of the molecules may play an important role [26]. It is known that a layer of water surrounding the DNA molecules can interact with the tip, resulting in the formation of a meniscus that can lead to an overestimation of the measured height [27].

After the TBA-15 hybridization with its complementary DNA sequence (c-TBA) (Figure II-14(f)), both, the surface roughness (3.1 nm,  $\sigma = 0.5$ nm), and the height of the structures (14.1 nm,  $\sigma = 7.2$ nm) were lower compared to the previous values obtained for the TBA–15 bioreceptor (roughness = 4.0, nm height of the structures = 23.7 nm) (Figure II-14(e)). In this case, the molecules on the surface would correspond to double-stranded DNA (Figure II-13 (b)), which must present a linear conformation for the hybridization to occur, explaining why their morphology is closer to the one obtained for the Seq 2 bioreceptor (roughness = 2.3 nm, structure's height = 12.6 nm) (Figure II-14(c)).

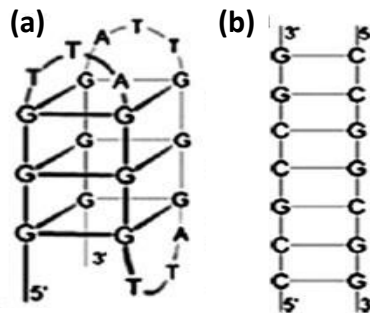


Figure II-13: DNA structure motifs: (a) G-quadruplex structure (b) double-stranded DNA structure [28].

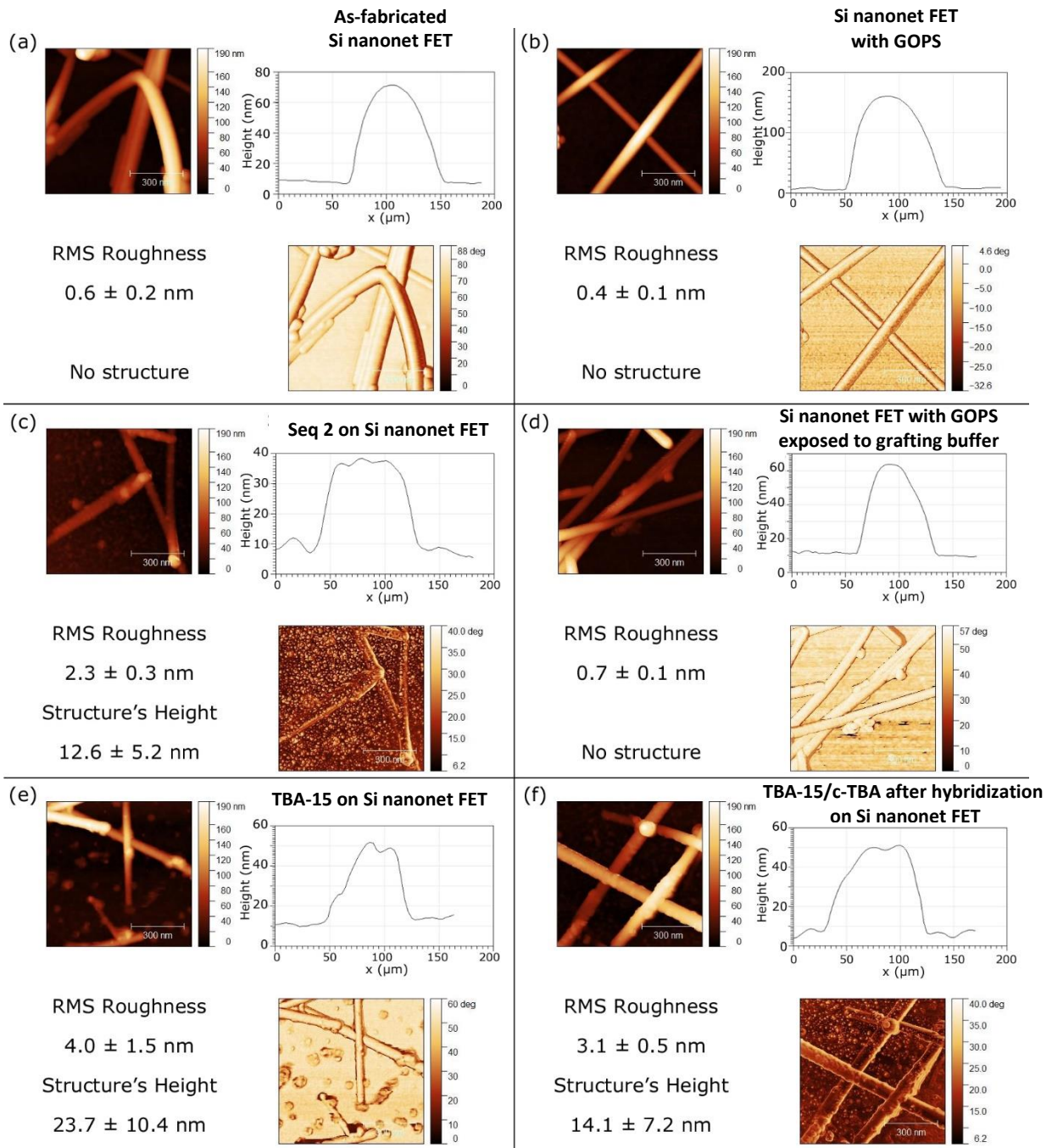


Figure II-14: AFM analyses on  $Al_2O_3$ -passivated Si nanonet-based FETs at the different steps of UV-assisted GOPS biofunctionalization process: (a) bare  $Al_2O_3$  passivated Si nanonet-based FET, (b) after UV-assisted GOPS silanization, (c) after Seq 2 bioreceptor grafting, (d) after UV-assisted GOPS silanization and exposition to the grafting phosphate buffer (without DNA bioreceptor), (e) after TBA-15 bioreceptor grafting, and (f) after TBA-15 hybridization with its complementary DNA sequence (c-TBA).

These results, on the one hand, led us to confirm the immobilization of the TBA-15 bioreceptor on the surface of Si nanonet-based FET devices. On the other hand, they allowed us to conclude that the base composition of the DNA sequence strongly influences its structure on the surface.

### II.3. Conclusions

The studies carried out in this chapter enabled the development of a biofunctionalization protocol allowing the immobilization of the TBA-15 bioreceptor on the surface of Si nanonet-based FET devices. Two different approaches were studied, both of them based on organosilanes: (3-Aminopropyl)triethoxysilane (APTES) and (3-Glycidyloxypropyl)trimethoxysilane (GOPS).

In the case of the APTES-based biofunctionalization process, a metal contact delamination problem was encountered, which occurred at the last step of the biofunctionalization process. Indeed, during the step consisting in the reduction of imine bonds by  $\text{NaBH}_4$ , the  $\text{H}_2$  bubbles generated as a by-product of reaction caused the detachment of the metal contacts in the Si nanonet-based FETs devices.

For the aforementioned reason, we worked on a second alternative: the GOPS-based biofunctionalization process. This protocol presented problems related to the homogeneity in the distribution of the immobilized bioreceptor on the surface. These issues were solved by optimizing the process using UVA radiation. The best results were obtained for 20 min of UVA irradiation prior to the TBA-15 bioreceptor drop casting. This UVA treatment resulted in major improvement in the homogeneity of the surface bioreceptor distribution.

Furthermore, STEM-EDS and AFM studies confirmed the immobilization of the TBA-15 bioreceptor on the surface of Si nanonet-based FET devices when using the UV-assisted GOPS-based biofunctionalization protocol. Additionally, the morphological study carried out by AFM, showed that the base composition in the DNA sequence drastically impacts its structure on the surface.

## **Chapter II: Development of Si nanonet-based FET biosensors**

---

Once the biofunctionalization of the Si nanonet-based devices has been optimized, it is possible to proceed with the electrical detection of the target molecule, which will be detailed in the next chapter.

# References

- [1] B. Deng, Y. Lin, C. Wang, F. Li, Z. Wang, H. Zhang, X.F. Li, X.C. Le, Aptamer binding assays for proteins: The thrombin example-A review, *Anal. Chim. Acta.* 837 (2014) 1–15. <https://doi.org/10.1016/j.aca.2014.04.055>.
- [2] M. Vallejo-Perez, C. Ternon, N. Spinelli, F. Morisot, C. Theodorou, G. Jayakumar, P.E. Hellström, M. Mouis, L. Rapenne, X. Mescot, B. Salem, V. Stambouli, Optimization of GOPS-based functionalization process and impact of aptamer grafting on the si nanonet FET electrical properties as first steps towards thrombin electrical detection, *Nanomaterials.* 10 (2020) 1–20. <https://doi.org/10.3390/nano10091842>.
- [3] P. Serre, Etude des propriétés structurales et électriques de réseaux aléatoires de nanofils de silicium. Application à la détection d'ADN., Université Grenoble Alpes, 2014. <https://www.theses.fr/2014GRENT110>.
- [4] M. Legallais, Conception, étude et modélisation d'une nouvelle génération de transistors à nanofils de silicium pour applications biocapteurs, Université Grenoble Alpes, 2017. <http://www.theses.fr/s119813>.
- [5] T.T.T. Nguyen, M. Legallais, F. Morisot, T. Cazimajou, V. Stambouli, M. Mouis, B. Salem, C. Ternon, First evidence of superiority of Si nanonet field effect transistors over multi-parallel Si nanowire ones in view of electrical DNA hybridization detection, *Mater. Res. Express.* 6 (2019). <https://doi.org/10.1088/2053-1591/aae0d5>.
- [6] T.T.T. Nguyen, T. Cazimajou, M. Legallais, T. Arjmand, V.H. Nguyen, M. Mouis, B. Salem, E. Robin, C. Ternon, Monolithic fabrication of nano-to-millimeter scale integrated transistors based on transparent and flexible silicon nanonets, *Nano Futur.* 3 (2019). <https://doi.org/10.1088/2399-1984/ab1ebc>.
- [7] Y. Wu, P. Yang, Direct observation of vapor-liquid-solid nanowire growth, *J. Am. Chem. Soc.* 123 (2001) 3165–3166. <https://doi.org/10.1021/ja0059084>.
- [8] Y. Cui, L.J. Lauhon, M.S. Gudiksen, J. Wang, C.M. Lieber, Diameter-controlled synthesis of single-crystal silicon nanowires, *Appl. Phys. Lett.* 78 (2001) 2214–2216. <https://doi.org/10.1063/1.1363692>.
- [9] C. Ternon, P. Serre, J.M. Lebrun, V. Brouzet, M. Legallais, S. David, T. Luciani, C. Pascal, T. Baron, J.M. Missiaen, Low Temperature Processing to Form Oxidation Insensitive Electrical Contact at

- Silicon Nanowire/Nanowire Junctions, *Adv. Electron. Mater.* 1 (2015) 1–8. <https://doi.org/10.1002/aelm.201500172>.
- [10] M. Legallais, T.T.T. Nguyen, T. Cazimajou, M. Mouis, B. Salem, C. Ternon, Material engineering of percolating silicon nanowire networks for reliable and efficient electronic devices, *Mater. Chem. Phys.* 238 (2019). <https://doi.org/10.1016/j.matchemphys.2019.121871>.
- [11] L. Fradetal, E. Bano, G. Attolini, F. Rossi, V. Stambouli, A silicon carbide nanowire field effect transistor for DNA detection, *Nanotechnology.* 27 (2016). <https://doi.org/10.1088/0957-4484/27/23/235501>.
- [12] P. Serre, V. Stambouli, M. Weidenhaupt, T. Baron, C. Ternon, Silicon nanonets for biological sensing applications with enhanced optical detection ability, *Biosens. Bioelectron.* 68 (2015) 336–342. <https://doi.org/10.1016/j.bios.2015.01.012>.
- [13] J. Kim, P. Seidler, L.S. Wan, C. Fill, Formation, structure, and reactivity of amino-terminated organic films on silicon substrates, *J. Colloid Interface Sci.* 329 (2009) 114–119. <https://doi.org/10.1016/j.jcis.2008.09.031>.
- [14] T. Demes, F. Morisot, M. Legallais, A. Calais, E. Pernot, I. Pignot-Paintrand, C. Ternon, V. Stambouli, DNA grafting on silicon nanonets using an eco-friendly functionalization process based on epoxy silane, *Mater. Today Proc.* 6 (2019) 333–339. <https://doi.org/10.1016/j.matpr.2018.10.427>.
- [15] T. Schüler, A. Nykytenko, A. Csaki, UV cross-linking of unmodified DNA on glass surfaces, *Anal. Bioanal. Chem.* (2009) 1097–1105. <https://doi.org/10.1007/s00216-009-3045-9>.
- [16] J. Escorihuela, R. Puchades, A. Maquieira, Development of Oligonucleotide Microarrays onto Si-Based Surfaces via Thioether Linkage Mediated by UV Irradiation, *Bioconjug. Chem.* (2012) 2121–2128. <https://doi.org/10.1021/bc300333a>.
- [17] P.L. Dolan, Y. Wu, L.K. Ista, R.L. Metznerberg, M.A. Nelson, G.P. Lopez, Robust and efficient synthetic method for forming DNA microarrays, *Nucleic Acids Res.* 29 (2001) 107–107. <https://doi.org/10.1093/nar/29.21.e107>.
- [18] C. V. Khoe, L.H. Chung, V. Murray, The sequence specificity of UV-induced DNA damage in a systematically altered DNA sequence, *J. Photochem. Photobiol. B Biol.* 183 (2018) 88–100. <https://doi.org/10.1016/j.jphotobiol.2018.04.023>.
- [19] V. Dapić, V. Abdomerović, R. Marrington, J. Peberdy, A. Rodger, J.O. Trent, P.J. Bates, Biophysical and biological properties of quadruplex oligodeoxyribonucleotides, *Nucleic Acids Res.* 31 (2003) 2097–2107. <https://doi.org/10.1093/nar/gkg316>.
- [20] V.C. Diculescu, A.M. Chiorcea-Paquim, R. Eritja, A.M. Oliveira-Brett, Thrombin-binding aptamer

- quadruplex formation: AFM and voltammetric characterization, *J. Nucleic Acids*. 2010 (2010). <https://doi.org/10.4061/2010/841932>.
- [21] A.M. Chiorcea-Paquim, P.V. Santos, R. Eritja, A.M. Oliveira-Brett, Self-assembled G-quadruplex nanostructures: AFM and voltammetric characterization, *Phys. Chem. Chem. Phys.* 15 (2013) 9117–9124. <https://doi.org/10.1039/c3cp50866h>.
- [22] T.C. Marsh, J. Vesenka, E. Henderson, A new DNA nanostructure, the G-wire, imaged by scanning probe microscopy, *Nucleic Acids Res.* 23 (1995) 696–700.
- [23] G. Oliviero, S. D’Errico, B. Pinto, F. Nici, P. Dardano, I. Rea, L. De Stefano, L. Mayol, G. Piccialli, N. Borbone, Self-assembly of g-rich oligonucleotides incorporating a 3’-3’ inversion of polarity site: A new route towards G-Wire DNA nanostructures, *ChemistryOpen*. 6 (2017) 599–605. <https://doi.org/10.1002/open.201700024>.
- [24] A.M. Varizhuk, A.D. Protopopova, V.B. Tsvetkov, N.A. Barinov, V. V. Podgorsky, M. V. Tankevich, M.A. Vlasenok, V. V. Severov, I.P. Smirnov, E. V. Dubrovin, D. V. Klinov, G.E. Pozmogova, Polymorphism of G4 associates: From stacks to wires via interlocks, *Nucleic Acids Res.* 46 (2018) 8978–8992. <https://doi.org/10.1093/nar/gky729>.
- [25] J.D. WATSON, F.H.. CRICK, Molecular Structure of Deoxyribose Nucleic Acids, *Nature*. 171 (1953) 738–740.
- [26] D. Humeník, D. Chorvát, I. Novotný, V. Tvarožek, T.S. Oretskaya, T. Hianik, AFM images of short oligonucleotides on a surface of supported lipid films, *Med. Eng. Phys.* 28 (2006) 956–962. <https://doi.org/10.1016/j.medengphy.2006.05.005>.
- [27] T. Heim, Transport électronique dans l’ADN, Université des Sciences et Technologie de Lille 1, 2003.
- [28] Y. Cordeiro, B. Macedo, J.L. Silva, M.P.B. Gomes, Pathological implications of nucleic acid interactions with proteins associated with neurodegenerative diseases, *Biophys. Rev.* 6 (2014) 97–110. <https://doi.org/10.1007/s12551-013-0132-0>.

**Chapter III: Electrical detection of  
DNA hybridization in dry  
environment using Si nanonet-based  
FET biosensors**

<b>Chapter III: Si nanonet-based FET biosensors for the electrical detection of DNA hybridization in dry environment .....</b>	<b>94</b>
III.1. Electrical characterizations of Si nanonet-based FETs.....	96
III.2. Electrical detection of DNA hybridization .....	99
III.2.1. Study of the biosensor formation.....	101
III.2.1.1. Stability of the transfer characteristics of biofunctionalized Si nanonet-based FETs.....	101
III.2.1.2. Hybridization capacity in time .....	103
III.2.1.3. Impact of the surface environment on the Si nanonet-based FET properties .....	105
III.3. Conclusions.....	108
<b>References.....</b>	<b>111</b>

This chapter explores the feasibility of using Si nanonet-based FET devices as biosensors for the electrical detection of DNA hybridization in dry environment. Herein, the devices were functionalized using the UV-assisted GOPS-based protocol previously optimized (Chapter II, II.2.1.1. Optimization of the GOPS-based biofunctionalization process using UV radiation), and the detection model was the electrical detection of DNA hybridization between the TBA-15 bioreceptor and its complementary DNA sequence, with measurements performed in dry conditions. This is a first step towards measurements in liquid medium and thrombin detection.

Indeed, this type of interaction (DNA hybridization) can be used for different applications, such as diagnostic test for mutations, monitoring gene expression, screening for viruses, illustration of gene rearrangement and oncogene amplification, assessment of medical treatment, environmental investigations, detection of genetically modified food components, biological warfare agent detection, among others [1–4].

The results obtained regarding the electrical properties of the Si nanonet-based FET devices, their stability after the biofunctionalization process and the optimization of the grafting step in order to obtain electrically stable devices for the detection of the DNA hybridization will be presented throughout this chapter. Some of these results were recently published [5].

### **III.1. Electrical characterizations of Si nanonet-based FETs**

As detailed in Chapter I, (I.4.1. Field-Effect Transistor (FET)-based biosensors), FET devices can be compared to an electrostatic switch controlled by the gate voltage. The gate voltage determining the transition from a blocking state (*Off-state*) to a state in which current can flow (*On-state*) is called threshold voltage ( $V_{th}$ ). In our case, Si nanonets were integrated into transistors with a back-gate configuration. Here, a Si substrate was used as a common back-gate for the Si nanonet-based FET devices, whereas the 200 nm thick  $\text{Si}_3\text{N}_4$  layer served as their gate dielectric.

Then, one of the ways to characterize Field-Effect Transistors is through their  $I_d - V_g$  transfer characteristics, (also detailed in depth in Chapter I, I.4.1. Field-Effect Transistor (FET)-based

biosensors). In summary, the drain current is plotted as a function of the back-gate voltage. The voltage between the drain and the source (drain voltage,  $V_d$ ) is kept constant, and it is chosen in order to bias the device in the linear region of operation. Here,  $V_d$  was set at -2 V.

As mentioned in the previous chapter, each chip is composed of 4 similar quarters, each of them containing Si nanonet-based transistors with different channel geometries (See Chapter II, Figure II-3). For this first study, we analyzed the electrical properties of Si nanonet-based FETs with 3 different channel lengths ( $L = 40, 50, \text{ and } 100 \mu\text{m}$ ) with a fixed width ( $W = 100 \mu\text{m}$ ). For each geometry, 5 Si nanonet-based FET devices were studied in each quarter of the chip.

The analyses were performed at IMEP-LAHC in a three probe Karl Süss station, controlled by a HP4155A parameter analyzer. All measurements were carried out in dry and dark environment, at room temperature and ambient conditions, using the same integration time (medium).

The transfer characteristics obtained for the different devices are shown in *Figure III-1(a), (b) and (c)*. The first observation that can be made from Figure III-1, is that increasing the channel length improves the reproducibility from one device to another. These results are in good agreement with those previously obtained for Si nanonet-based FETs with and without  $\text{Al}_2\text{O}_3$  passivation layer [6–9]. These previous investigations carried out at LMGP demonstrated that increasing the channel length results in a better averaging effect of the network. Then, the overall dispersion of the transistor parameters decreases when the channel length increases.

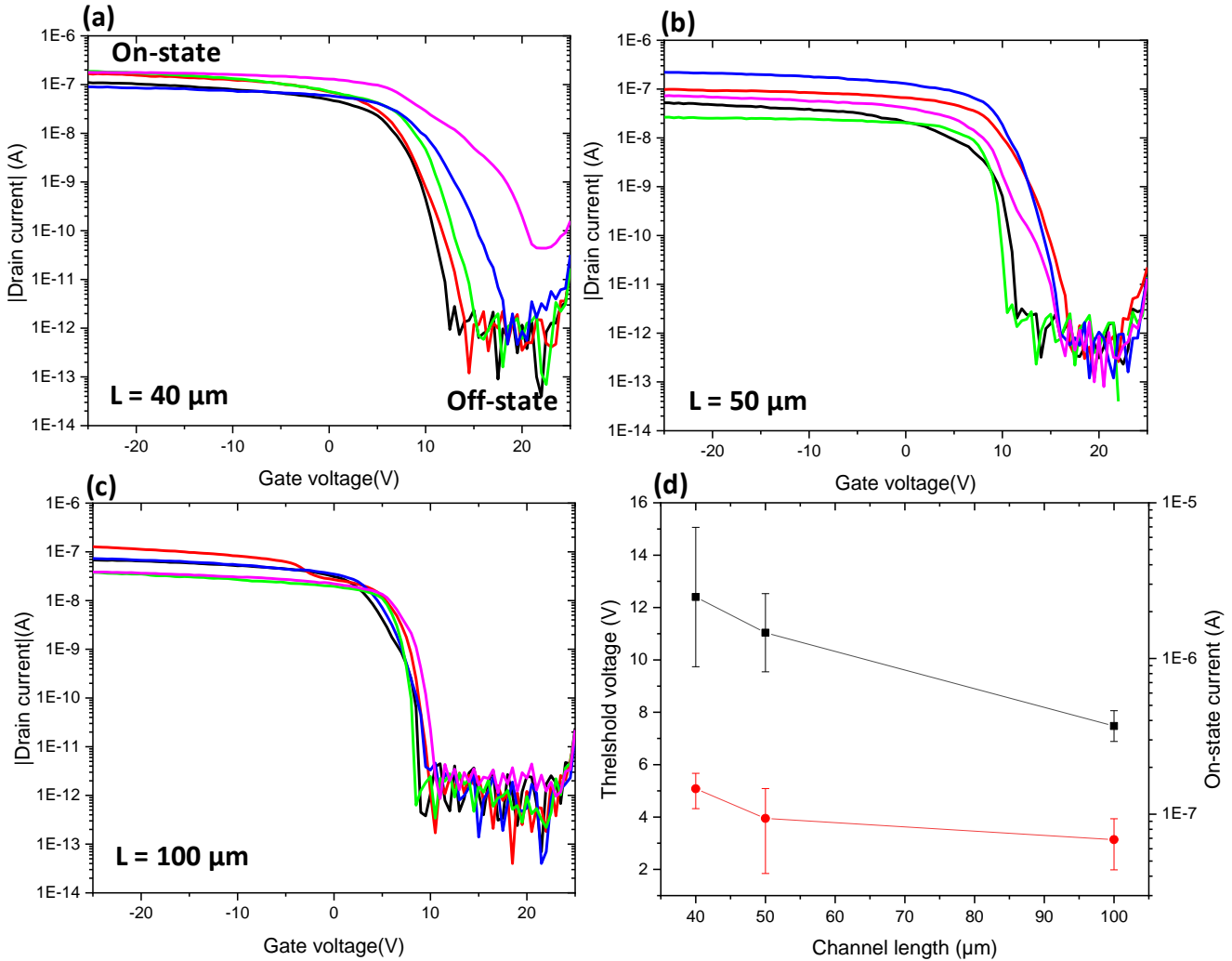


Figure III-1: Transfer characteristics obtained for Si nanonet-based FET devices with different channel length ( $W = 100 \mu\text{m}$  in all cases) (a)  $L = 40 \mu\text{m}$ , (b)  $L = 50 \mu\text{m}$ , and (c)  $L = 100 \mu\text{m}$ . (d) Variation in threshold voltage (black squares) and on-state current (at gate voltage = -25 V) (red circles), as a function of the channel length.  $V_d$  set at -2 V.

Regarding the performance of Si nanonet-based FETs, it can be seen from Figure III-1(d) that both the threshold voltage and the on-state current decrease with increasing channel length. On the one hand, the important decrease of the threshold voltage can be explained in terms of the threshold voltage dispersion for individual Si NWs. In fact, as described previously, the more NWs involved in series along the conduction channel, the less the threshold voltage dispersion for each Si NW impacts the overall behavior of the Si nanonet [6]. On the other hand, the decrease in the On-state current is also related to the high Si NWs density, which makes the nanonet behave in

the bulk regime and not in the percolating one. Then, the Pouillet's law for resistance (R) can be applied in here:

$$R = \rho \cdot L / S \quad \text{Equation III- 1}$$

where  $\rho$  is the resistivity of the material, L is the length, and S the cross-sectional area.

As can be concluded from the Equation III- 1, increasing the length of the Si nanonet channel implies the overall increase of its resistance, thus, decreasing the On-state current [6].

Finally, in a general way, it can be noted that the On-state ( $I_{on}$ ) drain current of the devices reached values around  $1 \times 10^{-7}$  A, while the Off-state ( $I_{off}$ ) values were around  $1 \times 10^{-12}$  A. As consequence, the ratio ( $I_{on}/I_{off}$ ) was about  $10^5$ , demonstrating once again the excellent performance of Si nanonet-based FETs devices.

### III.2. Electrical detection of DNA hybridization

Si nanonet-based FET biosensors rely on the field effect: the adsorption of charged species on the surface of the transistor channel modifies the surface charge. This in turn has an influence on the density of free carriers within the channel. In this case, for example, the adsorption of negative charges on the surface of the Si nanonet P-type channel attracts holes to the surface. As previously mentioned, the TBA-15 bioreceptor is a DNA molecule, (sequence detailed in Chapter II, Table II-1), therefore it is negatively charged, due to the 15 phosphate groups present in its backbone. When the TBA-15 bioreceptor is in solution, counter ions are present to preserve electroneutrality. However, when the TBA-15 bioreceptor is grafted at the surface of the semiconductor, and that sample is dried, the electroneutrality is expected from a free carrier reorganization inside the semiconductor. According to this, after the immobilization of the TBA-15 bioreceptor on the P-channel surface of the Si nanonet, the transfer characteristics of the Si nanonet-based FET (drain current as a function of gate voltage) should be shifted to a more positive gate voltage, to offset the negative charges brought by the TBA-15 bioreceptor. Subsequently, upon hybridization with its complementary DNA sequence (c-TBA target, sequence detailed in Chapter II, Table II-1), the transfer characteristic of the transistor should be shifted

even further to a more positive gate voltage, as additional negative charges are brought with the second DNA sequence. Thus, according to this approach, the detection of DNA hybridization can be achieved either by measuring the threshold voltage shift, or by measuring the change in the transistor drain current at a given gate voltage. The electrical detection of the DNA hybridization was studied on 80 Si nanonet-based FET devices. The devices were characterized before the biofunctionalization process (as-fabricated), after the TBA-15 bioreceptor grafting, and after hybridization with the c-TBA target. The biofunctionalization process was performed using the UV-assisted GOPS-based protocol previously optimized (Chapter II, section II.2.2.1), and the hybridization step was carried out as detailed earlier (Chapter II, section II.2.1).

The expected electrical behavior described above can be observed on some of the Si nanonet-based devices, as it is reported in Figure III-2. However, as the study was carried out on numerous Si nanonet-based devices (80), we noticed that this behavior was not the dominant one. Moreover, we also noticed that the results obtained were highly dependent of the experimental protocol. This suggests the existence of several mechanisms in competition for the electroneutrality of the system, and that the applied experimental protocol can favor one or the other. As a consequence, we decided to carry out a detailed study of the parameters involved in both the TBA-15 grafting and the hybridization with the c-TBA target steps, and their impact on the electrical detection of the DNA hybridization.

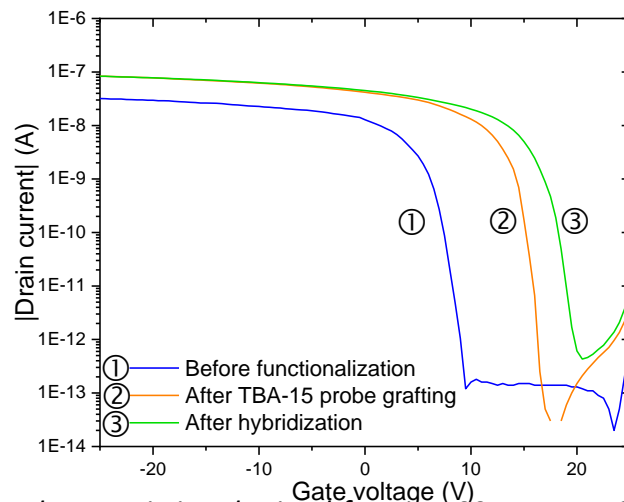


Figure III-2: Transfer characteristics obtained for a  $L=100\ \mu\text{m}$ ,  $W=100\ \mu\text{m}$  Si nanonet-based FET at a drain voltage of  $V_d = -2\text{V}$ . ① Before biofunctionalization process, ② after TBA-15 bioreceptor grafting, and ③ after hybridization with c-TBA target.

### III.2.1. Study of the biosensor formation

The biosensor is formed once the bioreceptor is grafted on the Si nanonet-based FET surface. The objective of this analysis is to explore the impact of the grafting step on the Si nanonet-based FET electrical properties. Therefore, this study was divided into 3 parts: (i) the stability of the transfer characteristics of the Si nanonet-based FET devices once they are biofunctionalized, (ii) the hybridization capacity in time, and (iii) the impact of the surface environment on the Si nanonet-based FET properties.

#### III.2.1.1. Stability of the transfer characteristics of biofunctionalized Si nanonet-based FETs

This study was carried out on 5 Si nanonet-based FETs, each of them presenting different channel length ( $L = 20, 40, 50, 100$  and  $200 \mu\text{m}$ ), but with a constant width ( $W = 100 \mu\text{m}$ ). The transfer characteristics of the FET devices were studied before the biofunctionalization process (as-fabricated devices), just after the TBA-15 grafting step using UV-assisted GOPS-based protocol, and at different times after this step.

*Figure III-3(a)* displays the transfer characteristics corresponding to the  $L = 100 \mu\text{m}$ ,  $W = 100 \mu\text{m}$  Si nanonet-based FET device, as a function of elapsed time after TBA-15 bioreceptor grafting, and subsequent exposure to ambient conditions. The sub-threshold slope ( $SS$ ) and the threshold voltage ( $V_{th}$ ) extracted from *Figure III-3(a)* are reported in *Figure III-3(b)*. From the latter figure, it was found that after TBA-15 grafting, the transfer curve was first shifted towards positive voltages, with a 10 V shift in  $V_{th}$  and a 0.3  $SS$  degradation. Then, an evolution was observed during 24h, followed by stabilization. In this elapsed time, the initial  $SS$  was recovered, and the  $V_{th}$  reached 8 V. It was found that whatever the Si nanonet-based FET channel length (20 – 200  $\mu\text{m}$ ), stabilization was reached after 24 h. After this time, the FET devices presented a  $SS$  recovery and stable  $V_{th}$  values, varying between 5 and 15 V, depending on the FET geometry.

At this point, solely hypothesis linked to the surface transformation or changes in the DNA hydration level or conformation can be formulated in order to explain this behavior. For that

reason, in the following investigation, it was explored the effect of the DNA strand conformation on the grafting step, and the impact of various surface environments on the hybridization ability.

Besides, for further electrical studies, it is important to wait for the electrical stabilization of the Si nanonet-based FET devices, which occurs 24 h after the TBA-15 grafting step, before acquiring initial transfer characteristics of the functionalized devices. Indeed, this initial transfer characteristics corresponds to the reference for the subsequent step of electrical detection of the DNA hybridization.

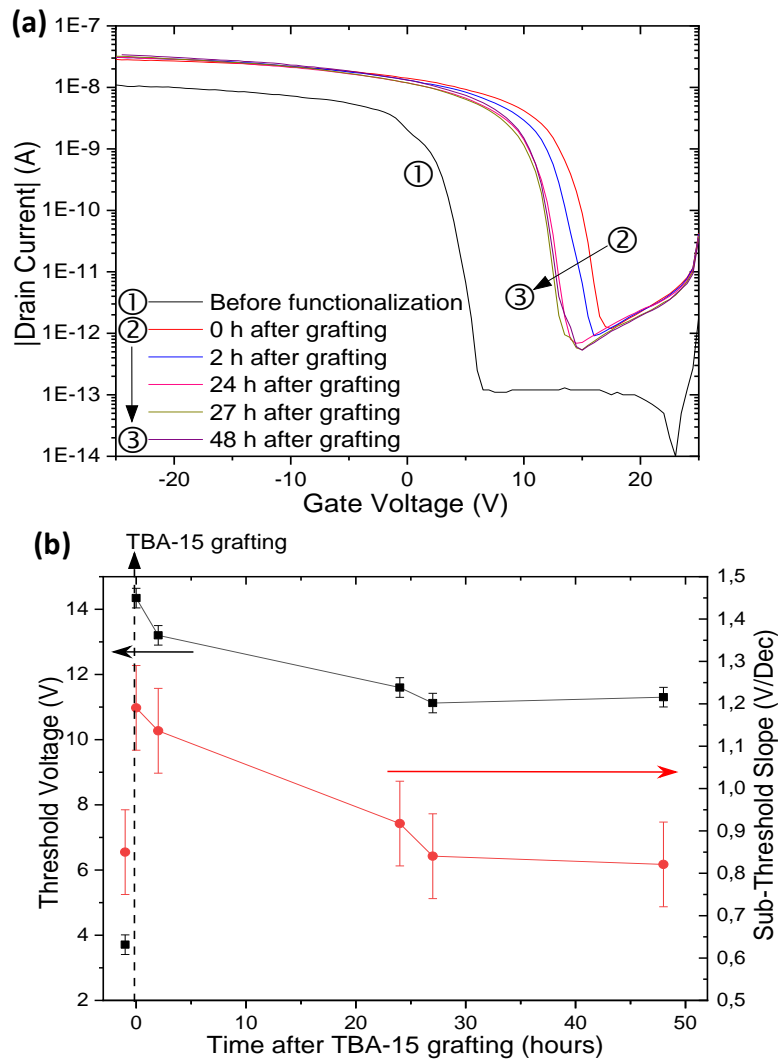


Figure III-3: (a) Transfer characteristics of a  $L = 100 \mu\text{m}$ ,  $W = 100 \mu\text{m}$  Si nanonet-based FET before functionalization and at different times after TBA-15 grafting. The drain voltage  $V_d$  was set at  $-2 \text{ V}$ . (b) Sub-threshold slope (SS) (red circles) and threshold voltage ( $V_{th}$ ) (black squares) variation for the different times analyzed. Points before time = 0 correspond to the electrical characterizations before TBA-15 probe grafting.

### III.2.1.2. Hybridization capacity in time

The first hypothesis to explain the need for 24 h before hybridization to obtain stable electrical properties in the Si nanonet-based-FETs is related to an evolution in the hydration and/or conformation of the grafted DNA bioreceptor. Thus, here is described the hybridization capacity in time of the TBA- bioreceptor through analyses performed by fluorescence microscopy.

To gain more sensitivity in fluorescence measurements, the experiments were conducted on Si/SiO<sub>2</sub> (100 nm) substrates biofunctionalized by UV-assisted GOPS protocol. The hybridization of the TBA-15 bioreceptor with its Cy3 labeled DNA complementary sequence (c-TBA) was conducted at different times after the TBA-15 grafting: immediately after, 1 day, 2 days, and 3 days after. The samples were kept in ambient conditions during the waiting time.

The parameters used to carry out the hybridization step and the fluorescence analyses were the same as those described in the previous chapter (II.2 biofunctionalization processes). The results reported in *Figure III-4*, where the fluorescence evolution is shown as a function of the time between the TBA-15 grafting and the hybridization with its complementary DNA sequence, indicate that the optimum time for the hybridization is 1 day after carrying out the grafting step. However, for a longer waiting time, the hybridization is no longer efficient. Such a result is then quite surprising, as we know from previous works that fluorescent biosensors are highly stable after probe deposition, as shown by fluorescence observations [8]. In particular, by studying hybridization capacity in time of the Seq 2 bioreceptor (DNA sequence detailed in Chapter II, Table II-1), we noted that the hybridization with its complementary DNA sequence was still efficient after more than one year of storage in air (result not shown here).

As a consequence, neither the hybridization protocol nor the storage conditions are responsible for the loss in fluorescence. Then, the difference in behavior between the two oligonucleotides arises probably from the particular sequence of the TBA-15. Indeed, as previously mentioned (Chapter II, II.2.1.2.2. Biofunctionalization monitoring by AFM), the TBA-15 bioreceptor is able to form characteristic G-quadruplex structures and has the potential to form complex multimers

such as wires [10,11]. As the stability of the multimers increases with dehydration [12], one can imagine that once stable wires have been formed, it would then be difficult to achieve the hybridization with the complementary DNA sequence. In parallel, such dehydration could explain the evolution of the electrical characteristics observed previously (*Figure III-3*). According to fluorescence analyses (*Figure III-4*), after 2 days in air, the hybridization is no longer favored over G-quadruplex structure or multimer formation. Such concurrent behavior between hybridization and multimer formation has already been demonstrated for TBA-15 [13]. In that work they demonstrated that when subjected to sodium-only buffer incubation, the TBA-15 hybridization is favored over G-quadruplex formation. In our case, the hybridization buffer was composed of different ions including potassium which, as mentioned before, facilitates the formation of the G-quadruplex structures for TBA-15 [14–16], thus reducing the possibility of hybridization to take place.

Therefore, for further analyses, the hybridization buffer composition ( $K^+$  and  $Na^+$  ions) and the time between TBA-15 bioreceptor grafting and the target recognition should be chosen according to the objective of the study, depending on whether the aim is to detect the TBA-15 hybridization with its complementary sequence, or thrombin detection which would be favored with the stabilization of the G-quadruplex structures.

As a conclusion, this study allowed to demonstrate that changes in the surface environment occurred during the first days after grafting step. These changes could have been generated by variations in the TBA-15 bioreceptor, including dehydration, followed by change in the structure conformation, which in turn were probably responsible for the observed evolution in the electrical properties of the Si nanonet-FET based devices (*Figure III-3*).

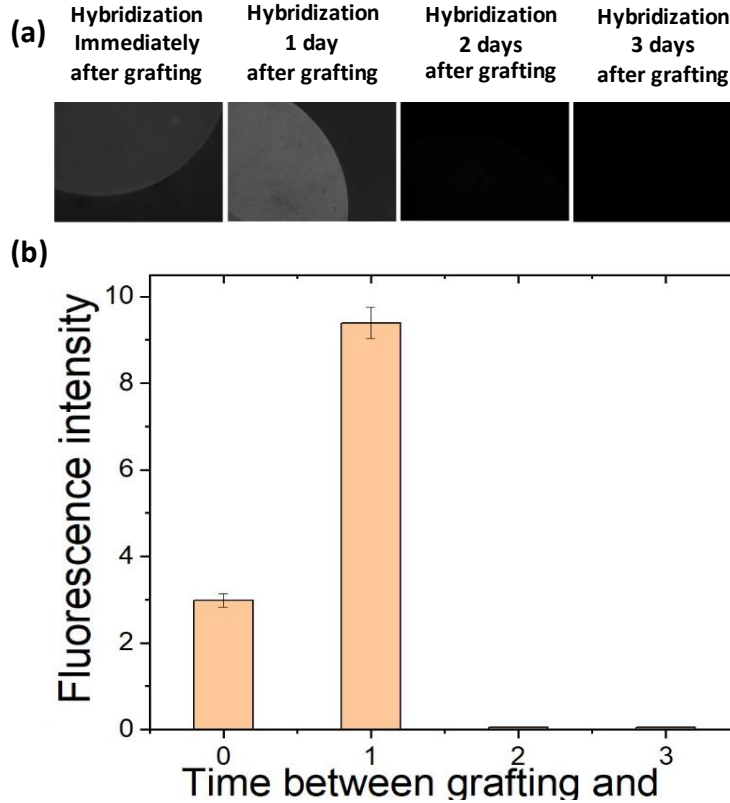


Figure III-4: Fluorescence intensity as a function of the time elapsed between the TBA-15 grafting and the hybridization with its complementary DNA sequence. Tests performed on Si/SiO<sub>2</sub> (100 nm) substrates functionalized by UV-assisted GOPS protocol and kept in ambient conditions. (a) Typical epifluorescence microscopy images when the hybridization with the complementary DNA sequence (c-TBA) was conducted at different times after the TBA-15 grafting (immediately after, 1 day, 2 days, and 3 days after). Exposure time = 3 s. (b) Fluorescence intensity, as measured on fluorescence micrographs, as a function of delay between TBA-15 bioreceptor grafting and hybridization. For all conditions, three fluorescent spots on the substrate were analyzed giving an average fluorescence intensity value and error bars corresponding to the minimum and maximum fluorescence intensity found for each sample.

### III.2.1.3. Impact of the surface environment on the Si nanonet-based FET properties

The grafting step was studied with the aim to understand the impact of the surface environment on the electrical properties of the Si nanonet-based FETs. A particular attention was paid to the impact of the grafting step. Apart from analyzing the impact generated by the grafting of the TBA-15 bioreceptor, it was also analyzed the effect generated by the grafting of another kind of sequence, namely the Seq 2 bioreceptor, in order to clarify whether the DNA base composition had any influence on the electrical properties of the FET devices after the grafting step.

Additionally, we also studied the impact of the exposure of the FET devices to the grafting phosphate buffer solution. So, to ensure homogeneity in the Si nanonet-based FET devices, the whole surface of the chip was biofunctionalized by the UV-assisted GOPS-based protocol, but at the grafting step, each quarter Q of the chip (See Chapter II, Figure II-3) was treated in a different way: Q2 and Q4 were modified with the TBA-15 bioreceptor, Q3 was modified with the Seq 2 bioreceptor, and Q1 was exposed solely to the grafting phosphate buffer solution, which corresponds to the solution used to solubilize the DNA bioreceptors at the grafting step, but in this case no DNA bioreceptor was added to it.

Figure III-5 displays the transfer characteristic for each case and for three different channel geometries ( $L=20, 40$  and  $50 \mu\text{m}$ , and  $W = 100 \mu\text{m}$ ), before functionalization (as-fabricated devices) and 24 h after the grafting step or the exposure to the phosphate buffer, in ambient conditions. Considering the as-fabricated devices (before functionalization), by comparing the ①, ③ and ⑤ transfer characteristic in each line, it can be noticed again that increasing the channel length improves the reproducibility from one device to another. As mentioned before, this phenomenon arises from the averaging effect of the network, implying that the overall dispersion of the Si nanonet-based FETs parameters decrease when the channel length increases.

The first important observation is that, irrespective of the case, even when no DNA bioreceptor was grafted on the NN (Figure III-5 (c)), the threshold voltage is shifted towards more positive values. This evidences that the surface modification with DNA bioreceptors was not the only mechanism responsible for variations in surface charge, and that another phenomenon should be involved. Regarding the phosphate buffer, this effect can be explained simply on the basis of the pH of the grafting phosphate buffer solution. Indeed, the chosen phosphate buffer was fixed at  $\text{pH} = 8.5$ . According to the literature, the point of zero charge (PZC) of alumina (Si nanonet passivation layer) is between 5.4 and 9.5 [17], and more precisely PZC of thin film alumina deposited by atomic layer deposition (ALD) is around 8.0 [18]. Moreover, it appears that GOPS silanization does not significantly change the PZC [19]. Then, when  $\text{pH} > \text{PZC}$ , the surface is negatively charged. As a consequence, in our configuration, at  $\text{pH} = 8.5$ , the channel surface

should be negatively charged when in contact with the phosphate buffer, implying therefore a charge reorganization within the channel, exactly as the DNA grafting does, and explaining the  $\Delta V_{th}$  shift observed toward positive values.

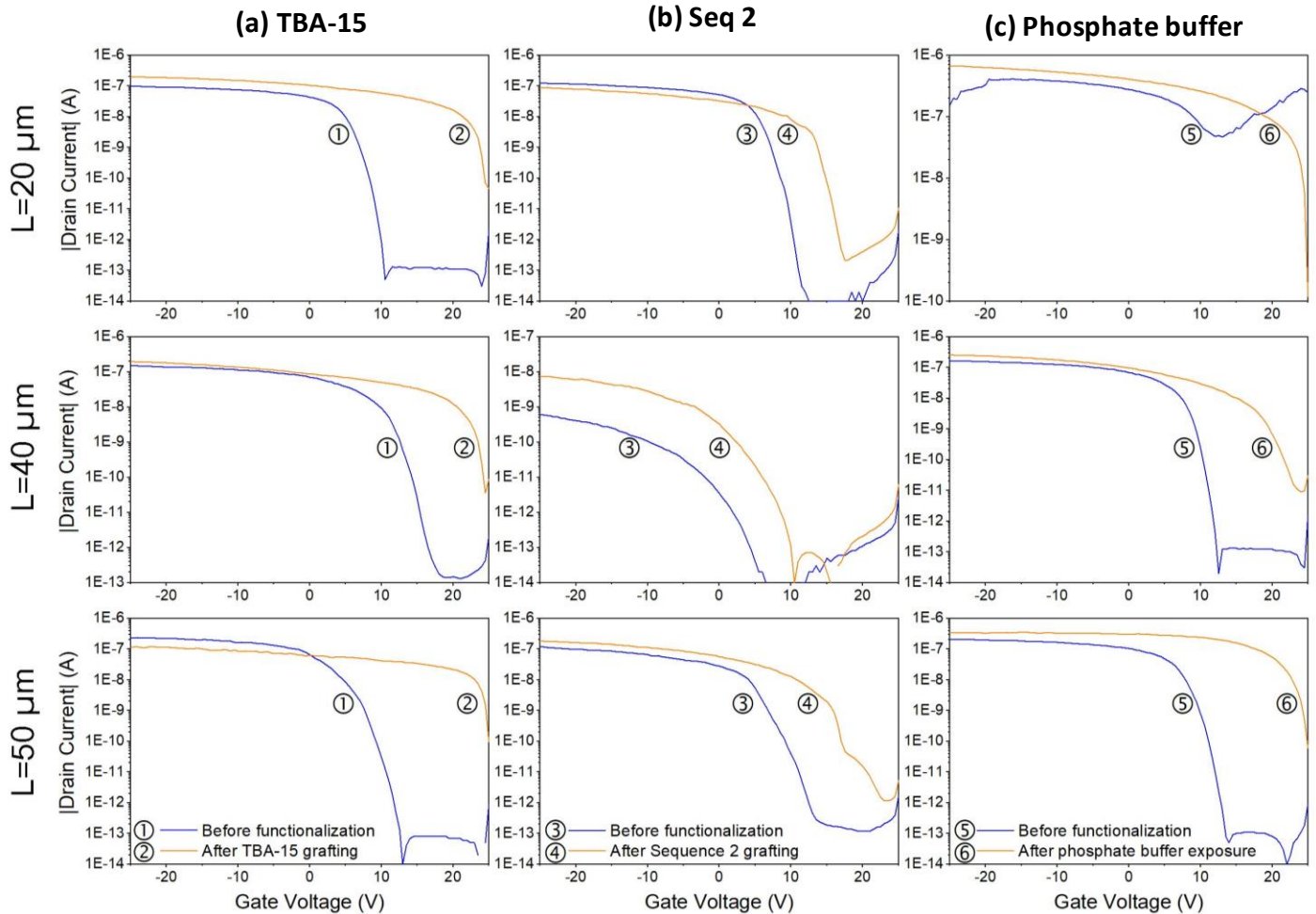


Figure III-5: Impact of: (a) TBA-15 bioreceptor, (b) Seq 2 bioreceptor and (c) phosphate buffer exposure, on the transfer characteristic of Si nanonet-FETs presenting different channel geometries after 24 h of exposure in ambient conditions. The drain voltage  $V_d$  was set at  $-2$  V.

The second observation is that the  $\Delta V_{th}$  shift was higher for the TBA-15 bioreceptor (Figure III-5(a)) than for Seq 2 bioreceptor (Figure III-5(b)). According to the literature, DNA bases exhibit different values of electronegativity, presenting the following order in a decreasing way: Thymine: 4.80 eV, Guanine: 4.68 eV, Cytosine: 4.51 eV, Adenine: 4.38 eV [20]. TBA-15 bioreceptor is composed exclusively of Thymine (T) and Guanine (G) bases (GGTTGGTGTGGTTGGTTTTT),

which are the most electronegative bases. By contrast, Seq 2 bioreceptor is composed of a combination of the four different bases (TTTTTGATAAACCCACTCTA). Then, with TBA-15 being a more electronegative sequence, it has the ability to generate a higher change in the surface charge, resulting in a larger  $\Delta V_{th}$  shift.

To conclude, on the basis of these obtained results, it appears that the positive  $V_{th}$  shift had at least two independent origins: the negative alumina surface charges (case of phosphate buffer in Figure III-5(c)) and the negative charges brought by the two kinds of DNA bioreceptors grafted on the Si nanonet-based FET surface (Figure III-5(a) and (b)). Further experiments are needed to complete these preliminary results. Notably, it is important to quantify and enlighten the respective contributions of each observed effect on the electrical properties. Regarding the impact of buffer solution on the surface device charge, and with the aim of eliminating this parameter, additional analyses should be carried out, using a buffer at pH = 8, which corresponds to the PZC of thin film alumina deposited by atomic layer deposition. In this case, only the DNA charges would be involved in the electrical characteristic modification on the Si nanonet-based FET devices.

### **III.3. Conclusions**

In this chapter we studied the feasibility of electrically detecting DNA hybridization in dry conditions using Si nanonet-based FET devices.

First, the initial properties of FET devices with different channel geometries were studied. The results obtained confirmed the excellent performance of the fabricated devices, for which an  $I_{on}/I_{off}$  of about  $10^5$  was obtained. In addition, consistent with previous studies, it was found that increasing the channel length improves the reproducibility from one device to another, thanks to a better averaging effect of the network.

Regarding the stability of the Si nanonet-based FET devices in ambient conditions, we demonstrated that their electrical properties after TBA-15 bioreceptor grafting were time dependent. This fact is probably related to the hydration evolution. After probe grafting, the transfer characteristics are shifted toward positive voltages with a sub-threshold slope degradation, then it takes 24 h to recover the initial sub-threshold slope and stabilize the threshold voltage.

Furthermore, from the biofunctionalization control experiments carried out by the hybridization of TBA-15 bioreceptor with its complementary sequence, it was observed that the hybridization capacity is also time dependent. The fact that no fluorescence was observed when hybridization was performed 2 days after the grafting step can be explained by the formation of the multimers from G-quadruplex structures. These multimers could have been stabilized by the dehydration of the structures as time elapsed, and then reinforced by the presence of potassium ions in the hybridization buffer. Thus, for further analyses, it is necessary to choose the buffer composition and the time between TBA-15 probe grafting and target recognition according to the objective of the study, depending on whether the aim is to detect the TBA-15 hybridization with its complementary DNA sequence, or thrombin detection, which would be favored with the stabilization of G-quadruplex structures.

Finally, a detailed study of the bioreceptor grafting step by means of electrical characterizations allowed us to demonstrate that not only the DNA grafted on the surface implies a threshold voltage positive shift, but also the immersion in the buffer solution, whose pH was higher than the surface PZC. Moreover, we have shown that the shift in  $V_{th}$  is dependent on the base sequence of the grafted DNA sequence, due to the variation of the bases's electronegativity.

All these behaviors are probably at the origin of the non-reproducibility in the DNA hybridization detection, since as mentioned in the section III.2, solely a small amount of devices exhibited the expected behavior upon hybridization.

As a consequence, for further studies, we can summarize the points of attention as follows:

- (i) The pH of the solutions used must be equal to the PZC of the surface materials or the surface material must be chosen so that its PZC is equal to the pH of the solutions.
- (ii) In the case of dry detection, the rate of hydration of the surface has an impact on the electrical response and must therefore be controlled by the storage conditions and/or the time before measurement.
- (iii) In the case where multimer formation may occur, it is important to choose the ions in solution according to the desired structure, single-strands or multimers.
- (iv) It should be taken into account that the DNA bases composition plays an important role on the electrical response of the device.

# References

- [1] N. Bhalla, P. Jolly, N. Formisano, P. Estrela, Introduction to biosensors, *Essays Biochem.* 60 (2016) 1–8. <https://doi.org/10.1042/EBC20150001>.
- [2] G.J. Netto, A.N. Tawil, J.T. Newman, D.A. Savino, DNA Hybridization: Current Clinical Applications, *Baylor Univ. Med. Cent. Proc.* 3 (1990) 45–52. <https://doi.org/10.1080/08998280.1990.11929739>.
- [3] M. Tichoniuk, M. Ligaj, M. Filipiak, Application of DNA hybridization biosensor as a screening method for the detection of genetically modified food components, *Sensors.* 8 (2008) 2118–2135. <https://doi.org/10.3390/s8042118>.
- [4] G.S. Sayler, A.C. Layton, Environmental application of nucleic acid hybridization, *Annu. Rev. Microbiol.* 44 (1990) 625–648. <https://doi.org/10.1146/annurev.mi.44.100190.003205>.
- [5] M. Vallejo-Perez, C. Ternon, N. Spinelli, F. Morisot, C. Theodorou, G. Jayakumar, P.E. Hellström, M. Mouis, L. Rapenne, X. Mescot, B. Salem, V. Stambouli, Optimization of GOPS-based functionalization process and impact of aptamer grafting on the si nanonet FET electrical properties as first steps towards thrombin electrical detection, *Nanomaterials.* 10 (2020) 1–20. <https://doi.org/10.3390/nano10091842>.
- [6] T.T.T. Nguyen, T. Cazimajou, M. Legallais, T. Arjmand, V.H. Nguyen, M. Mouis, B. Salem, E. Robin, C. Ternon, Monolithic fabrication of nano-to-millimeter scale integrated transistors based on transparent and flexible silicon nanonets, *Nano Futur.* 3 (2019). <https://doi.org/10.1088/2399-1984/ab1ebc>.
- [7] T. Cazimajou, M. Legallais, M. Mouis, C. Ternon, B. Salem, G. Ghibaud, Electrical characteristics of silicon percolating nanonet-based field effect transistors in the presence of dispersion, *Solid. State. Electron.* 143 (2018) 83–89. <https://doi.org/10.1016/j.sse.2017.11.013>.
- [8] P. Serre, Etude des propriétés structurales et électriques de réseaux aléatoires de nanofils de silicium. Application à la détection d'ADN., Université Grenoble Alpes, 2014. <https://www.theses.fr/2014GRENT110>.
- [9] M. Legallais, Conception, étude et modélisation d'une nouvelle génération de transistors à nanofils de silicium pour applications biocapteurs, Université Grenoble Alpes, 2017. <http://www.theses.fr/s119813>.
- [10] G. Oliviero, S. D'Errico, B. Pinto, F. Nici, P. Dardano, I. Rea, L. De Stefano, L. Mayol, G. Piccialli, N. Borbone, Self-assembly of g-rich oligonucleotides incorporating a 3'-3' inversion of polarity site: A

- new route towards G-Wire DNA nanostructures, *ChemistryOpen*. 6 (2017) 599–605. <https://doi.org/10.1002/open.201700024>.
- [11] A.M. Varizhuk, A.D. Protopopova, V.B. Tsvetkov, N.A. Barinov, V. V. Podgorsky, M. V. Tankevich, M.A. Vlasenok, V. V. Severov, I.P. Smirnov, E. V. Dubrovin, D. V. Klinov, G.E. Pozmogova, Polymorphism of G4 associates: From stacks to wires via interlocks, *Nucleic Acids Res.* 46 (2018) 8978–8992. <https://doi.org/10.1093/nar/gky729>.
- [12] M. Schmid, Conformational dynamics of G-quadruplex DNA probed by time-resolved circular dichroism, Université Paris-Saclay, 2018.
- [13] J.D. Munzar, A. Ng, D. Juncker, Comprehensive profiling of the ligand binding landscapes of duplexed aptamer families reveals widespread induced fit, *Nat. Commun.* 9 (2018). <https://doi.org/10.1038/s41467-017-02556-3>.
- [14] V. Dapić, V. Abdomerović, R. Marrington, J. Peberdy, A. Rodger, J.O. Trent, P.J. Bates, Biophysical and biological properties of quadruplex oligodeoxyribonucleotides, *Nucleic Acids Res.* 31 (2003) 2097–2107. <https://doi.org/10.1093/nar/gkg316>.
- [15] V.C. Diculescu, A.M. Chiorcea-Paquim, R. Eritja, A.M. Oliveira-Brett, Thrombin-binding aptamer quadruplex formation: AFM and voltammetric characterization, *J. Nucleic Acids.* 2010 (2010). <https://doi.org/10.4061/2010/841932>.
- [16] A.M. Chiorcea-Paquim, P.V. Santos, R. Eritja, A.M. Oliveira-Brett, Self-assembled G-quadruplex nanostructures: AFM and voltammetric characterization, *Phys. Chem. Chem. Phys.* 15 (2013) 9117–9124. <https://doi.org/10.1039/c3cp50866h>.
- [17] J.J. Gulicovski, L.S. Čerović, S.K. Milonjić, Point of zero charge and isoelectric point of alumina, *Mater. Manuf. Process.* 23 (2008) 615–619. <https://doi.org/10.1080/10426910802160668>.
- [18] D. Gu, S. Yalcin, H. Baumgart, S. Qian, O. Baysal, A. Beskok, Electrophoretic Light Scattering for Surface Zeta Potential Measurement of ALD Metal Oxide Films, *ECS Trans.* 33 (2010) 37–41.
- [19] N.R. Armstrong, V.R. Shepard, Voltammetric studies of silane-modified SnO<sub>2</sub> surfaces in selected aqueous and non-aqueous media, *J. Electroanal. Chem.* 115 (1980) 253–265. [https://doi.org/10.1016/S0022-0728\(80\)80330-5](https://doi.org/10.1016/S0022-0728(80)80330-5).
- [20] Q. Zhang, E.C.. Chen, The Experimental Hardness and Electronegativity of the Purines and Pyrimidines in DNA and RNA Supported by the AM1 Calculation of the Electron Affinities and Ionization Potentials, *Biochem. Biophys. Res. Commun.* 217 (1995) 755–760.

**Chapter IV: Development of Si  
nanonet-based electrochemical  
biosensors**

## Chapter IV: Development of Si nanonet-based electrochemical biosensors

---

<b>Chapter IV: Development of Si nanonet-based electrochemical biosensors .....</b>	<b>113</b>
IV.1. Au/Si nanonet-based electrodes .....	116
IV.1.1. Effect of the APTES-based functionalization process on bare Au electrodes .....	118
IV.1.1.1. Electrochemical analyses of the APTES functionalization process using different redox probes.....	119
IV.1.1.2. X-ray photoelectron spectroscopy analysis of APTES functionalized Au surfaces ...	126
IV.1.2. Effect of the GOPS-based functionalization process on bare Au electrodes .....	126
IV.1.2.1. Electrochemical analyses of the GOPS functionalization process using different redox probes.....	127
IV.1.3. Fabrication process of the Si/Au nanonet-based electrodes .....	131
IV.1.4. Electrochemical stability over time of Au/Si nanonet-based electrodes .....	132
IV.2. C/Si nanonet-based electrodes .....	134
IV.2.1. Fabrication process of the C/Si nanonet-based electrodes .....	134
IV.2.2. Choice of the redox probe .....	135
IV.2.3. Biofunctionalization of C/Si nanonet-based electrodes using poly(pyrrole-NTA) films.138	
IV.2.3.1. Poly(pyrrole-NTA) film fabrication processes.....	140
IV.2.3.1.1. Polypyrrole-NTA film fabrication by monomer adsorption in liquid conditions followed by chemical polymerization.....	141
IV.2.3.1.2. Polypyrrole-NTA film fabrication by monomer adsorption in dry conditions followed by electropolymerization .....	148
IV.2.3.2. Immobilization of the biotin labelled bioreceptor (TBA-15 aptamer).....	152
IV.2.3.2.1. Nitrilotriacetic acid (NTA)-Cu <sup>2+</sup> interaction.....	152
IV.2.3.2.2. Cu <sup>2+</sup> -biotin interaction .....	157
IV.3. Conclusions.....	160
<b>References .....</b>	<b>161</b>

## Chapter IV: Development of Si nanonet-based electrochemical biosensors

This chapter explores the possibility of using Si nanonets for the fabrication of electrochemical biosensors, aiming to detect thrombin. This implies to fabricate a working electrode involving the Si nanonets. Herein, the function of the Si nanonet is to increase the specific surface area of the biosensor, in order to develop a device presenting a high sensitivity. For this purpose, this work was divided into two parts:

- (i) First, the choice of the base conductor material that will serve as support for the Si nanonet, and which in combination with the latter will conform the working electrode. For this purpose two kinds of base material were studied: gold and carbon.
- (ii) The development of an biofunctionalization process allowing the proper grafting of the bioreceptor (TBA-15) on the Si nanonet-based electrode.

Before going into the chapter, a short theoretical section is presented, which will help to understand the results obtained. As explained in Chapter I, in Electrochemical Impedance Spectroscopy investigations, the electrochemical system can be studied by means of an equivalent electrical circuit (Figure I-1). The impedance spectrum can be divided into three parts depending on the frequency range considered. At high frequencies, it can be observed the resistance of the electrolyte " $R_s$ ". At intermediate frequencies, a resistance due to charge transfer " $R_{ct}$ " is observed in parallel with the electrochemical double layer capacitance " $C_{dl}$ ". However, in our case, it was decided to replace this capacitance by a constant phase element (CPE), in order to take into account the inhomogeneity of the working electrode surface, generated by the porous Si nanonet structure [1,2]. Finally, at low frequencies, a Warburg impedance " $Z_w$ " is introduced in series with  $R_{ct}$ . The Warburg impedance reflects the impedance due to the diffusion phenomena of the electroactive species towards the conducting surface. In our case, the diffusion occurs in a semi-infinite layer (natural diffusion), and it appears typically as a diagonal line with a 45° slope in the Nyquist plot.

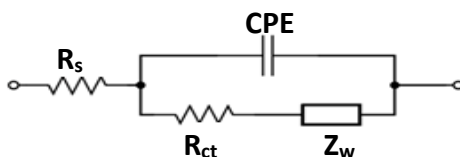


Figure I-1: Schematic representation of the equivalent circuit of the electrochemical system studied in this project.

Then, it is possible to calculate the value of the double layer capacitance from the constant phase element, by Equation IV-1:

$$C_{dl} = CPE^n \cdot R_{ct}^{\left(\frac{1}{n}-1\right)} \quad \text{Equation IV-1}$$

$n$  is a real number varying from 0 to 1 related to the geometry of the semicircle in the Nyquist representation. When  $n = 1$ , a purely capacitive behavior is observed [3].

A software (Zview, Scribner Associates Inc.) was used to simulate the data based on the equivalent electrical circuit, allowing us to calculate the corresponding values for the different components involved in it. In addition to these values, we also studied the characteristic frequency “ $f$ ”, which corresponds to the frequency at each maximum absolute value of the imaginary part of the impedance spectrum ( $Im Z_{max}$ ) in the Nyquist plot representation [4,5]. This value is an indicator of the reaction rate, and as will be seen later, it could be related to the changes generated on the surface of the electrochemical biosensor.

### IV.1. Au/Si nanonet-based electrodes

The selection of the working electrode (WE) material is critical for the success of the electrochemical process, since the electron transfer occurs at the interface between WE and the solution. A working electrode behaves as a source or sink of electrons for exchange with the molecules adjacent to its surface, so it must be an electronic conductor. Additionally, it must be electrochemically inert over a wide potential range (the so-called potential window), to allow a good degree of analyte characterization.

Then, it must be chosen a base conductor material (substrate) that fulfills the aforementioned characteristics, on which the Si nanonet could be transferred, and which in combination with the latter will constitute the working electrode. However, it must be considered that the Si nanonet is a porous structure. It implies that when the biofunctionalization process of the working electrode will be carried out, both the surfaces of the Si nanonet and the substrate will be exposed

to the chemical processes involved. Then, it is important to choose a material whose properties will not be significantly affected by these processes. It must be clarified that in our case, the Si nanonet cannot be biofunctionalized before being transferred onto a substrate.

First, it was studied the possibility of fabricating a working electrode (substrate/Si nanonet) that could benefit from the previously optimized biofunctionalization techniques, namely APTES and GOPS organosilane-based processes (see Chapter II). Ideally, in this case the substrate material should be chemically inert, in order to prevent it from reacting with the chemical processes carried out during biofunctionalization. Besides, the formation of the self-assembled monolayer (SAM) characteristic of these biofunctionalization processes must be avoided on the conductor material, as this layer would act as an insulating barrier resulting in a degradation of the electrical properties of the substrate. Therefore, the objective is that the biofunctionalization is performed only on the Si nanonet, but not on the substrate, avoiding a considerable degradation of the conductive properties of the working electrode.

For the reasons previously described, gold appears to be a promising candidate for the fabrication of the working electrode. Gold is a very good conductor material, presenting an electric conductivity ( $\sigma$ ) at 20°C of  $4,11 \times 10^7$  S/m [6]. As far as its presence in the field of electrochemistry is concerned, gold is a widely used material, as it presents very weak chemisorbing properties, an extensive double layer region that in the presence of most pure electrolytes is often assumed to be totally free of Faradaic behavior, and it exhibits a monolayer oxide formation/removal reaction at quite positive potentials (over the range of about 0 to 1.3 V in acid or 0 to 1.2 V in base conditions) [7]. In terms of reactivity, gold is normally regarded as the most inert element [8,9], then it should not be significantly affected during the biofunctionalization process using APTES and GOPS organosilanes, especially considering that at room temperature gold does not present an oxidation layer [8], which is necessary to generate the hydroxyl groups (OH) on the surface that will allow the subsequent covalent attachment of the silane [10]. To obtain the activation of the gold surface by the OH groups it would be necessary to expose the substrates to a chemical treatment, as for example the one reported by Sayikli et al, who developed a silane-based

functionalization method for gold electrodes, by modifying its surface by a mercaptohexanol solution (50 mM, in pure ethanol) overnight [11]. Then, in order to verify whether the gold substrates still exhibit conductive behavior after being subjected to biofunctionalization methods, their electrochemical properties were analyzed, before and after each of the main steps of the organosilane-based functionalization processes. This was analyzed in the case of APTES and GOPS based functionalization protocols.

### IV.1.1. Effect of the APTES-based functionalization process on bare Au electrodes

The APTES-based functionalization was previously described in Chapter II. Figure IV-2 summarizes the main steps of this process. Here, it was studied the impact of the APTES vapor phase silanization, the glutaraldehyde (GA) cross linking, and the reduction of imine bonds by  $\text{NaBH}_4$  solution, on the electrochemical properties of the bare Au electrode. The bioreceptor grafting step was not included in this study, as the idea was to evaluate the effect of the exposure of the gold surface to the different reagents involved in the process.

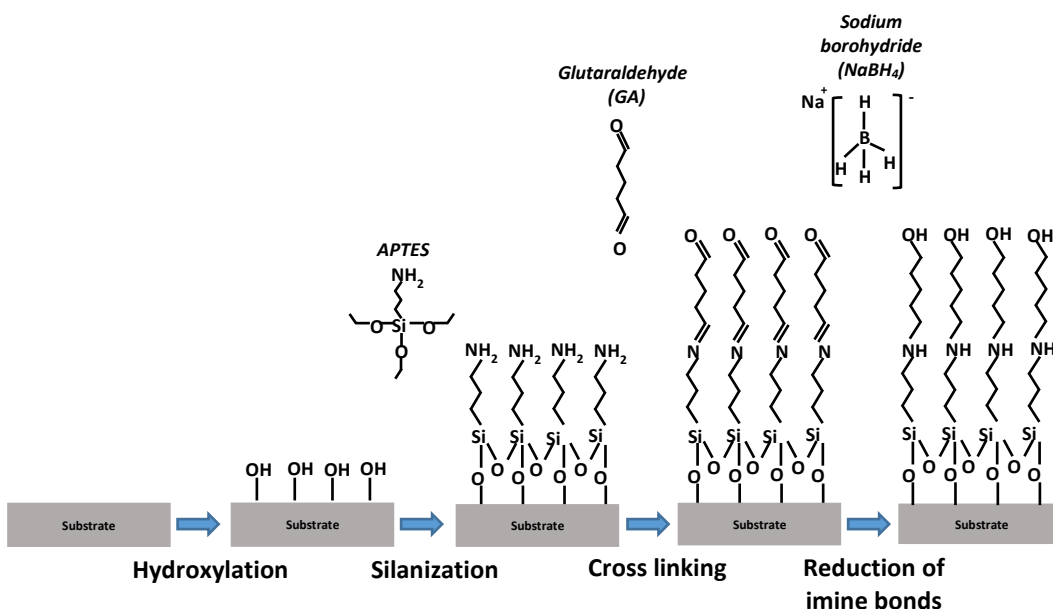


Figure IV-2: APTES functionalization steps for a material exhibiting an oxidized layer (bioreceptor grafting step not included here)

### IV.1.1.1. Electrochemical analyses of the APTES functionalization process using different redox probes

Gold substrates were fabricated from 3 cm x 1.8 cm Si substrates, on which a 150 nm thick Au layer was deposited using the Electron Beam Evaporation technique (prior to the deposition of the Au layer, a 10 nm thick Cr bond layer was deposited, in order to promote the Au adhesion on the Si substrate). They were subjected to the previously mentioned biofunctionalization steps and their electrochemical properties were studied using two different types of redox probes: hexaammineruthenium (II)/(III) ( $[\text{Ru}(\text{NH}_3)_6]^{2+/3+}$ ) and hexacyanoferrate (II)/(III) ( $[\text{Fe}(\text{CN})_6]^{3-/4-}$ ).

The electrochemical measurements were conducted in an Autolab potentiostat, using a conventional three-electrode configuration. Gold substrates were used as working electrodes, a platinum wire was used as auxiliary electrode and a saturated calomel electrode (SCE) was used as reference (the latter is the configuration used for all electrochemical analyses carried out in this project). The measurements were performed in a 0.1 M phosphate buffer solution at pH 7 containing the redox probe (2mM) and the electrochemical cell temperature was set at 25 °C. The voltammograms were recorded at scan rate of 10 mV/s. The impedance measurements were performed at a potential of -0.28 V vs SCE for  $[\text{Ru}(\text{NH}_3)_6]^{2+/3+}$  redox probe, and a potential of 0.18 V vs SCE for  $[\text{Fe}(\text{CN})_6]^{3-/4-}$  redox probe, with an amplitude of the alternating potential of 10 mV<sub>RMS</sub> and a frequency sweep from 50 000 Hz to 0.1 Hz for both probes. It is important to mention that each step of the biofunctionalization was evaluated on a different Au electrode, to avoid exposing the latter to the solutions used to carry out the analyses between the different steps, as this could affect the functionalization processes to be studied. However, all the electrodes came from the same Si wafer, and the gold deposition was carried out during the same process, in order to obtain electrodes with similar electrochemical properties. A PTFE-coated adhesive glass cloth was used to delimit the active area of the Au electrodes (11 mm x 11 mm).

Figure IV-3 shows the effects of the different steps of the APTES functionalization on gold bare electrodes, analyzed by cyclic voltammetry and impedance spectroscopy, using the two redox probes.

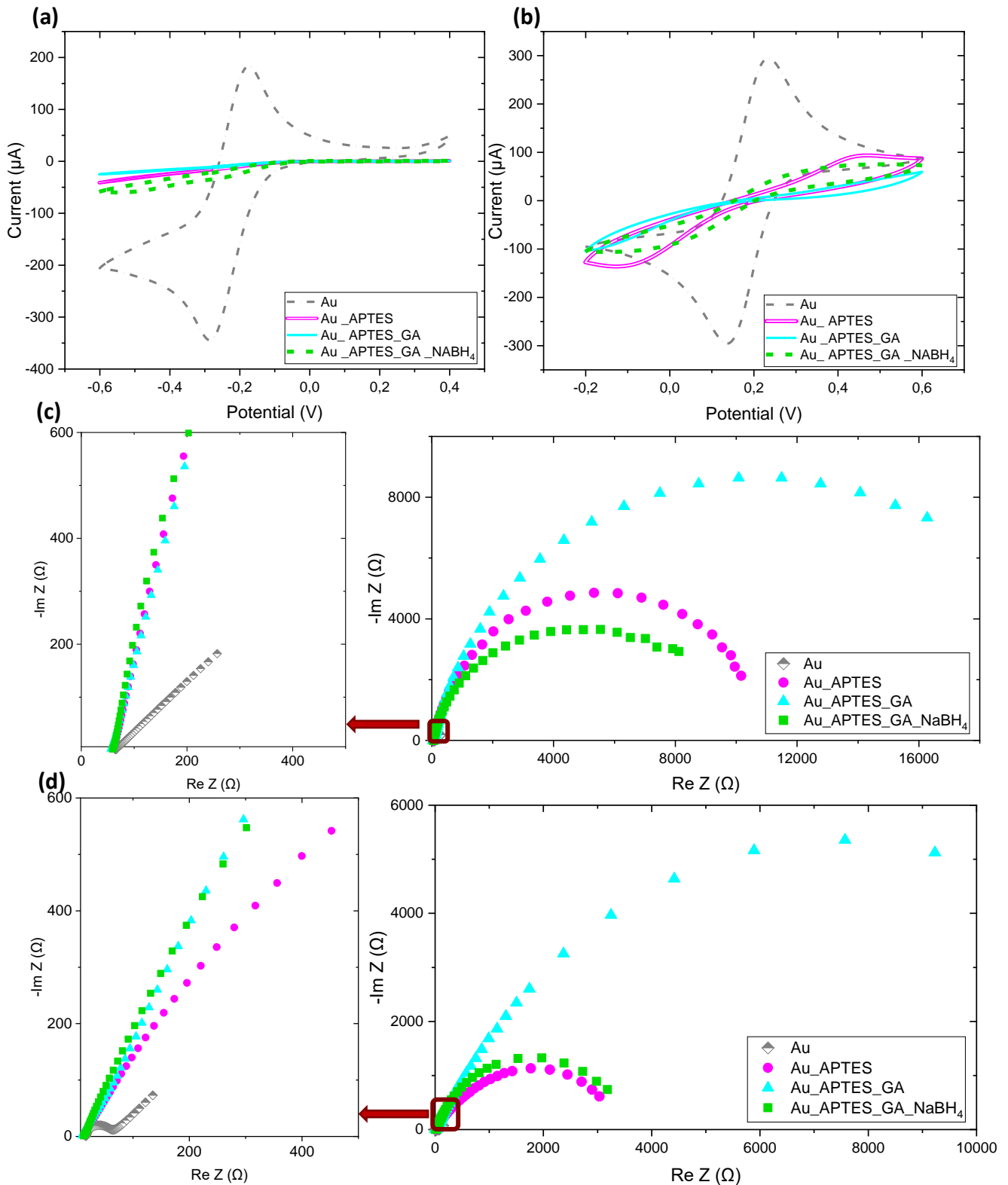


Figure IV-3: Electrochemical characterization of 11 mm x 11 mm Au electrodes after the different steps of the APTES-functionalization process, using (a) and (c) [Ru(NH<sub>3</sub>)<sub>6</sub>]<sup>2+/3+</sup> redox probe, and (b) and (d) [Fe(CN)<sub>6</sub>]<sup>3-/4-</sup> redox probe. The experimental parameters were indicated in the previous paragraph.

### A. Case of hexaammineruthenium (II)/(III) ( $[\text{Ru}(\text{NH}_3)_6]^{2+/3+}$ ) redox probe

Figure IV-3(a) corresponds to the cyclic voltammograms obtained for the  $[\text{Ru}(\text{NH}_3)_6]^{2+/3+}$  redox probe. The results show that the APTES functionalization process, from the first stage (APTES deposition), generates a blocking effect on the gold electrode surface, which makes it impossible to observe the electrochemical reactions by this technique.

The analysis carried out by impedance spectroscopy (Figure IV-3(c)), allows a better understanding of the phenomena occurring at each of the stages. First of all, in a general way it is possible to confirm the important degradation in the electrochemical properties of the gold electrode, generated by the APTES process. In fact, the change in impedance is so significant that it is necessary to zoom in on the curves in order to observe the initial properties of the electrode before the functionalization process. Table I-1 shows the changes in the impedance modulus at 0.1 Hz, which corresponds to the last frequency studied for the different steps of APTES functionalization process.

*Table I-1: Impedance modulus (Z) obtained for gold electrodes after the different steps of the APTES functionalization process, using  $[\text{Ru}(\text{NH}_3)_6]^{2+/3+}$  redox probe.*

	<b>Z (at 0.1 Hz) (<math>\Omega</math>)</b>
<b>Au</b>	315
<b>Au_APTES</b>	10385
<b>Au_APTES_GA</b>	17843
<b>Au_APTES_GA_NaBH<sub>4</sub></b>	8634

First, it can be seen that once the APTES vapor phase silanization is carried out, the impedance increases drastically, going from an impedance modulus "Z" value of 315  $\Omega$  (gold Surface) to 10385  $\Omega$  (after APTES silanization). This confirms the blocking effect of the silanization, probably due to the formation of an insulating layer of APTES adsorbed on the Au electrode. Second, when the glutaraldehyde (GA) crosslinking step is performed, Z increases even more, from 10385  $\Omega$  (after silanization) to 17843  $\Omega$  (after GA crosslinking). This is probably generated by an

increase in the thickness of the insulating layer, which further reduces the rate of electron transfer on the electrode surface. Finally, the last step of the process, corresponding to the reduction of imine bonds by  $\text{NaBH}_4$  solution, leads to a decrease in the impedance of the Au electrode, which results in an improvement in its electrochemical properties, from  $17843 \Omega$  (after GA crosslinking) to  $8634 \Omega$  (after  $\text{NaBH}_4$  reduction).

This last effect can be explained thanks to an optical study performed on gold substrates (Au coated Si/SiO<sub>2</sub> substrates), which were subjected to each of the different stages of the APTES biofunctionalization process (Figure IV-4). It is to be noted that these substrates were used only for an optical analysis. Indeed, as the intention was to observe the changes in the substrate surface after each stage of the functionalization, we used left-over parts of the material that could not be used for electrochemical analysis. Then, the substrates were not of the same size, because the latter was not a relevant parameter for this study. The different steps of functionalization were carried out during a single process, which was stopped at the corresponding stage to be analyzed for each sample.

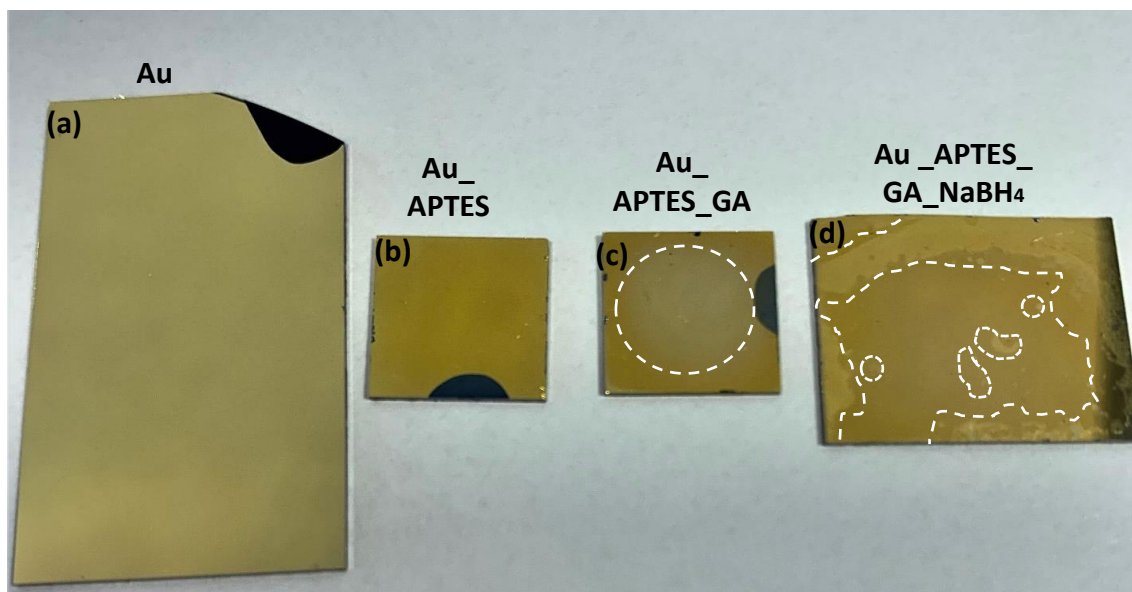


*Figure IV-4: Optical observation of the Au surfaces along the functionalization process: (a) gold electrode in its original state, (b) APTES vapor phase silanization in anhydrous conditions, (c) glutaraldehyde (GA) cross-linking and (d) reduction of imine bonds by  $\text{NaBH}_4$ . (The dark parts on the substrate correspond to portions that remained uncoated, since substrates are held by tweezers during the gold deposition process).*

From Figure IV-4, it is possible to observe some changes in the surface as the different steps are carried out. First, a change in the color intensity of the sample, from light (Figure IV-4(a)) to darker (Figure IV-4(b)) is evidenced after the APTES silanization step. As previously detailed, theoretically, the chemical reaction between gold and the APTES should not take place. However, the results of the electrochemical and optical analyses indicate that the Au surface is indeed affected by the silane deposition and the subsequent functionalization steps. This fact reinforced the idea of the possible adsorption of APTES on the substrate surface.

Second, the subsequent reaction with the glutaraldehyde solution shows a change in the homogeneity of the sample. The center is lighter in color than the edges of the substrate (Figure IV-4(c)). This indicates that a layer of GA was deposited on top of the previous one (APTES), but not uniformly. This is probably due to the fact that the first layer was deposited by adsorption, which is not a controlled process, giving rise to a layer with different characteristics along the substrate surface. This in turn has an influence on the subsequent layers, whose homogeneity depends on the characteristics of the preceding one.

Finally, in Figure IV-4(d), it can be observed the surface of the Au substrate after the last stage of the functionalization process, corresponding to the reduction of imine bonds by a  $\text{NaBH}_4$  solution. This image shows a non-uniform surface, with lighter spots randomly distributed on it. This fact could have been caused by the  $\text{H}_2$  bubbles that are produced as a by-product of the chemical reaction. These bubbles are able to detach some parts of the previously deposited layers, creating holes on the surface. This result is similar to the problems previously reported in Chapter II (section II.2.1.2), where the  $\text{H}_2$  bubbles detached the metal contacts of the surface of the Si nanonet-based FET devices. In turn, these holes may explain the improved electrochemical properties of the functionalized gold electrode after the  $\text{NaBH}_4$  imine reduction step, which was evidenced during the electrochemical analysis. In fact, by removing part of the deposited layers, the redox probe has again a better accessibility to the Au electrode surface, resulting in a significant improvement in its electrochemical properties, which can be clearly evidenced in the decrease of the impedance values after the last step of the functionalization process.

### B. Case of hexacyanoferrate (II)/(III) ( $[\text{Fe}(\text{CN})_6]^{3-/4-}$ ) redox probe

The electrochemical study of APTES functionalized gold electrodes using the  $[\text{Fe}(\text{CN})_6]^{3-/4-}$  redox probe (Figure IV-3 (b) and (d)) corroborated that the APTES-based biofunctionalization process strongly affects the electrochemical properties of the Au electrode. However, from these analyses, it is possible to note that when using  $[\text{Fe}(\text{CN})_6]^{3-/4-}$  redox probe, the electrochemical properties of the electrode obtained is higher in comparison with the results obtained when using  $[\text{Ru}(\text{NH}_3)_6]^{2+/3+}$  redox probe. On the one hand, this can be seen from the curves obtained by cyclic voltammetry (Figure IV-3 (b),  $[\text{Fe}(\text{CN})_6]^{3-/4-}$  redox probe). In this case it is possible to observe the peaks corresponding to the oxidation and reduction of the redox probe on the electrode surface after the different functionalization steps, contrary to the previous case (Figure IV-3 (a),  $[\text{Ru}(\text{NH}_3)_6]^{2+/3+}$  redox probe). In this latter case the interaction between the redox probe and the functionalized surface was not good enough to observe the electrochemical reactions. Nevertheless, the low intensity of the peaks and the shape of the voltammograms allow to conclude once again the blocking effect generated by the different layers deposited on the gold electrode after the functionalization process. On the other hand, the impedance values obtained using  $[\text{Fe}(\text{CN})_6]^{3-/4-}$  redox probe (Figure IV-3 (d)), are lower compared to those obtained for the  $[\text{Ru}(\text{NH}_3)_6]^{2+/3+}$  redox probe (Figure IV-3 (c)), thus confirming what was observed by cyclic voltammetry analysis. For comparison, the values obtained for the current intensity and impedance modulus for both redox probes are summarized in Table IV-2.

As in the previous case, the electrochemical analysis using  $[\text{Fe}(\text{CN})_6]^{3-/4-}$  redox probe (Figure IV-3 (b) and (d)), shows that after the APTES vapor phase silanization, the electrochemical properties of the electrode drops drastically. As can be seen in the cyclic voltammogram (Figure IV-3 (b)), the adsorption of the APTES induces an important decrease in both, the anodic current (upper peak,  $I_{pa}$ ) and the cathodic current (lower peak,  $I_{pc}$ ). Values vary from  $I_{pa} = 305 \mu\text{A}$  (gold electrode) to  $I_{pa} = 3.58 \mu\text{A}$  (after APTES silanization). Similarly, the cathodic current, presented a decrease from  $I_{pc} = -295 \mu\text{A}$  (gold electrode) to  $I_{pc} = -41.9 \mu\text{A}$  (after APTES silanization).

## Chapter IV: Development of Si nanonet-based electrochemical biosensors

Table IV-2: Values of the different parameters studied by electrochemical analyses (anodic and cathodic current intensities ( $I_{pa}$  and  $I_{pc}$  respectively) and impedance modulus ( $Z$ )), obtained for gold electrodes after the different steps of the APTES functionalization process, using two different redox probes.

	$[\text{Ru}(\text{NH}_3)_6]^{2+/3+}$			$[\text{Fe}(\text{CN})_6]^{3-/4-}$		
	$I_{pa}$ ( $\mu\text{A}$ )	$I_{pc}$ ( $\mu\text{A}$ )	$Z$ (at 0.1 Hz) ( $\Omega$ )	$I_{pa}$ ( $\mu\text{A}$ )	$I_{pc}$ ( $\mu\text{A}$ )	$Z$ (at 0.1 Hz) ( $\Omega$ )
<b>Au</b>	291	-262	315	305	-295	154
<b>Au_APTES</b>	---	---	10385	3.58	-41.9	3098
<b>Au_APTES_GA</b>	---	---	17843	---	---	10556
<b>Au_APTES_GA_NaBH<sub>4</sub></b>	---	---	8634	6.59	40.2	3270

The results obtained by impedance spectroscopy are coherent with the previous ones. It was obtained an increase in the values of the impedance modulus  $Z$  at 0.1 Hz from 154  $\Omega$  (gold electrode) to 3098  $\Omega$  (after APTES silanization).

Once again, when the electrode was exposed to the glutaraldehyde solution, the surface becomes more resistive. After this step it is not possible to observe the redox reaction by cyclic voltammetry, and the  $Z$  value increases from 3098  $\Omega$  (after APTES silanization) to 10556  $\Omega$  (after GA cross linking). Finally, the effect of improvement of the electrochemical properties of the interface after the  $\text{NaBH}_4$  reduction step is again confirmed. Low intensity peaks could be observed once more after this step, presenting values of  $I_{pa} = 6.59 \mu\text{A}$  and  $I_{pc} = 40.2 \mu\text{A}$ . In turn, the value of the impedance decreased from 10556  $\Omega$  (after GA cross linking) to 3270  $\Omega$  (after  $\text{NaBH}_4$  step).

In order to have a better understanding of why the Au electrode surface was strongly affected by the APTES functionalization process, and especially seeking to confirm the possible adsorption of this amino silane on the latter, a chemical analysis of the functionalized gold surface was carried out by X-ray photoelectron spectroscopy.

#### IV.1.1.2. X-ray photoelectron spectroscopy analysis of APTES functionalized Au surfaces

The XPS analyses were carried out on a gold substrate after APTES silanization. The obtained results confirmed the adsorption of the APTES on the Au surface. Indeed, the survey spectrum (Figure IV-5(a)) allowed to observe the presence of the different elements composing the APTES aminosilane (C, O, N and Si), in addition to the Au coming from the substrate. From the N 1s high resolution spectra (Figure IV-5(b)), the peaks observed around 398, 400 and 402 eV correspond to -NH=, -NH- and NH<sub>2</sub> respectively [12]. These findings explain the degradation of the electrical properties of bare Au electrodes after APTES exposure.

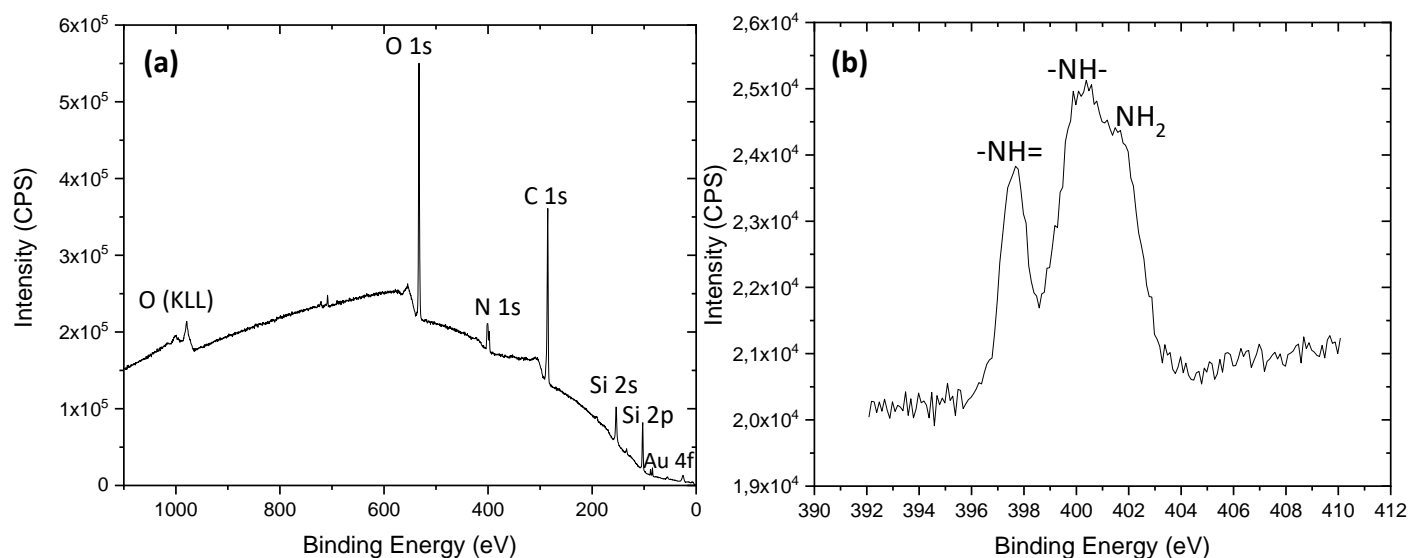


Figure IV-5: XPS analyses of a bare Au substrate after APTES silanization. (a) Survey spectrum, (b) N 1s high resolution spectra.

#### IV.1.2. Effect of the GOPS-based functionalization process on bare Au electrodes

The GOPS-based functionalization was previously described in Chapter II. As mentioned before, the GOPS epoxy silane allows the direct covalent grafting of NH<sub>2</sub>-probes via ring opening reaction. Since in this case there are no intermediate stages between the silanization and the grafting of the probe molecules, only the effect of the GOPS vapor phase silanization on the electrochemical properties of the bare Au electrode was studied. The analyzed step is illustrated in Figure IV-6, for a substrate composed of a material susceptible to activation by hydroxyl groups (oxide material).

Once again, the probe grafting step was not included in this study, as the idea was to evaluate the effect of the exposure of the gold surface to the organosilane involved in the process.

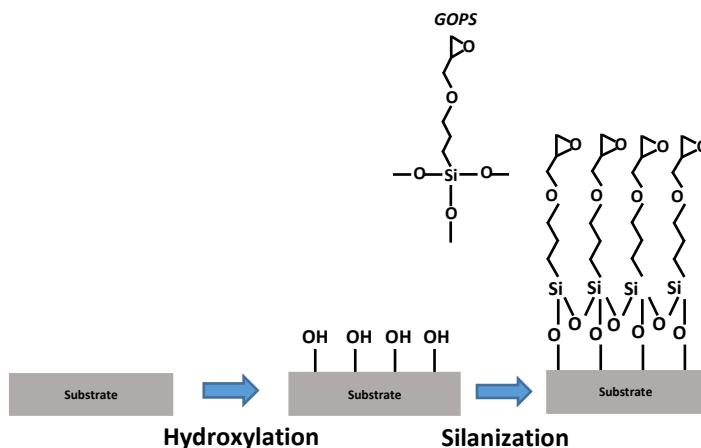


Figure IV-6: GOPS functionalization steps for a material exhibiting an oxidized surface layer (bioreceptor grafting step not included here)

### IV.1.2.1. Electrochemical analyses of the GOPS functionalization process using different redox probes

As in the previous case, both, initial and post-silanization characteristics were studied on different Au electrodes, to avoid exposing the latter to the solutions used to carry out the analysis between the different steps, as this could affect the functionalization processes to be studied. Figure IV-7 shows the effect of GOPS vapor phase silanization on gold bare electrodes, analyzed by cyclic voltammetry and impedance spectroscopy, using  $[\text{Ru}(\text{NH}_3)_6]^{2+/3+}$  and  $[\text{Fe}(\text{CN})_6]^{3-/4-}$  redox probes.

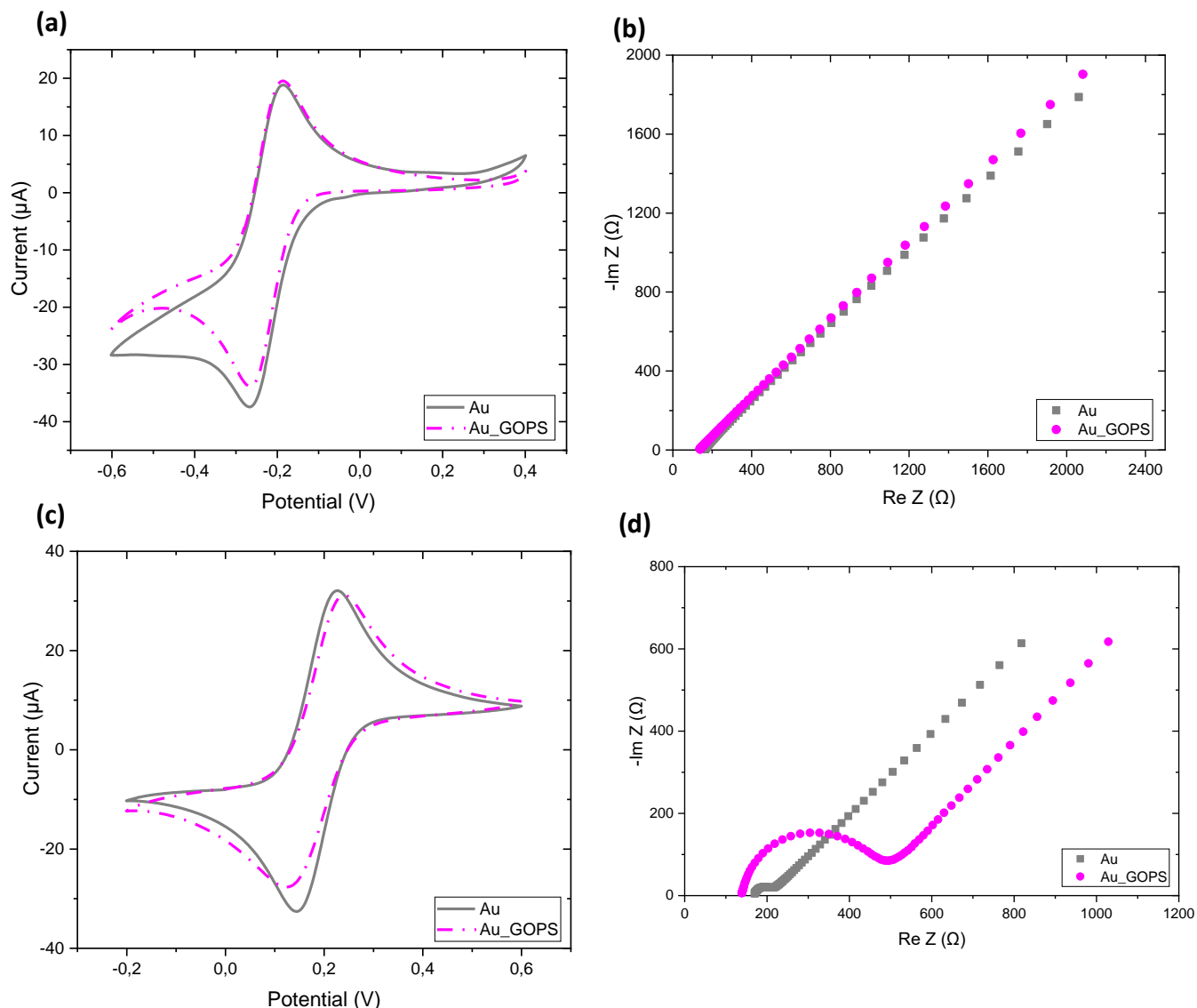


Figure IV-7: Electrochemical characterization of the GOPS vapor phase silanization on 11 mm x 11 mm bare Au electrodes using (a) and (b)  $[\text{Ru}(\text{NH}_3)_6]^{2+/3+}$  redox probe, and (c) and (d)  $[\text{Fe}(\text{CN})_6]^{3-/4-}$  redox probe. Measurements performed in a 0,1 M phosphate buffer solution at pH 7, containing the redox probe (2 mM). The voltammograms were recorded at 10 mV/s. The impedance measurements were performed at a potential of -0.28 V vs SCE for the  $[\text{Ru}(\text{NH}_3)_6]^{2+/3+}$  redox probe, and a potential of 0.18 V vs SCE for the  $[\text{Fe}(\text{CN})_6]^{3-/4-}$  redox probe, with an amplitude of the alternating potential of 10 mV<sub>RMS</sub> and a frequency sweep from 50000 Hz to 0.1 Hz for both probes. The electrochemical cell temperature was set at 25 °C.

#### A. Case of hexaammineruthenium (II)/(III) ( $[\text{Ru}(\text{NH}_3)_6]^{2+/3+}$ ) redox probe

As can be seen from Figure IV-7(a) and (b), the electrochemical properties of the Au electrode is not significantly affected after GOPS silanization, when the analysis is carried out using

$[\text{Ru}(\text{NH}_3)_6]^{2+/3+}$  redox probe. On the one hand, the cyclic voltammogram presented in the Figure IV-7(a) shows a small change in the cathodic current after the silanization stage, from  $I_{pc} = -26.5 \mu\text{A}$  (gold electrode) to  $I_{pc} = -26.1 \mu\text{A}$  (after GOPS silanization). However, it is important to take into account that such a small change could be due to the fact that the study was carried out on two different electrodes, which may involve a variability in the measurements. On the other hand, the analysis performed by impedance spectroscopy reveals a total lack of a semicircle in the Nyquist plot in both cases, before and after the silanization step, thus confirming that the electrical properties of the gold electrode are not affected by exposure to GOPS epoxy silane, when the analyses are carried out by using this redox probe.

### B. Case of hexacyanoferrate (II)/(III) ( $[\text{Fe}(\text{CN})_6]^{3-/4-}$ ) redox probe

Contrary to the previous results, the electrochemical analysis performed using the  $[\text{Fe}(\text{CN})_6]^{3-/4-}$  redox probe reveals a change in the electrochemical properties of the electrode once it is exposed to the vapor phase GOPS silanization. These changes are summarized in Table IV-3.

Table IV-3: Values of the different parameters studied by electrochemical analyses, obtained for gold electrodes before and after GOPS functionalization process, using the  $[\text{Fe}(\text{CN})_6]^{3-/4-}$  redox probe.

	$I_{pa}$ ( $\mu\text{A}$ )	$I_{pc}$ ( $\mu\text{A}$ )	$Z$ (at 0,1 Hz) ( $\Omega$ )
<b>Au</b>	34.2	-33.2	1 022
<b>Au_GOPS</b>	32.3	-26.5	1 200

First, as can be seen in the cyclic voltammogram Figure IV-7(c), the GOPS silanization step induces a decrease in both, the anodic current and the cathodic current (5.85% for  $I_{pa}$  and 20.18% for  $I_{pc}$ ). The results obtained by impedance spectroscopy are coherent with the last ones. In this case, from Nyquist plots (Figure IV-7(d)), it is possible to observe the presence of the region related to the charge transfer resistance ( $R_{ct}$ ), denoted by the small semicircle observed in the curve corresponding to the Au electrode, which increases after the GOPS silanization step. Additionally,

it can be noticed an increase in the values of the impedance modulus  $Z$  at 0.1 Hz from 1 022  $\Omega$  (gold electrode) to 1 200 (after GOPS silanization). These results confirmed that there was a change in the gold surface electrochemical properties after the latter was exposed to the GOPS silanization. However the small value of the impedance modulus obtained at the end of the semicircle, ( $Z = 502 \Omega$  at a frequency of 14.33 Hz), and the peak current values obtained from the cyclic voltammetry analyses, indicate that although the electrochemical properties of the electrode are slightly affected, the latter still exhibits a good accessibility after the functionalization process.

The fact that a change in the electrochemical properties of the electrode can be evidenced when carrying out electrochemical analysis using the  $[\text{Fe}(\text{CN})_6]^{3-/4-}$  redox probe, but not when using  $[\text{Ru}(\text{NH}_3)_6]^{2+/3+}$ , may be related to the difference in the heterogeneous rate constant " $k^0$ " and/or the diffusion coefficients " $D$ " of the two probes. On the one hand, the heterogeneous rate constant of electron transfer (ET) is the parameter which quantifies the reversibility of the electron transfer and gives an indication of the speed of the electron transfer between an electroactive species and an electrode surface [13]. It depends on both, the nature of the redox couple and the electrode material. On the other hand, the diffusion coefficient is an important physical parameter, and is related to the mobility of the ions.  $D$  is defined as the proportionality between the flux and concentration gradient, and it depends upon several factors, such as temperature, viscosity, electrolyte composition [14]. The values of the heterogeneous rate constant and the diffusion coefficient reported in the literature for the electrochemical species used in this study are shown in

Table IV-4. The values of heterogeneous rate constant reported here correspond to analyses carried out on platinum electrodes. Although the value presented on gold electrodes must be different, it can be assumed that the factor between the  $k^0$  of the two redox probes would be of the same order as the one found for platinum electrodes.

Table IV-4: Diffusion coefficient and heterogeneous rate constant of electron transfer for  $[Ru(NH_3)_6]^{2+/3}$  and  $[Fe(CN)_6]^{3-/4-}$  species in aqueous solutions [15–19]

	$[Ru(NH_3)_6]^{3+}$	$[Ru(NH_3)_6]^{2+}$	$[Fe(CN)_6]^{3-}$	$[Fe(CN)_6]^{4-}$
$D \times 10^{-5} (m^2 \cdot s^{-1})$	$0.843 \pm 0.003$	$1.19 \pm 0.01$	$0.720 \pm 0.018$	$0.666 \pm 0.013$
$k^0 (cm. s^{-1})$	0.3 to 0.6		0.08 to 0.1	

As can be seen from the above table, the values of heterogeneous rate constant of electron transfer and the diffusion coefficients corresponding to the  $[Fe(CN)_6]^{3-/4-}$  species are lower compared to those corresponding to the  $[Ru(NH_3)_6]^{2+/3+}$  species. In general terms, this indicates that the reaction rate is lower when the analysis is performed using  $[Fe(CN)_6]^{3-/4-}$  species. Then, the higher reaction rate occurring when the  $[Ru(NH_3)_6]^{2+/3+}$  redox probe was used, may have prevented the observation of the changes generated on the electrode after the functionalization process.

Thus, summarizing the results obtained for the section corresponding to the effects of APTES and GOPS functionalization processes on the bare Au electrodes, it was found on the one hand that the APTES process causes an important degradation of their electrochemical properties. On the other hand, the GOPS process generates slight changes in the electrodes properties. However, these changes would not compromise the proper functioning of the future sensor.

### IV.1.3. Fabrication process of the Si/Au nanonet-based electrodes

The process of transferring the Si nanonet on the Si/Au substrate (3 cm x 1,8 cm Si substrate + 150 nm thick Au layer) is the same as described in Chapter II. Here, the nitrocellulose membrane containing the Si nanonet was cut into squares of approximately 7 mm x 7 mm, and subsequently it was immersed in a dichlorobenzene solution for 30 seconds, with the aim of removing the air inside the pores and achieving a good adherence between the gold surface and the nanonet. The Si nanonet was immediately brought into contact with Au surface, and finally the membrane was dissolved through an acetone bath during 35 minutes. For this study, it was used a Si nanonet

with an approximate density of  $398 \times 10^6 \text{ NWs}\cdot\text{cm}^{-2}$ , which corresponds to a surface coverage of about 100%.

As the Si nanonet is the material of interest in this work, it was necessary to isolate a large part of the Si/Au substrate, so that only the part covered by the Si nanonet is in contact with the solution, allowing the electron transfer. Additionally, in order to obtain working electrodes with reproducible characteristics, it was essential that the size of the Au/Si nanonet region in contact with the electrolyte was always the same. For this purpose, PTFE-coated adhesive glass cloth was used, which is known for its good insulating and thermal properties [20]. This adhesive has been successfully integrated in previous works, for the fabrication of electrochemical biosensors for dengue virus detection [21]. Then, it was cut a square hole of smaller size than the transferred Si nanonet (5 mm x 5 mm) on the surface of the PTFE-coated adhesive glass cloth. Subsequently, the adhesive was placed on the Au/Si nanonet electrode (Figure IV-8). The insulated surface is not counted as part of the working electrode area. The upper part of the Au covered substrate is not insulated because this area was used to make the electrical contact between the working electrode and the potentiostat, meaning that this part was not in contact with the electrolyte. A photo of the obtained Si nanonet working electrode is shown in Figure IV-8.

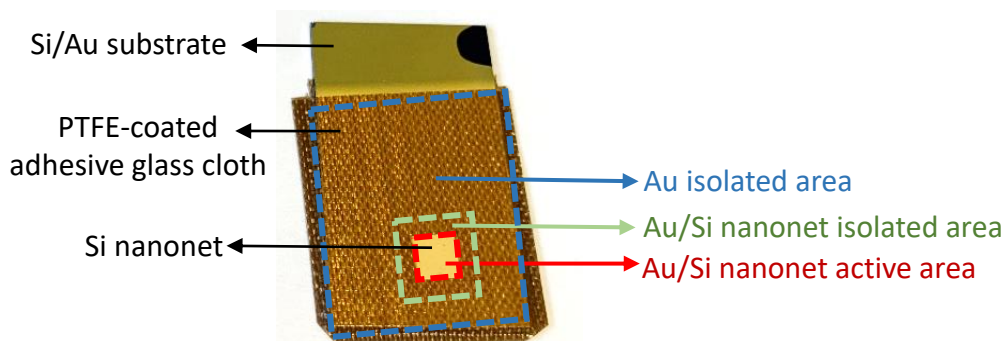


Figure IV-8: Au/Si nanonet-based working electrode

### IV.1.4. Electrochemical stability over time of Au/Si nanonet-based electrodes

In order to study the electrochemical properties and the stability over time of the Au/Si nanonet-based electrodes, an impedance spectroscopy analysis was carried out. For this purpose, a series

of consecutive EIS measurements were performed on the Au/Si nanonet-based electrode. As can be observed in the Nyquist plot presented in Figure IV-9(a), the area of the semicircle decreases as the measurements are repeated. This result indicates that while the Au/Si nanonet-based electrode was immersed in the electrolyte solution, there were changes occurring on its surface, which generated variations in its impedance, revealing an instability over time for this kind of electrodes.

In order to study if any evidence of Si nanonet detachment from the electrode could be evidenced after the electrochemical measurements, a SEM analysis was carried after performing the EIS measurements (Figure IV-9(c)). The entire Au/Si nanonet-based electrode surface was scanned, however, no evidence of detachment (holes in the structure or noticeable changes in the Si nanonet density) could be observed. Additionally, the image obtained looks similar to the one taken prior to the electrochemical analysis (Figure IV-9(b)). These results lead us to conclude that the impedance decrease is not generated by a detachment of the Si nanonet.

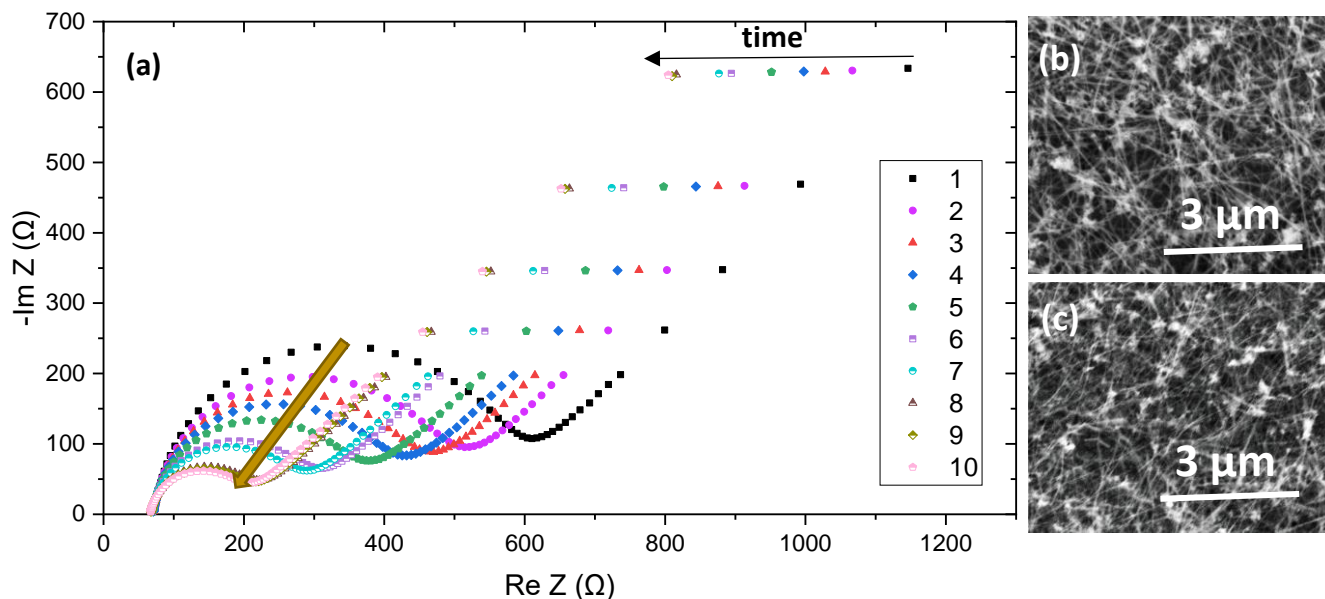


**Figure IV-9:** (a) Nyquist plot of impedance spectra obtained for 10 consecutive measurements on an Au/Si nanonet-based electrode. The order in which the measurements were performed is represented by their respective numbers (the entire analysis was carried out in about 1 h). Impedance measurements were performed using 2 mM  $[\text{Fe}(\text{CN})_6]^{3-/4-}$  redox probe in 0.1 M phosphate buffer (pH 7), at 0.18 V vs SCE, with an amplitude of the alternating potential of 10 mV<sub>RMS</sub> and a frequency sweep from 50000 Hz to 0.1 Hz. (b) and (c) SEM images of the Au/Si nanonet-based electrode before (a) and after (b) the electrochemical measurements (Si nanonet surface coverage  $\approx 100\%$ )

However, as seen in the SEM images, the Si nanonet is a porous and rough structure, which makes it difficult for the adhesive used to delimit the active area to fit in and stay fixed to this complex surface. Then, the impedance of the Si nanonet-based electrode decreases over the course of the analyses, probably as a consequence of an infiltration of the electrolyte into the isolated region of the Si nanonet, which has the effect of increasing the active area over time.

To solve this problem, it was necessary to develop another kind of Si nanonet-based working electrode, whose active area does not vary over the course of the measurements. For this purpose, we studied the possibility of transferring the Si nanonet on a glassy carbon electrode (abbreviated as CE in this work) which consists of a glassy carbon (C) cylinder, surrounded by an insulating polymer (polyetheretherketone (PEEK)). In this case, the active area is previously delimited by the PEEK polymer, thus avoiding the previously mentioned problems. The details of the C/Si nanonet-based working electrode, its fabrication process, as well as its biofunctionalization protocol are detailed below.

### IV.2. C/Si nanonet-based electrodes

For several decades glassy carbon has been widely used in the field of electrochemistry. This is due to its good electrical properties and high chemical resistance [22]. As mentioned above, these electrodes consist of a glassy carbon cylinder surrounded by an insulating polymer. Nowadays, it is possible to find in the market different types of glassy carbon electrodes. For this project, we used electrodes with a diameter of 3 mm (glassy carbon zone), on which were deposited the Si nanonet. The work done on such electrode, related to the fabrication, characterization and biofunctionalization is described as follows.

#### IV.2.1. Fabrication process of the C/Si nanonet-based electrodes

The process of transferring the Si nanonet onto the glassy carbon electrodes is similar to the procedure used for transferring Si nanonets onto flat substrates (Chapter II, Si nanonet-based FET fabrication). The glassy carbon electrodes were subjected to ultrasonic cleaning during 5 min, in

successive baths of acetone, ethanol and then deionized water. Herein, the nitrocellulose membrane containing the Si nanonet was cut a little larger than the carbon circumference (Figure IV-10(a)), in order to ensure that the entire active area of the electrode is completely covered by the Si nanonet. For this study, it was used a Si nanonet with an approximate density of  $468 \times 10^6$  NWs $\cdot$ cm $^{-2}$ , which corresponded to a surface coverage of about 100%. The membrane was then immersed in a dichlorobenzene solution for 30 seconds, and the latter was immediately brought into contact with the carbon surface. The assembly was left in air for 4 minutes, and finally the nitrocellulose membrane was dissolved through an acetone bath during 35 minutes, leaving the electrode in a vertical position with the Si nanonet on top. Finally, the whole is cleaned in acetone and isopropanol. The glassy carbon electrode before and after the Si nanonet transfer process is shown in Figure IV-10(a) and (b) respectively.

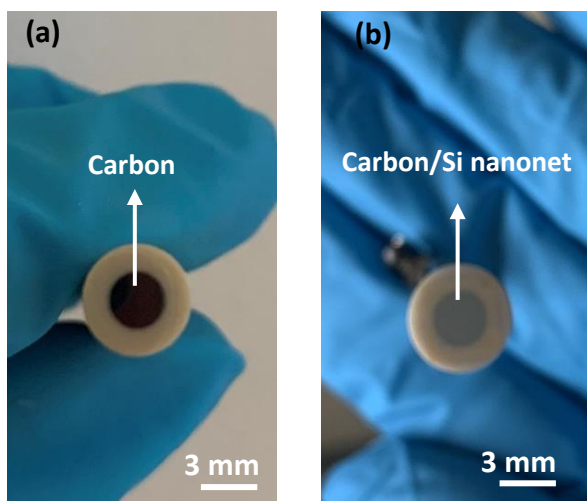


Figure IV-10: (a) C electrode. (b) C/Si nanonet-based electrode.

### IV.2.2. Choice of the redox probe

As seen previously, each redox probe can interact differently with the working electrode. It is therefore important to choose a probe that allows to characterize the different modifications carried out on the electrode electrode surface as the biosensor is built, and the subsequent detection of the target molecule. Then, as in the previous case, the electrochemical behavior of the glassy carbon electrodes after the modification of its surface with the Si nanonet was studied by cyclic voltammetry and impedance spectroscopy analyses, using two different redox probes:  $[\text{Ru}(\text{NH}_3)_6]^{2+/3}$  and  $[\text{Fe}(\text{CN})_6]^{3-/4}$ .

## Chapter IV: Development of Si nanonet-based electrochemical biosensors

The analyses were performed on different electrodes to avoid adherence problems between the Si nanonet and the CE due to electrolyte residues that may remain on the electrode surface after the measurements. The obtained results are presented in Figure IV-11.

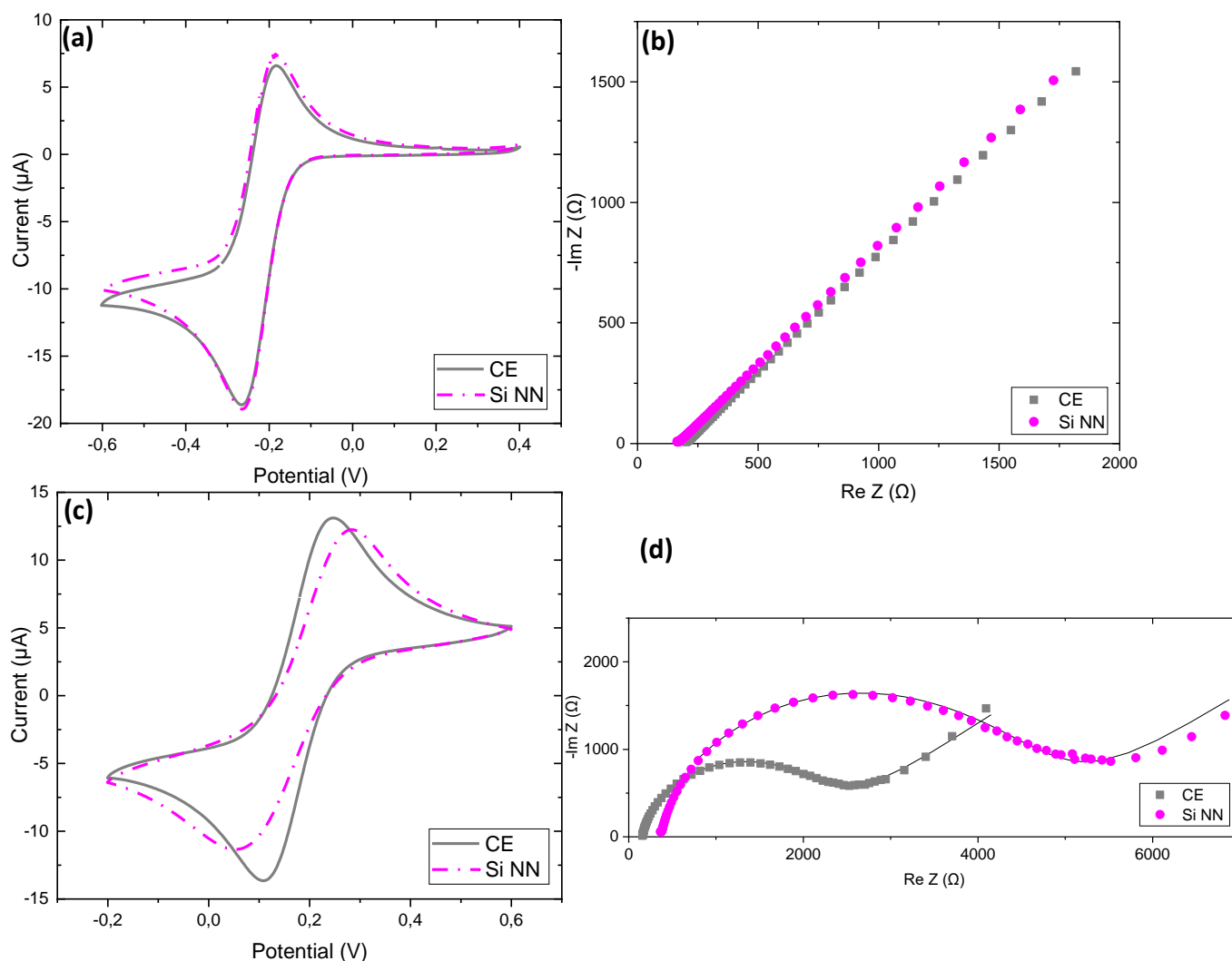


**Figure IV-11:** Electrochemical characterization of glassy carbon electrodes before and after its modification with Si nanonets (about 100% surface coverage). (a) and (b)  $[Ru(NH_3)_6]^{2+/3+}$  redox probe. (c) and (d)  $[Fe(CN)_6]^{3-/4-}$  redox probe. For (d), dots represent the experimental data and lines represent the fitted data. Measurements performed in a 0.1 M phosphate buffer solution at pH 7, containing the redox probe (2 mM). The voltammograms were recorded at 10 mV/s. The impedance measurements were performed at a potential of -0.28 V vs SCE for the  $[Ru(NH_3)_6]^{2+/3+}$  redox probe, and a potential of 0.18 V vs SCE for the  $[Fe(CN)_6]^{3-/4-}$  redox probe, with an amplitude of the alternating potential of 10 mV<sub>RMS</sub> and a frequency sweep from 50000 Hz to 0.1 Hz for both probes. The electrochemical cell temperature was set at 25 °C.

**A. Case of hexaammineruthenium (II)/(III) ( $[\text{Ru}(\text{NH}_3)_6]^{2+/3+}$ ) redox probe**

Neither the cyclic voltammetry (Figure IV-11(a)) nor electrochemical impedance spectroscopy (Figure IV-11(b)) analyses carried out using the  $[\text{Ru}(\text{NH}_3)_6]^{2+/3+}$  redox probe allowed to detect any change in the accessibility of the carbon electrode, generated by the modification of the surface with the Si nanonet. This means that the electron transfer is too fast when using this redox probe. This may in part be caused by the higher standard rate constant and diffusion coefficient of the  $[\text{Ru}(\text{NH}_3)_6]^{2+/3+}$  redox probe, compared to the the corresponding values for the  $[\text{Fe}(\text{CN})_6]^{3-/4-}$  redox probe (Table IV-4). Additionally, this effect could be increased by an electrostatic attraction generated by the negative charges on the surface of the Si nanonet. Indeed, as mentioned before, the Si nanonet is surrounded by a  $\text{SiO}_2$  native oxide layer. Cloarec et al. experimentally investigated the point of zero charge (PZC) of  $\text{SiO}_2$  surfaces, finding a value of  $2.7 \pm 0.2$  pH units [23], which is consistent with the theoretically calculated data. This means that at pH 7, the Si nanonet is negatively charged, thus attracting the positively charged redox probe.

**B. Case of hexacyanoferrate (II)/(III) ( $[\text{Fe}(\text{CN})_6]^{3-/4-}$ ) redox probe**

In contrast to the previous case, this  $[\text{Fe}(\text{CN})_6]^{3-/4-}$  redox probe does allow to evidence a change in the electrochemical properties of the glassy carbon electrode before and after the Si nanonet is transferred on it. Both, cyclic voltammetry (Figure IV-11(c)) and impedance spectroscopy curves (Figure IV-11(d)) show a modification in the electrode response when the electrode is covered by the Si nanonet. These changes are summarized in Table IV-5.

*Table IV-5: Table summarizing the values obtained for the main electrochemical parameters investigated on glassy carbon electrodes before and after its surface modification with Si nanonets. For cyclic voltammetry, the anodic and cathodic current intensities ( $I_{pa}$  and  $I_{pc}$  respectively), their associated potential values ( $E_{pa}$  and  $E_{pc}$  respectively) and the peak-to-peak separation ( $\Delta E_p$ ) are showed. For EIS, the charge transfer resistance ( $R_{ct}$ ) values obtained by fitting the experimental data are presented.*

	$I_{pa}$ ( $\mu\text{A}$ )	$I_{pc}$ ( $\mu\text{A}$ )	$E_{pa}$ (V)	$E_{pc}$ (V)	$\Delta E_p$ (V)	$R_{ct}$ ( $\Omega$ )
<b>CE</b>	13.47	-13.04	0.24	0.11	0.13	$2020 \pm 30$
<b>CE_Si NN</b>	12.89	-10.20	0.27	0.08	0.19	$4420 \pm 70$

In this case, the change in the electrochemical properties of the electrode is evidenced by both, the reduction of the peak currents (cathodic and anodic), and the increase in the charge transfer resistance, once its surface is modified by adding the Si nanonet. Additionally, the increased peak-to-peak separation proves that the redox reaction becomes less reversible once the surface is modified. The fact that  $[\text{Fe}(\text{CN})_6]^{3-/4-}$  redox probe did show the modification of the glassy carbon electrode surface, but this did not occur when using  $[\text{Ru}(\text{NH}_3)_6]^{2+/3+}$  redox probe, can be explained by two phenomena. On the one hand by an electrostatic repulsion created between the negative charges of the Si nanonet at pH 7 and the negatively charged redox probe, slowing down the reaching of the electrochemical species to the electrode surface, which allowed a better monitoring of the electrochemical reaction. On the other hand, it may have been favored by the lower standard rate constant and diffusion coefficient of the  $[\text{Fe}(\text{CN})_6]^{3-/4-}$  redox probe in comparison with the  $[\text{Ru}(\text{NH}_3)_6]^{2+/3+}$  redox probe (Table IV-4).

Based on these results, the next steps in the construction of the C/Si nanonet-based electrochemical biosensor, and the subsequent detection of the target molecule, will be evaluated using the  $[\text{Fe}(\text{CN})_6]^{3-/4-}$  redox probe.

### **IV.2.3. Biofunctionalization of C/Si nanonet-based electrodes using poly(pyrrole-NTA) films.**

The previously studied organosilane-based biofunctionalization techniques, using either APTES or GOPS, are not compatible with the use of glassy carbon electrodes. Indeed, the metal contacts located inside the electrode do not resist to the high temperatures required to carry out the silanization processes (110 °C and 140 °C respectively, (see Chapter II)). For that reason, it was necessary to explore a new alternative to achieve the grafting of the bioreceptors onto the C/Si nanonet-based electrodes, which must be performed at room temperature.

The studied technique consisted in the deposition of a poly(11-pyrrol-1-yl-undecanoic acid  $\text{Nr}'$ ,  $\text{Nr}$ -bis(carboxymethyl)-L-lysine amide) film, whose abbreviations can be found in the literature as poly(pyrrole-nitrilotriacetic acid), polypyrrole-NTA or PPy-NTA. Then, the immobilization of the

bioreceptor on the polymer film is carried out by affinity interactions, as will be described in detail below. The pyrrole-NTA monomer structure is presented in Figure IV-12.

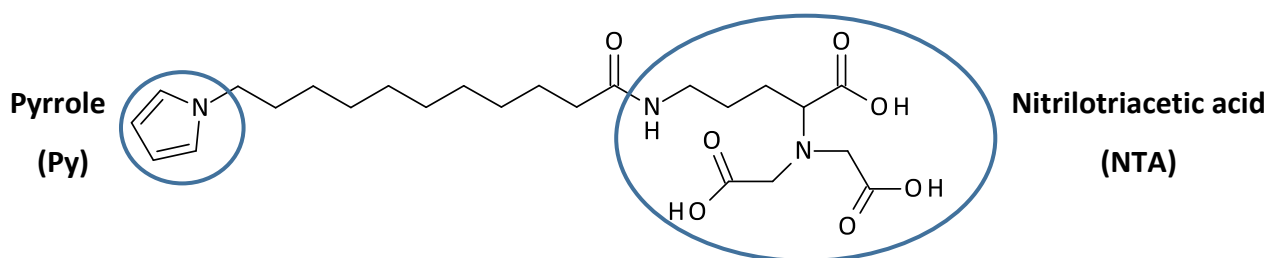


Figure IV-12: Pyrrole-NTA monomer structure

A large percentage of the transducers used in the field of biosensors are composed of conductive and in some cases electroactive polymers. Examples of some of the polymers used in the field of electrochemical biodetection can be found in [24–27]. Among these polymers, polypyrrole has been extensively studied [28–31]. The latter presents a high conductivity, whose values range from 10 - 100 S-cm at room temperature, for a film produced by electrochemical polymerization [32]. The deposition of polypyrrole films on highly conductive electrodes is generally performed by electropolymerization, through the electrochemical activation of the pyrrole monomer, in order to carry out its polymerization by oxidative electrolysis [33,34]. This technique enables to obtain highly reproducible and stable films.

Regarding the use of electropolymerized polypyrrole-NTA in the field of biosensors, several works have demonstrated its good performance as a platform for the immobilization of bioreceptors. This is due to the NTA chelator which allows to coordinate bivalent metal cations such as  $\text{Cu}^{2+}$ ,  $\text{Ni}^{2+}$ ,  $\text{Zn}^{2+}$  or  $\text{Co}^{2+}$ , leaving free coordination sites of the chelator-metal complex for the ligation of different kinds of bioreceptors, such as polyhistidine or biotin-tagged molecules [34–37]. This polymer has been successfully used in the DCM as bioreceptor immobilization layer in the construction of electrochemical biosensors, being applied for the detection of different targets, such as glucose [34], bisphenol A [38] and the complementary sequence of the HIV-DNA[39].

However, in our case it is not possible to generate the polymer film by electropolymerization, since the Si NWs covering the glassy carbon electrode are not metallic, but exhibit semiconducting

properties (doping level of about  $10^{16}$  at·cm<sup>-3</sup>). Additionally, they are covered by a SiO<sub>2</sub> native oxide layer, which reduces the conduction between the Si NWs. The glassy carbon, on the contrary, is a good electrical conductor. Under these conditions, if an electropolymerization process is carried out on the C/Si nanonet-based electrodes, the deposition of the polymer film would occur mainly on the conductive surface (glassy carbon), and not on the Si nanonet, which is the base material of this project.

Due to the previously mentioned reason, we explored the possibility of carrying out a chemical deposition of the polypyrrole-NTA film on the C/Si nanonet-based electrodes. A few studies in the literature report the chemical deposition of polypyrrole films on glass substrates. E. Pigois-Landereau et *al.* reported the deposition of polypyrrole films on surface-modified glasses by means of different treatments, obtaining variable results according to the surface modifications used [40]. In our particular case, it is preferable to avoid surface treatments on the electrode surface, because they could generate a degradation of its electrochemical properties. Likewise, C. Perruchot et *al.* studied the chemical deposition of thin polypyrrole films on untreated and silane-treated planar glass plates. They concluded that through chemical deposition it is possible to obtain a polypyrrole film on glass plates without previous surface treatment, which was corroborated by XPS and SEM analyses, showing wrinkled layers covering the surface of the untreated glass plates [41]. Thus, this information suggests that the chemical deposition of a layer of polypyrrole-NTA on the Si nanonet modified carbon electrodes, and the subsequent immobilization of the TBA-15 bioreceptor could be possible.

### IV.2.3.1. Poly(pyrrole-NTA) film fabrication processes

As in this case an additional structure will be added to the working electrode (polymeric film), it was decided to reduce the density of the Si nanonet, seeking to obtain a structure that is not too thick and compact, allowing the proper flow of the ionic species to the conductive surface (glassy carbon) to carry out the electrochemical reaction. In this context, the optimization of the polypyrrole-NTA film chemical deposition process was studied on carbon electrodes covered by

a Si nanonet with a density equivalent to  $199 \times 10^6 \text{ NWs}\cdot\text{cm}^{-2}$ , which corresponds to a surface coverage of about 54%.

The objective was to develop a technique which allows to deposit a polypyrrole-NTA film that covers the entire surface of the electrode, namely both, the Si nanonet and the spaces on the surface of the carbon that are not covered by the latter. In addition, it is essential that the deposited film fits the nanonet structure, and it should be thin enough to preserve the porous shape of the electrode, provided by the addition of the Si nanonet. For this purpose, two different deposition approaches were studied.

### **IV.2.3.1.1. Polypyrrole-NTA film fabrication by monomer adsorption in liquid conditions followed by chemical polymerization**

The chemical polymerization of the polypyrrole-NTA can be performed by chemical oxidative polymerization, in the presence of different oxidants such as  $\text{FeCl}_3$ ,  $\text{Fe}_2(\text{SO}_4)_3$  or  $\text{K}_2\text{S}_2\text{O}_8$  [42,43].

To our knowledge, the liquid chemical polymerization of polypyrrole films on Si NWs and nanonets structures has not been previously reported in the literature. Preceding studies have shown that pyrrole monomer can be adsorbed on both,  $\text{SiO}_2$  and carbon surfaces. In 1980, Scokart and Rouxhet studied the interactions between several oxides and the pyrrole monomer, and demonstrated through infrared spectroscopy the development of a broad band at low frequency ( $3550 \text{ cm}^{-1}$ ) due to H-bond formation between the hydroxyl groups of the  $\text{SiO}_2$  surface and the pyrrole molecules [44]. Besides, Devidas *et al.* studied the adsorption of heterocyclic nitrogenous compounds on granular activated carbon exposing the latter to an aqueous solution of pyrrole and indole. A Brunauer-Emmett-Teller (BET) surface area analysis allowed them to confirm the adsorption of the heterocyclic compounds by observing a decrease in pore volume on the granular carbon after exposure to the solution [45]. Once the monomer is adsorbed on the surface, it should be possible to carry out its chemical polymerization.

The following is the step-by-step process, developed for the polypyrrole-NTA chemical polymerization.

- 1. C/Si nanonet-based electrodes preparation:** Before carrying out polypyrrole-NTA film deposition, the C/Si nanonet electrodes were introduced in a vacuum pump at 40°C for 30 minutes, in order to improve the adherence between the carbon surface and the Si nanonet.
- 2. Surface activation of the C/Si nanonet-based electrode:** For this purpose, the C / Si NN electrodes were exposed to a UV-ozone treatment for 10 minutes, in order to activate the surface of the electrode, leading to the formation of hydroxyl (OH), carbonyl (C=O) or carboxylic acid (C(=O)OH) groups on its surface [46].
- 3. Pyrrole-NTA monomer adsorption in liquid conditions:** In this step, the C/Si NN electrode is immersed for 1 hour in 100 µL of a 5 mM solution of pyrrole-NTA in acetonitrile (C<sub>2</sub>H<sub>3</sub>N), which was acidified by the addition of perchloric acid (HClO<sub>4</sub>) to enable the solubilization of the monomer. The system comprising the electrode and the container holding the solution is hermetically sealed, in order to prevent the evaporation of the latter. After 1 hour of exposure to the pyrrole-NTA solution, the electrode is carefully washed for 10 min and under stirring (150 rpm), in a phosphate buffer solution at pH 7, in order to remove the excess pyrrole that was not adsorbed on the surface of the electrode.
- 4. Polypyrrole-NTA chemical oxidative polymerization:** In our case, the polypyrrole-NTA film was synthesized by dehydrogenation and oxidative coupling of the pyrrole-NTA monomer, which was previously adsorbed on the C/Si nanonet surface, by using the ferric chloride (FeCl<sub>3</sub>) as oxidant agent. Since the NTA group does not play any role in the formation of the polymer film, the polymerization reaction is illustrated from the pyrrole molecule (Figure IV-13). This reaction consists of three different stages. First, the pyrrole monomer is oxidized, which leads to the creation of radical cation species (Figure IV-13(a)), followed by the formation of a

pyrrole dimer (Figure IV-13(b)). Finally, the continued polymerization results in the generation of the polypyrrole film (Figure IV-13(c)).

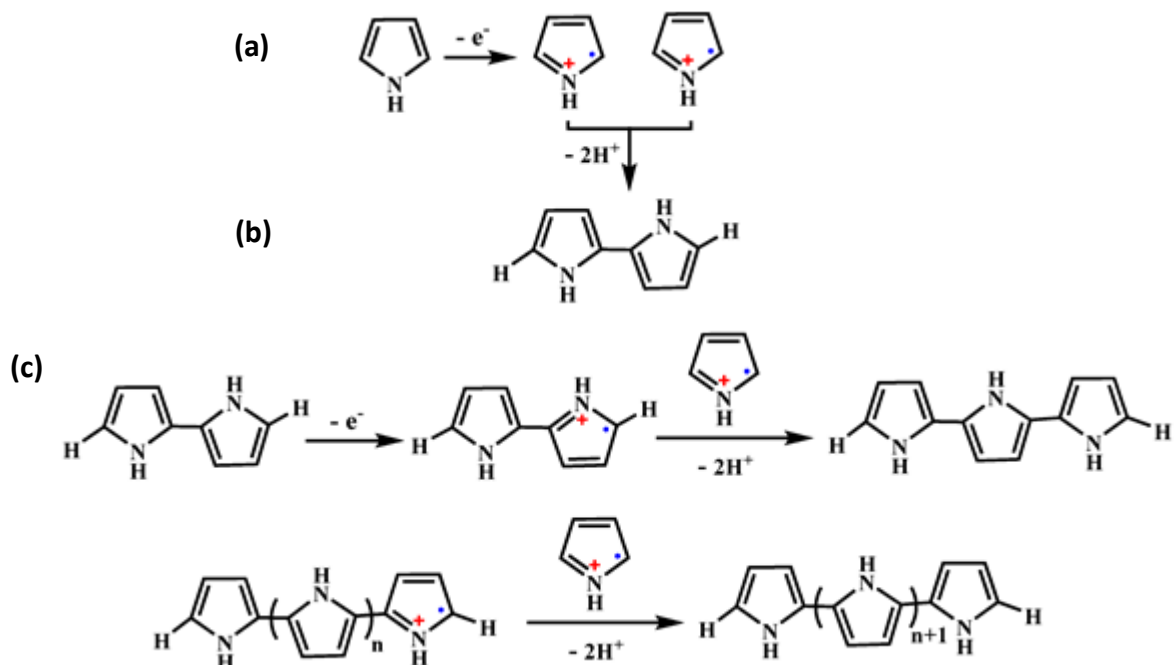


Figure IV-13: Oxidative polymerization of pyrrole to polypyrrole [47].

Thus, the electrode is exposed for 1 hour to a 0.1 M  $\text{FeCl}_3$  in HCl (0.1 M) solution. Subsequently, in order to remove the sections of the polymer film that were not properly attached to the surface, the electrode is rinsed overnight under stirring (150 rpm) in a phosphate buffer solution at pH 7. In order to verify if the polypyrrole-NTA chemical deposition process worked properly, electrochemical studies and Scanning Electron Microscopy (SEM) analyses were carried out.

- **Electrochemical verification of the polypyrrole-NTA film obtained by monomer adsorption in liquid conditions followed by chemical polymerization**

The electrochemical properties of a C/Si nanonet-based electrode before and after carrying out the polypyrrole-NTA chemical deposition process were studied by cyclic voltammetry (Figure IV-14) and electrochemical impedance spectroscopy (Figure IV-15).

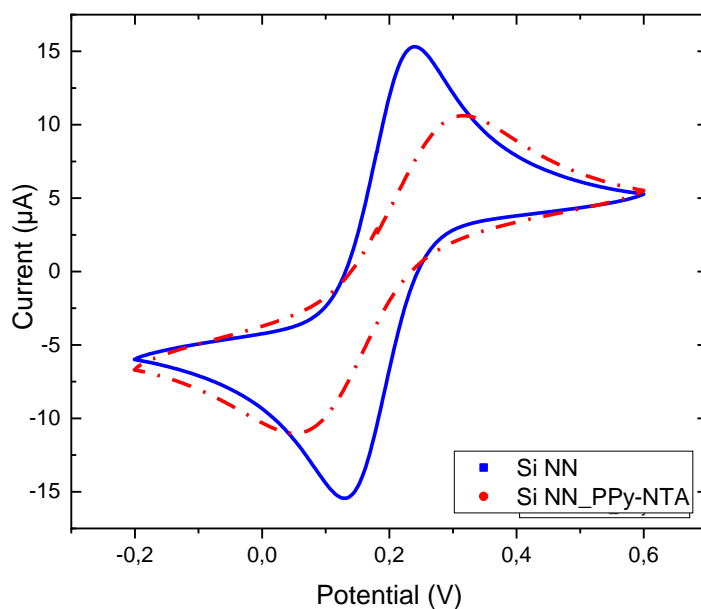


Figure IV-14: Cyclic voltammogram for a C/Si nanonet-based electrode before (Si NN) and after the deposition of the polypyrrole-NTA film (Si NN\_PPy-NTA). The test was carried out using 2 mM  $[Fe(CN)_6]^{3-/4-}$  redox probe in a 0,1 M phosphate buffer solution at pH 7. The voltammograms were recorded at scan rate of 10 mV/s, and the temperature was set at 25 °C.

On the one hand, as can be seen from the voltammogram (Figure IV-14), the electrochemical properties of the C/Si nanonet electrode change significantly after polymerization process, thus confirming its surface modification. The variations of the parameters studied by this technique are summarized in Table IV-6.

As expected, a decrease of the peaks current intensities was observed (40.19% for  $I_{pa}$  and 42.04% for  $I_{pc}$ ), as well as an increase of  $\Delta E_p$ , which may be generated for the electron transfer blocking produced for the deposited polymer.

Table IV-6: Electrochemical parameters obtained by cyclic voltammetry for a C/Si nanonet-based electrode before (Si NN) and after the deposition of the polypyrrole-NTA film (Si NN\_PPy-NTA).

	$I_{pa}$ ( $\mu A$ )	$I_{pc}$ ( $\mu A$ )	$E_{pa}$ (V)	$E_{pc}$ (V)	$\Delta E_p$ (V)
<b>Si NN</b>	16.05	-15.32	0.24	0.14	0.10
<b>Si NN_PPy NTA</b>	9.60	-8.88	0.30	0.07	0.23

On the other hand, EIS analyses confirmed the results obtained by CV. In this case, the significant increase in the radius of the semicircle once the polymerization process is performed, confirms the blocking effect generated on the electrode surface by the polypyrrole-NTA surface modification.

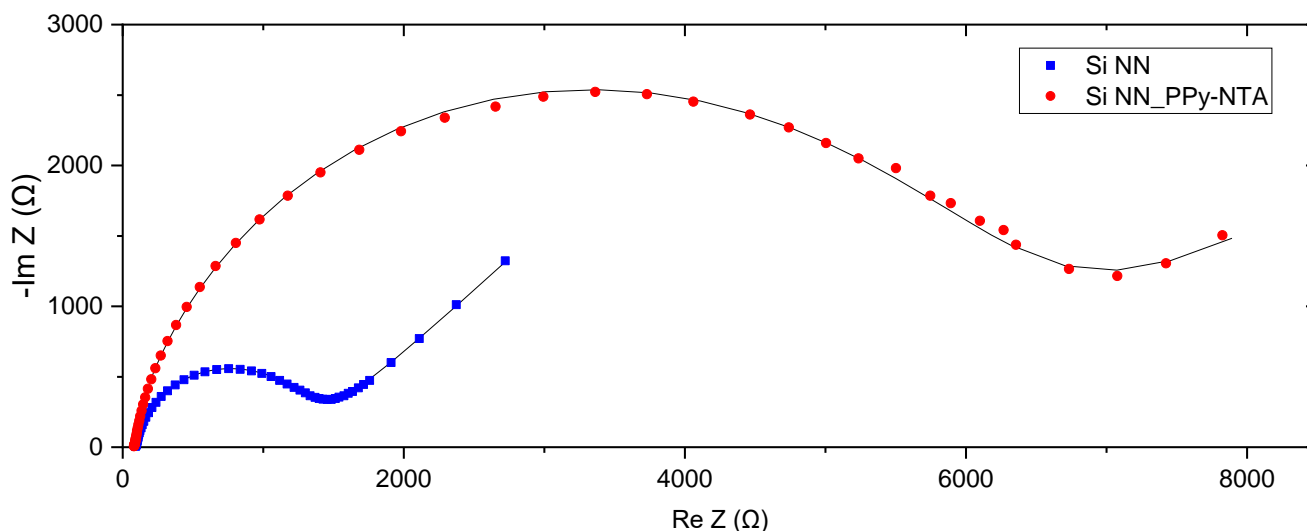


*Figure IV-15: Nyquist plot of impedance spectra obtained for a C/Si nanonet-based electrode before (Si NN) and after the deposition of the polypyrrole-NTA film (Si NN\_PPy-NTA). Dots represent the experimental data and lines represent the fitted data. Measurements performed using 2 mM  $[\text{Fe}(\text{CN})_6]^{3-/4-}$  redox probe in 0.1 M phosphate buffer (pH 7), at 0.18 V vs SCE, with an amplitude of the alternating potential of 10 mV<sub>RMS</sub> and a frequency sweep from 50000 Hz to 0.1 Hz. Dots represent the experimental data and lines represent the fitted data.*

Besides, the results corresponding to the equivalent circuit, obtained by data fitting (Table IV-7) helped to elucidate the phenomena occurring on the electrode after the polypyrrole-NTA deposition. First, as expected, it can be noted an important increase in the transfer charge resistance ( $R_{ct}$ ) of the C/Si NN electrode once the polypyrrole-NTA film was deposited on it. This result can be explained by the blocking effect generated by the polymer, preventing the efficient electron exchange between the electrode surface and the  $[\text{Fe}(\text{CN})_6]^{3-/4-}$  redox probe. As a consequence, the number of redox species reacting at the electrode surface is reduced, resulting in the increase of  $R_{ct}$ .

Concerning the double layer capacitance ( $C_{dl}$ ), it increased after the polymer deposition step. This results certainly indicates that either a decrease of the thickness of the double layer, or an increase of the surface area of the latter took place. In regards to the parameter  $n$ , which is related to the geometry of the semicircle, it was observed a decrease after polypyrrole-NTA deposition, indicating that surface homogeneity was affected after this step. These two decreases, ( $C_{dl}$  and  $n$ ), seem to indicate that it was rather the surface area of the double layer which increased. Indeed, after the polypyrrole-NTA deposition, the double layer was probably placed on the surface of the polymer, whereas previously it was probably located on the carbon surface. Finally, regarding the characteristic frequency ( $f$ ), as expected, an important decrease of this parameter was observed after the surface modification by the polymer film. Indeed,  $f$  is related to the reaction rate: a lower  $f$  value indicates that electrochemical reaction took place more slowly. Thus, the electrochemical species took longer to reach the electrode surface once the polypyrrole-NTA film was deposited, due to the blocking effect generated by the latter.

*Table IV-7 Values of the equivalent circuit elements ( $R_{ct}$ ,  $C_{dl}$ ,  $n$  and  $f$ ), obtained by data fitting for a C/Si nanonet-based electrode before (Si NN) and after the deposition of the polypyrrole-NTA film (Si NN\_PPy-NTA).*

	$R_{ct}$ ( $\Omega$ )	$C_{dl}$ ( $\mu F$ )	$n$	$f$ (Hz)
<b>Si NN</b>	1220 $\pm$ 20	1,89 $\pm$ 0.03	0.9 $\pm$ 0.01	69.2
<b>Si NN_PPy-NTA</b>	5800 $\pm$ 90	2.58 $\pm$ 0.04	0.86 $\pm$ 0.01	10.6

- **Scanning Electron Microscopy (SEM) characterization of the polypyrrole-NTA film obtained by monomer adsorption in liquid conditions followed by chemical polymerization**

SEM analyses were carried out in order to visualize the changes in the morphology and microstructure of the electrode after the polymerization process, and the characteristics of the deposited polypyrrole-NTA film. Analyses were performed on two types of substrates: first, on carbon electrodes (without Si nanonet), to observe the surface morphology of the parts of the electrode that would not be covered by the nanonet, and second, on C/Si nanonet-based electrodes.

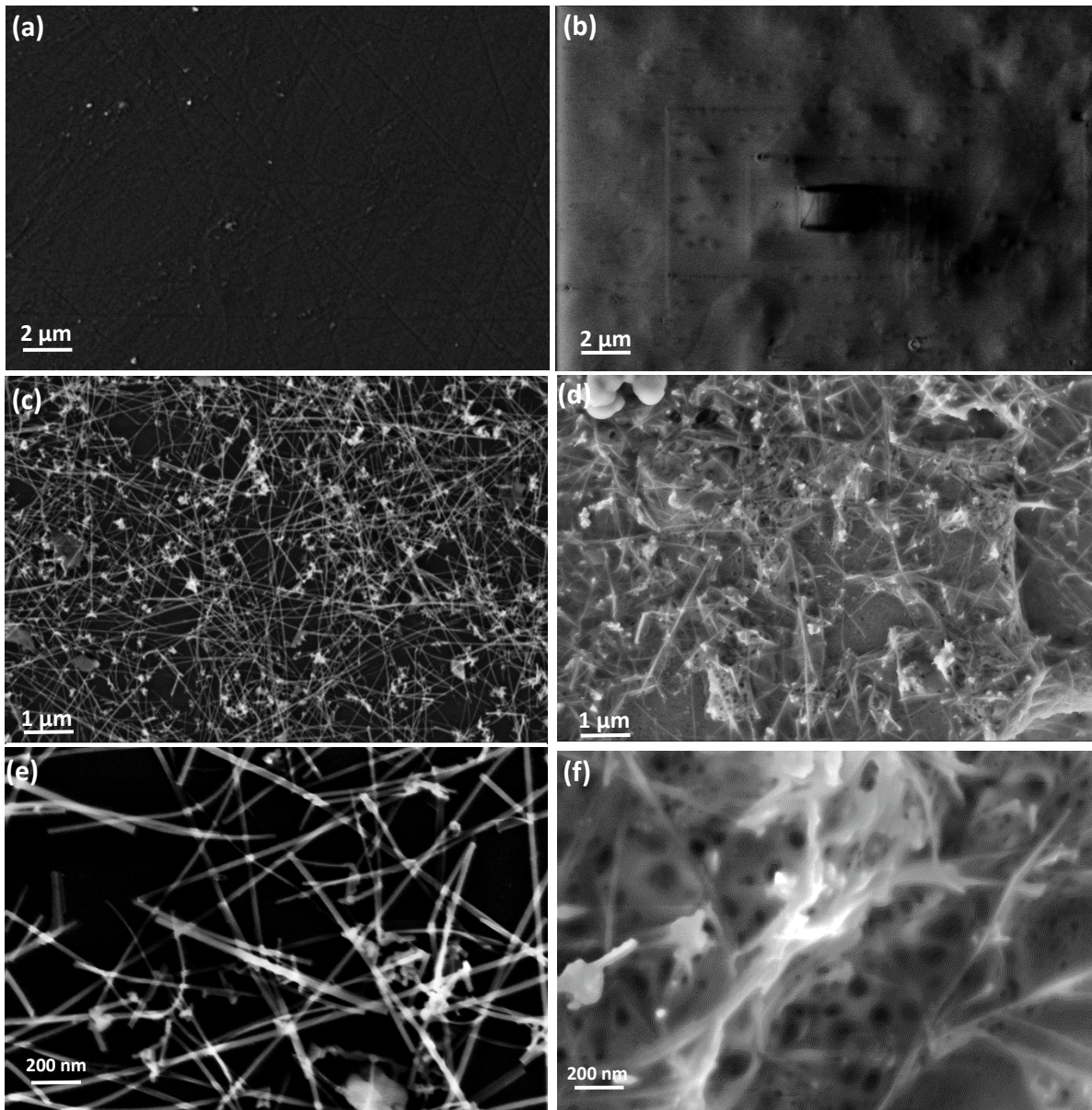


Figure IV-16: SEM images of: (a) C electrode (without Si nanonet). (b) Polypyrrole-NTA modified C electrode. (c) and (e) C/Si nanonet-based electrode before polypyrrole-NTA deposition. (d) and (f) Polypyrrole-NTA modified C/Si nanonet-based electrode. (Si nanonet surface coverage  $\approx$  54%)

The SEM images show a clear difference in the surface morphology for both cases C electrodes and C/Si nanonet-based electrodes- before (Figure IV-16(a),(c) and (e)), and after the polypyrrole-NTA deposition (Figure IV-16(b), (d) and (f)). In the case of the Figure IV-16(b), it is possible to observe several square-shaped marks on the surface of the polypyrrole-NTA modified C

electrode. These marks are the result of the degradation of the polypyrrole-NTA film, generated by the electron beam used to obtain the SEM images, thus confirming the correct deposition of the polymer on the carbon substrate. Furthermore, Figure IV-16(d) and (f) show that deposited film fits the structure of the nanonet, and it is also porous. This last result is very promising, since this type of structure facilitates the passage of the redox probe towards the electrode surface, and at the same time has the advantage of generating a high specific surface, which will lead to a higher amount of bioreceptors that could be grafted onto the surface in the subsequent stages.

### IV.2.3.1.2. Polypyrrole-NTA film fabrication by monomer adsorption in dry conditions followed by electropolymerization

The second polypyrrole-NTA film fabrication method studied consisted of four stages:

- 1. C/Si nanonet-based electrodes preparation:** As in the previous case, the electrodes are introduced in a vacuum pump at 40°C for 30 minutes, in order to eliminate possible solvent residues.
- 2. Surface activation of the C/Si nanonet-based electrode:** C / Si NN electrodes were exposed to a UV-ozone treatment for 10 minutes, in order to activate the surface of the electrode.
- 3. Pyrrole-NTA monomer adsorption in dry conditions:** The C/Si NN electrode is exposed to 10 µL of a 5 mM solution of pyrrole-NTA in C<sub>2</sub>H<sub>3</sub>N + 0.1 M LiClO<sub>4</sub>, acidified by HClO<sub>4</sub>. In this case, the solution is deposited on the electrode and the latter is introduced into a vacuum pump for 30 min at room temperature. The aim is to eliminate the organic solvent, so that only the monomer remains on the surface of the C/Si nanonet-based electrode.
- 4. Polypyrrole-NTA electropolymerization:** Contrary to the previous case where an oxidizing agent was used, here, the polymerization is carried out through the electrochemical activation of the pyrrole monomer by oxidative electrolysis. In conventional electropolymerization

processes, the monomer is dissolved in the electrolyte, and it is electrochemically oxidized on the conductive surface of the electrode. However, as mentioned above, the Si nanonet is not conductive, so the conventional electropolymerization technique would not achieve the deposition of the polymer on the latter. For this reason, the monomer solution was previously evaporated on the C/Si nanonet electrode, so that both, the carbon surface and the Si nanonet are completely covered by it. In this way, the electrochemical oxidation process of the pyrrole-NTA monomers, which here are stuck together along the whole structure after the adsorption process under dry conditions, should be carried out on the assembly, allowing the deposition of the polypyrrole-NTA film on the C/Si nanonet-based electrode.

To accomplish this process, the electroactivity of the pyrrole-NTA monomer was studied (Figure IV-17 (a)). This monomer presents an oxidation peak at 1,09 V, which coincides with the values reported in the literature for pyrrole oxidation (1.05 V - 1.15V) [48–50]. Then, the electropolymerization process was performed by chronoamperometry, applying a constant potential (0.85 vs CSE) during 100s (Figure IV-17(b)). This potential value is located at the beginning of the pyrrole oxidation peak (Figure IV-17(a)), thus ensuring the electropolymerization process, while limiting the overoxidation phenomenon.

Figure IV-17(b) represents the chronoamperogram recorded during electropolymerization process. It shows a decrease in obtained current as the exposure time to the constant potential increases, indicating a progressive electropolymerization of the polypyrrole-NTA film on the carbon electrode surface, which is completed at about 70 s, where the current has practically disappeared.

The obtained polypyrrole-NTA film was characterized by electrochemical and Scanning Electron Microscopy (SEM) analyses.

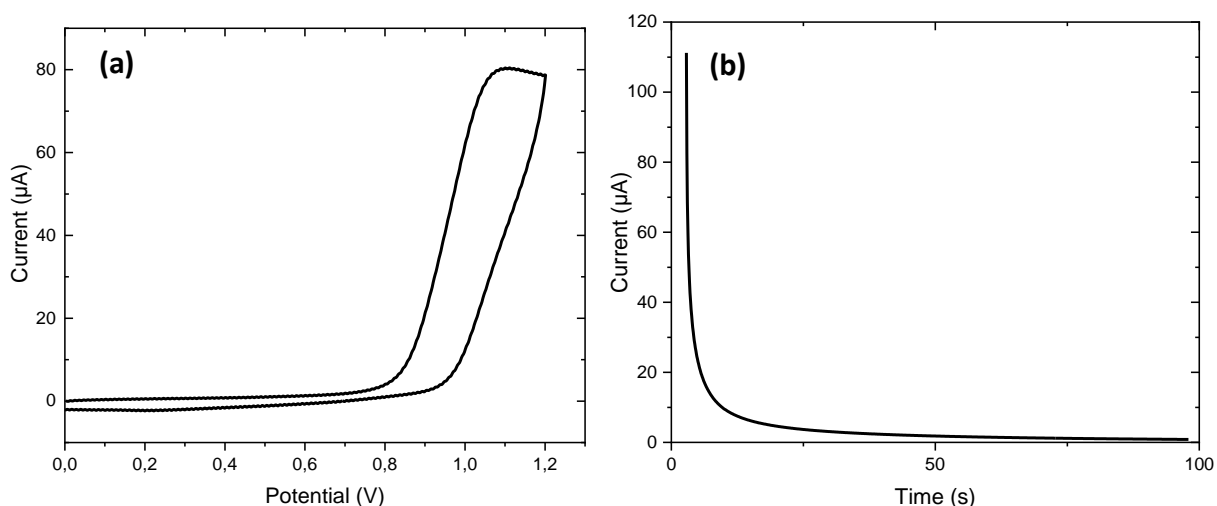


Figure IV-17: (a) Cyclic voltammogram of a 5 mM pyrrole-NTA in  $\text{CH}_3\text{CN} + 0.1 \text{ M LiClO}_4/\text{HClO}_4$  solution. The test was carried on a C electrode, and the voltammogram was recorded at scan rate of 100 mV/s. (b) Chronoamperogram obtained for the electropolymerization of the polypyrrole-NTA film on a C electrode, after pyrrole-NTA monomer adsorption in dry conditions. For both tests the temperature was set at 25 °C.

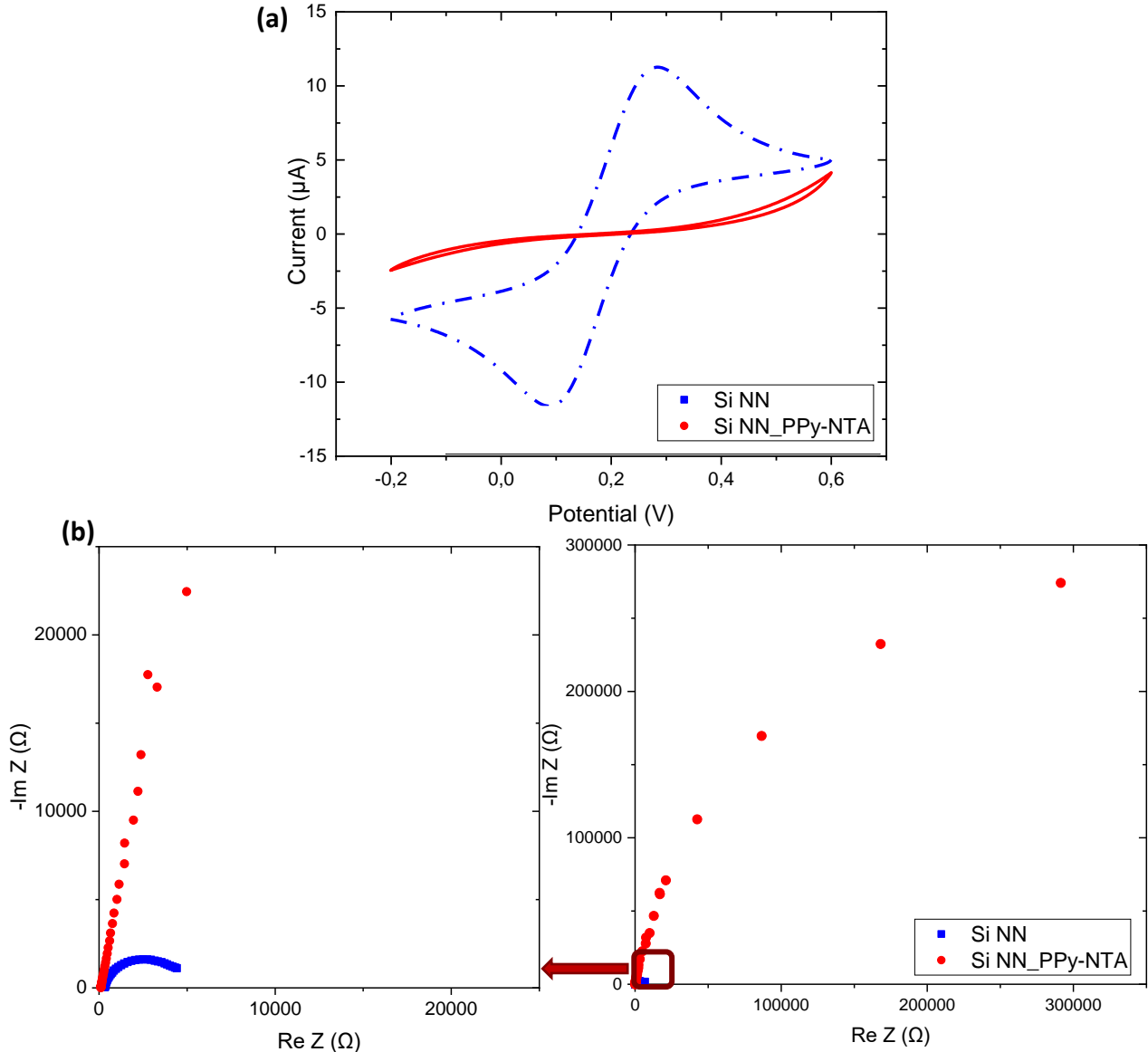
- **Electrochemical verification of the polypyrrole-NTA film obtained by monomer adsorption in dry conditions followed by electropolymerization**

The electrochemical properties of a C/Si nanonet-based electrode before and after the polypyrrole-NTA film deposition by monomer adsorption in dry conditions followed by electropolymerization were studied by cyclic voltammetry and electrochemical impedance spectroscopy. As can be seen in both the voltammograms and impedance spectra obtained, the surface of the Si nanonet-based electrode becomes completely insulating after the film deposition process, which is reflected in the impossibility of observing the electrochemical reaction by both methods. This is probably caused by the formation of a very thick and compact polypyrrole-NTA film, resulting in an overly resistive electrode.

- **Scanning Electron Microscopy (SEM) characterization of the polypyrrole-NTA film obtained by monomer adsorption in dry conditions followed by electropolymerization**

As can be seen in the figure, the SEM analysis showed a deposited film completely different from the one obtained by the previous technique (monomer adsorption in liquid conditions followed by chemical polymerization). Herein, the film does not fit the Si nanonet structure, and creates a

thick and compact layer covering the whole electrode. Additionally, there is no evidence of a porous structure, which is very important, since it generates a permeable interface, which would allow the passage of the redox probe towards the conductive surface of the C/Si nanonet-based



electrode.

Figure IV-18: Electrochemical characterization of the Si nanonet-based electrode before (Si NN) and after the polypyrrole-NTA film deposition (Si NN-PPy-NTA) by monomer adsorption in dry conditions followed by electropolymerization. (a) Cyclic voltammogram recorded at scan rate of 10 mV/s. (b) Nyquist plot of impedance spectra performed at 0.18 V vs SCE, with an amplitude of the alternating potential of 10 mV<sub>RMS</sub> and a frequency sweep from 50000 Hz to 0.1 Hz. Both measurements were carried out using 2 mM [Fe(CN)<sub>6</sub>]<sup>3-/4-</sup> redox probe in a 0.1 M phosphate buffer solution (pH 7) at 25 °C.

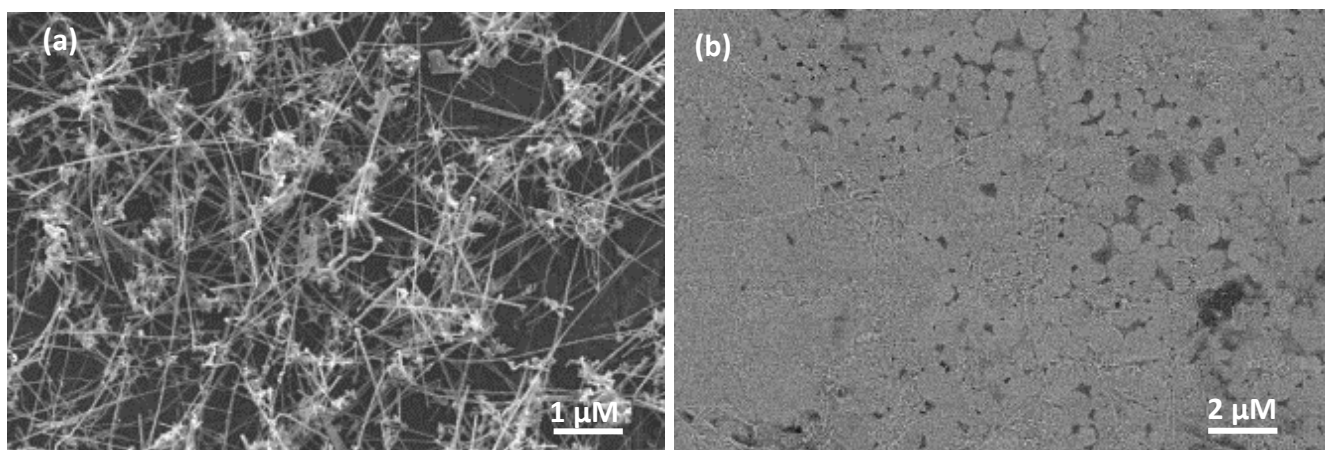


Figure IV-19: SEM images corresponding to: (a) C/Si nanonet-based electrode (b) C/Si nanonet-based electrode after polypyrrole-NTA modification by monomer adsorption in dry conditions followed by electropolymerization. (Si nanonet surface coverage  $\approx$  54%)

These last results allowed us to conclude that this type of polypyrrole-NTA film deposition is not suitable for the biosensor construction. Therefore, the next steps were investigated on C/Si nanonet electrodes whose surface was modified with polypyrrole-NTA films obtained by monomer adsorption in liquid conditions followed by chemical polymerization.

### IV.2.3.2. Immobilization of the biotin labelled bioreceptor (TBA-15 aptamer)

The immobilization of biotin labelled TBA-15 on a polypyrrole-NTA modified C/S nanonet-based electrode is carried out in two steps: the first one is the NTA-Cu<sup>2+</sup> complexation, and the second one is the coordination of the biotin groups on the NTA-Cu<sup>2+</sup> complex. Both steps will be detailed below.

#### IV.2.3.2.1. Nitrilotriacetic acid (NTA)-Cu<sup>2+</sup> interaction

The nitrilotriacetic acid (NTA) is a molecule able to interact with Me<sup>2+</sup> metal ions (Cu<sup>2+</sup>, Ni<sup>2+</sup>, Zn<sup>2+</sup>, Co<sup>2+</sup>, etc.). The binding mechanism involved in this interaction is called chelation. Herein, two or more groups of a molecule bond to the same metal atom conforming a ring structure. Nitrilotriacetic acid is therefore a quadridentate chelator, meaning that it forms four bonds. It strongly complexes copper. Once complexed, it keeps two vacant (accessible) sites that can be occupied either by water molecules or by other ligands [50].

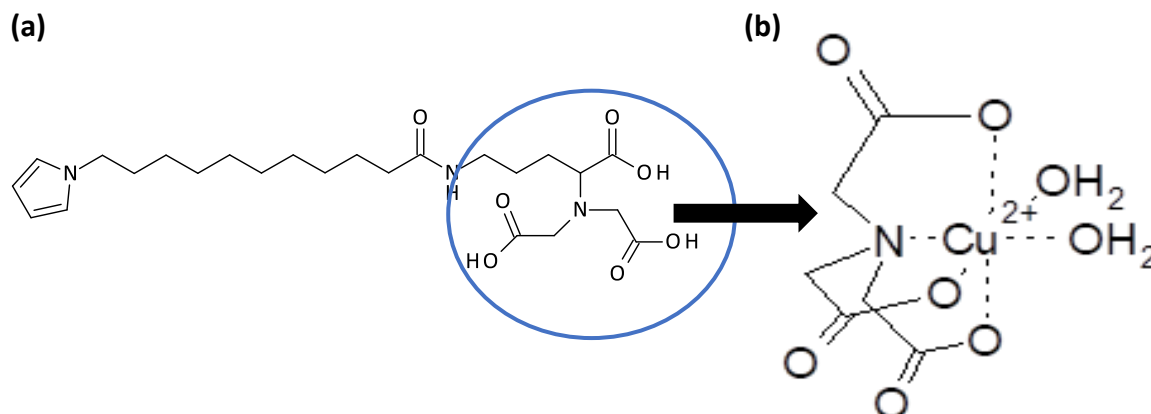


Figure IV-20: (a) Pyrrole-NTA monomer (b) schematic representation of the NTA/Cu<sup>2+</sup> complex. Here, the bonding capacity of the Cu<sup>2+</sup> ion is completed by water molecules.

To achieve this complexation process, the polypyrrole-NTA modified C/Si nanonet-based electrode was immersed for 20 min in a 0.01 M copper chloride (CuCl<sub>2</sub>) solution in acetate buffer (0.1 M) at pH 4.8. The electrode was then subjected to different rinsing processes under stirring (150 rpm). First in a 0.5 M sodium chloride (NaCl) solution for 5 minutes, followed by a rinsing in phosphate buffer solution at pH 7 during 5 minutes.

An electrochemical analysis carried out by voltammetry confirmed the success of the chelation process (Figure IV-21). First, an electrolysis at -0.9 V was carried out for 40 s, with the aim of generating a reduction of copper atoms to Cu<sup>0</sup>. This procedure was followed by a potential scan from -0.9 V to 0.5 V, inducing the appearance of a peak at -0.028 V, followed by a second peak at 0.064 V (Figure IV-21 (b)). These peaks correspond respectively to the oxidation of Cu<sup>0</sup> to Cu<sup>+</sup> and Cu<sup>+</sup> to Cu<sup>2+</sup>. Furthermore, Figure IV-21(a) shows the polypyrrole-NTA modified C/Si nanonet electrode before exposure to the CuCl<sub>2</sub> solution. As expected, in that case, the peaks corresponding to copper did not appear during CV analysis.

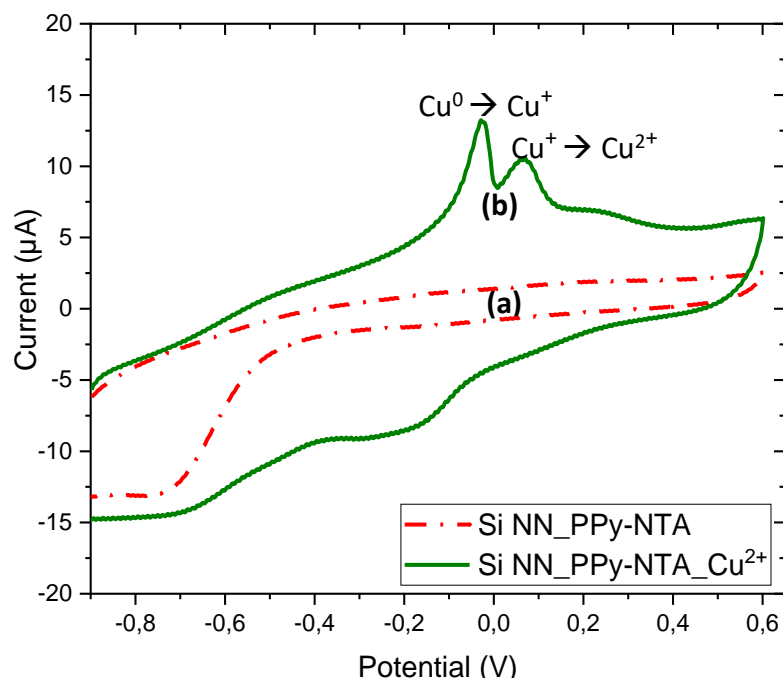


Figure IV-21: Cyclic voltammogram of a Polypyrrole-NTA modified C/Si NN/PPy-NTA electrode (a) before and (b) after  $\text{Cu}^{2+}$  complexation. Analysis performed in 0.1 M acetate buffer (pH 4.8) at scan rate of 100 mV/s.

On the other hand, the effect of this step on the electrochemical properties of polypyrrol-NTA modified C/Si nanonet electrode was also studied. As can be seen from the obtained voltammogram (Figure IV-22), the electrochemical properties of the polypyrrole modified C/Si nanonet electrode change significantly after the  $\text{Cu}^{2+}$  complexation process. These changes are summarized in Table IV-8.

Table IV-8: Electrochemical parameters obtained by CV for a C/Si NN/PPy-NTA electrode before (Si NN\_PPy) and after  $\text{Cu}^{2+}$  complexation (Si NN\_PPy\_  $\text{Cu}^{2+}$ )

	$I_{pa}$ ( $\mu\text{A}$ )	$I_{pc}$ ( $\mu\text{A}$ )	$E_{pa}$ (V)	$E_{pc}$ (V)	$\Delta E_p$ (V)
Si NN_PPy NTA	9.60	-8.88	0.30	0.07	0.23
Si NN_PPy NTA_ $\text{Cu}^{2+}$	13.71	-11.43	0.26	0.11	0.15

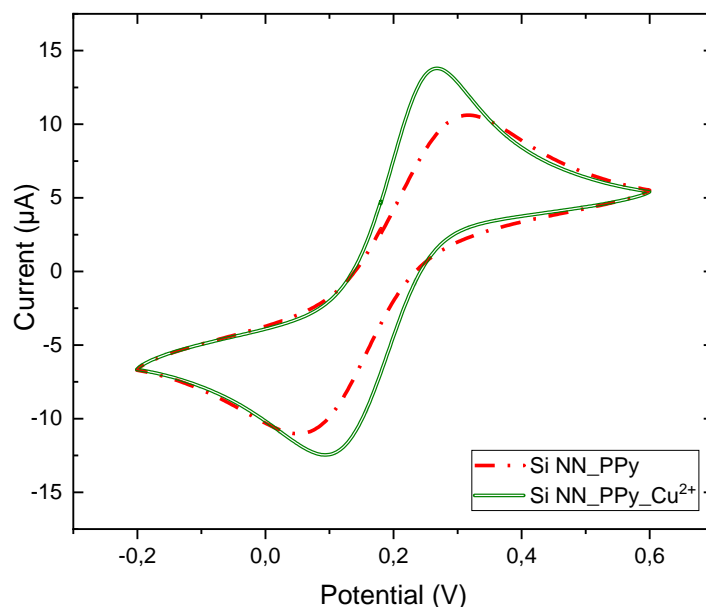


Figure IV-22: Cyclic voltammogram of a polypyrrole-NTA modified C/Si NN/PPy-NTA electrode before (Si NN\_PPy-NTA) and after the  $\text{Cu}^{2+}$  complexation step (Si NN\_PPy-NTA\_  $\text{Cu}^{2+}$ ). Test carried out using 2 mM  $[\text{Fe}(\text{CN})_6]^{3-/4-}$  redox probe in a 0.1 M phosphate buffer solution at pH 7. Voltammograms recorded at scan rate of 10 mV/s, and temperature set at 25 °C.

On this occasion, an increase in the intensity of both current peaks is observed (42.81% for  $I_{pa}$  and 28.72% for  $I_{pc}$ ), as well as an decrease of  $\Delta E_p$ , meaning that the electron transfer is faster after the  $\text{Cu}^{2+}$  complexation step. This result is probably caused by an electrostatic attraction between the negative charges of the redox probe ( $[\text{Fe}(\text{CN})_6]^{3-/4-}$ ), which were attracted by the positive charges brought by the  $\text{Cu}^{2+}$ , thus facilitating its passage through the electrode structure towards the conductive surface.

This result is coherent with the one obtained by impedance spectroscopy (Figure IV-23) and data fitting (Table IV-9). Figure IV-23 shows a significant decrease in the radius of the semicircle after the  $\text{Cu}^{2+}$  complexation step. This results confirms the improvement in the ionic exchange at the electrode surface, generated by the electrostatic attractive interactions between the  $\text{Cu}^{2+}$  and the negatively charged redox probe. At the same time, this explains the important decrease in the transfer charge resistance after the  $\text{Cu}^{2+}$  complexation step (Table IV-9).

With regard to the other parameters studied, it can be noted that the double layer capacitance decreased after the metallic complexation step. Here, it can be assumed that the charges added by the chelation of the  $\text{Cu}^{2+}$  ions on the electrode surface modified the structure of the double layer, resulting in an increase of its thickness. Regarding the  $n$  parameter, it can be considered that it remained stable after the  $\text{Cu}^{2+}$  step, indicating that the homogeneity of the electrode surface was not affected between the steps. Finally, the results obtained for the characteristic frequency showed that, as expected, the electrons reached the electrode surface faster once the  $\text{Cu}^{2+}$  was present on the electrode surface.

Table IV-9: Values of the equivalent circuit elements ( $R_{ct}$ ,  $C_{dl}$ ,  $n$  and  $f$ ), obtained by data fitting for a C/Si NN/PPy-NTA electrode before (Si NN) and after the deposition of the polypyrrole-NTA film (Si NN\_PPpy-NTA).

	$R_{ct}$ ( $\Omega$ )	$C_{dl}$ ( $\mu\text{F}$ )	$n$	$f$ (Hz)
Si NN_PPpy-NTA	$5800 \pm 90$	$2.58 \pm 0.04$	$0.86 \pm 0.01$	10.6
Si NN_PPpy-NTA_ $\text{Cu}^{2+}$	$3170 \pm 50$	$2.16 \pm 0.03$	$0.88 \pm 0.01$	23.3

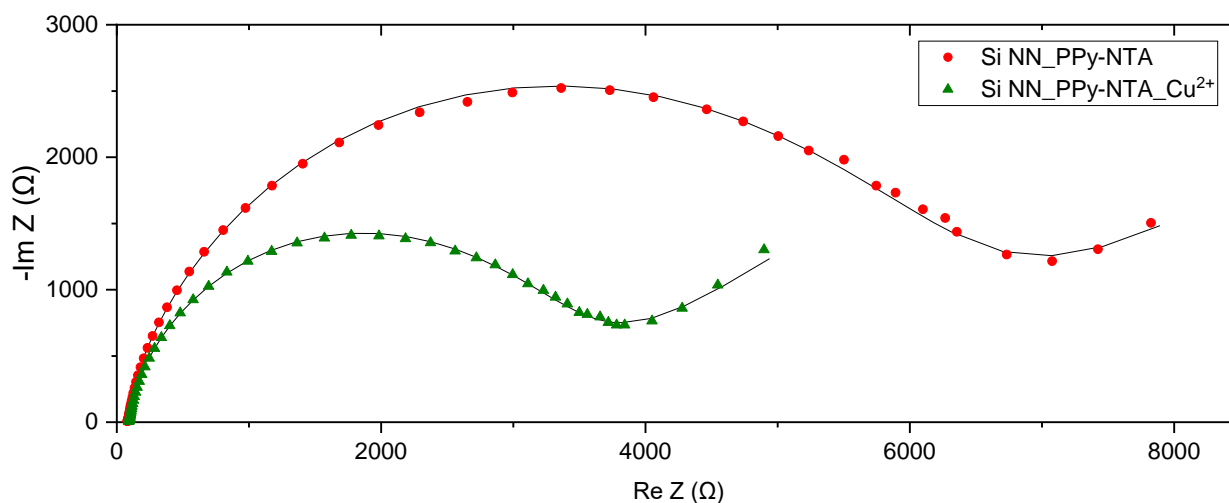


Figure IV-23: Nyquist plot of impedance spectra of a polypyrrole-NTA modified C/Si nanonet-based electrode before (Si NN-PPy-NTA) and after the  $\text{Cu}^{2+}$  complexation step (Si NN-PPy-NTA\_  $\text{Cu}^{2+}$ ). Dots represent the experimental data and lines represent the fitted data. Test carried out using 2 mM  $[\text{Fe}(\text{CN})_6]^{3-/4-}$  redox probe in 0.1 M phosphate buffer solution (pH 7), at 0.18 V vs SCE, with an amplitude of the alternating potential of 10 mV<sub>RMS</sub> and a frequency sweep from 50000 Hz to 0.1 Hz. Temperature set at 25°C

### IV.2.3.2.2. $\text{Cu}^{2+}$ -biotin interaction

In the late 1970s Sigel *et al* demonstrated that a coordination bond can be established between a biotin and metal ions such as  $\text{Mn}^{2+}$ ,  $\text{Cu}^{2+}$  and  $\text{Zn}^{2+}$ . Moreover, these authors suggested that the interaction with these divalent metal ions would involve the sulfur atom of biotin (Figure IV-24) [51]. About a decade ago, in the DCM, this strategy was used for the first time in the field of biosensors. During her thesis work, Jessica Baur achieved the immobilization of biotinylated macromolecules onto electropolymerized polypyrrole-NTA- $\text{Cu}^{2+}$  films, which were used for the glucose and DNA hybridization detection [34,52].

As previously mentioned, once nitrilotriacetic acid is complexed with  $\text{Cu}^{2+}$ , it keeps two vacant sites that in this case will be occupied by the biotinylated TBA-15 bioreceptor. The whole immobilization strategy is schematized in Figure IV-24.

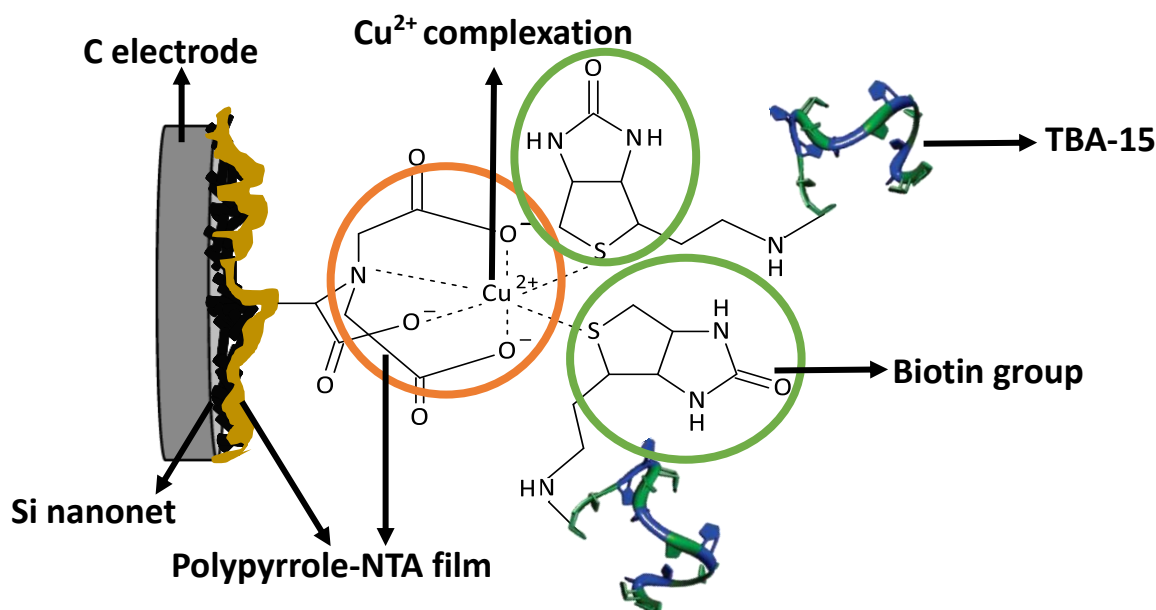


Figure IV-24: Schematic representation of the polypyrrole-NTA/ $\text{Cu}^{2+}$ /biotin immobilization strategy on C/Si nanonet-based electrodes.

Thus, the bioreceptor immobilization was carried out by exposing the C/Si nanonet/ $\text{Cu}^{2+}$  electrode to 100  $\mu\text{L}$  of 50  $\mu\text{M}$  TBA-15 solution in phosphate buffer at pH7, during 45 min. Before use, the TBA-15 solution was heated at 90  $^{\circ}\text{C}$  for 3 min, and was then cooled by immersion into

an ice bath, in order to obtain a proper folding structure [53]. Subsequently, the electrode was rinsed for 10 min (under stirring at 150 rpm) in a phosphate buffer solution at pH 7, to remove the TBA-15 probes that were not properly grafted to the electrode surface.

The results of the electrochemical characterization of this step are shown in Figure IV-25(a) and (b). On the one hand, it would be expected a decrease in current peaks, due to the steric effect induced by the grafted bioreceptor (TBA-15). However, the cyclic voltammetry technique was not sufficiently sensitive to detect this change (Figure IV-25 (a)). On the other hand, as observed in the impedance spectra (Figure IV-25 (b)), the obtained results showed a behavior opposite to the one expected, since there was a decrease in the radius of the semicircle, as well as a decrease in  $R_{ct}$  (from  $3170 \pm 50 \Omega$  to  $2871 \pm 40 \Omega$ ).

This analysis was carried out on 6 different biofunctionalized Si nanonet-based electrodes. In all cases a decrease in the impedance was observed after the TBA-15 immobilization step. Then, a stability analysis of the biofunctionalized electrodes was carried out, performing several measurements by cyclic voltammetry and electrochemical impedance spectroscopy over 24 h. The results of the study (not shown here) revealed that the electrochemical properties of the biofunctionalized Si nanonet-based electrodes remained stable.

One hypothesis that could explain the decrease in the impedance after the bioreceptor grafting step would be that the immobilization of the TBA-15 on the polypyrrole-NTA film generates a change in the morphology of the latter. This would lead to the creation of new sites through which the redox probe can diffuse towards the surface of the electrode, thus improving its permeability. Although at the moment we do not have any evidence to support this hypothesis, in future works it could be possible to perform microstructural analyses (such as by Atomic Force Microscopy (AFM)), in order to verify if the TBA-15 immobilization generates modifications in the polypyrrole-NTA film.

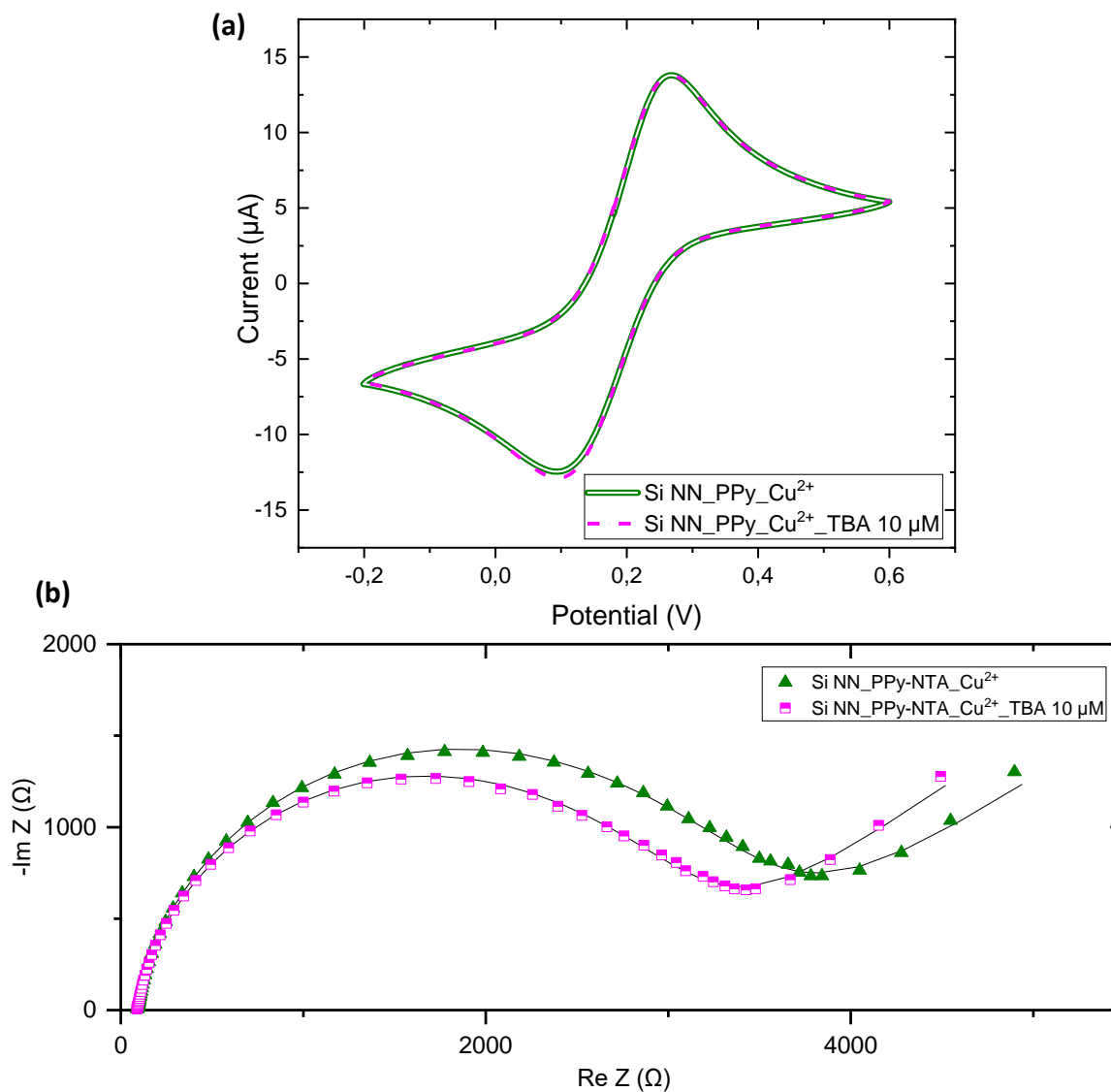


Figure IV-25: Electrochemical characterization of the C<sub>Si NN\_PPy-NTA\_Cu<sup>2+</sup></sub> electrode before and after the TBA-15 immobilization. (a) Cyclic voltammogram recorded at scan rate of 10 mV/s. (b) Nyquist plot of impedance spectra performed at 0.18 V vs SCE, with an amplitude of the alternating potential of 10 mV<sub>RMS</sub> and a frequency sweep from 50 000 Hz to 0.1 Hz. Dots represent the experimental data and lines represent the fitted data. Both measurements were carried out using 2 mM [Fe(CN)<sub>6</sub>]<sup>3-/4-</sup> redox probe in a 0.1 M phosphate buffer solution (pH 7), at 25 °C.

Besides, as will be detailed in the next chapter, the built electrode is capable of detecting thrombin. This, in combination with the selectivity analysis of the biosensor (which will also be shown latter), are indicators of an adequate immobilization of the TBA-15 bioreceptor on the C/Si NN/PPy/Cu<sup>2+</sup> electrode.

### IV.3. Conclusions

Throughout this chapter we explored two different approaches for the development of Si nanonet-based electrodes, to be used as electrochemical biosensors. In the first approach, it was studied the feasibility of building the Si nanonet-based electrode on gold substrates. When studying the possibilities for the biofunctionalization of the Au/Si nanonet-based electrode, it was found that it could be carried out using the GOPS protocol previously studied, since this process did not significantly affect the electrochemical properties of the Au substrate contrarily to APTES protocol. However, when stability studies were carried out, it was found that the electrochemical properties of the Au/Si nanonet-based electrode were not stable over time, due to a problem of delimitation of the active surface, which increased as the measurements were performed. Indeed, an electrolyte infiltration under the insulating tape occurred as the measurements were performed.

This problem led us to explore a second approach for the fabrication of Si nanonet-based electrodes. In this case, commercial glassy carbon electrodes were used as base material, acting as support for the Si nanonet, without the need of delimiting the active area. On this type of electrodes, the active surface is previously delimited, eliminating the aforementioned problem. Here, a new protocol for the biofunctionalization of the C/Si nanonet based electrodes was developed. The method established consisted in the deposition of a Polypyrrole-NTA film on the C/Si nanonet-based electrode. It was carried out by chemical polymerization. We found that this polypyrrole-NTA film is porous and fits the structure of the nanonet, thus facilitating the passage of the redox probe towards the electrode surface. In turn, this film was used as a platform for the immobilization of the TBA-15 bioreceptor, by means of NTA-  $\text{Cu}^{2+}$  ions complexation, which later enabled the immobilization of the biotinylated TBA-15, by coordination of the biotin groups on the NTA- $\text{Cu}^{2+}$  complex.

At this point it was considered that the Si nanonet-based electrode was ready to be evaluated in terms of its ability to detect its target molecule, namely the thrombin. Those results will be presented in the next chapter.

# References

- [1] E. Barsoukov, J.R. Macdonald, Impedance Spectroscopy. Theory, Experiment and applications, John Wiley & Sons, 2018. <https://doi.org/10.1021/bk-1989-0396.ch036>.
- [2] J.S. Daniels, N. Pourmand, Label-free impedance biosensors: Opportunities and challenges, *Electroanalysis*. 19 (2007) 1239–1257. <https://doi.org/10.1002/elan.200603855>.
- [3] Y. Gönüllü, K. Kelm, S. Mathur, B. Saruhan, Equivalent circuit models for determination of the relation between the sensing behavior and properties of undoped/Cr doped TiO<sub>2</sub> NTs, *Chemosensors*. 2 (2014) 69–84. <https://doi.org/10.3390/chemosensors2010069>.
- [4] M.E. Orazem, N. Pébère, B. Tribollet, Enhanced Graphical Representation of Electrochemical Impedance Data, *J. Electrochem. Soc.* 153 (2006) B129. <https://doi.org/10.1149/1.2168377>.
- [5] A.A. Moya, Identification of characteristic time constants in the initial dynamic response of electric double layer capacitors from high-frequency electrochemical impedance, *J. Power Sources*. 397 (2018) 124–133. <https://doi.org/10.1016/j.jpowsour.2018.07.015>.
- [6] A. Helmenstibe, What is the most conductive element?, (2020). <https://sciencenotes.org/what-is-the-most-conductive-element/>.
- [7] L.D. Burke, P.F. Nugent, The electrochemistry of gold: I. The redox behaviour of the metal in aqueous media, *Gold Bull.* 30 (1997) 43–53. <https://doi.org/10.1007/BF03214756>.
- [8] P. Jiang, S. Porsgaard, F. Borondics, M. Kober, A. Caballero, H. Bluhm, F. Besenbacher, M. Salmero, Room-temperature reaction of oxygen with gold: An in situ ambient-pressure x-ray photoelectron spectroscopy investigation, *J. Am. Chem. Soc.* 132 (2010) 2858–2859. <https://doi.org/10.1021/ja909987j>.
- [9] B. Hammer, J.K. Norskov, Why gold is the noblest of all the metals, *Nature*. 376 (1995) 238–240.
- [10] A. Hasan, L.M. Pandey, Self-assembled monolayers in biomaterials, in: *Nanobiomaterials Nanostructured Mater. Biomed. Appl.*, Elsevier Ltd., 2018: pp. 137–178. <https://doi.org/10.1016/B978-0-08-100716-7.00007-6>.
- [11] Ç. Sayikli Şimşek, M. Nur Sonuç Karaboğa, M. Kemal Sezgintürk, A new immobilization procedure for development of an electrochemical immunosensor for parathyroid hormone detection based on gold electrodes modified with 6-mercaptophexanol and silane, *Talanta*. 144 (2015) 210–218. <https://doi.org/10.1016/j.talanta.2015.06.010>.
- [12] V. Lavalley, Etude du système hybride constitué par l'ensemble film d'oxyde semi-

- conducteur/oligonucléotides de conformation « hairpin »/nanoparticules d'or, INP Grenoble, 2008.
- [13] E.P. Randviir, C.E. Banks, Electrochemical impedance spectroscopy : an overview of bioanalytical applications, *Anal. Methods.* (2013) 1098–1115. <https://doi.org/10.1039/c3ay26476a>.
- [14] J.E. Baur, Diffusion Coefficients, in: *Handb. Electrochem.*, Elsevier, 2007: pp. 829–848. <http://www.sciencedirect.com/science/article/pii/B9780444519580500367>.
- [15] Y. Wang, J.G. Limon-petersen, R.G. Compton, Measurement of the diffusion coefficients of [Ru(NH<sub>3</sub>)<sub>6</sub>]<sup>3+</sup> and [Ru(NH<sub>3</sub>)<sub>6</sub>]<sup>2+</sup> in aqueous solution using microelectrode double potential step chronoamperometry, *J. Electroanal. Chem.* 652 (2011) 13–17. <https://doi.org/10.1016/j.jelechem.2010.12.011>.
- [16] S.J. Konopka, B. Mcduffie, Diffusion Coefficients of Ferri- and Ferrocyanide Ions in Aqueous Media , Using Twin-Electrode Thin-Layer Electrochemistry, *Anal. Chem.* 42 (1970) 1741–1746. <https://doi.org/10.1021/ac50160a042>.
- [17] P.R. Birkin, S. Silva-Martinez, Determination of heterogeneous electron transfer kinetics in the presence of ultrasound at microelectrodes employing sampled voltammetry, *Anal. Chem.* 69 (1997) 2055–2062. <https://doi.org/10.1021/ac961128v>.
- [18] R.J. Klingler, J.K. Kochi, Electron-transfer kinetics from cyclic voltammetry. Quantitative description of electrochemical reversibility, *J. Phys. Chem.* 85 (1981) 1731–1741. <https://doi.org/10.1021/j150612a028>.
- [19] M. Muzikář, W.R. Fawcett, Use of ac admittance voltammetry to study very fast electron-transfer reactions. The [Ru(NH<sub>3</sub>)<sub>6</sub>]<sup>3+/2+</sup> system in water, *Anal. Chem.* 76 (2004) 3607–3611. <https://doi.org/10.1021/ac0499524>.
- [20] Y. Zhang, Q. Zhang, C. Zhou, Y. Zhou, Mechanical properties of PTFE coated fabrics, *J. Reinf. Plast. Compos.* 29 (2010) 3624–3630. <https://doi.org/10.1177/0731684410378542>.
- [21] M. Berthuel, Microstructuration de surface et protection par encapsulation : applications aux biocapteurs, Université Grenoble Alpes, 2020.
- [22] H.E. Zittel, F.J. Miller, A Glassy-Carbon Electrode for Voltammetry, *Anal. Chem.* 37 (1965) 200–203. <https://doi.org/10.1021/ac60221a006>.
- [23] J.P. Cloarec, C. Chevalier, J. Genest, J. Beauvais, H. Chamas, Y. Chevolot, T. Baron, A. Souifi, PH driven addressing of silicon nanowires onto Si<sub>3</sub>N<sub>4</sub>/SiO<sub>2</sub> micro-patterned surfaces, *Nanotechnology.* 27 (2016). <https://doi.org/10.1088/0957-4484/27/29/295602>.
- [24] B. Piro, J. Haccoun, M.C. Pham, L.D. Tran, A. Rubin, H. Perrot, C. Gabrielli, Study of the DNA

- hybridization transduction behavior of a quinone-containing electroactive polymer by cyclic voltammetry and electrochemical impedance spectroscopy, *J. Electroanal. Chem.* 577 (2005) 155–165. <https://doi.org/10.1016/j.jelechem.2004.12.002>.
- [25] X. Cetó, C.P. Saint, C.W.K. Chow, N.H. Voelcker, B. Prieto-Simón, Electrochemical detection of N-nitrosodimethylamine using a molecular imprinted polymer, *Sensors Actuators, B Chem.* 237 (2016) 613–620. <https://doi.org/10.1016/j.snb.2016.06.136>.
- [26] S. Brahim, A.M. Wilson, D. Narinesingh, E. Iwuoha, A. Guiseppi-Elie, Chemical and Biological Sensors Based on Electrochemical Detection Using Conducting Electroactive Polymers, *Microchim. Acta.* 143 (2003) 123–137. <https://doi.org/10.1007/s00604-003-0065-6>.
- [27] J.A. Ribeiro, C.M. Pereira, A.F. Silva, M.G.F. Sales, Electrochemical detection of cardiac biomarker myoglobin using polyphenol as imprinted polymer receptor, *Anal. Chim. Acta.* 981 (2017) 41–52. <https://doi.org/10.1016/j.aca.2017.05.017>.
- [28] H. Korri-Youssoufi, B. Makrouf, Electrochemical biosensing of DNA hybridization by ferrocenyl groups functionalized polypyrrole, *Anal. Chim. Acta.* 469 (2002) 85–92. [https://doi.org/10.1016/S0003-2670\(02\)00539-1](https://doi.org/10.1016/S0003-2670(02)00539-1).
- [29] C. Tlili, H. Korri-Youssoufi, L. Ponsonnet, C. Martelet, N.J. Jaffrezic-Renault, Electrochemical impedance probing of DNA hybridisation on oligonucleotide-functionalised polypyrrole, *Talanta.* 68 (2005) 131–137. <https://doi.org/10.1016/j.talanta.2005.04.069>.
- [30] T. Livache, A. Roget, E. Dejean, C. Barthet, G. Bidan, R. Teoule, Preparation of a DNA matrix via an electrochemically directed copolymerization of pyrrole and oligonucleotides bearing a pyrrole group, *Nucleic Acids Res.* 22 (1994) 2915–2921. <https://doi.org/10.1093/nar/22.15.2915>.
- [31] W. Hu, C.M. Li, H. Dong, Poly(pyrrole-co-pyrrole propylic acid) film and its application in label-free surface plasmon resonance immunosensors, *Anal. Chim. Acta.* 630 (2008) 67–74. <https://doi.org/10.1016/j.aca.2008.09.059>.
- [32] A. Diaz, Electrochemistry of conducting polypyrrole films, *J. Electroanal. Chem.* 129 (1981) 115–132. [https://doi.org/10.1016/0368-1874\(81\)87387-x](https://doi.org/10.1016/0368-1874(81)87387-x).
- [33] Q. Palomar, Intégration de matériaux nanostructurés dans la conception et la réalisation de biocapteurs sans marquage pour la détection de cibles d'intérêt, Université Grenoble Alpes, 2017.
- [34] J. Baur, M. Holzinger, C. Gondran, S. Cosnier, Immobilization of biotinylated biomolecules onto electropolymerized poly(pyrrole-nitrilotriacetic acid)-Cu<sup>2+</sup> film, *Electrochem. Commun.* 12 (2010) 1287–1290. <https://doi.org/10.1016/j.elecom.2010.07.001>.
- [35] N. Haddour, S. Cosnier, C. Gondran, Electrogenation of a poly(pyrrole)-NTA chelator film for a

- reversible oriented immobilization of histidine-tagged proteins, *J. Am. Chem. Soc.* 127 (2005) 5752–5753. <https://doi.org/10.1021/ja050390v>.
- [36] L. Schmitt, C. Dietrich, R. Tampé, Synthesis and Characterization of Chelator-Lipids for Reversible Immobilization of Engineered Proteins at Self-Assembled Lipid Interfaces, *J. Am. Chem. Soc.* 116 (1994) 8485–8491. <https://doi.org/10.1021/ja00098a008>.
- [37] S.R. Hart, M.D. Waterfield, A.L. Burlingame, R. Cramer, Factors governing the solubilization of phosphopeptides retained on ferric NTA IMAC beads and their analysis by MALDI TOFMS, *J. Am. Soc. Mass Spectrom.* 13 (2002) 1042–1051. [https://doi.org/10.1016/S1044-0305\(02\)00432-4](https://doi.org/10.1016/S1044-0305(02)00432-4).
- [38] I. Kazane, K. Gorgy, C. Gondran, N. Spinelli, A. Zazoua, E. Defrancq, S. Cosnier, Highly Sensitive Bisphenol-A Electrochemical Aptasensor Based on Poly(Pyrrole-Nitrilotriacetic Acid)-Aptamer Film, *Anal. Chem.* 88 (2016) 7268–7273. <https://doi.org/10.1021/acs.analchem.6b01574>.
- [39] J. Baur, C. Gondran, M. Holzinger, E. Defrancq, H. Perrot, S. Cosnier, Label-free femtomolar detection of target DNA by impedimetric DNA sensor based on poly(pyrrole-nitrilotriacetic acid) film, *Anal. Chem.* 82 (2010) 1066–1072. <https://doi.org/10.1021/ac9024329>.
- [40] E. Pigois-Landureau, Y.F. Nicolau, M. Delamar, XPS study of layer-by-layer deposited polypyrrole thin films, *Synth. Met.* 72 (1995) 111–119. [https://doi.org/10.1016/0379-6779\(94\)02336-W](https://doi.org/10.1016/0379-6779(94)02336-W).
- [41] C. Perruchot, M.M. Chehimi, M. Delamar, E. Cabet-Deliry, B. Miksa, S. Slomkowski, M.A. Khan, S.P. Armes, Chemical deposition and characterization of thin polypyrrole films on glass plates: Role of organosilane treatment, *Colloid Polym. Sci.* 278 (2000) 1139–1154. <https://doi.org/10.1007/s003960000372>.
- [42] Y.M. Yasuo Kudoh, Kenji Akami, Properties of chemically prepared polypyrrole with an aqueous solution containing  $\text{Fe}_2(\text{SO}_4)_3$ , a sulfonic surfactant and a phenol derivative, *Synth. Met.* 95 (1998) 191–196.
- [43] J.J. Villora-Picó, V. Belda-Alcázar, M.J. García-Fernández, E. Serrano, A. Sepúlveda-Escribano, M.M. Pastor-Blas, Conducting Polymer-TiO<sub>2</sub> Hybrid Materials: Application in the Removal of Nitrates from Water, *Langmuir.* 35 (2019) 6089–6105. <https://doi.org/10.1021/acs.langmuir.9b00174>.
- [44] P.O. Scokart, P.G. Rouxhet, Characterization of the basicity of oxides through the infrared study of pyrrole adsorption, *J. Chem. Soc. Faraday Trans. 1 Phys. Chem. Condens. Phases.* 76 (1980) 1476–1489. <https://doi.org/10.1039/F19807601476>.
- [45] A.D. Hiwarkar, V. Chandra Srivastava, I.D. Mall, Simultaneous adsorption of nitrogenous heterocyclic compounds by granular activated carbon: Parameter optimization and multicomponent isotherm modeling, *RSC Adv.* 4 (2014) 39732–39742.

- <https://doi.org/10.1039/c4ra06395c>.
- [46] Y. Perets, L. Matzui, L. Vovchenko, I. Ovsienko, O. Yakovenko, O. Lazarenko, A. Zhuravkov, O. Brusylovets, Influence of Ultraviolet/Ozonolysis Treatment of Nanocarbon Filler on the Electrical Resistivity of Epoxy Composites, *Nanoscale Res. Lett.* 11 (2016). <https://doi.org/10.1186/s11671-016-1577-4>.
- [47] M. Wang, Emerging multifunctional NIR photothermal therapy systems based on polypyrrole nanoparticles, *Polymers (Basel)*. 8 (2016). <https://doi.org/10.3390/polym8100373>.
- [48] S. Cosnier, B. Galland, C. Innocent, New electropolymerizable amphiphilic viologens for the immobilization and electrical wiring of a nitrate reductase, *J. Electroanal. Chem.* 433 (1997) 113–119. [https://doi.org/10.1016/S0022-0728\(97\)00207-6](https://doi.org/10.1016/S0022-0728(97)00207-6).
- [49] C. Mousty, B. Galland, S. Cosnier, Electrogeneration of a hydrophilic cross-linked polypyrrole film for enzyme electrode fabrication. Application to the amperometric detection of glucose, *Electroanalysis*. 13 (2001) 186–190. [https://doi.org/10.1002/1521-4109\(200103\)13:3<186::AID-ELAN186>3.0.CO;2-W](https://doi.org/10.1002/1521-4109(200103)13:3<186::AID-ELAN186>3.0.CO;2-W).
- [50] N. Haddour, Réalisation d'assemblages biologiques électroactifs : application aux biocapteurs d'affinité, 2005.
- [51] D. McCormick, L. Wright, H. Sigel, R. Griesser, B. Prijs, Metal ion complexes with biotin and biotin derivatives. Participation of sulfur in the orientation of divalent cations, *Biochemistry*. 8 (1969) 2687–2695.
- [52] J. Baur, Autoassemblage de macromolécules biologiques via des poly(pyrroles) et/ou des nanotubes de carbone fonctionnalisés, Université de Grenoble, 2010.
- [53] H. Xu, K. Gorgy, C. Gondran, A. Le Goff, N. Spinelli, C. Lopez, E. Defrancq, S. Cosnier, Label-free impedimetric thrombin sensor based on poly(pyrrole-nitrilotriacetic acid)-aptamer film, *Biosens. Bioelectron.* 41 (2013) 90–95. <https://doi.org/10.1016/j.bios.2012.07.044>.

**Chapter V: Electrochemical  
detection of thrombin using Si  
nanonet-based biosensors**

## Chapter V: Electrochemical detection of thrombin using Si nanonet-based biosensors

---

<b>Chapter V: Electrochemical detection of thrombin using Si nanonet-based biosensors.....</b>	<b>166</b>
V.1. Detection protocol.....	168
V.2. Detection ability without Si nanonet.....	169
V.3. Optimization of the Si nanonet-based electrochemical biosensors.....	169
V.3.1. Effect of the TBA-15 bioreceptor concentration on thrombin detection.....	170
V.3.2. Effect of the Si nanonet density on thrombin detection.....	174
V.3.2.1. Effect of the Si nanonet density on the electrochemical properties of the Si nanonet-based biosensors.....	176
V.3.2.2. Choice of the Si nanonet density.....	180
V.4. Sensitivity of the Si nanonet-based electrochemical biosensor.....	181
V.4.1. Biosensor sensitivity evaluated by cyclic voltammetry.....	181
V.4.2. Biosensor sensitivity evaluated by electrochemical impedance spectroscopy.....	183
V.5. Specificity of the Si nanonet-based electrochemical biosensor.....	188
V.6. Conclusions.....	190
<b>References.....</b>	<b>191</b>

Having previously established and optimized the technological steps necessary for the fabrication of Si nanonet-based electrochemical biosensor, the following objectives detailed in this chapter are first to optimize the biosensors in terms of characteristics (Si nanonet density and concentration of the TBA-15 bioreceptor used during the grafting step), and second, to characterize the biosensors in terms of sensitivity and specificity. As described previously, the target of this biosensor is the thrombin. On the one hand, this protein plays a crucial role in human health, since it is in charge of regulating hemostasis, which is the cessation of blood loss from a damaged vessel, and maintaining blood coagulation cascade. Disorders of coagulation can increase risk of bleeding (hemorrhage) or clotting (thrombosis) [1]. Besides the main role in the coagulation cascade, thrombin participates in other biological processes such as inflammatory responses, and cell proliferation, modulation, protection and apoptosis, making this protein a key piece in the progression of several diseases such as inflammatory disorders as multiple sclerosis, tumor cell proliferation involved in cancer development and neurodegenerative diseases such as Alzheimer's disease [2–4]. On the other hand, thrombin acts as a model protein in the development of the Si nanonet-based electrochemical biosensor proof-of-concept.

As the optimization of the sensor is evaluated from the capacity shown by the biosensors to detect thrombin, a first part of this chapter is dedicated to the detection protocol. Moreover, with this work, our aim is to demonstrate the use of Si nanonet to fabricate the electrode is a real added value. As a consequence, the second part of this chapter is dedicated to the detection of thrombin without the Si nanonet on top of the electrode.

### V.1. Detection protocol

The detection protocol is based on the two previously described experimental techniques: cyclic voltammetry and the electrochemical impedance spectroscopy. In all the studied cases, the Si nanonet-based electrodes were functionalized by the protocol described in the previous chapter (IV.2.3.1.1.). In summary, a Polypyrrole-NTA film is fabricated by monomer adsorption in liquid conditions, followed by chemical polymerization. Then, the formation of the chelate complex with copper allows the immobilization of the biotin labelled TBA-15 bioreceptor.

Subsequently, the Si nanonet-based biosensors were exposed to a given concentration of thrombin. For the purpose of optimization, a high concentration of thrombin was chosen ( $5 \times 10^{-7}$  M), as the objective was to obtain a high response signal. Once the biosensor was optimized, it was exposed to a range of thrombin concentrations, varying from  $5 \times 10^{-9}$  M to  $2 \times 10^{-6}$  M, in order to evaluate its sensitivity.

The thrombin recognition step is done as follows. The Si nanonet-based electrochemical biosensor is exposed to 100  $\mu$ L of a given concentration of thrombin in 0.1 M phosphate buffer at pH 7.4, containing 10 mM NaCl, 5 mM KCl and 1 mM  $\text{MgCl}_2$ . Subsequently, the electrode is rinsed under stirring (150 rpm) in phosphate buffer (pH 7) for 10 minutes.

### V.2. Detection ability without Si nanonet

In order to have an idea in terms of the usefulness of using the Si nanonet structure in the fabrication of the electrochemical biosensor, thrombin detection was carried out on PPy-NTA/ $\text{Cu}^{2+}$ /biotin/TBA-15 biofunctionalized carbon electrodes without Si nanonet, for a high thrombin concentration ( $5 \times 10^{-7}$  M). After the thrombin incubation there was no change compared to before incubation, neither in the electrochemical characteristics obtained by cyclic voltammetry, nor in the results' obtained by impedance spectroscopy electrochemistry. As a consequence, it is evident that the functionalized electrode solely is not able to carry out the thrombin detection, and that the detection ability, if able, is brought by the Si nanonet.

### V.3. Optimization of the Si nanonet-based electrochemical biosensors

In order to optimize the Si nanonet-based electrochemical biosensors, it was studied the effect of two different parameters on the ability of the biosensor to detect thrombin. These two parameters correspond to the TBA-15 bioreceptor concentration used during the grafting step and the Si nanonet density.

### V.3.1. Effect of the TBA-15 bioreceptor concentration on thrombin detection

To analyze whether the surface concentration of the TBA-15 bioreceptor grafted on the Si nanonet-based electrochemical biosensor has an effect on thrombin detection, different bioreceptor concentrations were analyzed for a given Si nanonet density of  $199 \times 10^6 \text{ NWS} \cdot \text{cm}^{-2}$ , corresponding to a surface coverage of about 54%. For this purpose, during the biofunctionalization process, at the time of carrying out the grafting step, the Si nanonet-based electrodes were exposed to two different TBA-15 bioreceptor concentrations:  $10 \mu\text{M}$  and  $50 \mu\text{M}$ , assuming that the more concentrated the solution of TBA-15 is, the more TBA-15 is grafted on the surface. The Si nanonet-based biosensors were analyzed by cyclic voltammetry and electrochemical impedance spectroscopy before and after thrombin incubation, using  $[\text{Fe}(\text{CN})_6]^{3-/4-}$  redox probe, as optimized in the previous chapter. The analyses obtained by cyclic voltammetry (not shown here) did not allow to observe a significant difference in the electrochemical properties of the Si nanonet-based electrochemical biosensors before and after thrombin exposure. However, the results obtained by impedance spectroscopy, being a more sensitive technique compared to cyclic voltammetry, allowed to evidence the thrombin recognition event (Figure V-1).

The analyses showed that as expected, increasing the concentration of TBA-15 bioreceptor improves the signal obtained. Indeed, from the Nyquist representations of the impedance spectra (Figure V-1), it can be observed that, in both cases, the radii of the semicircles increases upon addition of thrombin, however, this increase is more significant for the electrode exposed to a higher concentration of TBA-15 bioreceptor ( $50 \mu\text{M}$ ) (Figure V-1(b)).

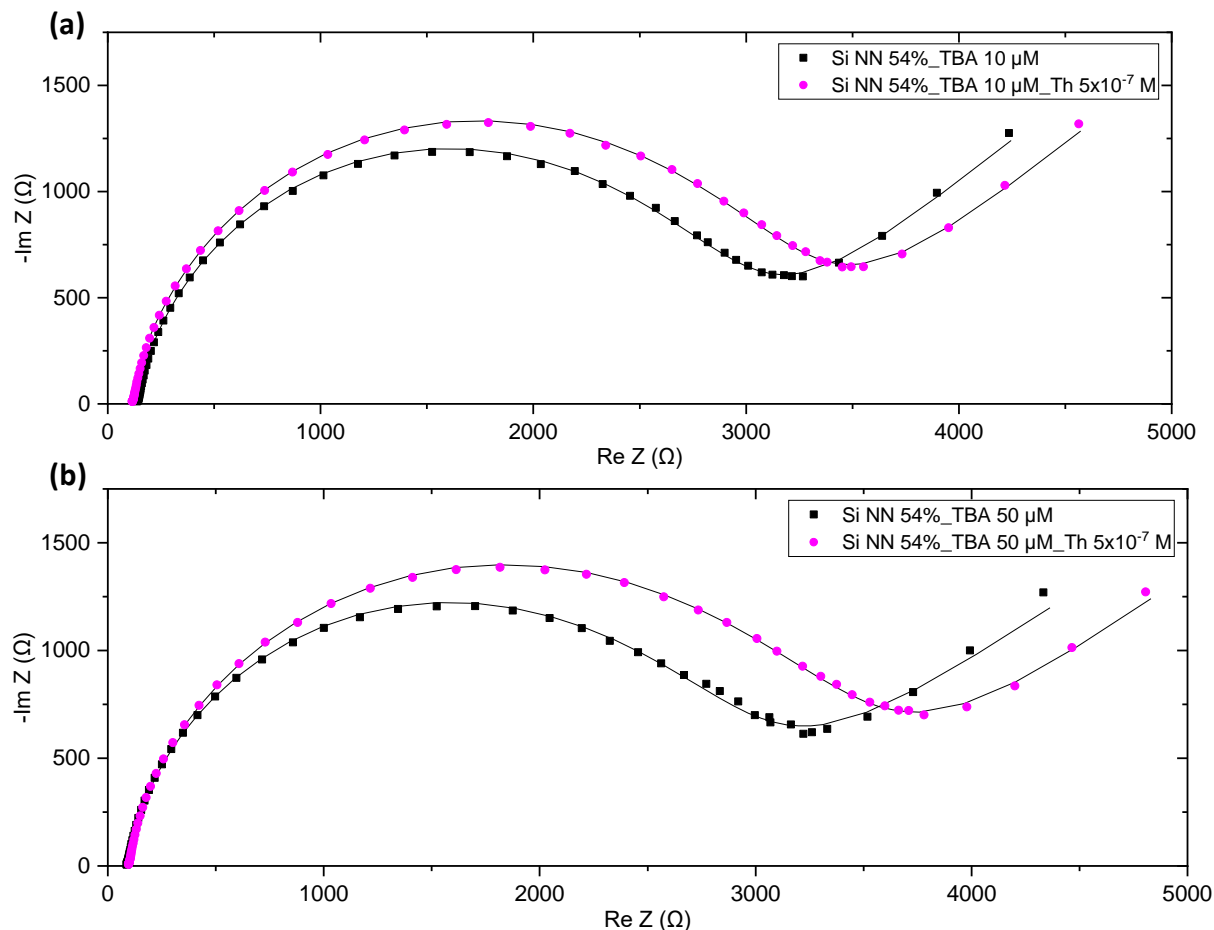


Figure V-1: Nyquist plot of impedance spectra obtained for a Si nanonet-based biosensor before and after thrombin incubation. Si nanonet surface coverage  $\approx 54\%$ . Measurements performed using  $2 \text{ mM } [\text{Fe}(\text{CN})_6]^{3-/4-}$  redox probe in  $0.1 \text{ M}$  phosphate buffer ( $\text{pH } 7$ ), at  $0.18 \text{ V}$  vs SCE, with an AC amplitude of  $10 \text{ mV}_{\text{RMS}}$  and a frequency sweep from  $50\,000 \text{ Hz}$  to  $0.1 \text{ Hz}$ . The temperature was set at  $25 \text{ }^\circ\text{C}$ . Dots represent the experimental data and lines represent the fitted data.

Besides, the results corresponding to the equivalent circuit, obtained by data fitting (Table V-1), help to elucidate the phenomena occurring on the Si nanonet-based biosensors once recognition of the target molecule occurs. First, it can be noted in both cases ( $10$  and  $50 \text{ } \mu\text{M}$  TBA-15 bioreceptor), an increase in the transfer change resistance ( $R_{ct}$ ) of the Si nanonet-based electrochemical biosensors after thrombin incubation. This result can be explained by the steric hindrances generated by the thrombin anchorage, preventing the efficient electron transfer between the electrode surface and the  $[\text{Fe}(\text{CN})_6]^{3-/4-}$  redox probe. As a consequence, the number of redox species that can react at the electrode surface is reduced, resulting in an increase of  $R_{ct}$ .

## Chapter V: Electrochemical detection of thrombin using Si nanonet-based biosensors

Table V-1: Values of the equivalent circuit elements ( $R_{ct}$ ,  $C_{dl}$ ,  $n$  and  $f$ ), obtained by data fitting, for Si nanonet-based electrochemical biosensors before and after  $5 \times 10^{-7}$  M thrombin incubation for different TBA-15 bioreceptor concentrations. Si nanonet surface coverage  $\approx 54\%$ .

	$R_{ct}$ ( $\Omega$ )	$C_{dl}$ ( $\mu\text{F}$ )	$n$	$f$ (Hz)
<b>10 <math>\mu\text{M}</math> TBA-15</b>	$2710 \pm 40$	$2.26 \pm 0.03$	$0.89 \pm 0.01$	26
<b>10 <math>\mu\text{M}</math> TBA-15_5 x 10<sup>-7</sup> M thrombin</b>	$3020 \pm 50$	$2.15 \pm 0.03$	$0.89 \pm 0.01$	24.5
<b>50 <math>\mu\text{M}</math> TBA-15</b>	$2660 \pm 40$	$2.13 \pm 0.03$	$0.9 \pm 0.01$	28.2
<b>50 <math>\mu\text{M}</math> TBA-15_5 x 10<sup>-7</sup> M thrombin</b>	$3200 \pm 50$	$2.09 \pm 0.03$	$0.87 \pm 0.01$	23.7

In agreement with what was observed in the Nyquist plots (Figure V-1), the increase in  $R_{ct}$  was more significant in the case where a higher concentration of TBA-15 bioreceptor (50  $\mu\text{M}$ ) was used during the grafting step, presenting an increase of 20%, compared to the 11% increase obtained for the 10  $\mu\text{M}$  TBA-15 concentration. These results indicate that a higher amount of thrombin was detected in the case of the electrode that was exposed to a more concentrated solution of TBA-15 bioreceptor. Indeed, as expected, when the electrode was exposed to a more concentrated bioreceptor solution, a higher amount of them could be immobilized on its surface. This in turn resulted in a higher amount of thrombin that could be detected, consequently generating a more significant increase in the total impedance of the electrochemical system once the recognition event took place.

Concerning the double layer capacitance ( $C_{dl}$ ), in both cases, a very slight decrease was observed after thrombin incubation (5% and 2%, for 10  $\mu\text{M}$  TBA-15 and 50  $\mu\text{M}$  TBA-15 respectively). This decrease is very small compared to the increase obtained for the charge transfer resistance (Table V-1). Previous studies conducted by Jessica Baur at DCM for the HIV-DNA electrochemical detection showed that the recognized target is generating a purely geometric effect on the electrochemical interface, resulting in a certain type of passivation of the electrode surface when the recognition of the biological target leads to a decrease in the double layer capacitance, which is proportional to the increase in the charge transfer resistance, in addition to a characteristic frequency that remains stable. In such a purely geometric effect, the electron transfer is not slowed, but merely occurs on a smaller surface area [5]. In the present case, on the one hand, the

charge transfer resistance increased much more than the double layer capacitance decreased, and, on the other hand there was a change in the characteristic frequency, which characterizes the speed of the electron transfer (Table V-1). As a consequence, it can be concluded that the thrombin did not generate this purely geometric effect, and therefore, other phenomena must be involved in the biosensor response.

In this context, the change in  $C_{dl}$  could have been caused by the presence of ions of different nature and/or in different concentrations in the double layer, generated by the thrombin recognition at the electrochemical interface, which perhaps led to a variation in its thickness. In regards to the parameter  $n$ , which is related to the geometry of the semicircle, it was observed a small decrease after thrombin incubation, only in the case of the biosensor biofunctionalized using 50  $\mu\text{M}$  TBA-15 bioreceptor. This indicates that surface homogeneity was more affected after thrombin recognition for the case where the Si nanonet-based electrode was biofunctionalized with 50  $\mu\text{M}$  TBA-15 bioreceptor, again confirming a higher amount of thrombin on its surface, compared to the case where 10  $\mu\text{M}$  TBA-15 bioreceptor was used, whose homogeneity was not affected after the thrombin exposure. Finally, regarding the characteristic frequency ( $f$ ), in both cases, a decrease of this parameter was observed after thrombin incubation, which is in agreement with the expected results. Indeed,  $f$  is related to the reaction rate: a lower  $f$  value indicates that electrochemical reaction took place more slowly. Thus, as expected, the electrochemical species took longer to reach the electrode surface after thrombin recognition, due to the steric hindrance generated by the latter. Additionally, this effect was more important for the Si nanonet-based biosensor biofunctionalized with a more concentrated TBA-15 bioreceptor solution, again due to higher amount of thrombin on the electrode surface after the recognition event. In conclusion, it was found that increasing the concentration of the TBA-15 bioreceptor during the grafting step improves the signal obtained for the thrombin detection. Consequently, all the analyses presented hereafter were carried out on Si nanonet-based electrochemical biosensors biofunctionalized using a concentration of 50  $\mu\text{M}$  TBA-15 bioreceptor. These results in turn allowed to prove indirectly that biofunctionalization process previously developed worked properly.

### V.3.2. Effect of the Si nanonet density on thrombin detection

The second parameter studied was the effect of the Si nanonet density on the performance of the biosensor. For this purpose, in addition to the Si nanonet density studied in the previous part ( $199 \times 10^6 \text{ NWS} \cdot \text{cm}^{-2}$ , surface coverage  $\approx 54\%$ ), it was studied a Si nanonet-based electrochemical biosensor presenting a lower Si nanonet density:  $56 \times 10^6 \text{ NWS} \cdot \text{cm}^{-2}$ , corresponding to a surface coverage of about 15%. The latter density represents less than 1/3 of the density studied before (54%). The analyses were again evaluated in terms of the performance of the Si nanonet-based electrochemical biosensor in recognizing thrombin at the same concentration as the one studied before ( $5 \times 10^{-7} \text{ M}$ ). Figure V-2 exhibits the results obtained from cyclic voltammetry and electrochemical impedance spectroscopy for this lower density.

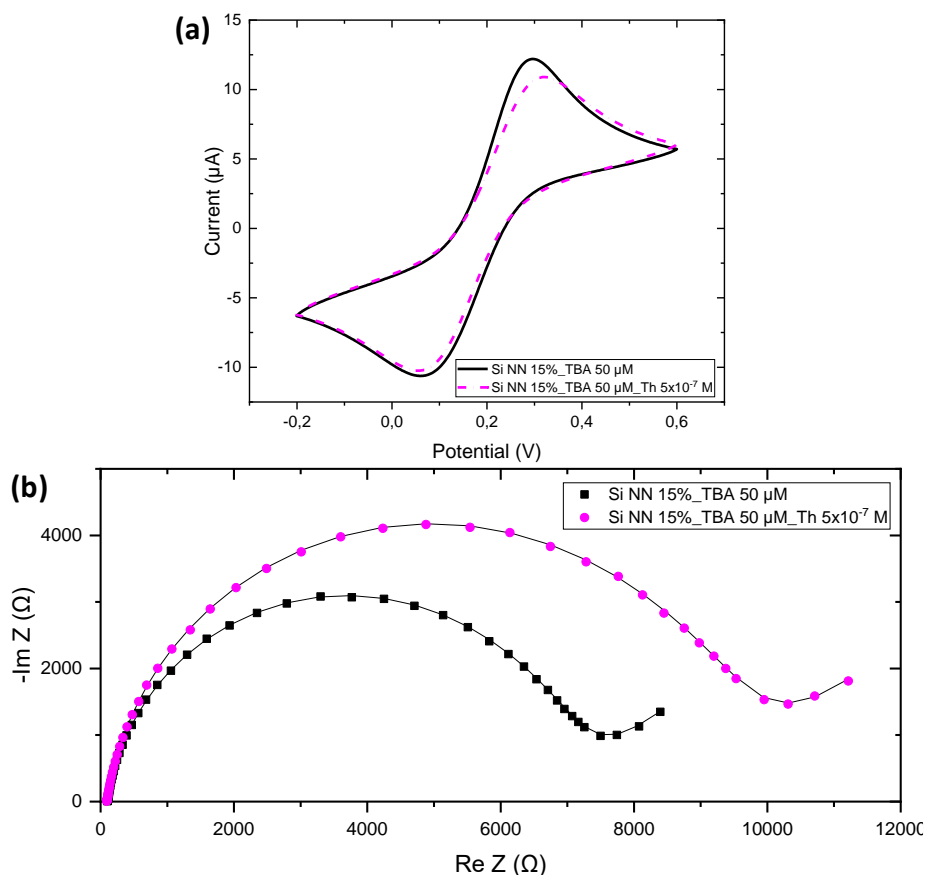


Figure V-2: Electrochemical characterization of a Si nanonet-based biosensor presenting a Si nanonet surface coverage  $\approx 15\%$ . The analyses were performed before and after  $5 \times 10^{-7} \text{ M}$  thrombin incubation. (a) Cyclic voltammogram recorded at scan rate of  $10 \text{ mV/s}$ , and (b) Nyquist plot of impedance spectra obtained at  $0.18 \text{ V}$  vs SCE, with an AC amplitude of  $10 \text{ mV}_{\text{RMS}}$  and a frequency sweep from  $50\,000 \text{ Hz}$  to  $0.1 \text{ Hz}$  (dots represent the experimental data and lines represent the fitted data). Both tests were performed using  $2 \text{ mM}$   $[\text{Fe}(\text{CN})_6]^{3-/4-}$  redox probe in  $0.1 \text{ M}$  phosphate buffer ( $\text{pH} 7$ ). The temperature was set at  $25 \text{ }^\circ\text{C}$ .

## Chapter V: Electrochemical detection of thrombin using Si nanonet-based biosensors

As can be seen from Figure V-2(a), in the case of the cyclic voltammetry analyses, with such a low nanonet density, it was possible to observe a change in the peak currents after thrombin incubation, which had not been evidenced for the higher density. As described in Table V-2, where the results are summarized, the change in signal was more important in the case of the anodic peak current.

*Table V-2: Values obtained for the different parameters investigated by cyclic voltammetry on Si nanonet-based electrochemical biosensors presenting a lower Si nanonet surface coverage: 15%. Measurements obtained before and after  $5 \times 10^{-7}$  M thrombin incubation. The studied parameters correspond to the anodic and cathodic current intensities ( $I_{pa}$  and  $I_{pc}$  respectively), their associated potential values ( $E_{pa}$  and  $E_{pc}$  respectively) and the peak-to-peak separation ( $\Delta E_p$ )*

	$I_{pa}$ ( $\mu\text{A}$ )	$I_{pc}$ ( $\mu\text{A}$ )	$E_{pa}$ (V)	$E_{pc}$ (V)	$\Delta E_p$ (V)
<b>Before <math>5 \times 10^{-7}</math> M Th incubation</b>	11.25	-9.21	0.29	0.08	0.21
<b>After <math>5 \times 10^{-7}</math> M Th incubation</b>	9.39	-8.65	0.30	0.08	0.22

On the other hand, the analyses carried out by means of electrochemical impedance spectroscopy corroborated a better sensitivity of the Si nanonet-based biosensor when it exhibits a lower Si nanonet surface coverage (15%). This can be evidenced both, in the obtained Nyquist plot (Figure V-2(b)), where it is observed that the increase in the radius of the semicircle is greater than that obtained in the previous studies (Figure V-1), and in the information obtained by data fitting (Table V-3). As in the previous case, after thrombin incubation there was a strong increase in the charge transfer resistance (36%), which was much higher than the one obtained for the Si nanonet-based electrochemical biosensor presenting a 54% Si nanonet surface coverage (20%), for the same concentration of TBA-15 bioreceptor (Table V-3).

Additionally, as observed before, it can be noted that the  $n$  parameter remained stable and the characteristic frequency decreased. As previously mentioned, this decrease is related to reduction in the electrochemical reaction rate. However, a discrepancy appeared in the behavior of the double layer capacitance. Whereas it decreased in the case of high Si nanonet density, it increased for the low density, indicating that the ions in the double layer were probably different in nature and/or concentration.

Table V-3: Values of the equivalent circuit elements ( $R_{ct}$ ,  $C_{dl}$ ,  $n$  and  $f$ ), obtained by data fitting, for Si nanonet-based electrochemical biosensors presenting different Si nanonet surface coverage: 15% and 54%. Measurements obtained before and after  $5 \times 10^{-7}$  M thrombin incubation.

		$R_{ct}$ ( $\Omega$ )	$C_{dl}$ ( $\mu\text{F}$ )	$n$	$f$ (Hz)
15%	Before $5 \times 10^{-7}$ M Th incubation	$6900 \pm 100$	$1,75 \pm 0.03$	$0.92 \pm 0.01$	13.2
	After $5 \times 10^{-7}$ M Th incubation	$9300 \pm 100$	$1.92 \pm 0.03$	$0.91 \pm 0.01$	8.9
54%	Before $5 \times 10^{-7}$ M Th incubation	$2660 \pm 40$	$2.13 \pm 0.03$	$0.9 \pm 0.01$	28.2
	After $5 \times 10^{-7}$ M Th incubation	$3200 \pm 50$	$2.09 \pm 0.03$	$0.87 \pm 0.01$	23.7

### V.3.2.1. Effect of the Si nanonet density on the electrochemical properties of the Si nanonet-based biosensors

In order to understand why the performance of Si nanonet-based biosensors improves when the Si nanonet density is reduced to less than 1/3, it was carried out a study in which the electrochemical properties of 4 different electrodes were analyzed:

- (i) A carbon electrode without any surface modification (CE).
- (ii) A carbon electrode modified by a Si nanonet covering 54% of its surface. The polypyrrole-NTA film was subsequently deposited (CE\_Si NN 54%\_PPy-NTA).
- (iii) A carbon electrode modified by a Si nanonet covering 15% of its surface. The polypyrrole-NTA film was subsequently deposited (CE\_Si NN 15%\_PPy-NTA).
- (iv) A carbon electrode on which a polypyrrole-NTA film was directly deposited (without Si nanonet) (CE\_PPy-NTA)

Figure V-3 shows the results obtained by cyclic voltammetry and electrochemical impedance spectroscopy, for the different electrodes analyzed. In addition, Table V-4 presents the values obtained for each of the parameters studied.

As expected, the electrode presenting the best electrochemical activity was the carbon electrode without any surface modification (CE). This was evidenced by the higher values of the peak

currents ( $I_{pa}$  and  $I_{pc}$ ) in the cyclic voltammetry analyses (Figure V-3(a), Table V-4), and the smaller radius of the semicircle, together with the lower value of the charge transfer resistance for the electrochemical impedance spectroscopy analyses (Figure V-3(b), Table V-4).

The opposite case was found for electrode on which solely a polypyrrole-NTA film was deposited (CE\_PPy-NTA). This electrode showed a poor electrochemical activity, evidenced by the low peak current values, as well as the large value of  $\Delta E_p$ , indicating an important decrease in the reversibility of the electrochemical reaction on its surface (Figure V-3(a), Table V-4). Likewise, the EIS analysis showed a strong increase in the impedance of the system, where the charge transfer resistance increased by 10 times with respect to the carbon electrode without any surface modification (Figure V-3(b), Table V-4). The origin of these results can be the formation of a dense and compact polypyrrole film on the electrode surface, preventing a proper ion exchange between the redox probe and the conductive surface of the electrode.

Between these two extreme cases, the electrodes whose surface was modified with the Si nanonet were present. As can be seen from Figure V-3(a) and (b) and Table V-4, a lower density of Si nanonets results in a less accessible electrode surface for the redox probe. This is evidenced on the one hand by the lower current peaks obtained: 10.51  $\mu\text{A}$  (15% Si nanonet surface coverage) compared to 12.94  $\mu\text{A}$  (54% Si nanonet surface coverage) for  $I_{pa}$ , and -10.83  $\mu\text{M}$  (15% Si nanonet surface coverage) compared to -8.55  $\mu\text{A}$  (54% Si nanonet surface coverage) for  $I_{pc}$ . This result, on the other hand, is confirmed by the high value of the charge transfer resistance obtained in the case of the less dense Si nanonet (6800  $\Omega$ , for 15% Si nanonet surface coverage) compared to the value obtained in the case of the denser Si nanonet (3920  $\Omega$ , for 54% Si nanonet surface coverage).

Here, it is important to mention that the adsorption time of the pyrrol-NTA monomer remained constant in all the studied cases during the polypyrrole-NTA film fabrication step. Thus, it can be assumed that the amount of polypyrrole-NTA film formed is similar in quantity of pyrrole-NTA units for each of the electrodes studied.

Then, it appears that the Si nanonets behave like the backbone of the three-dimensional structure of the developed electrode. Indeed, the absence of Si nanonets leads to the formation of a thick and compact polypyrrole-NTA film. Concerning the carbon electrode modified by a Si nanonet covering 15% of its surface, because of the low nanowire density, large areas of the substrate were free of Si nanowires, and thus, would lead to the formation of thick layer of polypyrrole-NTA film, which was distributed between the free areas of the electrode, and the porous architecture of Si nanonet. Then, for the carbon electrode modified by a Si nanonet covering 54% of its surface, the higher Si nanonet density allowed the formation of a thinner polypyrrole-NTA film, mainly present on the Si nanonet, but also covering a smaller part of the electrode surface. These results allowed us to conclude that the backbone formed by the Si nanonet induced a structuration in the obtained polypyrrole-NTA film, instead of having a thick and compact layer. Thus, the denser the nanonet, the more structured the polymer film, allowing the redox probe to have an easier access to the underlying carbon electrode. As a consequence, the denser Si nanonet-based electrode (CE\_Si NN 54%) was more permeable for the passage of the redox towards the electrode surface.

Besides, in both cases (CE\_Si NN 54% and CE\_Si NN 15%), the better permeability generated by the modification of the carbon electrode with Si nanonet was reflected in the results obtained for the three parameters: charge transfer resistance, double layer capacitance and characteristic frequency. As shown in Table V-4, thanks to the presence of the Si nanonet structure, these three parameters were closer to those obtained for the bare carbon electrode, than those obtained for the electrode modified only by the polypyrrole-NTA film (without Si nanonet). Thus, the presence of the Si nanonet structure allowed the modified electrode to maintain a good electrochemical response. In turn, the results obtained for  $n$  parameter indicated that the deposition of the polypyrrole-NTA film improved the homogeneity of the carbon electrode surface.

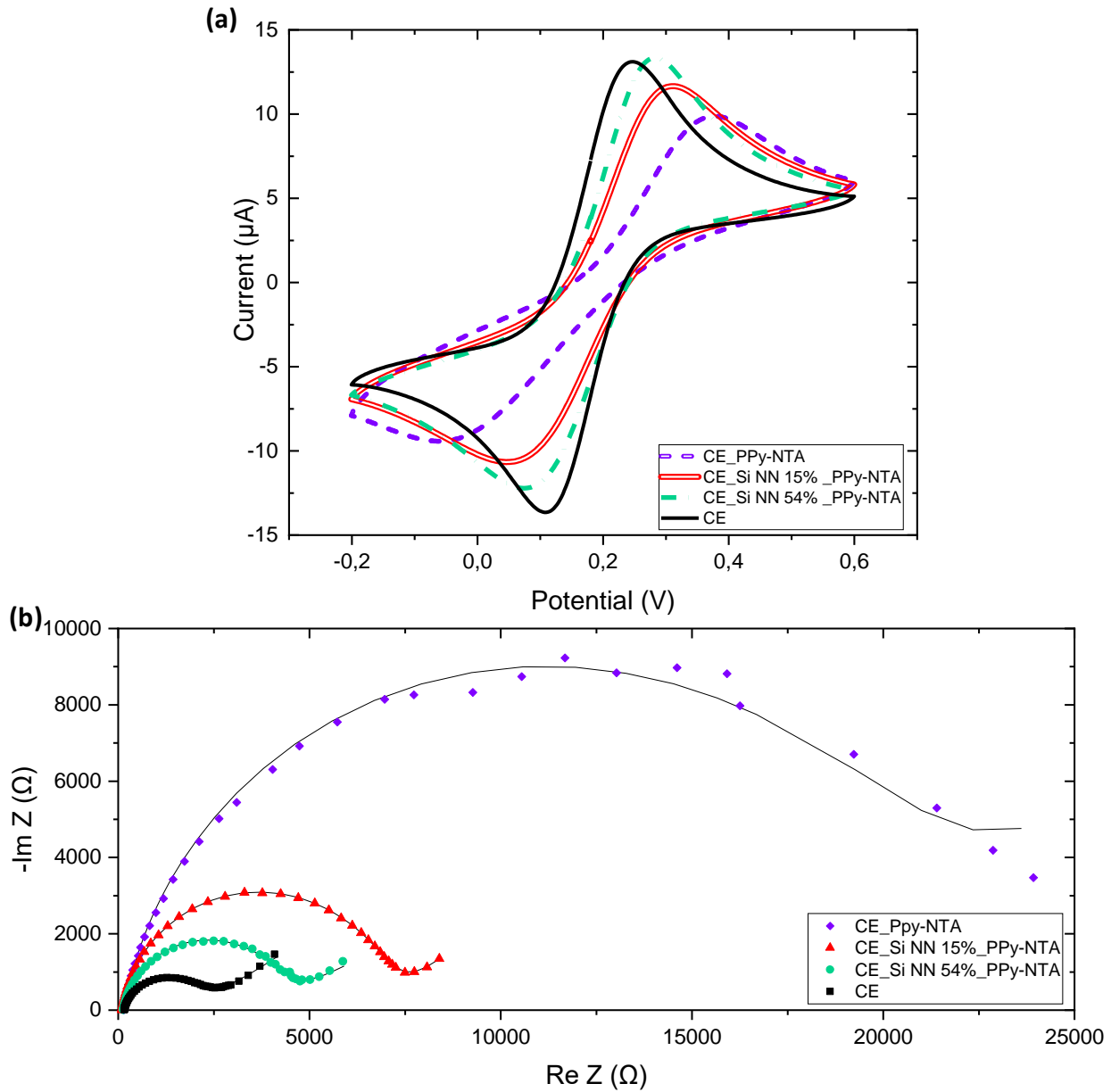


Figure V-3: Electrochemical characterization of 4 electrodes presenting different surfaces modifications, as described above, and as indicated in each figure. (a) Cyclic voltammogram recorded at scan rate of 10 mV/s, and (b) Nyquist plot of impedance spectra obtained at 0.18 V vs SCE, with an AC amplitude of 10 mV<sub>RMS</sub> and a frequency sweep from 50 000 Hz to 0.1 Hz (dots represent the experimental data and lines represent the fitted data). Both tests were performed using 2 mM  $[\text{Fe}(\text{CN})_6]^{3-/4-}$  redox probe in 0.1 M phosphate buffer (pH 7). The temperature was set at 25 °C.

Table V-4: Values obtained for the different parameters investigated by cyclic voltammetry and electrochemical impedance spectroscopy (values of the equivalent circuit elements obtained by data fitting) on 4 electrodes presenting different surfaces modifications, as described above.

	$I_{pa}$ ( $\mu\text{A}$ )	$I_{pc}$ ( $\mu\text{A}$ )	$\Delta E_p$ (V)	$R_{ct}$ ( $\Omega$ )	$C_{dl}$ ( $\mu\text{F}$ )	$n$	$f$ (Hz)
CE	13.47	-13.04	0.13	$2020 \pm 30$	$1,27 \pm 0.2$	0.81	59.5
CE_Si NN 54%_PPy-NTA	12.94	-10.83	0.19	$3920 \pm 60$	$1,76 \pm 0.3$	0.9	23.1
CE_Si NN 15%_PPy-NTA	10.51	-8.55	0.22	$6800 \pm 100$	$1.75 \pm 0.3$	0.92	13.3
CE_PPy-NTA	7.28	-4.71	0.37	$20300 \pm 300$	$3.66 \pm 0.5$	0.89	2.1

### V.3.2.2. Choice of the Si nanonet density

These analyses allowed to conclude why the Si nanonet-based electrochemical biosensors presenting a lower density of Si nanonets (15% surface coverage), resulted in a higher signal upon thrombin detection, compared to the one obtained for the electrode presenting a higher density of Si nanonets (54% surface coverage). In the case of low density, the previous study allowed to evidence a slower electron transfer on the surface of the electrode, related to a higher presence of the polypyrrole-NTA film on it (Table V.4). As a consequence, this slow transfer could have favored the observation of the general changes occurred on the complete structure once the thrombin recognition occurred. Indeed, as showed in the previous chapter (IV.2.1. Fabrication process of the C/Si nanonet-based electrodes, choice of the redox probe), when the electrochemical reactions are too fast, it may prevent the identification of surface changes. So, slowing down the electron transfer appears as an interesting solution to improve the thrombin recognition. As a consequence, an optimum in the Si nanonet density should appear. Indeed, in absence of nanonet, no signal was detected upon thrombin incubation due to a fully insulating polymer layer (Section V.2). But in case of a high Si nanonet density, the charge transfer was too fast, so the changes generated were more difficult to detect, resulting in a lower obtained signal. Further developments could be carried out, seeking to identify the optimum Si nanonet density for the thrombin detection. As a conclusion, thanks to this study, the parameters involving the Si nanonet-based electrochemical biosensor formation were optimized, allowing the subsequent studies of the biosensor characteristics, namely the sensitivity and specificity. Thus, the studies

presented hereafter were carried out on Si nanonet-based electrochemical biosensors presenting the characteristics that showed the best results: A Si nanonet covering 15% of the electrode surface and biofunctionalized using a 50  $\mu\text{M}$  TBA-15 bioreceptor solution.

### V.4. Sensitivity of the Si nanonet-based electrochemical biosensor

The objective of this section, having already optimized the Si nanonet-based electrochemical biosensor, was to evaluate the range of concentrations in which the latter can detect thrombin. For this purpose, the Si nanonet-based biosensors were exposed to different concentrations of thrombin, following the process described in section V.1, and the detection was carried out by cyclic voltammetry and electrochemical impedance spectroscopy.

#### V.4.1. Biosensor sensitivity evaluated by cyclic voltammetry

Figure V-4 presents the results of the sensitivity study obtained by cyclic voltammetry. The increase in thrombin concentration from  $5 \times 10^{-9}$  M to  $2 \times 10^{-6}$  M implies a systematic decrease in the anodic current response ( $I_{pa}$ ) (Figure V-4(a). Table V-5 summarizes the  $I_{pa}$  values obtained for each thrombin concentration. Figure V-4(b) illustrates the anodic current response ( $I_{pa}$ ) obtained as a function of the logarithm of thrombin concentration. Based on the observed linearity in this linear-log representation, the biosensor sensitivity can be defined as the slope of the curve, whose value corresponds to  $0.64 \pm 0.04$   $\mu\text{A}$  per order of magnitude, presenting a linear correlation coefficient  $R^2 = 0.999$ . These results evidenced that the recognition of the thrombin by the TBA-15 aptamer generated new steric hindrances to the redox probe diffusion toward the electrode surface, as the concentration of thrombin raised.

*Table V-5: Values of found for the anodic current peak ( $I_{pa}$ ) of the Si nanonet-based electrochemical biosensor upon detection of different thrombin concentrations.*

	$I_{pa}$ ( $\mu\text{A}$ )
TBA	11.25
TBA_Th $5 \times 10^{-9}$ M	10.56
TBA_Th $2 \times 10^{-8}$ M	10.16
TBA_Th $5 \times 10^{-7}$ M	9.40
TBA_Th $2 \times 10^{-6}$ M	8.85

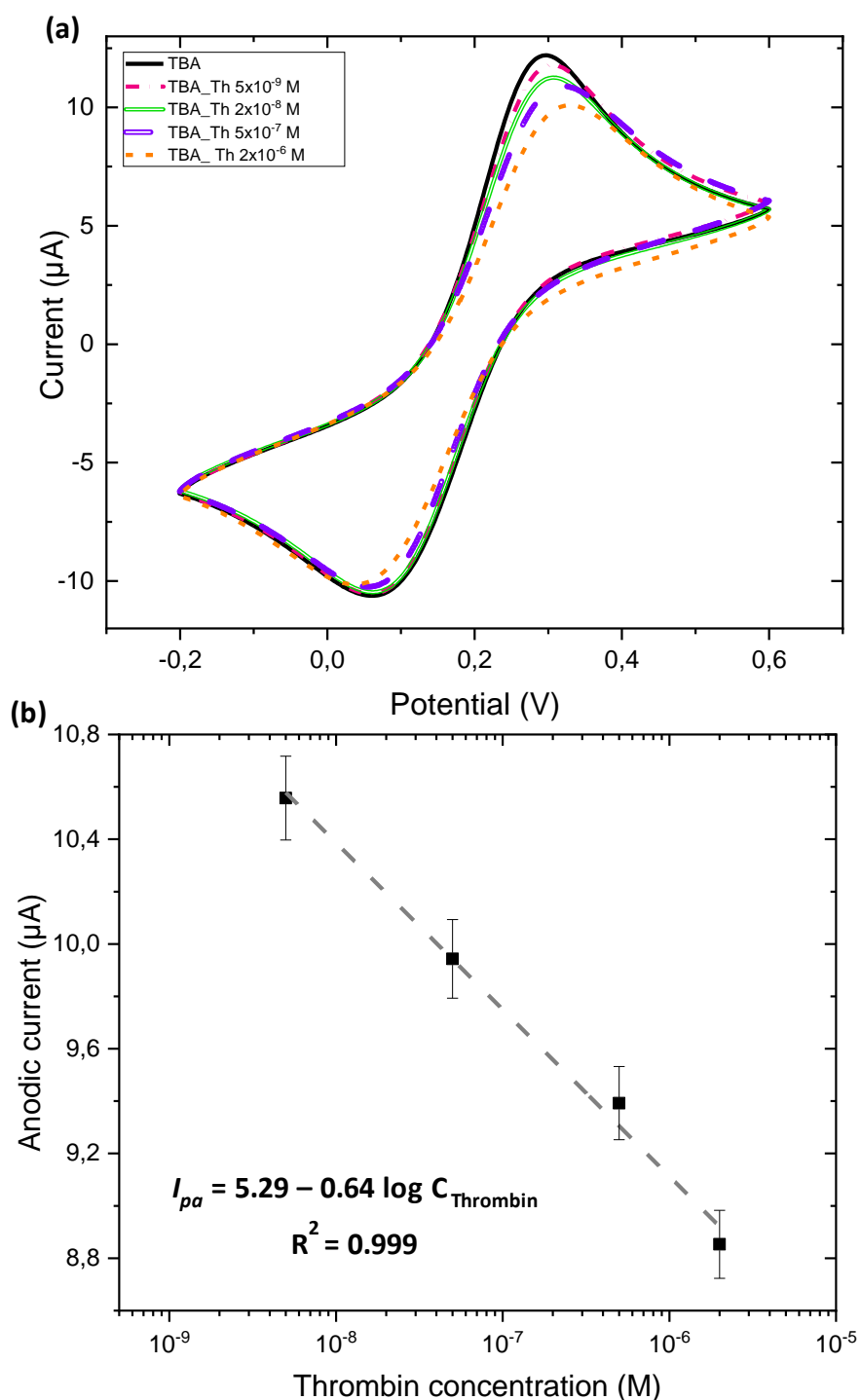


Figure V-4: (a) Cyclic voltammogram obtained for the Si nanonet-based biosensor after incubation in different thrombin concentrations. TBA corresponds to the initial characteristics of the biosensor (without exposure to thrombin). Test performed using 2 mM  $[\text{Fe}(\text{CN})_6]^{3-/4-}$  redox probe in 0.1 M phosphate buffer (pH 7), recorded at scan rate of 10 mV/s. Temperature set at 25 °C. (b) Calibration curve for the thrombin biosensor corresponding to the changes in the anodic current peak ( $I_{pa}$ ) upon detection of different thrombin concentrations. Experimental data (squares) and linear regression (line) are presented.

#### V.4.2. Biosensor sensitivity evaluated by electrochemical impedance spectroscopy

In this case, we decided to extend the range of concentrations studied was extended to the limit of thrombin solubility ( $2 \times 10^{-6}$  M). The results obtained by EIS are in good agreement with those obtained by CV. In the Nyquist plot obtained it is clearly evidenced that the radii of semicircle increased gradually with the thrombin concentration in a range from  $5 \times 10^{-9}$  M to  $5 \times 10^{-7}$  M. However, it increased drastically when the  $5 \times 10^{-6}$  M thrombin incubation was carried out. This result suggests that the phenomenon occurring in the range from  $5 \times 10^{-9}$  M to  $5 \times 10^{-7}$  M was indeed due to the recognition of thrombin by the TBA-15 bioreceptor. The proteins bind with the TBA-15 and act then as a barrier towards the permeation of the  $[\text{Fe}(\text{CN})_6]^{3-/4-}$  redox probe to the underlying electrode structure. In contrast, the response obtained after incubation of  $2 \times 10^{-6}$  M thrombin was probably due to a blocking effect of the electrode surface generated by protein precipitates that could not dissolve properly due to the solubility limit of the protein, and which probably adhered to the biosensor surface. Consequently, the analyses presented below do not take the latter concentration into account.

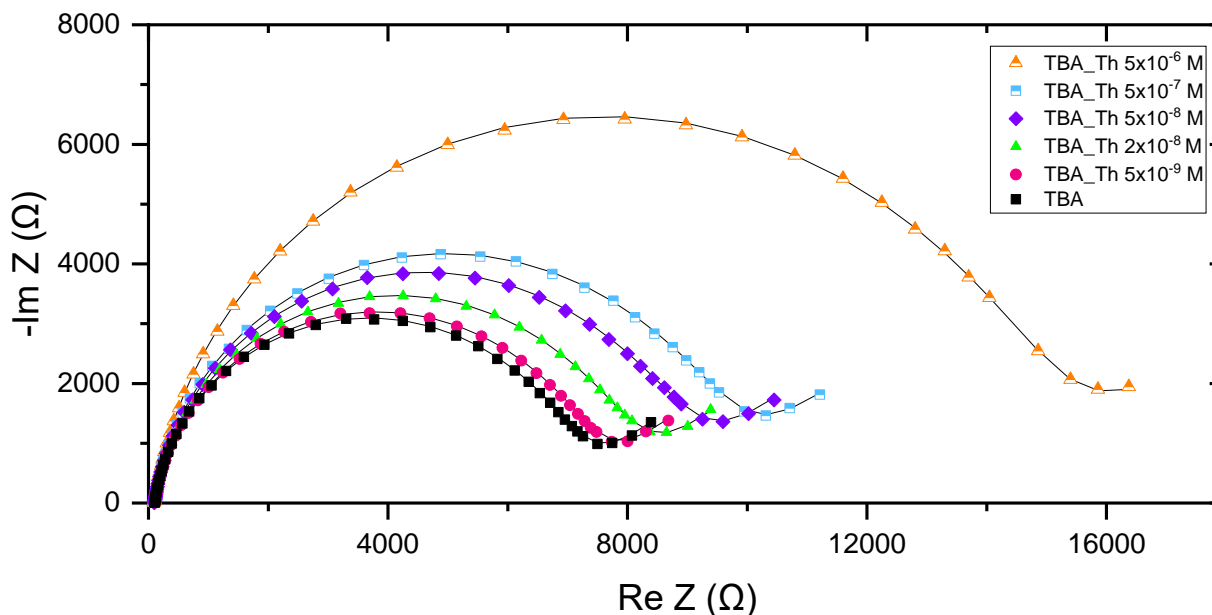


Figure V-5: Nyquist plot of impedance spectra obtained for the Si nanonet-based biosensor after incubation in different thrombin concentrations. TBA corresponds to the initial characteristics of the biosensor (without exposure to thrombin). Results obtained using 2 mM  $[\text{Fe}(\text{CN})_6]^{3-/4-}$  redox probe in 0.1 M phosphate buffer (pH 7) at 0.18 V vs SCE, with an AC amplitude of 10 mV<sub>RMS</sub> and a frequency sweep from 50 000 Hz to 0.1 Hz (dots represent the experimental data and lines represent the fitted data).

Table V-6 shows the obtained values after fitting the data to standard Randles equivalent circuit. With the exception of the  $n$  parameter, which stayed constant when the thrombin concentration increased, all the studied parameters changed after thrombin recognition. The values corresponding to the charge transfer resistance ( $R_{ct}$ ), the double layer capacitance ( $C_{dl}$ ), and the characteristic frequency ( $f$ ) were plotted in log-linear scale, as showed in FigureV-6 (a), (c) and (d) respectively. In addition, taking into account that standard EIS requires to record the impedance spectra over a wide frequency range, followed by the modeling process, and is then highly time consuming and quite complicated to apply, we propose here a simplification for the operating mode of the Si nanonet-based impedimetric biosensor. This interesting alternative consists in taking a single measurement at a given frequency. Herein, we measured the impedance modulus at 3.46 Hz. Indeed, this frequency value is located near the end of the semicircle, the greatest impedance variations are observed after thrombin incubation. This approach would allow to elaborate a calibration curve for the Si nanonet-based impedimetric biosensor in an easier and faster way. Then,  $Z_{3.46\text{ Hz}}$  was also plotted in the log-linear scale (FigureV-6(b)), in order to validate the simplified protocol.

*Table V-6: Values of the equivalent circuit elements obtained by data fitting for a Si nanonet-based electrochemical biosensor upon detection of different thrombin concentrations.*

	$R_{ct}$ ( $\Omega$ )	$Z_{3.46\text{ Hz}}$ ( $\Omega$ )	$C_{dl}$ ( $\mu\text{F}$ )	$n$	$f$ (Hz)
<b>TBA</b>	6900 $\pm$ 100	6667 $\pm$ 100	1.75 $\pm$ 0.3	0.92 $\pm$ 0.01	13.2
<b>TBA_Th 5 x 10<sup>-9</sup> M</b>	7100 $\pm$ 100	6991 $\pm$ 100	1.81 $\pm$ 0.3	0.91 $\pm$ 0.01	12.3
<b>TBA_Th 2 x 10<sup>-8</sup> M</b>	7700 $\pm$ 100	7310 $\pm$ 100	1.84 $\pm$ 0.3	0.91 $\pm$ 0.01	11.2
<b>TBA_Th 5 x 10<sup>-8</sup> M</b>	8600 $\pm$ 100	7951 $\pm$ 100	1.89 $\pm$ 0.3	0.91 $\pm$ 0.01	9.8
<b>TBA_Th 5 x 10<sup>-7</sup> M</b>	9300 $\pm$ 100	8469 $\pm$ 100	1.92 $\pm$ 0.3	0.91 $\pm$ 0.01	8.9

In FigureV-6, every curve evidenced a linear correlation in the concentration range studied. However, the parameters that varied the most during the thrombin detection process were the charge transfer resistance and the impedance modulus (FigureV-6 (a) and (b)). The calibration curves obtained for this parameters presented a sensitivity of 1100  $\pm$  200  $\Omega$  ( $R^2 = 0.976$ ) and 800

## Chapter V: Electrochemical detection of thrombin using Si nanonet-based biosensors

$\pm 100 \Omega$  ( $R^2 = 0.976$ ) per order of magnitude, respectively. It can be noted that, as expected, the sensitivity is better when the charge transfer resistance ( $R_{ct}$ ) was determined. However, measuring the impedance at a single frequency ( $Z_{3.46 \text{ Hz}}$ ), which is easier to carry out, also provided a very good sensitivity.

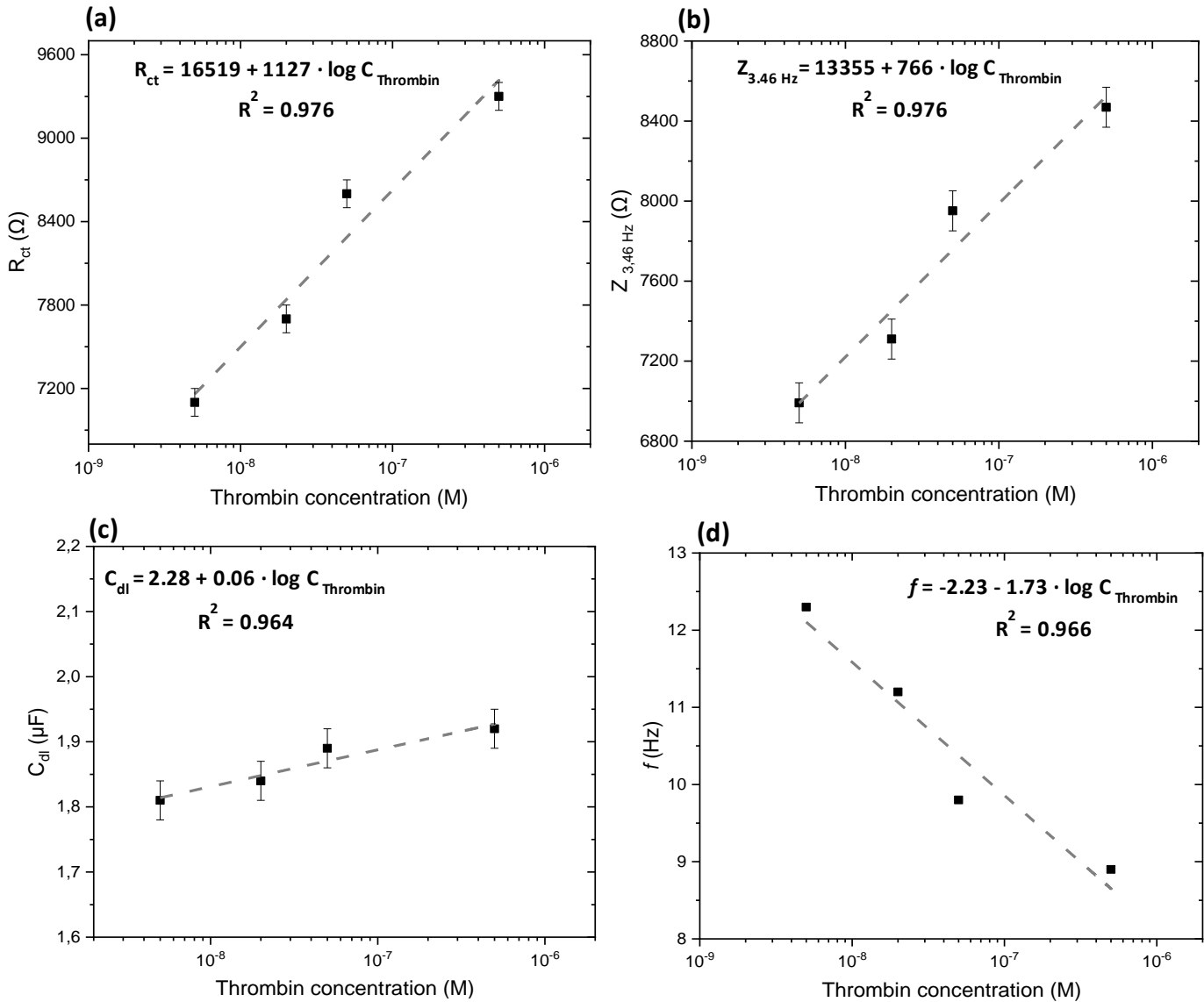


Figure V-6: Study of the different parameters obtained by EIS as a function of thrombin concentration: (a) charge transfer resistance, (b) impedance modulus at 3.46 Hz, (c) double layer capacitance, and (d) characteristic frequency. Experimental data (squares) and linear regression (lines) are presented.

As far as the other studied parameters are concerned, it can be observed that the double layer capacitance increased slightly with the thrombin concentration. As mentioned above and surprisingly, the  $n$  parameter remained stable over the course of the measurements, indicating that the homogeneity of the electrode surface was not drastically affected between the TBA-15 bioreceptor grafting step, and the thrombin recognition. These two results, the variation of  $C_{dl}$  and the stability of the parameter  $n$ , may indicate that although the fixation of the protein on the TBA-15 bioreceptor generated a disturbance in the flow of  $[\text{Fe}(\text{CN})_6]^{3-/4-}$  redox species towards the electrode surface, the thrombin molecules had only a minor effect on the structure of the electrochemical interface. Finally, the results obtained for the characteristic frequency showed that, as expected, the electrochemical species took longer time to reach the electrode surface as the steric hindrances generated by the increase in the concentration of thrombin are raised, which is reflected in the decrease of this parameter.

In order to check the reproducibility of the devices and of the results obtained, the same analyses (CV and EIS) were repeated on three different Si nanonet-based electrochemical biosensors with exactly the same parameters. For each studied biosensor, similar results to those reported in this section were found, over the same thrombin concentration ranges.

As a conclusion, the highly interesting results obtained by both techniques (cyclic voltammetry and electrochemical impedance spectroscopy) are really promising. Indeed, the Si nanonet-based electrochemical biosensor developed in this project could detect thrombin at concentrations that represent a risk to human health. In brief, the role of thrombin in the human body depends on its concentration [6]. At low concentration (pM range), thrombin is constantly circulating in the body in order to instantaneously respond to injury by a burst of thrombin at the site of vascular damage, giving rise to a coagulation event. At the site of injury, the concentration of thrombin reaches several hundred nM, promoting the coagulation reactions [7]. However, this process is very localized, and rigorously regulated by the thrombin natural inhibitors [8]. Thus, the risk of thrombosis arises when uninhibited thrombin escapes from the injury site at concentration above 5 nM [7]. Then, free thrombin levels from 5 to 20 nM in blood could indicate a high risk of

thrombosis, while thrombin concentrations above 20 nM already means the presence of thrombosis [9]. As previously showed, the Si nanonet-based electrochemical biosensors evaluated by the two techniques studied were able to detect thrombin from 5 nM to the  $\mu\text{M}$  range, thus offering promising results for their use in the detection of thrombosis.

Regarding the performance of the device, as mentioned in Chapter I corresponding to the state of the art, there are few reports in the literature corresponding to electrochemical sensors based on Si NWs, but most of them are built from 3D vertically oriented Si nanonet structures [10,11,20–22,12–19]. However, to our knowledge, only two electrochemical biosensors based on 2D Si nanonets have been reported so far[23,24]. In both cases, these were voltammetric sensors. However, only in the first case a comparison with the sensor developed in this project can be made, since in the second case, the 2D Si nanonet was superficially modified with gold nanoparticles, in order to increase the performance of the biosensor. In the first case, the 2D Si nanonet was used as supporting material for enzyme immobilization to construct a glucose biosensors. This electrochemical biosensor showed a linear response in the range of 0.1 – 15 mM [23]. However, the detection mechanism used in that work (enzyme-catalyzed reaction) is completely different from the one used in this project, thus, it is not possible to make a comparison between them. Concerning the second reported case, as mentioned before, the surface of the 2D Si nanonet was modified with gold nanoparticles in order to improve biosensor performances. This electrochemical device was used to detect the DNA hybridization, showing a linear response from 0.01 nM to 50 nM [24].

Then, based on the previous information, it is possible to think that the performance of the Si nanonet-based electrochemical biosensors developed in this project could be improved by surface modifications, either by the use of metallic particles, as in the case mentioned above, or by the deposition of a thin metallic layer, completely covering the nanonet, but preserving its porous structure. This in order to improve the conductivity of the biosensor, which would probably increase the performance of the device, allowing to detect lower thrombin concentrations, which has already been achieved in previously reported works [25–28].

Moreover, as far as we know, the results reported here show for the first time the development of an impedimetric biosensor based on 2D Si nanonets. Thus, the doors are open for new and promising projects for the use of 2D Si nanonets in the field of the electrochemical biosensors.

### V.5. Specificity of the Si nanonet-based electrochemical biosensor

In order to investigate the specificity of the Si nanonet-based electrochemical biosensors, control experiments were carried out. For this purpose the Si nanonet-based electrochemical devices, biofunctionalized until the TBA-15 grafting step, were incubated during 40 min in different aqueous protein solutions ( $5 \times 10^{-7}$  M): lysozyme from hen egg white (lysozyme), Human immunoglobulin G (IgG) and bovine serum albumin (BSA). The determination of the possible non-specific adsorption of these proteins was evaluated by cyclic voltammetry and electrochemical impedance spectroscopy. The results obtained were evaluated in terms of the relative variations of the anodic peak current ( $\Delta I_{pa}$ ), in the case of CV, and the charge transfer resistance ( $\Delta R_c$ ), in the case of EIS, with respect to the values obtained for the biosensor before exposure to the corresponding protein. These results in turn were compared with the values obtained for the detection of thrombin at the same concentration (Table V-7).

*Table V-7: Relative variations in the anodic peak current ( $\Delta I_{pa}$ ), and the charge transfer resistance ( $\Delta R_c$ ) for Si nanonet-based biosensors exposed to different aqueous protein solutions ( $5 \times 10^{-7}$  M)*

	$\Delta I_{pa}$ (%)	$\Delta R_c$ (%)
<b>Thrombin</b>	-18.26	+34.78
<b>Lysozyme</b>	-7.38	+16.99
<b>IgG</b>	-10.47	+8.75
<b>BSA</b>	+9.83	-18.89

As known, for the non-specific adsorption of a protein on the surface of the biosensor, it is expected to observe a decrease in the peak current obtained during the analyses carried out by cyclic voltammetry, which in turn should be evidenced as an increase in the charge transfer resistance for the impedance analyses. This behavior was obtained for the interaction of lysozyme

and IgG with the Si nanonet-based electrochemical biosensor. As can be seen from Table V-7, for these proteins a decrease in the anodic peak of 7% and 10%, respectively, was obtained, which in turn were related to an increase in impedance of 16% and 8% respectively. Although the response of the Si nanonet-based electrochemical biosensor to these proteins appears considerable, as can be seen in Table V-7, it is much lower than the response obtained in the case of thrombin recognition, which presented in most cases a relative variation of the studied properties of more than double compared to the one obtained for lysozyme and IgG.

Concerning the results obtained for BSA, they were quite surprising. For this protein, the behavior obtained was opposite to that expected. This means that the interaction with BSA improved the charge transfer in the electrochemical system. In the literature it was found that at high BSA concentrations (above 800 nM) non-specific interactions between TBA-15 and BSA can occur [9]. Then, one hypothesis that could explain this result would be that the interaction between the TBA-15 bioreceptor and BSA may result in an aptamer folding that could favor the passage of the redox probe towards the electrode surface. This would mean for example that under this interaction, TBA-15 would present a more linear conformation, instead of the G-quadruplex conformation necessary for thrombin recognition. However, this is only a hypothesis, as no information was found in the literature regarding the folding of TBA-15 aptamer upon interaction with BSA. Additionally, it should be necessary to confirm the results obtained, because due to time constraints this selectivity analysis could only be carried out once, so in order to obtain a real conclusion it would be necessary to verify these results.

With regard to the general results obtained for the selectivity of Si nanonet-based biosensors, there are several methods that would allow to reduce the non-specific interactions of the biosensor. These methods are based on the modification of the biosensor surface, with the aim of blocking the free sites where the adsorption of interfering molecules could occur, for example, by the creation of a thin hydrophilic and non-charged boundary layer to thwart this non-specific interaction [29,30]. Thus, the possibilities for improving the selectivity of Si nanonet-based biosensors are open for future works.

### V.6. Conclusions

In the course of this chapter we studied the optimization of the parameters involved in the fabrication of Si nanonet-based electrochemical biosensors, aiming to obtain sensors presenting a good sensitivity for thrombin detection.

First, it was found that increasing the concentration of the TBA-15 bioreceptor from 10  $\mu\text{M}$  to 50  $\mu\text{M}$  during the grafting step, improved the signal obtained for the thrombin detection. Second, it was concluded that the decrease of the Si nanonet density on the carbon electrode (from 54% to 15% of surface coverage) resulted in a higher signal upon thrombin detection. This was probably generated by a slower electron transfer on the biosensor presenting the lower Si nanonet density, due to the formation of a denser polypyrrole film on its surface. This slower electron transfer may in turn have favored the observation of the phenomena occurring on the electrode surface upon thrombin recognition.

Regarding the detection of the target molecule, very good results were obtained. For the first time, it was developed an electrochemical biosensor based on 2D Si nanonets capable of detecting thrombin in concentrations considered as a marker of risk or presence of thrombosis. On the one hand, the analysis carried out by cyclic voltammetry evidenced a linear correlation between the obtained current and the thrombin concentration from 5 nM a 2  $\mu\text{M}$ , presenting a sensitivity of 0.64  $\mu\text{A}$  per order of magnitude. On the other hand, the impedimetric sensor presented a linear relationship between the transfer charge resistance or the impedance modulus (at 3.46 Hz), and the thrombin concentration, in a range from 5 nM a 0.5  $\mu\text{M}$ , presenting a sensitivity of  $1100 \pm 200 \Omega$  and  $800 \pm 100 \Omega$  respectively.

These promising results open the door to new projects for the use of 2D Si nanonet structures in the field of electrochemical biosensing, which should be focused on increasing the sensitivity and selectivity of Si nanonet-based electrochemical devices.

## References

- [1] E. Di Cera, Thrombin, *Mol. Aspects Med.* 29 (2008) 203–254. <https://doi.org/10.1016/j.mam.2008.01.001>.
- [2] H. Krenzlin, V. Lorenz, S. Danckwardt, O. Kempfski, B. Alessandri, The importance of thrombin in cerebral injury and disease, *Int. J. Mol. Sci.* 17 (2016). <https://doi.org/10.3390/ijms17010084>.
- [3] M.E. Parsons, K. O’Connell, S. Allen, K. Egan, P.B. Szklanna, C. McGuigan, F. Ní Áinle, P.B. Maguire, Thrombin generation correlates with disease duration in multiple sclerosis (MS): Novel insights into the MS-associated prothrombotic state, *Mult. Scler. J. - Exp. Transl. Clin.* 3 (2017) 205521731774762. <https://doi.org/10.1177/2055217317747624>.
- [4] M. Marchetti, E. Diani, H. ten Cate, A. Falanga, Characterization of the thrombin generation potential of leukemic and solid tumor cells by calibrated automated thrombography, *Haematologica.* 97 (2012) 1173–1180. <https://doi.org/10.3324/haematol.2011.055343>.
- [5] J. Baur, C. Gondran, M. Holzinger, E. Defrancq, H. Perrot, S. Cosnier, Label-free femtomolar detection of target DNA by impedimetric DNA sensor based on poly(pyrrole-nitrilotriacetic acid) film, *Anal. Chem.* 82 (2010) 1066–1072. <https://doi.org/10.1021/ac9024329>.
- [6] W. Bode, Structure and interaction modes of thrombin, *Blood Cells, Mol. Dis.* 36 (2006) 122–130. <https://doi.org/10.1016/j.bcmed.2005.12.027>.
- [7] K.G. Mann, Thrombin: Can’t live without it; probably die from it, *Chest.* 124 (2003) 1S–3S. <https://doi.org/10.1378/chest.124.3>.
- [8] J.M. Siller-Matula, M. Schwameis, A. Blann, C. Mannhalter, B. Jilma, Thrombin as a multi-functional enzyme: Focus on in vitro and in vivo effects, *Thromb. Haemost.* 106 (2011) 1020–1033. <https://doi.org/10.1160/TH10-11-0711>.
- [9] A. Trapaidze, J.P. Héroult, J.M. Herbert, A. Bancaud, A.M. Gué, Investigation of the selectivity of thrombin-binding aptamers for thrombin titration in murine plasma, *Biosens. Bioelectron.* 78 (2016) 58–66. <https://doi.org/10.1016/j.bios.2015.11.017>.
- [10] J. Huang, Y. Zhu, H. Zhong, X. Yang, C. Li, Dispersed CuO nanoparticles on a silicon nanowire for improved performance of nonenzymatic H<sub>2</sub>O<sub>2</sub> detection, *ACS Appl. Mater. Interfaces.* 6 (2014) 7055–7062. <https://doi.org/10.1021/am501799w>.
- [11] B. Tao, J. Zhang, S. Hui, L. Wan, An amperometric ethanol sensor based on a Pd-Ni/SiNWs electrode, *Sensors Actuators, B Chem.* 142 (2009) 298–303. <https://doi.org/10.1016/j.snb.2009.08.004>.

- [12] L. Maiolo, D. Polese, A. Pecora, G. Fortunato, Y. Shacham-Diamand, A. Convertino, Highly Disordered Array of Silicon Nanowires: An Effective and Scalable Approach for Performing and Flexible Electrochemical Biosensors, *Adv. Healthc. Mater.* 5 (2016) 575–583. <https://doi.org/10.1002/adhm.201500538>.
- [13] Y. Liu, A. Rahimian, S. Krylyuk, T. Vu, B. Crulhas, G. Stybayeva, M. Imanbekova, D.S. Shin, A. Davydov, A. Revzin, Nanowire Aptasensors for Electrochemical Detection of Cell-Secreted Cytokines, *ACS Sensors*. 2 (2017) 1644–1652. <https://doi.org/10.1021/acssensors.7b00486>.
- [14] Q. Yan, Z. Wang, J. Zhang, H. Peng, X. Chen, H. Hou, C. Liu, Nickel hydroxide modified silicon nanowires electrode for hydrogen peroxide sensor applications, *Electrochim. Acta.* 61 (2012) 148–153. <https://doi.org/10.1016/j.electacta.2011.11.098>.
- [15] J. Yin, X. Qi, L. Yang, G. Hao, J. Li, J. Zhong, A hydrogen peroxide electrochemical sensor based on silver nanoparticles decorated silicon nanowire arrays, *Electrochim. Acta.* 56 (2011) 3884–3889. <https://doi.org/10.1016/j.electacta.2011.02.033>.
- [16] S. Hui, J. Zhang, X. Chen, H. Xu, D. Ma, Y. Liu, B. Tao, Study of an amperometric glucose sensor based on Pd-Ni/SiNW electrode, *Sensors Actuators, B Chem.* 155 (2011) 592–597. <https://doi.org/10.1016/j.snb.2011.01.015>.
- [17] D.H. Kwon, H.H. An, H.S. Kim, J.H. Lee, S.H. Suh, Y.H. Kim, C.S. Yoon, Electrochemical albumin sensing based on silicon nanowires modified by gold nanoparticles, *Appl. Surf. Sci.* 257 (2011) 4650–4654. <https://doi.org/10.1016/j.apsusc.2010.12.109>.
- [18] H. Shashaani, M. Faramarzpour, M. Hassanpour, N. Namdar, A. Alikhani, M. Abdolahad, Silicon nanowire based biosensing platform for electrochemical sensing of Mebendazole drug activity on breast cancer cells, *Biosens. Bioelectron.* 85 (2016) 363–370. <https://doi.org/10.1016/j.bios.2016.04.081>.
- [19] S. Su, Y. He, M. Zhang, K. Yang, S. Song, X. Zhang, C. Fan, S.T. Lee, High-sensitivity pesticide detection via silicon nanowires-supported acetylcholinesterase-based electrochemical sensors, *Appl. Phys. Lett.* 93 (2008). <https://doi.org/10.1063/1.2959827>.
- [20] K. Yang, H. Wang, K. Zou, X. Zhang, Gold nanoparticle modified silicon nanowires as biosensors, *Nanotechnology.* 17 (2006). <https://doi.org/10.1088/0957-4484/17/11/S08>.
- [21] B. Nasr, G. Chana, T.T. Lee, T. Nguyen, C. Abeyrathne, G.M. D'Abaco, M. Dottori, E. Skafidas, Vertical Nanowire Electrode Arrays as Novel Electrochemical Label-Free Immunosensors, *Small.* 11 (2015) 2862–2868. <https://doi.org/10.1002/smll.201403540>.
- [22] N. Mintz-Hemed, T. Yoetz-Kopelman, A. Convertino, A. Freeman, Y. Shacham-Diamand, Whole-Cell

- Electrochemical Biosensor Integrating Microbes with Si Nanowire-Forest, *J. Electrochem. Soc.* 164 (2017) B253–B257. <https://doi.org/10.1149/2.1471706jes>.
- [23] W. Chen, H. Yao, C.H. Tzang, J. Zhu, M. Yang, S.T. Lee, Silicon nanowires for high-sensitivity glucose detection, *Appl. Phys. Lett.* 88 (2006). <https://doi.org/10.1063/1.2206102>.
- [24] J.I. Abdul Rashid, N.A. Yusof, J. Abdullah, U. Hashim, R. Hajian, Surface modifications to boost sensitivities of electrochemical biosensors using gold nanoparticles/silicon nanowires and response surface methodology approach, *J. Mater. Sci.* 51 (2016) 1083–1097. <https://doi.org/10.1007/s10853-015-9438-6>.
- [25] H. Xu, K. Gorgy, C. Gondran, A. Le Goff, N. Spinelli, C. Lopez, E. Defrancq, S. Cosnier, Label-free impedimetric thrombin sensor based on poly(pyrrole-nitrilotriacetic acid)-aptamer film, *Biosens. Bioelectron.* 41 (2013) 90–95. <https://doi.org/10.1016/j.bios.2012.07.044>.
- [26] Y. Xu, L. Yang, X. Ye, P. He, Y. Fang, An Aptamer-Based Protein Biosensor by Detecting the Amplified, (2006). <https://doi.org/10.1002/elan.200603566>.
- [27] C. Deng, J. Chen, Z. Nie, M. Wang, X. Chu, X. Chen, X. Xiao, C. Lei, S. Yao, Impedimetric Aptasensor with Femtomolar Sensitivity Based on the Enlargement of Surface-Charged Gold Nanoparticles, 81 (2009) 739–745.
- [28] Y. Wang, B. Liu, Conjugated Polyelectrolyte-Sensitized Fluorescent Detection of Thrombin in Blood Serum Using Aptamer-Immobilized Silica Nanoparticles as the Platform, 25 (2009) 12787–12793. <https://doi.org/10.1021/la901703p>.
- [29] J.Y. Lichtenberg, Y. Ling, S. Kim, Non-Specific Adsorption Reduction Methods in Biosensing, (2019) 1–17.
- [30] S. Pan, H. Zhang, W. Liu, Y. Wang, W. Pang, X. Duan, Biofouling Removal and Protein Detection Using a Hypersonic Resonator, (2017). <https://doi.org/10.1021/acssensors.7b00298>.

# General conclusion

During the last 20 years, semiconducting Si nanowires have been extensively investigated in the field of biosensors because of their interesting properties, among which are the expertise and current knowledge allowing to control and modify every aspect of their fabrication process. This knowledge in turn enables to integrate them into devices, notably in the area of MOSFETs. In addition, Si nanowires are extremely sensitive to their external electrical environment, and their size is comparable to that of many biological entities, making them excellent candidates for electrical biosensing.

However, their integration on an industrial scale remains complex, costly and the devices produced currently present important problems of reproducibility of their characteristics. Aiming to overcome the aforementioned problems, we have focused on Si nanonets, which are composed of a 2D random network of silicon nanowires. Indeed, working with a large quantity of Si nanowires facilitates considerably their integration in functional devices. Moreover, the nanonets not only benefit from the intrinsic properties of each nanowire, but also offer remarkable new properties related to the nanonet structure, namely a better reproducibility, and high fault tolerance and flexibility, compared to individual Si nanowires.

For this purpose, two different types of biosensing devices were fabricated and developed, using Si nanonets as building blocks in view of electrical or electrochemical detection of two kinds of biomolecules:

- (i) Si nanonet-based FET biosensors for the electrical detection of DNA hybridization in dry environment
- (ii) Si nanonet-based electrochemical biosensors for thrombin detection. In both cases, the used bioreceptor was the same, namely the TBA – 15 aptamer.

The latter was grafted on the surface of Si nanonets, but differently according to the device. In this aim, various processes have been carefully studied and implemented.

Regarding the Si nanonet-based FET biosensors, in previous works carried out at LMGP, it was developed a fabrication process allowing to obtain Si nanonet-based FET devices with excellent electrical properties and reproducibility. On this basis, this work focused on the study of a biofunctionalization protocol, enabling the covalent immobilization of the bioreceptor on the surface of the Si nanonet-based FET, in an efficient and homogeneous way, while preserving the integrity of the FET devices. This goal was achieved by optimizing a process based on GOPS silane, using UV irradiation.

Once the Si nanonet-based FET devices were biofunctionalized, their ability to electrically detect the DNA hybridization in dry environment was carefully studied. However, we encountered some problems related to the reproducibility of the results. For this reason, it was carried out a detailed analysis of each of the parameters involved in the grafting stage, as well as the detection process. The obtained results allowed us to conclude that it is crucial to control some variables, such as the composition and pH of the solutions, and the level of hydration of the surface, in order to obtain devices with stable initial characteristics.

As far as the Si nanonet-based electrochemical biosensors are concerned, it was developed for the first time a process allowing the fabrication and biofunctionalization of an electrochemical biosensor based on 2D Si nanonets, aiming to detect thrombin. This Si nanonet-based biosensor was functionalized by means of a polypyrrole-NTA film fabricated by chemical polymerization, acting as a platform for the immobilization of the TBA-15 bioreceptor.

Finally, the parameters playing a role in the electrochemical properties of the biosensor, such as the Si nanonet density and TBA-15 bioreceptor concentration were optimized. This optimization process allowed to obtain electrochemical biosensors that can detect thrombin in a concentration as low as 5 nM. This important result reveals that the developed biosensor could detect either

the risk (5 to 20 nM thrombin in blood circulation), or the presence of thrombosis (above 20 nM thrombin in blood circulation).

These promising results open the door to future projects, which should be focused on improving the 2D nanonet based electrochemical sensor selectivity, as well as its performances.

# Résumé de la thèse en Français

## Développement de biocapteurs à base de réseaux de nanofils de silicium aléatoirement orientés pour une détection électrochimique ou à effet de champ

La nécessité croissante de développer des dispositifs portables permettant la détection et la quantification d'espèces biologiques de manière fiable, rapide et économique est l'un des défis auxquels la science est confrontée aujourd'hui. L'essor des nanotechnologies au cours des dernières décades a permis le développement d'une nouvelle génération de biocapteurs basés sur des nanostructures, qui présentent des caractéristiques très intéressantes, telles qu'une surface spécifique élevée, de taille comparable à la plupart des molécules biologiques. Ces propriétés ont ouvert la voie au développement de capteurs ultrasensibles, capables de fournir des informations en temps réel.

Parmi ces nanostructures, les nanofils de silicium semi-conducteurs ont été largement étudiés. Au-delà des propriétés mentionnées, ces nanostructures bénéficient d'une large expertise concernant leurs procédés de fabrication et leur intégration dans des dispositifs électroniques. Cependant, les dispositifs fabriqués à partir de ce type de nanostructures nécessitent l'utilisation de procédés technologiques complexes, longs et coûteux, présentant souvent des problèmes de reproductibilité.

Dans ce contexte, et pour la première fois, ce projet étudie la possibilité d'utiliser un assemblage 2D de nanofils de silicium aléatoirement orientés, appelé *nanonet de silicium*, comme matériau de base pour la fabrication et le développement de deux types différents de dispositifs: des biocapteurs à effet de champ (FET), et des biocapteurs électrochimiques. En effet, ce type de réseau 2D bénéficie des propriétés intrinsèques de chaque nanofil 1D le constituant, et notamment de leur très grande surface spécifique. De plus, par rapport aux dispositifs composés de nanofils de Si uniques, l'utilisation d'un réseau 2D offre d'autres propriétés très intéressantes,

telles qu'une haute tolérance aux défauts, flexibilité mécanique, et une meilleure reproductibilité électrique.

Ces deux types de biocapteurs basés ainsi sur des nanonets de silicium visent à détecter, d'une part, l'hybridation de l'ADN dans un environnement sec pour le cas du biocapteur FET, et d'autre part, la détection de la thrombine en milieu liquide dans le cas du biocapteur électrochimique. Ces deux dispositifs ont été biomodifiés en utilisant le même biorécepteur : l'aptamère TBA-15. Cependant, le mode de biomodification a été différent selon le dispositif considéré.

Ainsi, ce travail est divisé en cinq chapitres :

**Le chapitre I** présente un aperçu de la définition et des composants d'un biocapteur, des différentes méthodes utilisées pour sa biofonctionnalisation et des techniques de transduction employées.

De manière générale, un biocapteur a pour but de détecter et, dans certains cas, de quantifier une cible spécifique, grâce à l'interaction entre un élément biologique ou biorécepteur, capable de générer un événement de reconnaissance au moment de l'interaction avec sa cible, et un élément physique qui agit comme un transducteur, convertissant l'événement de reconnaissance en un signal physiquement détectable. Ces dispositifs sont actuellement utilisés dans une grande variété de domaines, tels que le diagnostic clinique, la traçabilité, la qualité et la sécurité des aliments, la détection de médicaments ou de substances dangereuses, la gestion de la qualité de l'eau et la surveillance de la pollution. La recherche dans ce domaine est actuellement orientée vers la miniaturisation des dispositifs pour plusieurs raisons, comme le besoin de développer des dispositifs portables pour une analyse rapide (résultats obtenus en quelques minutes), la demande croissante pour le développement de biocapteurs jetables, et en raison de la recherche permanente de réduction des coûts. Dans le cas de ce projet, le biorécepteur utilisé est l'aptamère TBA-15, le transducteur est construit à partir du nanonet de silicium, et l'événement de

reconnaissance peut être observé à partir d'un changement des propriétés électriques du dispositif.

En ce qui concerne la biofonctionnalisation du dispositif, il s'agit d'une étape fondamentale dans le développement du biocapteur, puisque le but est de réaliser le greffage des molécules sondes de manière appropriée, et cela a un impact direct sur les performances du dispositif, tels que la sensibilité, la sélectivité et le temps de réponse. Diverses approches de biofonctionnalisation ont été utilisées dans le domaine de la biodétection, cependant, dans ce projet, l'immobilisation des biorécepteurs a été réalisée de deux manières différentes : un greffage covalent et un greffage par affinité.

Finalement, le mécanisme de transduction du biocapteur est chargé de convertir l'événement de reconnaissance de la molécule cible en un signal électrique qui peut être traité, enregistré et transmis à l'aide de systèmes électroniques. Dans notre cas, (biocapteur électrique), il signale la reconnaissance de la cible à travers d'un signal de courant ou de tension généré au moment de la reconnaissance.

**Le chapitre II** aborde le procédé de fabrication des dispositifs FET à base nanonets de silicium, ainsi que les différentes voies étudiées pour leur biofonctionnalisation, via deux organosilanes différents : (3-Aminopropyl)triéthoxysilane (APTES) and (3-Glycidylxypropyl)triméthoxysilane (GOPS).

Dans le cas du procédé de biofonctionnalisation APTES, un problème de décollement des contacts métalliques a été rencontré, qui s'est produit lors de la dernière étape du procédé de biofonctionnalisation. En effet, lors de l'étape consistant en la réduction des liaisons imines, des bulles d' $H_2$  générées comme sous-produit de la réaction ont provoqué le décollement des contacts métalliques dans les dispositifs FETs. Pour cette raison, il a été décidé de travailler sur la deuxième alternative : le procédé de biofonctionnalisation GOPS. Ce protocole a présenté des problèmes liés à l'homogénéité de la distribution du biorécepteur immobilisé sur la surface.

Cependant, ces problèmes ont été résolus en optimisant la procédure à l'aide d'un traitement par rayonnement UVA. Les meilleurs résultats ont été obtenus avec une irradiation 20 minutes. Ce traitement a permis d'améliorer considérablement l'homogénéité de la distribution des biorécepteurs en surface.

Des études STEM-EDS et AFM ont confirmé la correcte immobilisation du biorécepteur TBA-15 sur la surface des dispositifs FET lors de l'utilisation du protocole de biofonctionnalisation GOPS assisté par UVA. Finalement, l'étude morphologique réalisée par AFM a montré que la composition des bases dans la séquence d'ADN a un impact considérable sur sa structure à la surface du biocapteur.

**Le chapitre III** porte sur la détection électrique de l'hybridation de l'ADN, en utilisant des dispositifs FET à base de nanonets de silicium dans un environnement sec. Dans ce but, les différents paramètres impliqués dans le processus de détection ont été étudiés et optimisés. En ce qui concerne la stabilité des dispositifs FET dans des conditions environnementales, il a été démontré que leurs propriétés électriques après le greffage du biorécepteur TBA-15 sont dépendantes du temps. Ce fait est probablement lié à l'évolution de l'hydratation du biorécepteur qui diminue avec le temps.

Par ailleurs, il a été noté que la capacité d'hybridation du biorécepteur TBA-15 est également dépendante du temps, ce qui peut s'expliquer par la formation des multimères à partir des structures G-quadruplex. Ces multimères peuvent être stabilisées par la déshydratation des structures au fur et à mesure que le temps avance, et peuvent être renforcés par la présence d'ions potassium dans le tampon d'hybridation.

Finalement, il a été démontré que le pH de la solution tampon joue également un rôle important dans la réponse électrique du biocapteur, ce qui en fait un paramètre qui doit être soigneusement contrôlé.

**Le chapitre IV** présente le développement du biocapteur électrochimique à base de nanonets de silicium pour la détection de la thrombine. À cette fin, différentes études ont été menées, telles que le choix du matériau de l'électrode de travail à utiliser comme substrat pour le nanonet, le développement d'un protocole permettant la fabrication et la biofonctionnalisation des électrodes et le choix de la sonde redox appropriée pour le système électrochimique.

Les études réalisées ont permis le développement d'un biocapteur électrochimique basé sur des nanonets de silicium, fabriqué sur une électrode de travail en carbone vitreux, et fonctionnalisé au moyen d'une nouvelle méthode développée dans ce projet. Cette méthode s'effectue par le dépôt d'un film de polypyrrole-NTA réalisé par polymérisation chimique. Ce film sert de plateforme pour l'immobilisation du biorécepteur TBA-15, par complexation des ions  $\text{NTA-Cu}^{2+}$ , ce qui ultérieurement facilite l'immobilisation du TBA-15 biotinylé, par coordination des groupes biotine sur le complexe  $\text{NTA-Cu}^{2+}$ .

Finalement, **le chapitre V** explore la détection de la thrombine à partir de biocapteurs électrochimiques à base de nanonets de silicium et fonctionnalisés par de films de polypyrrole-NTA. Ainsi, les différents paramètres impliqués dans les performances du biocapteur, tels que la densité du nanonet et la concentration du biorécepteur ont été optimisés, visant à obtenir des capteurs présentant une bonne sensibilité pour la détection de la molécule cible.

Premièrement, il a été constaté que l'augmentation de la concentration du biorécepteur TBA-15 de  $10\ \mu\text{M}$  à  $50\ \mu\text{M}$  pendant l'étape de greffage, améliore le signal obtenu pour la détection de la thrombine. Deuxièmement, et de manière contre-intuitive, il a été conclu que la diminution de la densité de nanonets de silicium sur l'électrode de carbone (de 54% à 15% de recouvrement de surface) permet d'obtenir un signal plus élevé lors de la détection de la thrombine. Ceci est probablement généré par un transfert d'électrons plus lent sur le biocapteur présentant la plus faible densité de nanonets, en raison de la formation d'un film de polypyrrole plus dense à sa surface. Ce transfert d'électrons plus lent peut à son tour favoriser une meilleure observation de

des phénomènes se produisant à la surface de l'électrode lors de la reconnaissance de la thrombine.

En ce qui concerne la détection de la thrombine, de très bons résultats ont été obtenus. Pour la première fois, il a été développé un biocapteur électrochimique basé sur des nanonets silicium 2D capable de détecter la thrombine à des concentrations considérées comme un marqueur de risque ou de présence de thrombose.

Ces résultats prometteurs ouvrent la porte à de nouveaux projets d'utilisation des nanonets de silicium 2D dans le domaine de la biodétection, qui pourrait être axés sur l'augmentation de la sensibilité et de la sélectivité des dispositifs.

## Abstract

Randomly oriented nanowire networks (nanonets) exhibit interesting properties, arising from the intrinsic properties of the individual nanostructures, but also offer remarkable new properties related to the nanonet structure, namely a better reproducibility, and high fault tolerance and flexibility. In this context, this project investigated the possibility of using a 2D assembly of randomly oriented Si nanowires (Si nanonet), as building blocks for the fabrication and development of two different types of biosensors: Field-effect transistor (FET) biosensors for the electrical detection of DNA hybridization, and electrochemical biosensors for thrombin detection.

For this purpose, the development of each type of sensor was divided into three parts: (i) fabrication of the Si nanonet-based device, (ii) biofunctionalization of the device allowing the grafting of the bioreceptor (TBA-15 aptamer), and (iii) detection of the target molecule.

Regarding the Si nanonet-based FET biosensors, the work focused on the implementation and the optimization of a biofunctionalization protocol, enabling the proper immobilization of the bioreceptor on the surface of the Si nanonet-based FETs. Then, the ability to electrically detect the DNA hybridization in dry environment was studied. Concerning the electrochemical biosensors, it was developed for the first time a process allowing the fabrication and biofunctionalization of a 2D Si nanonet-based biosensor, enabling thrombin detection in nM concentrations, which indicates either the risk or the presence of thrombosis. These promising results open the door to future projects implying the use of 2D Si nanonet-based devices in the field of biodetection.

## Résumé

Les réseaux de nanofils aléatoirement orientés (nanonets) présentent des propriétés intéressantes, liées aux propriétés intrinsèques des nanostructures individuelles, mais offrent également de nouvelles propriétés remarquables associées à la structure du réseau, à savoir, une bonne reproductibilité, une grande tolérance aux défauts et une flexibilité importante. Dans ce contexte, ce projet a étudié la possibilité d'utiliser un assemblage 2D de nanofils de Si aléatoirement orientés (Si nanonet), comme élément de base pour la fabrication et le développement de deux types différents de biocapteurs: des biocapteurs à effet de champ (FET) pour la détection électrique de l'hybridation de l'ADN, et des biocapteurs électrochimiques pour la détection de la thrombine.

À cette fin, le développement de chacun de ces biocapteurs a été divisé en trois parties : (i) fabrication d'un dispositif à base de nanonets de silicium, (ii) biofonctionnalisation du dispositif permettant le greffage du biorécepteur (TBA-15 aptamère) et (iii) détection de la molécule cible.

En ce qui concerne les biocapteurs FET à base de nanonets de silicium, le travail effectué s'est concentré sur la mise au point et l'optimisation d'un protocole de biofonctionnalisation, permettant l'immobilisation correcte du biorécepteur sur la surface du dispositif FET. Puis, la capacité des biocapteurs FET à détecter électriquement l'hybridation de l'ADN en milieu sec a été étudiée. Concernant les biocapteurs électrochimiques à base de nanonets de silicium, il a été développé pour la première fois une procédure pour la fabrication et la biofonctionnalisation d'un biocapteur électrochimique à base de nanofils de silicium 2D, permettant la détection de la thrombine dans des concentrations de l'ordre du nM, indiquant le risque ou la présence d'une thrombose. Ces résultats prometteurs ouvrent la porte à de futurs projets impliquant l'utilisation de dispositifs basés sur des nanonets de silicium dans le domaine de la biodetection.